

# Characterization of High-Temperature Corrosion and Self-Healing of Rare Earth-Silicate for Environmental Barrier Coatings

金, 昇炫

<https://hdl.handle.net/2324/6787638>

---

出版情報 : Kyushu University, 2022, 博士 (工学), 課程博士  
バージョン :  
権利関係 :

Ph. D. Thesis

**Characterization of High-Temperature Corrosion  
and Self-Healing of Rare Earth-Silicate for  
Environmental Barrier Coatings**

**耐環境コーティング用 RE-シリケートの  
高温腐食及び自己治癒特性評価**

Department of Applied Science for Electronics and Materials  
Interdisciplinary Graduate School of Engineering Sciences  
Kyushu University

金昇炫

**KIM SEUNG HYEON**

Supervisor: Prof. Byung-Koog Jang

January, 2023

博士学位論文

**Characterization of High-Temperature Corrosion  
and Self-Healing of Rare Earth-Silicate for  
Environmental Barrier Coatings**

耐環境コーティング用 RE-シリケートの  
高温腐食及び自己治癒特性評価

九州大学

大学院総合理工学府

量子プロセス理工学専攻

金昇炫

**KIM SEUNG HYEON**

指導教員: 張炳國

**2023年 1月**

**論文調査委員会**

主査 九州大学 教授 張炳國

副査 九州大学 教授 波多聰

副査 九州大学 教授 島ノ江憲剛

## Abstract

In general, fuel efficiency can be achieved by increasing the gas inlet temperature of the hot section of a gas turbine engine. This is possible by replacing some of the hot section Ni-based superalloys of gas turbine engines with SiC/SiC ceramic matrix composites (CMCs). However, non-oxide silicon-based ceramics are unstable in the presence of gaseous combustion products such as water vapor and carbon dioxide, their application requires the development of environmental barrier coatings (EBCs) for application as external shielding. However, during high-temperature operation of a gas turbine engine, chemical attack on EBCs by molten silicate deposits known as calcia-magnesia-alumina-silica (CMAS) leads to degradation and physical attack (mechanical fatigue and thermal shock) by gas residues or particle collisions causes cracks on the surface of EBCs. To solve these problems, rare-earth (RE) silicates ( $\text{RE}_2\text{SiO}_5$  and  $\text{RE}_2\text{Si}_2\text{O}_7$ ) have been proposed as promising EBC materials. RE-silicates exhibit many attractive properties such as high temperature resistance, low coefficient of thermal expansion (CTE), good chemical stability and good adhesion to SiC.

The main purpose of this thesis is that high-temperature corrosion resistance and self-healing properties of rare earths (RE) silicate applied to EBCs were evaluated. Comparison of reaction layers according to corrosion parameters (volcanic ash and CMAS (CaO:SiO<sub>2</sub> ratio), disilicate ( $\text{RE}_2\text{Si}_2\text{O}_7$ ) and monosilicate ( $\text{RE}_2\text{SiO}_5$ ), ionic radius, dual disilicate) to improve high-temperature corrosion behavior. In addition, it is performed to compare the crack healing rate according to the healing parameters (time, temperature, and SiC vol.%) in which nano healing agent (SiC) is added to  $\text{RE}_2\text{Si}_2\text{O}_7$  and to improve self-healing properties. The following shows the achievements of this thesis.

**In chapter 1**, the general introduction of this study was presented. The background information and research trends are included to help you understand EBCs material such as

RE-silicate, and the high-temperature corrosion behavior and self-healing properties are included. In particular, the motivation and final objectives of this study and the main purpose of each chapter were briefly summarized.

**In chapter 2**, the sintered  $\text{Gd}_2\text{SiO}_5$  by spark plasma sintering (SPS) was prepared and high-temperature corrosion behavior to volcanic ash was evaluated at  $1400^\circ\text{C}$  for 48 h. The sintered  $\text{Gd}_2\text{SiO}_5$  was partially dissolved in the molten ash to form a reaction layer.  $\text{Gd}_2\text{SiO}_5$  and Ca component of volcanic ash react at  $1300^\circ\text{C}$  to form  $\text{Ca}_2\text{Gd}_8(\text{SiO}_4)_6\text{O}_2$  phase. The  $\text{Ca}_2\text{Gd}_8(\text{SiO}_4)_6\text{O}_2$  particles observed in the reaction layer are needle morphology and the heat-treatment time increases. A dense reactive layer is described as impeding the penetration of molten volcanic ash.

**In chapter 3**, the reaction layer thickness was compared according to the  $\text{CaO}:\text{SiO}_2$  ratios (CMAS (0.73), volcanic ash (0.11)). High-temperature corrosion behavior was evaluated by isothermal heat treatment of sintered  $\text{Gd}_2\text{SiO}_5$  and CMAS at  $1400^\circ\text{C}$  for 48 h. CMAS analyzed melting at  $1243^\circ\text{C}$  or higher through DSC and chemically reacted with  $\text{Gd}_2\text{SiO}_5$  to form a reaction layer ( $\text{Ca}_2\text{Gd}_8(\text{SiO}_4)_6\text{O}_2$ ). As the heat-treatment time increased,  $\text{Ca}_2\text{Gd}_8(\text{SiO}_4)_6\text{O}_2$  particles were needle morphology and grew vertically at the interface between  $\text{Gd}_2\text{SiO}_5$  and CMAS. CMAS (0.73) with a high  $\text{CaO}:\text{SiO}_2$  ratio has a thicker reaction layer than volcanic ash (0.11) in chapter 2, preventing additional molten CMAS penetration.

**In chapter 4**, to develop an understanding of the high temperature corrosion behavior of  $\text{RE}_2\text{SiO}_5$  and  $\text{RE}_2\text{Si}_2\text{O}_7$  to CMAS affecting the durability of EBCs systems. The high-temperature corrosion behavior of sintered  $\text{Gd}_2\text{Si}_2\text{O}_7$  with calcia-magnesia-alumina-silica (CMAS) melt was evaluated at  $1400^\circ\text{C}$  for 0.5 to 100 h. CMAS and sintered  $\text{Gd}_2\text{Si}_2\text{O}_7$  were

chemically reacted to form  $\text{Ca}_2\text{Gd}_8(\text{SiO}_4)_6\text{O}_2$  at  $1300^\circ\text{C}$ . The reaction layer became thicker as the heat treatment time increased, and the thickness of the reaction layer increased along a parabola. It was confirmed that  $\text{Ca}_2\text{Gd}_8(\text{SiO}_4)_6\text{O}_2$  grew perpendicular to the  $\text{Gd}_2\text{Si}_2\text{O}_7$  surface.  $\text{RE}_2\text{Si}_2\text{O}_7$  reacts with  $\text{CaO}$  in the melt to form the apatite phase, releasing  $\text{SiO}_2$ , whereas  $\text{RE}_2\text{SiO}_5$  reacts with both  $\text{CaO}$  and  $\text{SiO}_2$ , with only the apatite phase being produced. That is,  $\text{Gd}_2\text{Si}_2\text{O}_7$  has a thicker reaction layer than  $\text{Gd}_2\text{SiO}_5$  in chapter 3, so that additional molten CMAS permeation can be prevented.

**In chapter 5**, comparison of the high-temperature layer thicknesses by CMAS according to the ionic radius ( $\text{Gd}$  ( $1.107 \text{ \AA}$ ) and  $\text{Er}$  ( $1.004 \text{ \AA}$ )). The suitability of sintered  $\text{Er}_2\text{Si}_2\text{O}_7$  as a promising material for EBCs was characterized by high-temperature corrosion behavior in contact with CMAS melt. High-temperature corrosion behavior was performed by applying CMAS to sintered  $\text{Er}_2\text{Si}_2\text{O}_7$  and heating it to  $1400^\circ\text{C}$  for 48 h.  $\text{Er}_2\text{Si}_2\text{O}_7$  and CMAS were observed to react chemically to form  $\text{Ca}_2\text{Er}_8(\text{SiO}_4)_6\text{O}_2$  phase.  $\text{Ca}_2\text{Er}_8(\text{SiO}_4)_6\text{O}_2$  particles were observed to grow vertically on the  $\text{Er}_2\text{Si}_2\text{O}_7$  surface. When the reaction layer was compared under the same conditions (CMAS component, temperature, time), a thinner reaction layer thickness than that of  $\text{Gd}_2\text{Si}_2\text{O}_7$  was formed in chapter 4. That is, it was confirmed that the smaller the ionic radius, the thinner the reaction layer thickness formation.

**In chapter 6**, the high-temperature corrosion mechanism was successfully improved by comparing the corrosion layer of single  $\text{RE}_2\text{Si}_2\text{O}_7$  and dual  $\text{RE}_2\text{Si}_2\text{O}_7$ . Sintered  $\text{Gd}_2\text{Si}_2\text{O}_7$  (70%)+ $\text{SC}_2\text{Si}_2\text{O}_7$  (30%) and CMAS melts applied as promising EBC materials is evaluated for 48 h at  $1400^\circ\text{C}$ . As a result of high-temperature corrosion of  $\text{Gd}_2\text{Si}_2\text{O}_7$  (70%)+ $\text{SC}_2\text{Si}_2\text{O}_7$  (30%) and CMAS,  $\text{SC}_2\text{Si}_2\text{O}_7$  did not react with CMAS and  $\text{Gd}_2\text{Si}_2\text{O}_7$  reacted with  $\text{Ca}$  of CMAS to form  $\text{Ca}_2\text{Gd}_8(\text{SiO}_4)_6\text{O}_2$ . When comparing the single  $\text{Gd}_2\text{Si}_2\text{O}_7$  (100%) and the high-temperature

corrosion reaction layer of CMAS in chapter 5, it was reduced by 20% ( $306 \rightarrow 238 \mu\text{m}$ ). This suggests a way to modulate the CMAS interaction in dual RE-disilicate, which could lead to excellent EBCs lifespan extension.

**In chapter 7**, self-healing properties were successfully improved in composites containing nano-healing agents (SiC) in  $\text{RE}_2\text{Si}_2\text{O}_7$  ( $\text{Sc}_2\text{Si}_2\text{O}_7$ ,  $\text{Yb}_2\text{Si}_2\text{O}_7$ ) depending on time, temperature, and SiC vol.%. We evaluated the high-temperature oxidation and self-healing behavior of nanocomposites dispersed with 10 vol.% SiC nanoparticles in  $\text{Sc}_2\text{Si}_2\text{O}_7$ , and nanocomposites dispersed with 20 vol.% SiC nanoparticles in  $\text{Yb}_2\text{Si}_2\text{O}_7$  which are promising as materials for EBCs. The artificially induced 2 kgf surface cracks did not fully recover after 10 h at  $1100^\circ\text{C}$ , but fully recovered after heat treatment at  $1300^\circ\text{C}$  for 5 h in air in  $\text{Sc}_2\text{Si}_2\text{O}_7/\text{SiC}$  10 vol.%. Crack-healing after 2 h at  $1100^\circ\text{C}$  was about 10% and increased to about 49% after 5 h, but at  $1300^\circ\text{C}$  a recovery of more than 90% was achieved from 0.5 h in  $\text{Yb}_2\text{Si}_2\text{O}_7/20$  vol.% SiC. The self-healing mechanism is due to the volume expansion of SiC at high temperatures due to oxidation to  $\text{SiO}_2$ . As a result, the crack healing rate increased as time ( $0.5 \rightarrow 10$  h), temperature ( $1100 \rightarrow 1300^\circ\text{C}$ ), and SiC vol.% ( $10 \rightarrow 20$  vol.%) increased.

The comprehensive experimental results and conclusions of each chapter of Ph.D. thesis are summarized **in chapter 8**.

## List of Figures

Figure 1.	Schematic of a gas turbine engine .....	1
Figure 2.	The evolution of turbine inlet gas temperature with generations of high temperature technologies including single crystal (SX) superalloys, ceramic matrix composite (CMCs), film cooling, thermal barrier coatings (TBCs) and environmental barrier coatings (EBCs). .....	2
Figure 3.	Conventional EBCs structure. ....	4
Figure 4.	Schematic of the main five requirements that any successful EBCs. ....	7
Figure 5.	Timeline of the evolution in the design of EBCs. ....	9
Figure 6.	Sintered mullite reacted with Icelandic VA after heat treatment. ....	10
Figure 7.	Coating-systems for CMCs. a Cross-sectional SEM image of BSAS/BSAS+Mullite/Si EBC on melt-infiltrated (MI) CMCs. b Cross sectional optical micrograph of multilayer T/EBC on CMCs. ....	14
Figure 8.	Schematic of a typical environmental barrier coating system (EBCs) for SiC/SiC ceramic matrix composites (CMCs) with in-service degradation mechanisms. .	18
Figure 9.	Sintered $\text{Yb}_2\text{SiO}_5$ was reacted with CMAS ash after heat treatment. ....	19
Figure 10.	Functional comparison of monociliate and disilicate for application of EBCs. .... .....	20
Figure 11.	Schematic diagram of self-crack healing of EBCs applied to aircraft gas turbine. . .....	23
Figure 12.	Schematic diagram of self-crack healing caused by oxidation reaction. ....	25
Figure 13.	DDSC results of volcanic ash powder and volcanic ash– $\text{Gd}_2\text{SiO}_5$ (1 : 1 wt.%) mixed powder. ....	41
Figure 14.	SEM images of a cross section after heat treatment at 1400°C with volcanic ash:	

(a), (d) 2 h; (b), (e) 12 h; and (c), (f) 48 h. ....	42
Figure 15. EDS mapping results of heat-treated Gd <sub>2</sub> SiO <sub>5</sub> at 1400°C for 12 h with volcanic ash. .....	43
Figure 16. SEM images of heat-treated Gd <sub>2</sub> SiO <sub>5</sub> at 1400°C for 12 h with volcanic ash of the red area in Fig. 15. ....	44
Figure 17. EDS mapping results of heat-treated Gd <sub>2</sub> SiO <sub>5</sub> at 1400°C for 48 h with volcanic ash. .....	45
Figure 18. Results by compositional line analysis of heat-treated Gd <sub>2</sub> SiO <sub>5</sub> at 1400°C for 48 h with volcanic ash: (a) cross sectional SEM image of the specimen and analyzed part of the red area in Fig. 17 and (b) result of compositional line analysis. ....	46
Figure 19. HT-XRD patterns of mixed volcanic ash–Gd <sub>2</sub> SiO <sub>5</sub> powder (1 : 1 wt.%) during a heating step at (a) 25°C, (b) 1100°C, (c) 1200°C, (d) 1300°C, (e) 1400°C, and a cooling step at (f) 25°C. ....	48
Figure 20. Thickness of the reacted layer with the heat-treatment time. ....	49
Figure 21. Comparison of DSC results of CMAS powder and CMAS + Gd <sub>2</sub> SiO <sub>5</sub> powder. .... .....	59
Figure 22. SEM images of cross section after CMAS corrosion at 1400°C: (a) CMAS-2 h, (b) CMAS-12 h, and (c) CMAS-48 h. ....	60
Figure 23. EDS element mapping of cross-sectional results of sintered Gd <sub>2</sub> SiO <sub>5</sub> at 1400°C for 2 h with CMAS. ....	61
Figure 24. High magnification of SEM images of the red area in Fig. 23. ....	62
Figure 25. EDS element mapping of cross-sectional results of sintered Gd <sub>2</sub> SiO <sub>5</sub> at 1400°C for 12 h with CMAS. ....	64
Figure 26. EDS linear scan of cross sections of sintered Gd <sub>2</sub> SiO <sub>5</sub> after CMAS corrosion at 1400°C for 12 h. (a) SEM image of the result by CMAS of heat-treated Gd <sub>2</sub> SiO <sub>5</sub>	

	and (b) result of the compositional red line analysis in (a). .....	65
Figure 27.	HT-XRD patterns of $Gd_2SiO_5$ powder (a) 25°C, (b) 1300°C and CMAS – $Gd_2SiO_5$ mixed powder (1 : 1 wt.%). From heating step at (c) 25°C, (d) 1100°C, (e) 1200°C, (f) 1300°C, and (g) 1400°C and from cooling step at (h) 25°C. ....	67
Figure 28.	Revised CaO-SiO <sub>2</sub> -GdO <sub>1.5</sub> ternary phase diagram at 1400°C. ....	69
Figure 29.	Thickness of the reacted area for sintered $Gd_2SiO_5$ ( $Gd_{9.33}(SiO_4)_6O_2$ ) as a function of heat treatment times at 1400°C. ....	70
Figure 30.	A schematic illustration of the mechanism of CMAS corrosion on sintered $Gd_2SiO_5$ ( $Gd_{9.33}(SiO_4)_6O_2$ ) at 1400°C: (a) the initial condition, (b) formation of the reaction area between CMAS and sintered $Gd_2SiO_5$ ( $Gd_{9.33}(SiO_4)_6O_2$ ), (c) formation of the reaction area and sintered $Gd_2SiO_5$ ( $Gd_{9.33}(SiO_4)_6O_2$ ), (d) morphology of the reaction area. ....	72
Figure 31.	(a) SEM micrograph of a thermally-etched sintered $Gd_2Si_2O_7$ and (b) HT-XRD results of $Gd_2Si_2O_7$ powder. ....	87
Figure 32.	HT-XRD patterns of mixed CMAS + $Gd_2Si_2O_7$ powder (1 : 1 wt.%): at (a) 25°C, (b) 1100°C, (c) 1200°C, (d) 1300°C, and during cooling at (e) 25°C. ....	89
Figure 33.	Cross-sectional SEM micrograph of sintered $Gd_2Si_2O_7$ after the interaction with CMAS at 1400°C: for (a) 0.5 h, (b) 2 h, (c) 12 h, (d) 48 h, and (e) 100 h. ....	90
Figure 34.	SEM micrograph of sintered $Gd_2Si_2O_7$ after the interaction with CMAS at 1400°C for 2 h: (a) cross-sectional SEM micrograph of CMAS, $Ca_2Gd_8(SiO_4)_6O_2$ , and sintered $Gd_2Si_2O_7$ , (b) EDS line analysis results for the region shown with the yellow arrow. ....	92
Figure 35.	EDS map (Ca, Si, Al, O, and Gd) of sintered $Gd_2Si_2O_7$ after the interaction with CMAS at 1400°C for 12 h. ....	93
Figure 36.	(a) Low- and (b) cross-sectional SEM micrographs of sintered $Gd_2Si_2O_7$ after the	

interaction with CMAS at 1400°C for 12 h: parts A, B (CMAS), and C, D (reaction region). .....	94
Figure 37. Average thickness of reaction layer at 1400°C as a function of heat-treatment time. ....	95
Figure 38. Cross-sectional SEM micrograph of sintered $Gd_2Si_2O_7$ after the interaction with CMAS at 1400°C: for (a) 0.5 h, (b) 2 h, (c) 12 h, (d) 48 h, and (e) 100 h. ....	98
Figure 39. The average grain size as a function of the distance from the $Gd_2Si_2O_7$ surface for different heat-treatment time. ....	100
Figure 40. DDSC results of (a) CMAS powder and (b) mixed CMAS/ $Er_2Si_2O_7$ (1:1 wt.%) powder. ....	111
Figure 41. Results of SEM images of (a) surface and (b) cross-section of sintered $Er_2Si_2O_7$ , (c) XRD patterns on $Er_2Si_2O_7$ powder. ....	113
Figure 42. HT-XRD spectra of mixed CMAS/ $Er_2Si_2O_7$ powders (1:1 wt.%) at different temperatures: (a) 25°C before heat-treatment, (b) 1100°C, (c) 1200°C, (d) 1300°C, (e) 1400°C, and (f) after cooling back to 25°C. ....	114
Figure 43. Cross-sectional SEM images of sintered $Er_2Si_2O_7$ after exposure to CMAS at 1400°C for heat-treatment times of (a) 2 h, (b) 12 h, and (c) 48 h. ....	115
Figure 44. Average thickness of the reaction layer between CMAS and $Er_2Si_2O_7$ at 1400°C as a function of heat-treatment time. ....	116
Figure 45. EDS maps of elements Si, Ca, O, and Er in sintered $Er_2Si_2O_7$ after contact with CMAS at 1400°C for 48 h: Regions A, B, and C correspond to CMAS, reaction product, and $Er_2Si_2O_7$ regions, respectively. ....	117
Figure 46. Average concentrations (at.%) of elements in molten CMAS near the reaction layer as a function of heat-treatment time. ....	119
Figure 47. (a) High-magnification SEM image of sintered $Er_2Si_2O_7$ after exposure to CMAS	

at 1400°C for 48 h showing $\text{Er}_2\text{Si}_2\text{O}_7$ grains and $\text{Ca}_2\text{Er}_8(\text{SiO}_4)_6\text{O}_2$ grains; (b) EDS line measurements taken along the yellow scan line in (a). .....	121
Figure 48. Schematic illustration of the formation of the reaction layer on sintered $\text{Er}_2\text{Si}_2\text{O}_7$ in contact with CMAS: (a) initial state, (b) formation of reaction layer between CMAS and $\text{Er}_2\text{Si}_2\text{O}_7$ at high temperature, and (c) a magnified view of the reaction layer showing the particle morphologies. ....	123
Figure 49. The results of (a) SEM image of a sintered Gd7-Sc3 and (b) XRD patterns on Gd7-Sc3 powder. ....	134
Figure 50. The results of XRD patterns on (a) sintered Gd7-Sc3 after heat treatment for (b) 0.5 h, (c) 2 h, (d) 12 h, and (e) 48 h. ....	135
Figure 51. Cross-sectional SEM micrograph of sintered Gd7-Sc3 which have interacted with CMAS at 1400°C: (a) 0.5 h, (b) 2 h, (c) 12 h, and (d) 48 h. ....	136
Figure 52. Sintered Gd7-Sc3 average value of thickness of reaction layer at 1400°C as a function of heat-treatment time. ....	137
Figure 53. EDS mapping components (Si, Ca, Sc, and Gd) of sintered Gd7-Sc3 which have interacted with CMAS at 1400°C for 0.5 h. ....	139
Figure 54. EDS mapping components (Si, Ca, Sc, and Gd) of sintered Gd7-Sc3 which have interacted with CMAS at 1400°C for 48 h. ....	140
Figure 55. (a) Low- and (b) cross-sectional SEM micrograph of sintered Gd7-Sc3 which have interacted with CMAS at 1400°C for 2 h in the red box of Fig. 55 (a). ....	141
Figure 56. EDS mapping components (Si, Ca, Sc, and Gd) of reaction layer of sintered Gd7-Sc3 which have interacted with CMAS in the red box of Fig.55 (b). ....	142
Figure 57. EBSD maps show the image quality (IQ) + inverse pole figure (IPF) maps of the $\text{Ca}_2\text{Gd}_8(\text{SiO}_4)_6\text{O}_2$ . ....	143
Figure 58. Schematic illustration of the formation of the corrosion behavior on sintered Gd7-	

Sc3 in contact with CMAS: (a) initial state, (b) formation of reaction layer between CMAS and Gd7-Sc3 at high temperature, and (c) a magnified view of the reaction layer. ....	144
Figure 59. SEM micrograph of sintered $\text{Sc}_2\text{Si}_2\text{O}_7/10$ vol.% SiC composite showing EDS results for regions enclosed by region A and B. ....	157
Figure 60. HT-XRD spectra of mixed (1:1 wt.%) $\text{Sc}_2\text{Si}_2\text{O}_7/\text{SiC}$ powders at (a) 25°C, (b) 1100°C, (c) 1200°C, and (d) 1300°C. ....	158
Figure 61. SEM micrographs of surface cracks in $\text{Sc}_2\text{Si}_2\text{O}_7/10$ vol.% SiC composites before and after heat treatment at 1100°C for 2 h and 10 h: (a) 0.5 h, (b) 2 h, (c) 5 h, and (d) 10 h. ....	160
Figure 62. SEM micrograph of surface cracks in $\text{Sc}_2\text{Si}_2\text{O}_7/10$ vol.% SiC composites before and after heat treatment at 1300°C for 2 h and 10 h: (a) 0.5 h, (b) 2 h, (c) 5 h, and (d) 10 h. ....	161
Figure 63. SEM micrograph of surface cracks in $\text{Sc}_2\text{Si}_2\text{O}_7/10$ vol.% SiC composites (a) before and (b) after heat treatment at 1300°C for 2 h, (c) a magnified view of yellow box in (b) and (d) a magnified view of the crack healed in yellow box (c). ....	162
Figure 64. Cross-sectional SEM micrographs of oxidized zones in $\text{Sc}_2\text{Si}_2\text{O}_7/10$ vol.% SiC after exposure to air at (a) for 0 h, (b) 1100, and (c) 1300°C for 10 h, respectively. ....	166
Figure 65. Thickness of the oxidized zone in $\text{Sc}_2\text{Si}_2\text{O}_7/10$ vol.% SiC in air at 1100 and 1300°C; (a) as a function of oxidation time and (b) parabolic plot on growth of oxidized zone. ....	168
Figure 66. SEM micrograph of sintered $\text{Yb}_2\text{Si}_2\text{O}_7/20$ vol.% SiC composite showing EDS results for regions enclosed by region A. ....	169

Figure 67. XRD spectra of sintered $\text{Yb}_2\text{Si}_2\text{O}_7/\text{SiC}$ before heat treatment. ....	170
Figure 68. XRD spectra of sintered $\text{Yb}_2\text{Si}_2\text{O}_7/\text{SiC}$ after heat treatment. ....	171
Figure 69. XRD spectra of $\text{SiO}_2$ in sintered $\text{Yb}_2\text{Si}_2\text{O}_7/\text{SiC}$ after heat treatment. ....	172
Figure 70. SEM micrographs of surface cracks in $\text{Yb}_2\text{Si}_2\text{O}_7/20$ vol.% SiC composites before and after heat treatment at $1100^\circ\text{C}$ : (a) 0.5 h, (b) 2 h, (c) 5 h, and (d) 10 h. ....	173
Figure 71. SEM micrograph of surface cracks in $\text{Yb}_2\text{Si}_2\text{O}_7/20$ vol.% SiC composites before and after heat treatment at $1300^\circ\text{C}$ : (a) 0.5 h, (b) 2 h, (c) 5 h, and (d) 10 h. ....	174
Figure 72. SEM micrograph of surface cracks in $\text{Yb}_2\text{Si}_2\text{O}_7/20$ vol.% SiC composites (a) before and (b) after heat treatment at $1300^\circ\text{C}$ for 10 h, (c) a magnified view of the crack healed in (b) yellow box. ....	175
Figure 73. Schematic of the crack healing mechanism in $\text{RE}_2\text{Si}_2\text{O}_7/\text{SiC}$ composites in plan view: (left) as-cracked material (before healing); (middle) partial healing during heat treatment in air; and (right) fully healed crack. ....	179

## List of Tables

Table 1. Relevant CTE of promising EBCs materials. ....	13
Table 2. Structure and function of T/EBC materials. ....	15
Table 3. Chemical composition of Kagoshima volcanic ash (wt.%). ....	40
Table 4. Normalized elemental ratio (at.%) at points A, B, and C of Fig. 16 were measured using EDS point analysis. ....	44
Table 5. EDS point analysis of the chemical composition of the cross section with CMAS at parts A, B, and C of Fig. 24. ....	63
Table 6. Parameters used to calculate CMAS infiltration times from Eq. (3). ....	73
Table 7. Viscosity of CMAS from Eq. (2) and calculated times for CMAS melt to infiltrate sintered $Gd_2SiO_5$ using Eq. (3) at 1215°C–1519°C. ....	74
Table 8. Experimental conditions (temperature, CaO:SiO <sub>2</sub> ratios, and heat-treatment time) from previous studies on CMAS. ....	83
Table 9. The average compositions (at.%) of the cross-section with CMAS at parts A, B, C and D in Fig. 36. ....	94
Table 10. Average concentrations of chemical elements (at.%) in regions A, B, and C of a $\beta$ - $Er_2Si_2O_7$ compact coated with molten CMAS after a heat treatment at 1400°C for 48 h as determined from the EDS maps in Fig. 45. ....	117
Table 11. The average compositions (at. %) of the cross-section with CMAS in Fig. 55 (b). ..	141
Table 12. Proportion of Vickers indentation cracks in $Sc_2Si_2O_7/10$ vol.% SiC specimens closed after heat treatment in air. ....	163
Table 13. Proportion of Vickers indentation cracks in $Yb_2Si_2O_7/20$ vol.% SiC specimens closed after heat treatment in air. ....	175

# Contents

<b>Abstract</b> .....	<b>I</b>
<b>List of Figures</b> .....	<b>V</b>
<b>List of Tables</b> .....	<b>VII</b>
<b>Contents</b> .....	<b>VIII</b>
<b>Chapter 1. Introduction</b> .....	<b>1</b>
1.1. Backgrounds .....	1
1.1.1. Advances in Gas Turbine Engine .....	1
1.1.2. Evolution from Thermal Barrier Coatings (TBCs) to Environmental Barrier Coatings (EBCs) .....	4
1.2. Environmental Barrier Coatings (EBCs) Materials .....	9
1.2.1. First Generation EBCs Materials .....	9
1.2.1.1. Mullite .....	9
1.2.2. Second Generation EBCs Materials.....	11
1.2.2.1. Rare-Earth Silicate .....	11
1.2.3. Next Generation of EBCs Materials .....	14
1.3. High-Temperature Corrosion Behavior for EBCs.....	17
1.3.1. High-Temperature Corrosion Mechanisms of Volcanic Ash and CMAS .....	17
1.4. Self-Healing Ceramics for EBCs .....	22
1.4.1. Self-Healing Mechanisms .....	22
1.5. Motivation and Objectives .....	27
References .....	29
<b>Chapter 2. High-Temperature Corrosion of Gd<sub>2</sub>SiO<sub>5</sub> with Volcanic Ash for EBCs</b> .....	<b>36</b>
2.1. Introduction .....	36
2.2. Experimental Procedure .....	38
2.2.1. Sample Preparation and Heat Treatment .....	38
2.2.2. Characterization .....	38
2.3. Results and Discussion .....	40
2.3.1. Characterization of Volcanic Ash .....	40
2.3.2. High-Temperature Corrosion of Sintered Gd <sub>2</sub> SiO <sub>5</sub> with Volcanic Ash .....	42
2.4. Conclusions .....	50
References .....	51

<b>Chapter 3. High-Temperature Corrosion of Gd<sub>2</sub>SiO<sub>5</sub> with CMAS for EBCs</b> .....	55
3.1. Introduction .....	55
3.2. Experimental Procedure .....	57
3.2.1. Sample Preparation and Heat Treatment .....	57
3.2.2. Characterization .....	58
3.3. Results and Discussion .....	59
3.3.1. Characterization of CMAS .....	59
3.3.2. High-temperature Corrosion of Sintered Gd <sub>2</sub> SiO <sub>5</sub> with CMAS .....	60
3.4. Conclusions .....	76
References .....	77
<b>Chapter 4. High-Temperature Corrosion of Gd<sub>2</sub>Si<sub>2</sub>O<sub>7</sub> with CMAS for EBCs</b> .....	82
4.1. Introduction .....	82
4.2. Experimental Procedure .....	85
4.2.1. Sample Fabrication .....	85
4.2.2. Characterization .....	85
4.3. Results and Discussion .....	87
4.3.1. Characterization of Sintered Gd <sub>2</sub> Si <sub>2</sub> O <sub>7</sub> .....	87
4.3.2. High-Temperature Corrosion Behavior .....	88
4.4. Conclusions .....	102
References .....	103
<b>Chapter 5. High-Temperature Corrosion of Er<sub>2</sub>Si<sub>2</sub>O<sub>7</sub> with CMAS for EBCs</b> .....	107
5.1. Introduction .....	107
5.2. Experimental Procedure .....	109
5.2.1. Sample Preparation .....	109
5.2.2. High-Temperature Corrosion Behavior .....	110
5.3. Results and Discussion .....	111
5.3.1. Characterization of CMAS .....	111
5.3.2. High-Temperature Corrosion Behavior .....	112
5.4. Conclusions .....	125
References .....	126

<b>Chapter 6. High-Temperature Corrosion of Gd<sub>2</sub>Si<sub>2</sub>O<sub>7</sub>/Sc<sub>2</sub>Si<sub>2</sub>O<sub>7</sub> with CMAS for EBCs</b> .....	<b>130</b>
6.1. Introduction .....	130
6.2. Experimental Procedure .....	132
6.2.1. Sample Preparation .....	132
6.2.2. High-Temperature Corrosion Behavior .....	132
6.3. Results and Discussion .....	134
6.3.1. Characterization of Sintered Gd <sub>2</sub> Si <sub>2</sub> O <sub>7</sub> (70%) + Sc <sub>2</sub> Si <sub>2</sub> O <sub>7</sub> (30%) .....	134
6.3.2. High-Temperature Corrosion Behavior .....	134
6.4. Conclusions .....	146
References .....	147
<b>Chapter 7. Self-Healing Behavior of RE<sub>2</sub>Si<sub>2</sub>O<sub>7</sub>/SiC Composites for EBCs</b> .....	<b>151</b>
7.1. Introduction .....	151
7.2. Experimental Procedure .....	154
7.2.1. Sample Preparation .....	154
7.2.2. Self-Healing and High-Temperature Oxidation .....	155
7.2.3. Nanoindentation Tests .....	156
7.3. Results and Discussion .....	157
7.3.1. Phase Assemblages and Microstructures of Sc <sub>2</sub> Si <sub>2</sub> O <sub>7</sub> /10 vol% SiC Composites .....	157
7.3.2. Crack-Healing in Sc <sub>2</sub> Si <sub>2</sub> O <sub>7</sub> /10 vol.% SiC Composites .....	159
7.3.3. High-Temperature Oxidation Behavior .....	164
7.3.4. Phase Assemblages and Microstructures of Yb <sub>2</sub> Si <sub>2</sub> O <sub>7</sub> /20 vol% SiC Composites .....	169
7.3.5. Crack-Healing in Yb <sub>2</sub> Si <sub>2</sub> O <sub>7</sub> /20 vol.% SiC Composites .....	173
7.3.6. Self-Healing Mechanisms .....	178
7.4. Conclusions .....	181
References .....	182
<b>Chapter 8. Conclusions</b> .....	<b>187</b>
<b>Research Achievements</b> .....	<b>192</b>
<b>Acknowledgements</b> .....	<b>196</b>

# Chapter 1. Introduction

## 1.1. Backgrounds

### 1.1.1. Advances in Gas Turbine Engine

A gas turbine engine is an internal combustion engine that obtains rotational kinetic energy by rotating a turbine by a flow of high-temperature gas generated by fuel combustion. Since the gas turbine engine is relatively light, it is used in aircraft as a jet engine that obtains thrust using jet streams and is used as an emergency power generation device in power generation systems of various sizes. Therefore, gas turbine engines are indispensable for maintaining the quality of life in modern society. Especially, gas turbine engines are having a profound impact on the transportation, energy and defense sectors of the global economy. Current engines work great and are very efficient, but there is always a demand for higher performance, better fuel efficiency and lower NO<sub>x</sub> emissions.

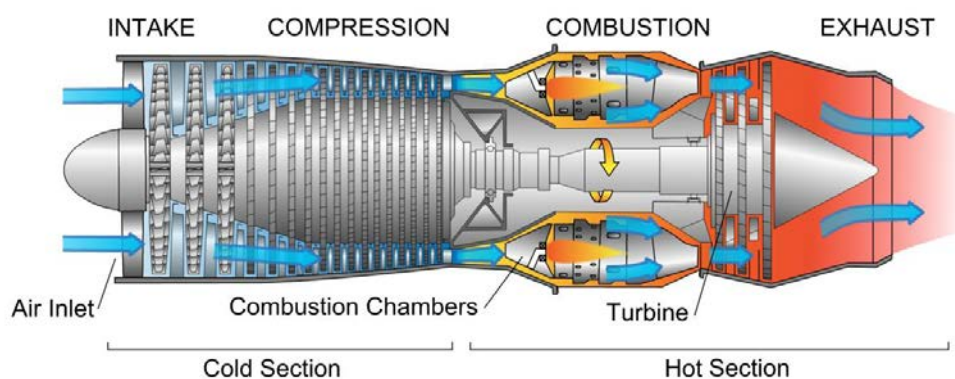


Fig. 1. Schematic of a gas turbine engine [1].

Technology development of high-temperature components for combustors and turbines exposed to high-temperature combustion gases are one of the most important tasks for improving the performance of turbine engines in Fig. 1 [1]. In general, this can be achieved by

increasing the gas inlet temperature in the hottest section of the gas turbine engine (hot section). Here, the core power and efficiency are proportional to the corresponding temperature. Ni-based superalloys have been the standard for high-temperature parts of gas turbine engines for decades. Improvements in thermal barrier coatings and cooling mechanisms have allowed the industry to increase gas inlet temperatures up to 1500°C [2,3], increasing thermal efficiency, thrust-to-weight ratio, and reducing hazardous emissions.

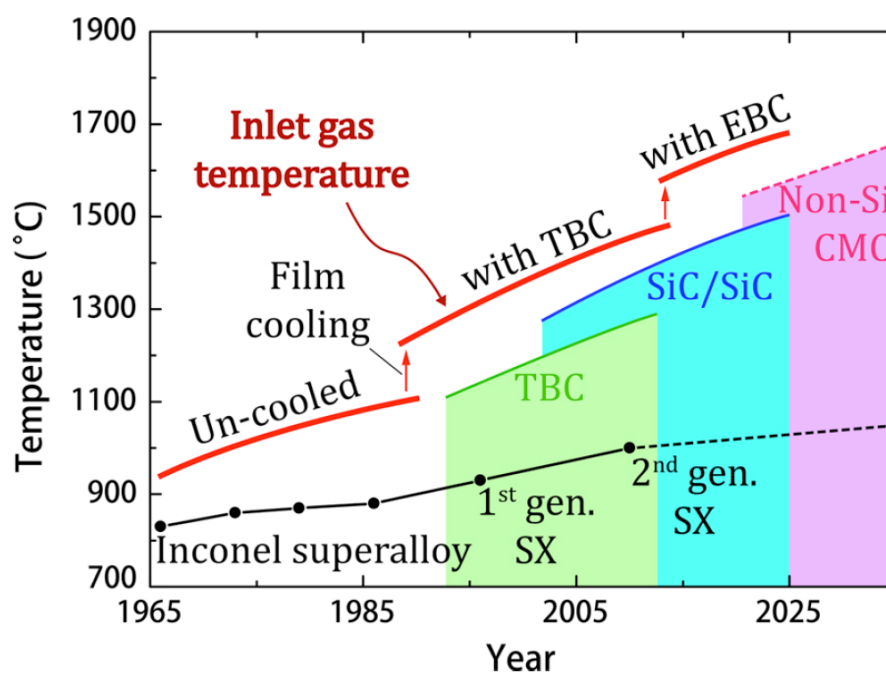


Fig. 2. The evolution of turbine inlet gas temperature with generations of high temperature technologies including single crystal (SX) superalloys, ceramic matrix composite (CMC), film cooling, thermal barrier coatings (TBCs) and environmental barrier coatings (EBCs) [13].

Nevertheless, this strategy is approaching the intrinsic limit imposed by the melting point of Ni-based superalloys, and new strategies will be needed to further increase the gas inlet temperature. Improvements in superalloys and the use of thermal barrier coatings (TBCs) along with internal air cooling of superalloy components have resulted in unprecedented gas inlet temperatures in today's gas turbine engines [4-10]. However, to increase the efficiency and

power of a gas turbine engine, the combustion gas temperature (Turbine Inlet Temperature (TIT)) must be increased further. However, since the combustion gas temperature exceeds the endurance temperature of high-temperature materials, it is urgent to develop materials that can be used at high temperatures in next-generation gas turbines. Therefore, to achieve higher TIT temperatures to increase the power and efficiency of a turbine engine requires. Ni-based superalloys require the application of lightweight ceramic matrix composites (CMCs) with excellent high-temperature durability in Fig. 2 [11-13].

### 1.1.2. Evolution from Thermal Barrier Coatings (TBCs) to Environmental Barrier Coatings (EBCs)

CMCs are the most promising candidate in terms of heat resistance and mechanical properties required for high-temperature parts of turbine engines. CMCs are very light and has excellent heat resistance and mechanical properties compared to Ni-based superalloys for TBCs. These advantages are applicable to important issues for improving the thermal efficiency of the system, improving fuel economy, and reducing CO<sub>2</sub> emissions. However, oxidation/volatilization and thickness reduction in high-temperature water vapor environments are major drawbacks of Si-based ceramic materials. For SiC<sub>f</sub>/SiC to be used as a high-temperature material for turbine engines, the problem of oxidative thickness reduction must be overcome. Therefore, the application of environmental barrier coatings (EBCs) are required to prevent the deterioration of SiC<sub>f</sub>/SiC in a high-temperature steam environment. However, these coatings degrade in the highly hostile environment of gas turbine engines consisting of a combination of high gas temperature, pressure and speed. Therefore, EBCs development targets EBCs systems composed of multilayer coatings with various functions. Multi-layer EBCs consists of a bond coat layer, intermediate coat layer, and a top coat layer in Fig. 3.

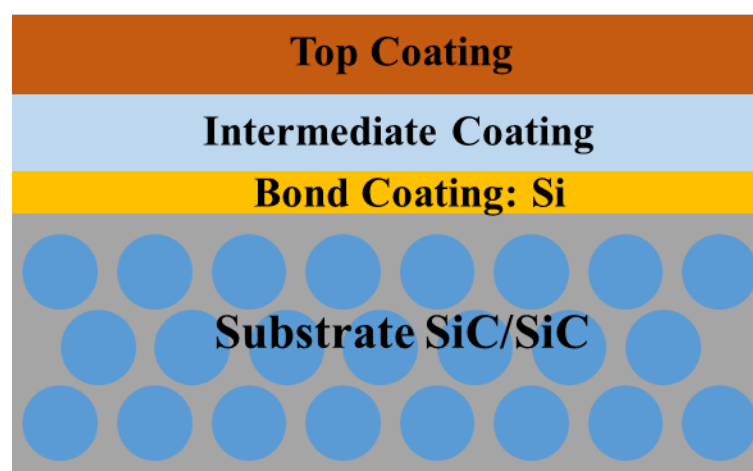


Fig. 3. Conventional EBCs structure.

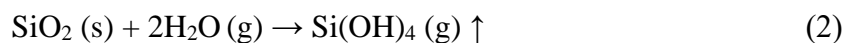
Generally, Si is used as a bond coat material, and the main role of the bond coat is to ensure high adhesion between the CMCs and the top coat. In addition, durability is advantageous when the coefficient of thermal expansion with the substrate is matched. Top coat and intermediate coat require various functions (chemical compatibility, matching bond coat and thermal expansion coefficient, stability against high temperature steam, high temperature mechanical properties, environment resistance, low thermal conductivity, corrosion resistance) depending on the application environment.

The next generation of innovation in jet engines requires a new approach, and SiC/SiC ceramic matrix composites are the most promising materials to play that role. The effect of steam on CMCs have been extensively studied over the past few decades because it was realized early in development that an increase in steam content accelerated the oxidation rate. Gas turbine engines with hot section components made of CMCs consisting of matrix made of SiC are already in commercial use for propulsion and power generation of aircraft.

SiC-based CMCs are oxidized at high temperature to produce a SiO<sub>2</sub> TGO protective layer according to the following reaction [14].



However, the high-temperature, high-pressure, high-velocity gas flow in a gas turbine engine always contains steam, which results in active volatilization of TGO and rapid retreat of SiC according to the following reactions [15].



EBCs should be of low volatility to minimize vapor-induced corrosion. Opila et al. [15] studied the exact mechanism of silica volatilization and established an additional step after reacting SiC and O<sub>2</sub> to form silica. In reaction (1), silica further reacts with H<sub>2</sub>O to form gaseous Si-OH. Si(OH)<sub>4</sub> [16] causes silica volatilization as shown in reaction (2). This volatilization process is accompanied by retraction of the part surface, which has been calculated to be up to

1  $\mu\text{m/h}$  under normal gas turbine operating conditions (temperature  $1350^\circ\text{C}$ , gas velocity 300 m/s) [17]. These stagnation rates mean unacceptable levels of corrosion to components that are expected to operate without maintenance for at least 30,000 h.

On the other hand, the negative effects of molten salts have been extensively studied for decades. Unlike steam, salt decomposition can be caused by a variety of compounds, making research and prevention more difficult. Federer [18] reported applying several alumina-based coatings in an attempt to limit the corrosion experienced by SiC. In his study, thermal cycling up to  $1200^\circ\text{C}$  and corrosion tests up to  $1200^\circ\text{C}$  in an atmosphere containing  $\text{Na}_2\text{CO}_3$  were used, as a result of which mullite ( $3\text{Al}_2\text{O}_3 \cdot 2\text{SiO}_2$ ) provided the best match in CTE to prevent rupture. Improved resistance in corrosive conditions due to stresses during thermal cycling. As mullite has been found as a promising candidate in SiC component protection, these experiments highlighted the importance of the closely matched coefficient of thermal expansion between SiC and the deposited coating.

Since the early 1990s, reports of the effects of volcanic material ingestion by airplanes flying near volcanic columns were reported [19-21]. This facilitated the shift from the high-temperature corrosion previously studied by  $\text{Na}_2\text{SO}_4$  to other corrosion mechanisms coming from the more generalized constituent groups represented by  $\text{CaO-MgO-Al}_2\text{O}_3\text{-SiO}_2$  or CMAS [22-25]. Therefore, as summarized above, the early discovery of the harmful effects of vapors and corrosive compounds (such as alkali salts or debris) on the lifespan of CMCs led to the desire to develop protective coatings that could prevent environmental attack of SiC components. With this goal in mind, EBCs were first introduced as a solution to the corrosion deterioration experienced by CMCs in typical service environments.

EBCs are phase stability; chemical compatibility with other layers; properties such as mechanical robustness (high hardness and toughness) against fracture, erosion and impact damage are required. A key point for EBCs to remain functional is the effect of CTE mismatch

in Fig. 4 [26]. The presence of heating and cooling cycles during service causes thermal expansion and contraction for each component of the EBCs. If the CTEs are too different from each other, cracks form due to the induced thermal stress. In addition, evaluation of the mechanical properties of EBCs operating at high temperatures is also important for improving durability [27]. The presence of various debris and impurities leads to molten deposits of corrosive species (CMAS, generalized by the term  $\text{CaO-MgO-Al}_2\text{O}_3\text{-SiO}_2$ ) that can have a detrimental effect on the coating.

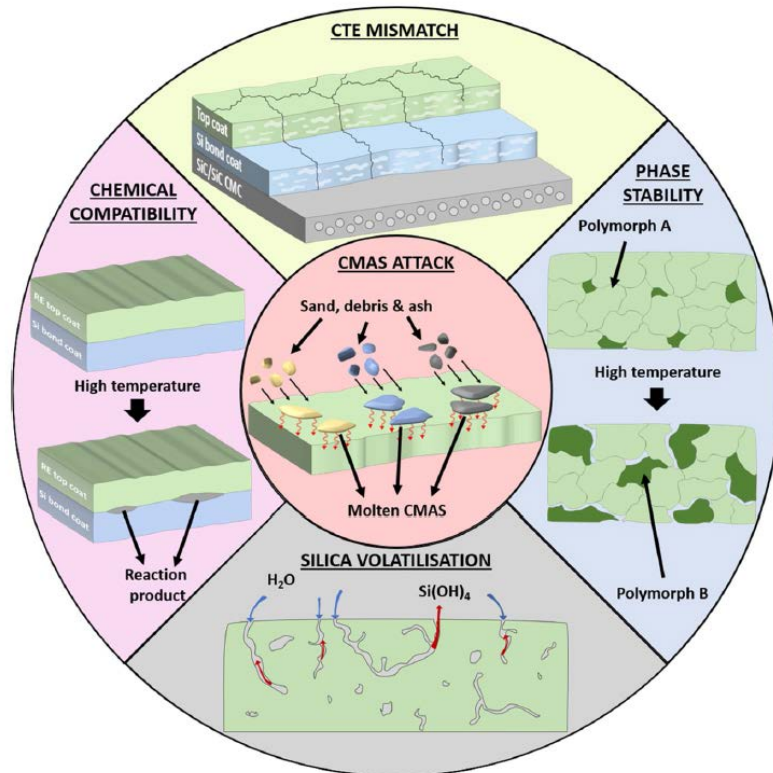


Fig. 4. Schematic of the main five requirements that any successful EBCs [25].

The development of a successful EBC is a complex task and still requires extensive research to this day. In this study, a historical overview of EBCs development is first presented, with a special focus on the processes that have established the practical requirements for state-of-the-art EBCs construction. A detailed review of the above-mentioned specifications and the

most promising candidates in the most common environments (CMAS corrosion and self-healing) are provided. Finally, an overview of future developments in the field of EBCs is summarized.

## 1.2. Environmental Barrier Coatings (EBCs)

### 1.2.1. First Generation EBCs Materials

#### 1.2.1.1. Mullite

The development of EBCs is commonly classified into different generations based on the major composition used. In this section, a more detailed review of the various generations are provided, with particular focus on the features and shortcomings that led to the following constructions and the knowledge gathered.

First-generation EBCs are generally limited by early developments in the 1990s, including mullite and BSAS, with the introduction of rare earth silicates in the early 2000s. Initially,  $(1-x)\text{BaO} \cdot x\text{SrO} \cdot \text{Al}_2\text{O}_3 \cdot 2\text{SiO}_2$  ( $0 < x < 1$ ; BSAS) ceramics were considered to have a lower CTE ( $\sim 4.3 \times 10^{-6} \text{C}^{-1}$ ). Here, a typical EBC structure consists of three layers: Si bond-coat, BSAS/mullite inter-layer, and BSAS top-coat in Fig. 5.

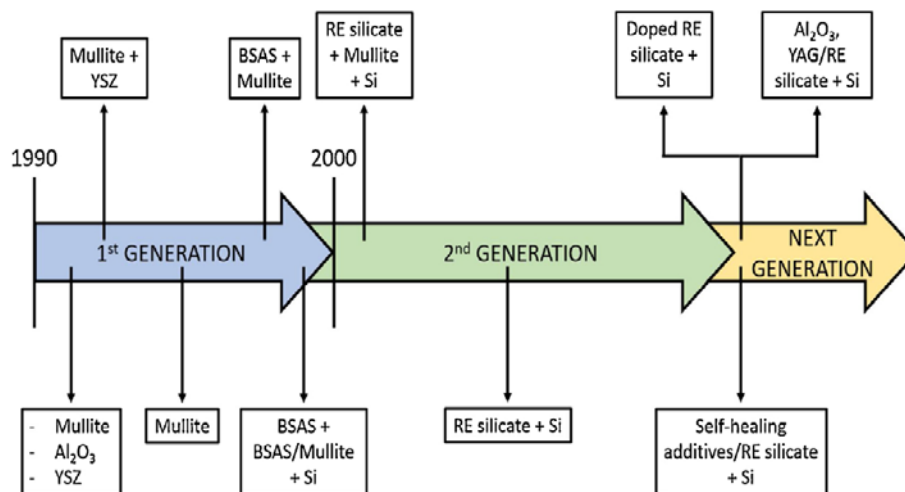


Fig. 5. Timeline of the evolution in the design of EBCs [25].

All these layers are usually deposited using thermal spray methods. A Si-bonded coating is required because oxide coatings generally do not bond well to non-oxide CMCs. It also provides the CMC with anti-oxidation capabilities by forming a dense, slow-growing SiO<sub>2</sub> thermally grown oxide (TGO) layer.

The initial work was based on the findings of Federer [28], and mullite became a major candidate investigated because of its environmental durability, chemical compatibility, and CTE match with SiC, with SiC being  $\sim 4.5 \times 10^{-6} \text{ K}^{-1}$  and mullite wright is  $\sim 5 \times 10^{-6} \text{ K}^{-1}$  [29]. According to Jang et al. [21], the high-temperature corrosion behavior of volcanic ash (VA) attacking sintered mullite was investigated, and the corrosion resistance of mullite EBCs against VA was predicted in Fig. 6.

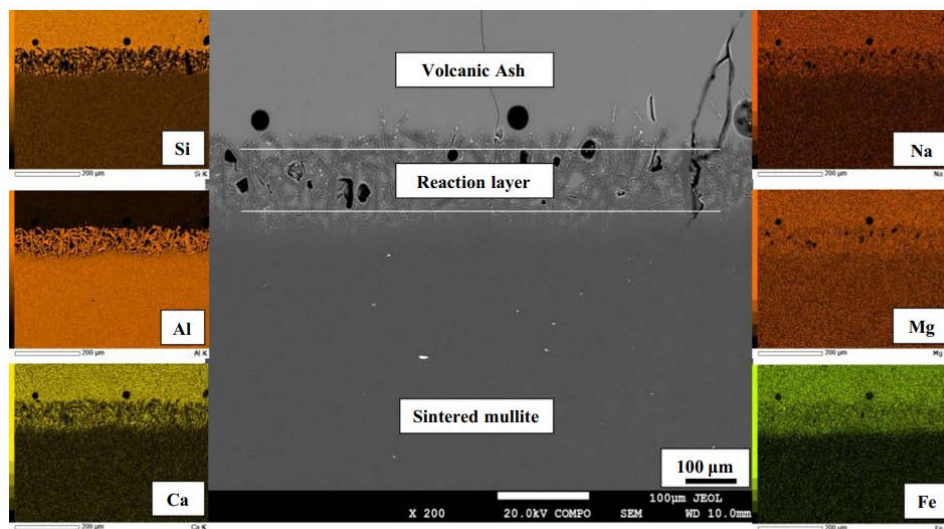


Fig. 6. Sintered mullite reacted with Icelandic VA after heat treatment [21].

Further studies have been conducted on the protective function of air plasma spray (APS) refractory oxide coatings such as mullite, yttria stabilized zirconia (YSZ), and alumina ( $\text{Al}_2\text{O}_3$ ) [30]. Mullite has proven to have the ability to remain attached to sprayed parts while providing protection against corrosive environments. Despite the CTE agreement already mentioned, APS mullite coatings show cracks after thermal cycling, severely impairing their ability to protect the substrate. Studies of the phase stability and microstructure of coatings have shown that the cause of failure was not CTE mismatch, but residual crystallization of metastable amorphous mullite formed due to rapid cooling during APS deposition [31].

## 1.2.2. Second Generation EBCs Materials

### 1.2.2.1. Rare-Earth Silicate

Despite major advances since the first generation of EBC, it was soon realized that mullite and BSAS-based systems would not live up to expectations. To summarize the requirements identified in the late 1990s, a successful EBCs system had to present the following characteristics: First, a close CTE match between the forming layer and the SiC substrate is required to prevent thermal stress and cracking. Next, the coating should not undergo any phase transformation during high temperature exposure, or at least if phase transformation occurs, the CTE values of the polymorphs involved should be close and volume changes should be minimal. Third, EBCs should be characterized by low silica activity under various conditions, such as dry or humid environments. Finally, emphasizing the experimental evidence that a multilayer system is necessary, chemical compatibility must exist between the relevant configurations of different layers to prevent the formation of deleterious reaction products of EBCs. Thus, realizing that mullite and BSAS were not ideal candidates, a research program was launched at NASA in 1999 with clear requirements for a next-generation EBC. The Ultra High Efficiency Engine Technology (UEET) program aims at extensive research to identify key materials that can withstand temperatures of 1316°C (2400°F) and 1482°C (2700°C) at the EBC–SiC substrate interface [32].

The program has identified a family of novel compositions with promising properties that are classified under the names of rare earth (RE) silicates. Rare earth silicates have two main compositions: rare earth monosilicate ( $\text{RE}_2\text{SiO}_5$ ) and rare earth disilicate ( $\text{RE}_2\text{Si}_2\text{O}_7$ ). With increasing temperature requirements, EBCs based on  $\text{RE}_2\text{SiO}_5$ ,  $\text{RE}_2\text{Si}_2\text{O}_7$  and their variants are being developed [33,34].  $\text{RE}_2\text{SiO}_5$  are more stable at high temperatures than  $\text{RE}_2\text{Si}_2\text{O}_7$  and are more stable in hot steam environments. Meanwhile, the coefficient of thermal expansion of  $\text{RE}_2\text{Si}_2\text{O}_7$  is smaller than that of  $\text{RE}_2\text{SiO}_5$  and has a value similar to that of the CMC base

material. Regarding the rate of oxidative evaporation in a water vapor environment,  $\text{RE}_2\text{Si}_2\text{O}_7$  show almost the same values as BSAS and  $\text{RE}_2\text{SiO}_5$  show much lower values. RE-silicates also show good chemical compatibility with Si-based ceramic materials. Among the rare earth silicates identified as suitable candidates are silicates with rare elements such as scandium (Sc), lutetium (Lu), ytterbium (Yb), yttrium (Y) and erbium (Er) [35]. There is also gadolinium (Gd) applied for high temperature corrosion resistance of TBCs. As mentioned earlier, the first condition that all potential configurations must meet for use as an EBCs is a close CTE match with the SiC substrate. Table 1 shows the CTEs of RE-silicates with SiC and silicon.

Table 1. Relevant CTE of promising EBCs materials.

<b>Material</b>	<b>CTE (<math>\times 10^{-6} \text{ K}^{-1}</math>)</b>	<b>Reference</b>
SiC	4.5-5.5	[37]
Si	3.5-4.5	[37]
Mullite	5-6	[37]
Y <sub>2</sub> SiO <sub>5</sub>	6.9	[38]
Y <sub>2</sub> Si <sub>2</sub> O <sub>7</sub>	3.9	[39]
Er <sub>2</sub> SiO <sub>5</sub>	5.9	[38]
Er <sub>2</sub> Si <sub>2</sub> O <sub>7</sub>	2.57	[40]
Gd <sub>2</sub> SiO <sub>5</sub>	10.3	[38]
Gd <sub>2</sub> Si <sub>2</sub> O <sub>7</sub>	7.3	[38]
Yb <sub>2</sub> SiO <sub>5</sub>	7.2	[38]
Yb <sub>2</sub> Si <sub>2</sub> O <sub>7</sub>	3.6-4.5	[36]
Lu <sub>2</sub> SiO <sub>5</sub>	6.7	[38]
Lu <sub>2</sub> Si <sub>2</sub> O <sub>7</sub>	4.2	[41]
Sc <sub>2</sub> Si <sub>2</sub> O <sub>7</sub>	5.4	[41]
Sc <sub>2</sub> Si <sub>2</sub> O <sub>7</sub> +Sc <sub>2</sub> O <sub>3</sub>	5-6	[37]

### 1.2.3. Next Generation of EBCs Materials

Research into better performing EBCs isn't over. Recently, in addition to the environmental protection and protection aspects of rare earth silicates against molten CMAS attack, new research is being conducted.

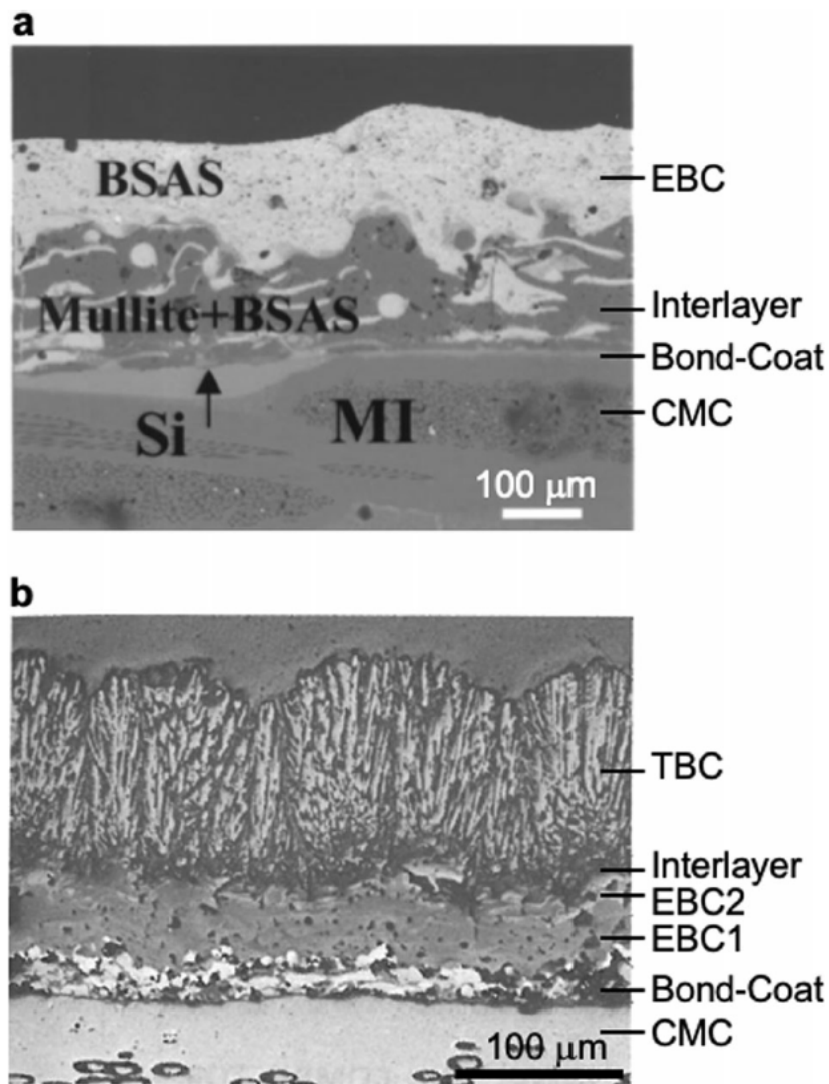


Fig. 7. Coating-systems for CMCs. a Cross-sectional SEM image of BSAS/BSAS+Mullite/Si EBC on melt-infiltrated (MI) CMCs. b Cross-sectional optical micrograph of multilayer T/EBC on CMCs [42].

Various developments of EBCs presenting complex compositions beyond single rare earth

silicates are presented. As already mentioned in this work, one of the primary functions of a successful EBC is to provide protection for the environment in which it will operate during service.

The further increase in high temperature requirements (up to 1700°C) necessitates the use of an additional insulating topcoat (TBC) in the thermal/environment barrier coating (T/EBC) in Fig. 7. For example, ZrO<sub>2</sub>-based and HfO<sub>2</sub>-based TBCs are being considered for their applications [42]. However, the CTE of these TBCs is quite high, most recently the use of monolayer (T/EBC) to replace the TBC/EBC layer has been proposed. As an example, RE<sub>x</sub>RE'<sub>(2-x)</sub>Si<sub>2</sub>O<sub>7</sub> disilicate ceramic with low thermal conductivity with SiC and good CTE match is proposed [36].

Table 2. Structure and function of T/EBC materials.

<b>Material</b>	<b>Function</b>
Re <sub>2</sub> SiO <sub>5</sub>	CMAS resistance
	Thermal shock resistance
Re <sub>2</sub> Si <sub>2</sub> O <sub>7</sub> + (SiC)	CMAS resistance
	Coefficient of thermal expansion matching with SiC
	Water vapor shielding
	Self-healing properties
Si, SiC	Bond coating
Substrate SiC/SiC	

Notably, Turcer et al. [36] describes a quest called thermal environmental barrier coatings (T/EBC), which combines the insulation of TBCs with the environmental protection concepts of EBCs. Four main requirements have been established for the development of T/EBC. That

is, hermetic protection, high temperature performance or phase stability, low thermal conductivity, and resistance to CMAS attack achieved through good CTE matching with the substrate. Table 2 shows the structure and function of T/EBC materials. To match CTE with Si and SiC,  $\text{RE}_2\text{Si}_2\text{O}_7$  is applied over the bond coating. Also, CMAS resistance and self-healing properties are required. Self-healing properties can be obtained by dispersing SiC in  $\text{RE}_2\text{Si}_2\text{O}_7$ . The top layer of T/EBC can have excellent CMAS resistance by applying  $\text{RE}_2\text{SiO}_5$ , which has a high melting point and is excellent in heat resistance.

### 1.3. High-Temperature Corrosion Behavior for EBCs

#### 1.3.1. High-Temperature Corrosion Mechanisms of Volcanic Ash and CMAS

A major concern during the initial development of first-generation EBCs was the degradation experienced by SiC CMC substrates by melt corrosion. In particular, the term CMAS ( $\text{CaO-MgO-Al}_2\text{O}_3\text{-SiO}_2$ ) is used to denote a number of impurities that present a threat when ingested by an engine or turbine. CMAS has been a significant hurdle that potential EBCs systems must overcome, and research continues to understand the interaction between molten CMAS and EBCs. In this study, research on RE silicates is presented. One of the characteristics of the interaction of CMAS with coatings is that temperature plays an important role. The exact melting point of CMAS depends on the exact configuration used, but the generally agreed melting point for CMAS is  $\sim 1200^\circ\text{C}$ , well below the service temperature at which EBCs are expected to operate at  $\sim 1400^\circ\text{C}$ . Decomposition is mainly in the form of EBCs/CMAS reactions, with the formation of uncontrolled microstructure and reaction products with undesirable properties such as high CTE and low toughness, leading to eventual failure of EBCs [43]. Corrosion evaluation by CMAS is not a new problem as it is an investigated topic in relation to YSZ coatings for thermal barrier coatings (TBCs) applications. In this study, studies conducted on rare earth silicates will be presented. However, in the case of rare earth silicate, additional research is required because the corrosion mechanism is different from that of YSZ coating. Despite considerable research being conducted on the interaction between CMAS and EBCs at high temperatures, the underlying mechanisms controlling the interaction are not yet fully understood.

The degradation of EBCs due to CMAS is highly variable depending on the test temperature, time, the composition of the CMAS used, and the deposition method chosen. As mentioned above, the composition of EBCs topcoats found several common aspects when studying the interaction of rare earth silicates with CMAS at elevated temperatures (Fig. 8).

Two major degradation mechanisms have been identified. The first interaction observed involves a reaction between molten CMAS and EBCs top coating. These mechanisms have been reported for  $Y_2SiO_5$  and  $Y_2Si_2O_7$  [45–49], and reaction with CMAS results in dissolution of EBCs and recrystallization of yttrium monosilicate and Y-Ca-Si apatite as solids. It forms a unique needle-like structure.

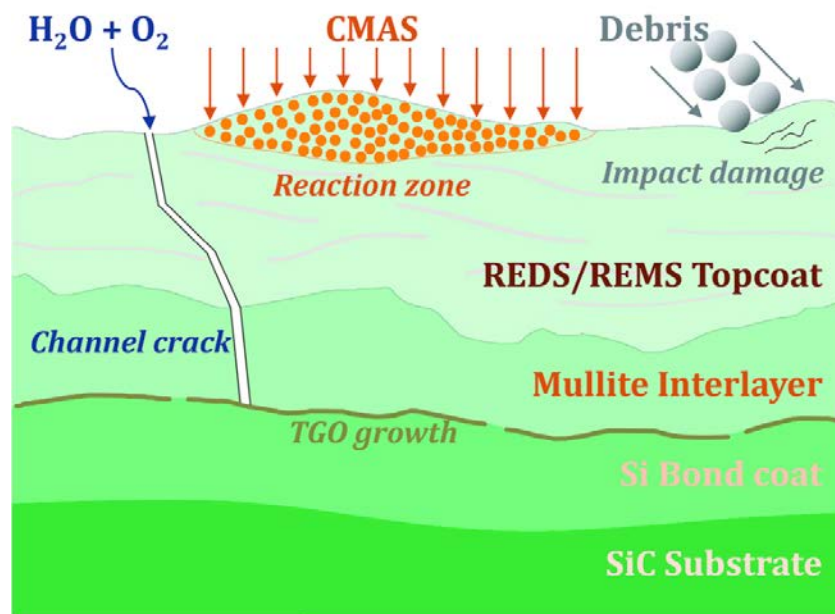


Fig. 8. Schematic of a typical environmental barrier coating system (EBCs) for SiC/SiC ceramic matrix composites (CMCs) with in-service degradation mechanisms [44].

The second possibility is not based on the reaction between the CMAS and the top coating, but rather on the penetration of the CMAS material along the grain boundary for  $Yb_2Si_2O_7$ , to reach the deeper layers of the EBCs, causing "blister" damage. This is due to the expansion gradient due to the slow penetration of CMAS. In addition to the chemical composition of the EBCs top coating, the morphology of the coating (depending on the chosen deposition method) and the presence of the phase mixture also influence the decomposition mechanism present. For example, for  $Yb_2SiO_5$  and  $Yb_2Si_2O_7$  [47,50–54], there are differences in the mechanisms

involved when EBCs are exposed to CMAS attack at high temperatures.

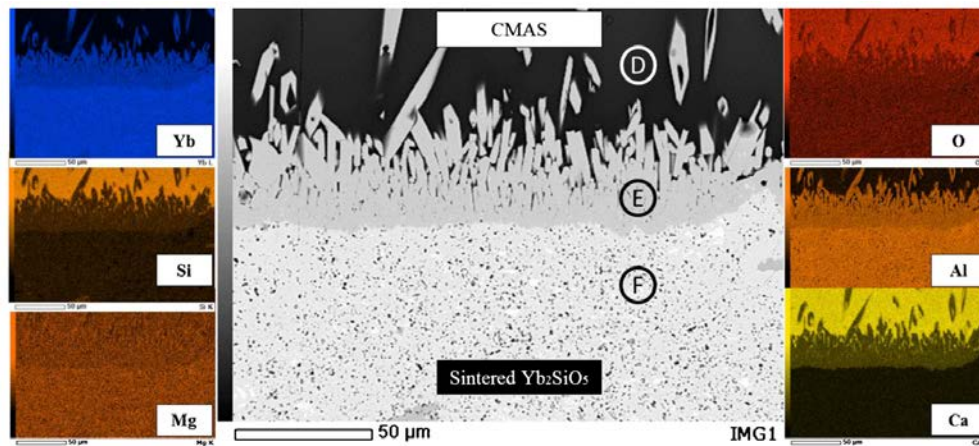


Fig. 9. Sintered  $\text{Yb}_2\text{SiO}_5$  was reacted with CMAS ash after heat treatment [25].

The mechanism for  $\text{Yb}_2\text{SiO}_5$  is needle-shaped apatite particles with residual CMAS regions, forming a reactive layer based on the discussed dissolution of  $\text{Yb}_2\text{SiO}_5$  and precipitation. According to Jang et al. [25], high-temperature corrosion behavior of sintered  $\text{Yb}_2\text{SiO}_5$  with CMAS as an environmental barrier coating material, are investigated in Fig. 9. After high-temperature reaction of  $\text{Yb}_2\text{SiO}_5$  and CMAS at  $1400^\circ\text{C}$ , a reaction layer was formed, and the thickness of the reaction layer became thicker with the increase of time. For the  $\text{Yb}_2\text{Si}_2\text{O}_7$ , the initial apatite particles are coarser and larger in size and have an irregular reaction layer where no clear reaction lines can be determined. As corrosion continues, the molten CMAS preferentially attacks the  $\text{Yb}_2\text{SiO}_5$ -rich areas of the coating. Due to the lamellar structure of the plasma-deposited coating, the  $\text{Yb}_2\text{SiO}_5$ -rich splats are long and parallel to the surface, allowing the reaction to proceed rapidly in this direction. Precipitation of apatite particles results in a "cracking" effect. This effect is one of the clearest examples reported for the various corrosion attack mechanisms seen in deposited coatings and sintered bodies. A summary of the various CMAS corrosion experiments is provided here, considering the deposition techniques for both the substrate and the CMAS, and the specific CMAS

configuration and testing used. Conditions (eg. temperature, CMAS mass loading, or high temperature exposure time). In addition, a comparison of the resistance to CMAS of monosilicate and disilicate should be considered for EBCs applications (Fig. 10).

RE-silicates	Corrosion resistance to CMAS	Melting point	CTE match with SiC	Phase stability
RE <sub>2</sub> SiO <sub>5</sub> (Monosilicate)	?	↑	↓	↓
RE <sub>2</sub> Si <sub>2</sub> O <sub>7</sub> (Disilicate)		↓	↑	↑

Fig. 10. Functional comparison of monosilicate and disilicate for application of EBCs.

First of all, when the reaction between rare earth silicate and CMAS occurs, the precipitation of RE-Ca-Si apatite is the most common product. This reaction produces retraction of the coating and the appearance of defects such as cracks or porosity. However, reaction with CMAS is not always guaranteed and penetration of CMAS can occur with little interaction, especially for low Ca-containing CMAS compositions.

Second, the CaO content present in the CMAS composition has a significant impact on the observed corrosion mechanism and its severity. The higher CaO content, the more severe the interaction with the top coating in terms of stagnation rate and apatite precipitation. As in the case of vapor volatilization, evaluation of various rare earth silicate compositions and CMAS corrosive properties are required to evaluate suitability for the desired application. The information about CMAS makes it clear. Corrosion to molten CMAS is still a challenge that the current generation of EBCs cannot solve. To solve this problem, Gd has already been applied to TBCs (Gd<sub>2</sub>Zr<sub>2</sub>O<sub>7</sub>) to confirm the excellent high-temperature corrosion properties of CMAS. Therefore, gadolinium silicates (Gd<sub>2</sub>Si<sub>2</sub>O<sub>7</sub>, Gd<sub>2</sub>SiO<sub>5</sub>) were evaluated for application to developed high-temperature corrosion of EBCs. Also, Er<sub>2</sub>Si<sub>2</sub>O<sub>7</sub>, which has the most similar

CTE values for bond coatings (Si and SiC), is evaluated by comparing the high-temperature corrosion reaction layer for  $\text{Gd}_2\text{Si}_2\text{O}_7$  and CMAS according to the size of the ionic radius. In this study, the high-temperature corrosion behavior evaluation was studied by comparing the reaction layer according to volcanic ash and CMAS (CaO:SiO<sub>2</sub> ratio), disilicate ( $\text{RE}_2\text{Si}_2\text{O}_7$ ) and monosilicate ( $\text{RE}_2\text{SiO}_5$ ), ionic radius, time, and dual disilicate.

## 1.4. Self-Healing Ceramics for EBCs

### 1.4.1. Self-Healing Mechanisms

CMCs are promising candidates for high-temperature components in gas turbines. However, in a high-temperature combustion environment, high-temperature corrosion by water vapor occurs, and EBCs are essential to protect CMCs from water vapor corrosion. In addition, mechanical fatigue and thermal shock are caused by the collision of gas residues or particulate matter, which causes cracks on the surface of EBCs in a high-temperature combustion environment. As a result, the protective function of EBCs is impaired and exposed to environments such as oxygen and water vapor. The occurrence of unpredictable cracks in such a high-temperature combustion environment has serious consequences such as damage to high-temperature members. The self-healing properties of EBCs are effective to inhibit cracking in high-temperature environments.

R&D is being promoted in various industrial fields such as defense and power plants. However, the realization of a self-healing agent that can exert its power in a harsh corrosive environment is required. In addition, long-term durability verification of self-healing ceramics in a wide range of operating temperatures are essential for such practical use. If the surface cracks that occur during use can be healed by applying the self-crack healing function to ceramics for EBCs, it can greatly contribute to reliability improvement and cost reduction. In particular, the composite material of RE-silicate and SiC exhibits excellent self-crack healing properties and is effective in improving life and durability.

The significance of the self-healing properties is that cracks can be repaired under high-temperature use environments, and crack healing proceeds through high-temperature oxidation reactions in Fig. 11. By mixing a healing agent (HA) with high strength and high oxidizing properties to the oxide ceramic, the HA is protected from being oxidized by the oxide ceramic base material until damage occurs. When a crack occurs due to damage and the HA is exposed

to high temperature atmosphere, oxidation reaction is induced on the surface of the damaged area, and an autonomous crack repair process proceeds. Studies have been conducted with the goal of developing self-healing functions aimed at extending the lifespan of the EBCs system.

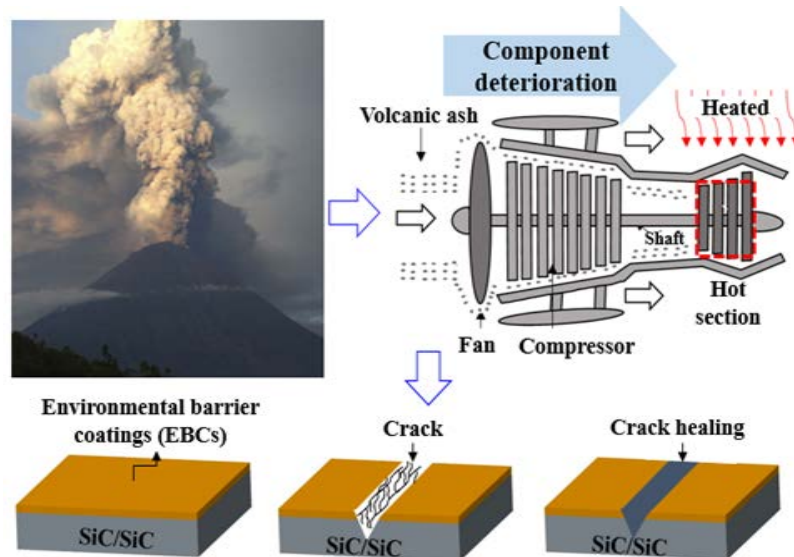


Fig. 11. Schematic diagram of self-crack healing of EBCs applied to aircraft gas turbine.

Silicon carbide (SiC) is a representative self-healing material as HA and a lot of research is being done. The mechanism of self-healing in this case has been postulated to be the filling of surface cracks by the oxidation product of SiC, namely SiO<sub>2</sub>, which is formed as a result of a chemical reaction (dependent on temperature and oxidizing environment) [55].



That is, the original strength is restored because the cracks are healed by an increase in volume according to the oxidation reaction of SiC shown in Equation (1).

As shown in Fig. 12, Since SiC particles are embedded in the base material, they are in a stable state in a high-temperature atmosphere, but when cracks occur on the surface, the SiC particles are exposed to a high-temperature oxidizing atmosphere and oxidation proceeds

according to Equation (1). Here, SiC on the surface is oxidized, but in SiC present in the base material, oxygen diffusion is slow, so it is not oxidized. In addition, it is effective to apply nano-sized SiC particles to improve the rate of oxidation reaction for crack healing. The presence of SiC nanoparticles greatly contributes to the improvement of mechanical properties as well as self-healing properties [56]. For example, the bending strength of  $\text{Al}_2\text{O}_3$  is around 400 MPa, but it is known that it is improved to about 800 MPa by compounding SiC nanoparticles. This is because the particles are refined by SiC nanoparticles [57].

As described above, various ceramics in which SiC nanoparticles are complexed can exhibit a function as a self-cracking healing agent with excellent mechanical properties. By combining SiC with various base materials, a variety of self-healing ceramics can be obtained. There are no special restrictions on the selection of the base material, and it can be selected according to the purpose. So far, it has been reported that silicon nitride ( $\text{Si}_3\text{N}_4$ ), alumina ( $\text{Al}_2\text{O}_3$ ), and mullite ( $3\text{Al}_2\text{O}_3 \cdot 2\text{SiO}_2$ ) exhibit excellent crack healing properties. According to Jang et al., 5 vol% nano-sized SiC was composited with  $\text{Al}_2\text{O}_3$  [58], and the dispersed SiC effectively suppressed particle growth and improved mechanical properties [59-61]. Ytterbium (Yb) and Yttrium (Y) are examples of rare earth materials that are being actively studied for application to EBCs. Nguyen et al. evaluated the crack healing properties of composite oxides in which 0~20 vol% of SiC was added to  $\text{Yb}_2\text{Si}_2\text{O}_7$  [62]. In addition, the proposed mechanism is based on adding 10 vol.%  $\beta$ -SiC nanocomposites (nanoparticles, nanofibers or nanowhiskers) to the YbDS/YbMS system. When cracks appear, atmospheric oxygen can access the material. During annealing at  $1250^\circ\text{C}$ , SiC nanopillars react with atmospheric oxygen to produce a viscous  $\text{SiO}_2$  glass. This viscous amorphous  $\text{SiO}_2$  can fill cracks and reacts with YbMS present within the system to form YbDS, effectively sealing the cracks due to the associated volumetric expansion.

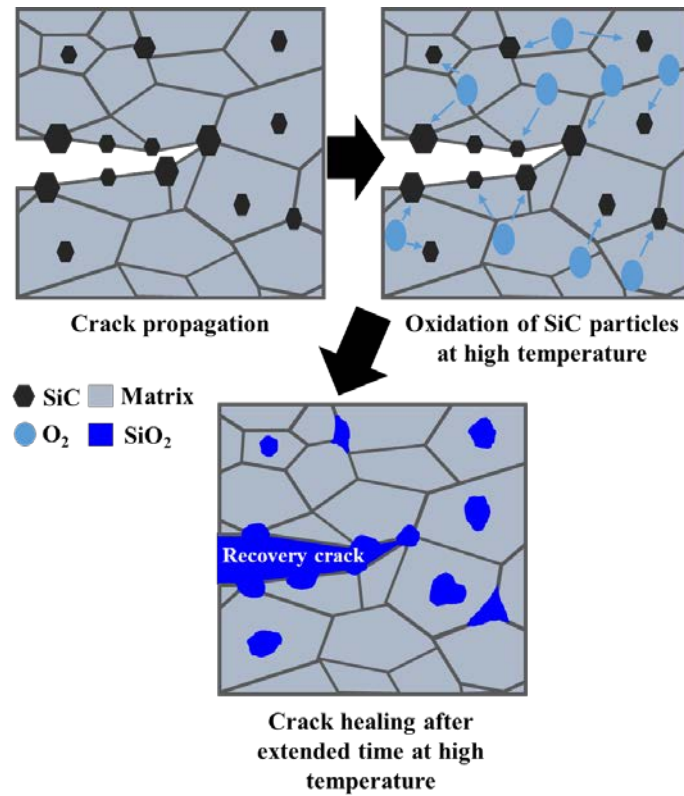


Fig. 12. Schematic diagram of self-crack healing caused by oxidation reaction.

Kunz et al. evaluated the self-healing behavior of  $\text{Yb}_2\text{Si}_2\text{O}_7$  composites with 1% SiC added  $\text{Yb}_2\text{SiO}_5$  [63]. Vu evaluated the effect of treatment temperature and time on the high-temperature oxidation-crack healing behavior of a material composited with Yttrium (Y) silicate and 5 vol% SiC. The results of the evaluation of crack healing of the SiC/ $\text{Y}_2\text{SiO}_5$ - $\text{Y}_2\text{Si}_2\text{O}_7$  composite material in the air at 1000 to 1300°C, 1 to 24 h after oxidation treatment. Overall, with the increase of the healing temperature and time, the crack healing effect is excellent [64]. Closing of surface cracks proceeds by formation of an oxidation product layer and volume expansion. In particular, it has been reported that the main factor inducing self-healing of SiC/ $\text{Y}_2\text{Si}_2\text{O}_7$  is the volume expansion generated during the oxidation of SiC to  $\text{SiO}_2$ .

The main factors affecting self-healing are the treatment atmosphere, temperature, stress, and the size and content of HA. Self-crack healing only occurs when heat treated in air or in an oxidizing atmosphere. According to a study by Nguyen et al., in the case of a composite of

$\text{Yb}_2\text{Si}_2\text{O}_7$  and SiC, almost complete self-healing proceeded in air heat treatment, but recovery of strength was hardly recognized in Ar gas treatment [62]. In this study, the self-healing of RE-disilicates ( $\text{RE}_2\text{Si}_2\text{O}_7$ ) applied to EBCs were evaluated. In detail, the self-healing properties according to the SiC vol.%, time, and temperature were evaluated in air.

## 1.5. Motivation and Objectives

This thesis is addressed by advancing our understanding of high-temperature corrosion and self-healing factors that affect the durability of EBCs systems. Chemical attack on EBCs by molten silicate deposits known as calcia-magnesia-alumina-silica (CMAS) during high-temperature engine operation is an important issue. Furthermore, the self-healing property is caused by the collision of gas residues or particles in a high-temperature combustion environment, resulting in physical behavior (mechanical fatigue, thermal shock) and cracking on the EBC surface.

To solve these problems, rare earths (RE) silicate with high temperature resistance, low coefficient of thermal expansion (CTE) and excellent chemical stability are required as promising EBCs materials. For example, Gd has already been applied to TBCs ( $Gd_2Zr_2O_7$ ) to confirm the excellent high-temperature corrosion properties of CMAS. Therefore, gadolinium silicates ( $Gd_2Si_2O_7$ ,  $Gd_2SiO_5$ ) were evaluated for application to developed high-temperature corrosion of EBCs.  $Gd_2SiO_5$  is evaluated by volcanic ash and CMAS to evaluate the high-temperature corrosion behavior of  $CaO:SiO_2$ . Additionally, it is also to evaluate the quantitative high-temperature corrosion properties of  $Gd_2Si_2O_7$  and  $Gd_2SiO_5$ , which have not yet been studied. In addition,  $Er_2Si_2O_7$ , which has the most similar CTE values for bond coatings (Si and SiC), is evaluated by comparing the high-temperature corrosion reaction layer for  $Gd_2Si_2O_7$  and CMAS according to the size of the ionic radius.  $Sc_2Si_2O_7$  is also the lightest of the rare earths, making it most desirable when component weight is an important consideration.  $Yb_2Si_2O_7$  has low thermal conductivity and the best water vapor corrosion resistance among RE elements with a CTE suitable for SiC substrate.

However, there has been rarely reported for the main factors ( $CaO:SiO_2$ ,  $RE_2Si_2O_7$  and  $RE_2SiO_5$ , ionic radius, time, and dual disilicate) of the above RE-silicates' high-temperature corrosion resistance and main factors (time, temperature, and SiC vol.%) of self-healing

properties of EBCs. The originality and value of this study are fully demonstrated through the improvement of the high-temperature corrosion behavior and self-healing properties of RE-silicate applied to EBCs. This thesis is divided into two parts, chapter 2 ~ 6 about the high-temperature corrosion behavior of RE-silicate, and the self-healing characteristics of RE-silicate are composed in chapter 7. The main purpose of each chapter is briefly presented below.

In chapter 2, the main purpose is to investigate the effect of the reaction time on the formation of the reaction layer for the high-temperature corrosion behavior of  $\text{Gd}_2\text{SiO}_5$  and volcanic ash, which are promising materials for EBCs.

Chapter 3 focuses on the comparison of the reaction layer formation (in chapter 2) according to the  $\text{CaO}:\text{SiO}_2$  ratios (volcanic ash: 0.11, CMAS: 0.73) through the high-temperature corrosion behavior of  $\text{Gd}_2\text{SiO}_5$  and artificial CMAS.

In chapter 4, the main purpose is to improve the comparison of reaction layer formation between  $\text{RE}_2\text{SiO}_5$  ( $\text{Gd}_2\text{SiO}_5$ : in chapter 3) and  $\text{RE}_2\text{Si}_2\text{O}_7$  ( $\text{Gd}_2\text{Si}_2\text{O}_7$ ) through the high-temperature corrosion behavior of  $\text{Gd}_2\text{Si}_2\text{O}_7$  and CMAS.

In chapter 5, the main purpose is to improve the comparison of reaction layer formation (in chapter 4) according to the ionic radius ( $\text{Gd}$  (1.107 Å) and  $\text{Er}$  (1.004 Å)) through the high-temperature corrosion behavior of  $\text{Er}_2\text{Si}_2\text{O}_7$  and CMAS.

In chapter 6, the main purpose is to improve the high-temperature corrosion behavior of dual  $\text{RE}_2\text{Si}_2\text{O}_7$  ( $\text{Gd}_2\text{Si}_2\text{O}_7+\text{Sc}_2\text{Si}_2\text{O}_7$ ) and CMAS through comparison of reaction layer formation between single  $\text{RE}_2\text{Si}_2\text{O}_7$  ( $\text{Gd}_2\text{Si}_2\text{O}_7$ ) and CMAS (in chapters 5).

In chapter 7, the main purpose is to improvement of self-healing properties with time, temperature, and SiC vol.% in composites containing nano-sized healing agent (SiC) in  $\text{RE}_2\text{Si}_2\text{O}_7$  ( $\text{Sc}_2\text{Si}_2\text{O}_7$ ,  $\text{Yb}_2\text{Si}_2\text{O}_7$ ).

## References

- [1] Harris. Alan, Cyclic Durability of Thermal Barrier Coatings Subject to CMAS Attack (2018) Doctoral Dissertations.
- [2] N.P. Padture, Advanced structural ceramics in aerospace propulsion, *Nat. Mater.* 15 (2016) 804–809.
- [3] K.N. Lee, Protective coatings for gas turbines, *Gas Turbine Handb.*, (2006) 419–437.
- [4] N.P. Padture, M. Gell & E.H. Jordan, Thermal barrier coatings for gas-turbine engine applications, *Science*. 296 (2002) 280–284.
- [5] D.R. Clarke, M. Oechsner & N.P. Padture, Thermal-barrier coatings for more efficient gas-turbine engines. *MRS Bull.* 37 (2012) 891–898.
- [6] R. Darolia, Thermal barrier coating technology: critical review, progress update, remaining challenges and prospects. *Int. Mater. Rev.* 58 (2013) 315–348.
- [7] B.K. Jang, H. Matsubara, Influence of porosity on hardness and young's modulus of nanoporous EB-PVD TBCs by nanoindentation, *Mater. Lett.* 59 (2005) 3462–3466.
- [8] B.K. Jang, S.H. Kim, C.A.J. Fisher, H.T. Kim, Effect of isothermal heat treatment on nanoindentation hardness and young's modulus of 4 mol%  $Y_2O_3$ - $ZrO_2$  EB-PVD TBCs, *Mater. Today Commun.* 31 (2022) 103330.
- [9] B.K. Jang, H. Matsubara, Influence of porosity on hardness and young's modulus of nanoporous EB-PVD TBCs by nanoindentation, *Mater. Lett.* 59 (2005) 3462–3466.
- [10] B.K. Jang, H. Matsubara, Hardness and Young's modulus of nanoporous EB-PVD YSZ coatings by nanoindentation, *J. Alloy. Compd.* 402 (2005) 237–241.
- [11] J.A. DiCarlo, in *Ceramic Matrix Composites: Materials, Modelling, and Technology* (eds Bansal, N. P. & Lamon, J), (Wiley, Hoboken, 2016) 217–235.
- [12] F.W. Zok, Ceramic-matrix composites enable revolutionary gains in turbine engine efficiency. *Am. Ceram. Soc. Bull.* 95 (2016) 22–28.

- [13] B. Richards, Ytterbium Silicate Environmental Barrier Coatings, Doctoral Dissertation University of Virginia, 2015.
- [14] N.S. Jacobson, Corrosion of silicon-based ceramics in combustion environment, *J. Am. Ceram. Soc.* 76 (1993) 3–28.
- [15] E.J. Opila, R. Hann, Paralinear oxidation of CVD SiC in water vapor, *J. Am. Ceram. Soc.* 80 (1997) 197–205.
- [16] E.J. Opila, D.S. Fox, N.S. Jacobson, Mass spectrometric identification of Si-O-H(g) species from the reaction of silica with water vapor at atmospheric pressure, *J. Am. Ceram. Soc.* 80 (2005) 1009–1012.
- [17] S.L. dos Santos e Lucato, O.H. Sudre, D.B. Marshall, A method for assessing reactions of water vapor with materials in high-speed, high-temperature flow, *J. Am. Ceram. Soc.* 94 (2011) 186–195.
- [18] J.I. Federer, Alumina base coatings for protection of SiC ceramics, *J. Mater. Eng.* 12 (1990) 141–149,
- [19] J. Kim, M.G. Dunn, A.J. Baran, D.P. Wade, E.L. Tremba, Deposition of volcanic materials in the hot sections of two gas turbine engines, in: *Coal, Biomass Altern. Fuels; Combust. Fuels; Oil Gas Appl. Cycle Innov.*, Vol. 3, American Society of Mechanical Engineers, (1992) 641–651.
- [20] B.K. Jang, S.W. Kim, Y.S. Oh, H.T. Kim, High temperature corrosion of ZrO<sub>2</sub>-4mol% Y<sub>2</sub>O<sub>3</sub> thermal barrier coatings with volcanic ash, *Mater. Sci. Tech. Jpn.* 54 (2017) 128–131.
- [21] B.K. Jang, F.J. Feng, K. Suzuta, H. Tanaka, Y. Matsushita, K.S. Lee, S.W. Kim, Y.S. Oh, H.T. Kim, Corrosion behavior of volcanic ash on sintered mullite for environmental barrier coatings, *Ceram. Int.* 43 (2017) 1880–1886.
- [22] K.M. Grant, S. Krämer, J.P.A. L'ofvander, C.G. Levi, CMAS degradation of

- environmental barrier coatings, *Surf. Coatings Technol.* 202 (2007) 653–657.
- [23] K.M. Grant, S. Kramer, G.G.E. Seward, C.G. Levi, Calcium-magnesium aluminosilicate interaction with yttrium monosilicate environmental barrier coatings, *J. Am. Ceram. Soc.* 93 (2010) 3504–3511.
- [24] B.K. Jang, F.J. Feng, K.S. Lee, E. García, A. Nistal, N. Nagashima, S.W. Kim, Y.S. Oh, H.T. Kim, Thermal behavior and mechanical properties of  $Y_2SiO_5$  environmental barrier coatings after isothermal heat treatment, *Surf. Coat. Technol.* 308 (2016) 24–30.
- [25] B.K. Jang, H. Tanaka, K. Suzuta, Y. Matsushita, K.S. Lee, F.J. Feng, S. Ueno, Corrosion behavior of volcanic ash and calcium magnesium aluminosilicate on  $Yb_2SiO_5$  environmental barrier coatings, *J. Ceram. Soc. Jpn.* 125 [4] (2017) 326–332.
- [26] T.M. Daniel, B. Chris, H. Tanvir, A review on environmental barrier coatings: History, current state of the art and future developments, *J. Eur. Ceram. Soc.* 41 (2021) 1747–1768.
- [27] B.K. Jang, N. Nagashima, S.W. Kim, Y.S. Oh, S.M. Lee, H.T. Kim, Mechanical properties and microstructure of  $Yb_2SiO_5$  environmental barrier coatings under isothermal heat treatment, *J. Eur. Ceram. Soc.* 40 (2020) 2667–2673.
- [28] J.I. Federer, Alumina base coatings for protection of SiC ceramics, *J. Mater. Eng.* 12 (1990) 141–149.
- [29] K.N. Lee, D.S. Fox, N.P. Bansal, Rare earth silicate environmental barrier coatings for SiC/SiC composites and  $Si_3N_4$  ceramics, *J. Eur. Ceram. Soc.* 25 (2005) 1705–1715.
- [30] J.R. Price, M. van Roode, C. Stala, Ceramic oxide-coated silicon carbide for high temperature corrosive environments, *Key Eng. Mater.* 72–74 (1992) 71–84.
- [31] K.N. Lee, R.A. Miller, N.S. Jacobson, New generation of plasma-sprayed mullite coatings on silicon carbide, *J. Am. Ceram. Soc.* 78 (1995) 705–710.
- [32] K.N. Lee, M. van Roode, Environmental barrier coatings enhance performance of

- SiC/SiC ceramic matrix composites, *Am. Ceram. Soc. Bull.* 98 (2019) 46–53.
- [33] K.N. Lee, in *Ceramic Matrix Composites: Materials, Modeling and Technology* (eds Bansal, N. P. & Lamon, J.), (Wiley, Hoboken, 2015) 430–451.
- [34] D. Zhu, in *Engineered Ceramics: Current Status and Future Prospects* (eds Ohji, T. & Singh, M.), (Wiley, Hoboken, 2016) 187–202.
- [35] K.N. Lee, D.S. Fox, N.P. Bansal, Rare earth silicate environmental barrier coatings for SiC/SiC composites and Si<sub>3</sub>N<sub>4</sub> ceramics, *J. Eur. Ceram. Soc.* 25 (2005) 1705–1715.
- [36] L.R. Turcer, N.P. Padture, Towards multifunctional thermal environmental barrier coatings (TEBCs) based on rare-earth pyrosilicate solid-solution ceramics, *Scr. Mater.* 154 (2018) 111–117.
- [37] Y. Xu, X. Hu, F. Xu, K. Li, Rare earth silicate environmental barrier coatings: present status and prospective, *Ceram. Int.* 43 (2017) 5847–5855.
- [38] A.J. Fernández-Carrión, M. Allix, A.I. Becerro, Thermal expansion of rare-earth pyrosilicates, *J. Am. Ceram. Soc.* 96 (2013) 2298–2305.
- [39] N. Al Nasiri, N. Patra, D. Horlait, D.D. Jayaseelan, W.E. Lee, Thermal properties of rare-earth monosilicates for EBC on Si-based ceramic composites, *J. Am. Ceram. Soc.* 99 (2016) 589–596.
- [40] M.D. Dolan, B. Harlan, J.S. White, M. Hall, S.T. Misture, S.C. Bancheri, B. Bewlay, Structures and anisotropic thermal expansion of the  $\alpha$ ,  $\beta$ ,  $\gamma$ , and  $\delta$  polymorphs of Y<sub>2</sub>Si<sub>2</sub>O<sub>7</sub>, *Powder Diffr.* 23 (2008) 20–25.
- [41] P.J. Meschter, E.J. Opila, N.S. Jacobson, Water vapor-mediated volatilization of high-temperature materials, *Annu. Rev. Mater. Res.* 43 (2013) 559–588.
- [42] A.R. Krause, H.F. Garces, C.E. Herrmann & N.P. Padture, Resistance of 2ZrO<sub>2</sub>·Y<sub>2</sub>O<sub>3</sub> top coat in thermal/environmental barrier coatings to calcia-magnesia-aluminosilicate attack at 1500°C, *J. Am. Ceram. Soc.* 100 (2017) 3175–3187.

- [43] D.L. Poerschke, R.W. Jackson, C.G. Levi, Silicate deposit degradation of engineered coatings in gas turbines: progress toward models and materials solutions, *Ann. Rev. Mater. Sci.* 47 (2017) 297–330.
- [44] L. Bowen, J. Xiaochao, C. Jie, X. Baosheng, W. Yiguang, F. Daining, Advances in numerical modeling of environmental barrier coating systems for gas turbines, *J. Eur. Ceram. Soc.* 40 (2020) 3363–3379.
- [45] J. Liu, L. Zhang, Q. Liu, L. Cheng, Y. Wang, Calcium–magnesium–aluminosilicate corrosion behaviors of rare-earth disilicates at 1400°C, *J. Eur. Ceram. Soc.* 33 (2013) 3419–3428.
- [46] N.L. Ahlborg, D. Zhu, Calcium–magnesium aluminosilicate (CMAS) reactions and degradation mechanisms of advanced environmental barrier coatings, *Surf. Coatings Technol.* 237 (2013) 79–87.
- [47] L.R. Turcer, A.R. Krause, H.F. Garces, L. Zhang, N.P. Padture, Environmental-barrier coating ceramics for resistance against attack by molten calcia-magnesia-aluminosilicate (CMAS) glass: part II,  $\beta$ -Yb<sub>2</sub>Si<sub>2</sub>O<sub>7</sub> and  $\beta$ -Sc<sub>2</sub>Si<sub>2</sub>O<sub>7</sub>, *J. Eur. Ceram. Soc.* 38 (2018) 3914–3924.
- [48] W.D. Summers, D.L. Poerschke, M.R. Begley, C.G. Levi, F.W. Zok, A computational modeling framework for reaction and failure of environmental barrier coatings under silicate deposits, *J. Am. Ceram. Soc.* (2020) 5196–5213.
- [49] W.D. Summers, D.L. Poerschke, A.A. Taylor, A.R. Ericks, C.G. Levi, F.W. Zok, Reactions of molten silicate deposits with yttrium monosilicate, *J. Am. Ceram. Soc.* 103 (2020) 2919–2932.
- [50] F. Stolzenburg, M.T. Johnson, K.N. Lee, N.S. Jacobson, K.T. Faber, The interaction of calcium–magnesium–aluminosilicate with ytterbium silicate environmental barrier materials, *Surf. Coatings Technol.* 284 (2015) 44–50.

- [51] D.L. Poerschke, D.D. Hass, S. Eustis, G.G.E. Seward, J.S. Van Sluytman, C.G. Levi, Stability and CMAS resistance of ytterbium-silicate/hafnate EBCs/TBC for SiC composites, *J. Am. Ceram. Soc.* 98 (2015) 278–286.
- [52] H. Zhao, B.T. Richards, C.G. Levi, H.N.G. Wadley, Molten silicate reactions with plasma sprayed ytterbium silicate coatings, *Surf. Coatings Technol.* 288 (2016) 151–162.
- [53] F. Stolzenburg, P. Kenesei, J. Almer, K.N. Lee, M.T. Johnson, K.T. Faber, The influence of calcium–magnesium–aluminosilicate deposits on internal stresses in Yb<sub>2</sub>Si<sub>2</sub>O<sub>7</sub> multilayer environmental barrier coatings, *Acta Mater.* 105 (2016) 189–198.
- [54] V.L. Wiesner, D. Scales, N.S. Johnson, B.J. Harder, A. Garg, N.P. Bansal, Calcium–magnesium aluminosilicate (CMAS) interactions with ytterbium silicate environmental barrier coating material at elevated temperatures, *Ceram. Int.* 46 (2020) 16733–16742.
- [55] T. Osada, W. Nakao, K. Takahashi, K. Ando, *Advances in Ceramic Matrix Composites.*, 410 (2014)
- [56] K. Ando, B.S. Kim, M.C. Chu, S. Saito, K. Takahashi, Crack-healing and mechanical behaviour of Al<sub>2</sub>O<sub>3</sub>/SiC composites at elevated temperature, *Fatigue Fract. Engng. Mat. Struct.*, 27 (2004) 531–541.
- [57] W. Nakao, Y. Tsutagawa, K. Ando, *J. Intell. Mat. Sys. Struct.*, 19 (2008) 407.
- [58] B.K. Jang, M. Enoki, T. Kishi, S.H. Lee, H.K. Oh, Fracture behaviour and toughening of alumina-based composites fabricated by microstructural control, *Fracture Mechanics of Ceramics*, 12 (1996) 371-382.
- [59] B.K. Jang, M. Enoki, T. Kishi, H.K. Oh, Effect of second phase on mechanical properties and toughening of Al<sub>2</sub>O<sub>3</sub> based ceramic composites, *Composites Engineering*, 5 (1995) 1275-1286.
- [60] B.K. Jang, M. Enoki, T. Kishi, Control of microstructure of alumina ceramics by dispersion of nano SiC particulates, *J. Ceram. Soc. Jpn. International Edition*, 102 (1994)

861–865.

- [61] B.K. Jang, S.Y. Kim, I.S. Han, D.W. Seo, K.S. Hong, S.K. Woo, Y. Sakka, Influence of uni and bi-modal SiC composition on mechanical properties and microstructure of reaction-bonded SiC ceramics, *J. Ceram. Soc. Jpn.* 118 [11] (2010) 1028–1031.
- [62] S.T. Nguyen, T. Nakayama, H. Suematsu, T. Suzuki, L. He, H.B. Cho, K. Niihara, Strength improvement and purification of  $\text{Yb}_2\text{Si}_2\text{O}_7$ -SiC nanocomposites by surface oxidation treatment, *J. Am. Ceram. Soc.*, 100 (2017) 3122–3131.
- [63] W. Kunz, H. Klemm, A. Michaelis, Crack-healing in ytterbium silicate filled with silicon carbide particle, *J. Eur. Ceram. Soc.*, 40 (2020) 5740–5748.
- [64] H.D. Vu, M. Nanko, Crack-healing performance and oxidation behavior of SiC dispersed yttrium silicate composites, *J. Asian Ceram. Soc.*, 8 (2020) 298–308.

## **Chapter 2. High-Temperature Corrosion of $Gd_2SiO_5$ with Volcanic Ash for EBCs**

### **2.1. Introduction**

In April 2010, European airspace was closed for six days due to the ashes generated from the eruption of Iceland's Eyjafjallajökull volcano. Thousands of flights have been canceled and millions of passengers stranded because of the danger volcanic ash (VA) poses to aircraft engines. The International Air Transport Association (IATA) has estimated that the disruption has cost airlines nearly \$2 billion [1]. In addition, volcanic ash can damage engine components, leading to engine failure [2]. Environmental barrier coatings (EBCs) are required that can withstand volcanic ash deposits when applied to gas turbines [3–7]. The required properties [8–11] of EBC materials include good corrosion resistance, thermochemical stability, and a low evaporation rate, of which corrosion resistance is especially important [12–15]. The main function of EBCs is to actively interact with the molten volcanic ash to be highly effective against attack by volcanic ash and should result in the rapid crystallization of the refractory oxide phase, forming a sealing layer to prevent further penetration. In the past, many researchers have focused on the vapor corrosion behavior of EBC materials [16,17]. Recently, volcanic ash and calcium–magnesium–aluminosilicate (CMAS) have been found to significantly impact the durability of EBC materials. Researchers [18,19] used real volcanic ash to identify Fe and Na components penetrating the substructure that were not included in CMAS. During gas turbine operation, the volcanic ash accumulating on the surface of the EBCs is a silicate mineral. This problem seriously impacts aircraft engines when an aircraft is flying in an ash-containing environment [20]. A jet engine draws air forward and compresses it at high pressure. The principle is to ignite the compressed air together with the fuel and to eject the high-temperature and high-pressure gas to gain propulsion.

Rare earth (RE) silicates have been applied to EBCs to protect silicon-based ceramics from corrosion [21,22]. Therefore, the application of EBCs of RE silicates is required to prevent the volatilization of silicon hydroxides having good oxidation resistance [23,24]. These findings can contribute to identifying, preventing, and minimizing the damage to matrix components with EBCs caused by volcanic ash. The corrosion behavior of RE monosilicate ( $\text{RE}_2\text{SiO}_5$ ) high-temperature water vapor has been already studied [16]. Unfortunately, most research on  $\text{RE}_2\text{SiO}_5$  focuses on the corrosion behavior of  $\text{Y}_2\text{SiO}_5$  and  $\text{Yb}_2\text{SiO}_5$ , and the investigation has revealed that the mechanism of  $\text{RE}_2\text{SiO}_5$  corrosion according to various RE materials at high temperatures is unknown. Studies have shown that materials with smaller RE cations (Y and Yb) show excellent resistance to CMAS with components similar to volcanic ash. Conversely, it was proposed that materials with larger RE cations (La and Gd) reacted vigorously with the CMAS melt and quickly formed a crystalline RE apatite phase to prevent further CMAS infiltration. Also, Gd has already been applied to TBCs ( $\text{Gd}_2\text{Zr}_2\text{O}_7$ ) [25,26] to confirm the excellent high-temperature corrosion properties of CMAS [18]. Therefore,  $\text{Gd}_2\text{SiO}_5$  was evaluated for application to developed high-temperature corrosion behavior of EBCs, it is possible to study the optimum resistance to corrosion of a wide range of RE elemental materials. In addition, few studies have been conducted on the high-temperature corrosion properties of volcanic ash in the sintered body of RE materials used in EBCs. The purpose of this study was to investigate the application of EBCs by the high-temperature corrosion evaluation of sintered  $\text{Gd}_2\text{SiO}_5$  by volcanic ash.

## 2. 2. Experimental Procedure

### 2.2.1. Sample Preparation and Heat Treatment

Sintered  $\text{Gd}_2\text{SiO}_5$  was prepared using spark plasma sintering (SPS) equipment (Dr. Sinter 1050, SCM, Japan).  $\text{Gd}_2\text{SiO}_5$  powder was synthesized by solid-state reaction with  $\text{Gd}_2\text{O}_3$  (Rare Metallic Corporation, Japan) and  $\text{SiO}_2$  (Waco Pure Chemical Industries, Japan) powders. The mass fractions of two powders were determined as having a molar ratio of 1 : 1. The ball-mill method with  $\text{ZrO}_2$  balls and ethanol were used for 24 h. After the ball-milling process, the suspension was dried in a furnace at  $60^\circ\text{C}$ , and the  $\text{Gd}_2\text{O}_3$ - $\text{SiO}_2$  mixed powder was heated at  $1400^\circ\text{C}$  for 24 h and synthesized using an  $\text{Al}_2\text{O}_3$  crucible. After putting synthesized  $\text{Gd}_2\text{SiO}_5$  powder into the graphite mold, the graphite mold (30 mm in diameter) was put into the SPS equipment, and the temperature was raised to  $1400^\circ\text{C}$  in a vacuum of  $10^{-2}$  Pa at a temperature rate of  $10^\circ/\text{min}$  and under 60 MPa of pressure. Sintered  $\text{Gd}_2\text{SiO}_5$  was cut by a diamond saw that was 10 x 5 mm and 3 mm thick. Using acetone and ethanol, sintered  $\text{Gd}_2\text{SiO}_5$  was cleaned for 5 min. The volcanic ash (Kagoshima, Japan) was sprinkled on the polished surface of each specimen using paste at a concentration of  $40 \text{ mg}/\text{cm}^2$ . The volcanic ash-sprinkled sintered  $\text{Gd}_2\text{SiO}_5$  was exposed to  $1400^\circ\text{C}$  for 2 h, 12 h, and 48 h by heat treatment at  $5^\circ\text{C}/\text{min}$ . Sintered  $\text{Gd}_2\text{SiO}_5$  was cut to 5 x 5 mm to analyze the cross section. Thereafter, polishing was carried out using 9, 3, and 1  $\mu\text{m}$  diamond suspensions.

### 2.2.2. Characterization

The corrosive state of each specimen were investigated using a scanning electron microscope (SEM S-4300, Hitachi, Ltd., Japan) with energy-dispersive X-ray spectrometry (EDS) to determine the elemental infiltrated ingredients, distribution, and content ratio. To estimate the reaction temperatures of volcanic ash and  $\text{Gd}_2\text{SiO}_5$  under air, differential scanning calorimetry (DSC6300, Hitachi, Ltd., Japan) measurements were carried out. At room

temperature, the homogeneity samples (volcanic ash :  $\text{Gd}_2\text{SiO}_5 = 1 : 1$  wt.%) for DSC measurement were prepared and stirred in EtOH under Ar-gas flow condition. Under air, the phase relations of the same mixed powder of DSC workup to  $1300^\circ\text{C}$  were measured using a high-temperature X-ray diffraction (HT-XRD, Smart Lab, Rigaku, Japan) with Cu  $\text{K}\alpha_1$  radiation ( $\lambda = 1.54056\text{\AA}$ ), with a  $2\theta$  range of  $10\text{--}70^\circ$ , a scan speed of  $1^\circ/\text{min}$ , and a scan step of  $0.02^\circ/\text{min}$ .

## 2.3. Results and Discussion

### 2.3.1. Characterization of Volcanic Ash

Table 3 shows the chemical composition of Kagoshima volcanic ash [27]. The volcanic ash included considerable amounts of Si, together with Al, Fe, Na, Ca, and Mg.

Table 3. Chemical composition of Kagoshima volcanic ash (wt.%).

Composition of Volcanic Ash	
Components	Contents
SiO <sub>2</sub>	58.7
Fe <sub>2</sub> O <sub>3</sub>	8.9
Al <sub>2</sub> O <sub>3</sub>	13.6
MgO	8.1
CaO	6.8
Na <sub>2</sub> O	3.9

Fig. 13 shows the dynamic differential scanning calorimetry (DDSC) results of volcanic ash powder and volcanic ash–Gd<sub>2</sub>SiO<sub>5</sub> mixed powder according to temperature. In general, chemical reactions and phase changes occur at temperatures where endothermic and exothermic reactions occur. As reported in the literature [14], the target heat-treatment temperature of the sample is set after confirming the endothermic and exothermic temperatures. DDSC corresponds to the differential of DSC and is designed to make it easy to see the variations of DSC. If the DSC curve shifts down as the temperature rises, it obtains the value of DDSC plus. As a result, DDSC takes the maximum value at the inflection point that determines the melting point initiation temperature in DSC. The sharpest exothermal peak can be seen at 1140°C in Fig. 13 (a). This can be seen as the melting point of the volcanic ash powder.

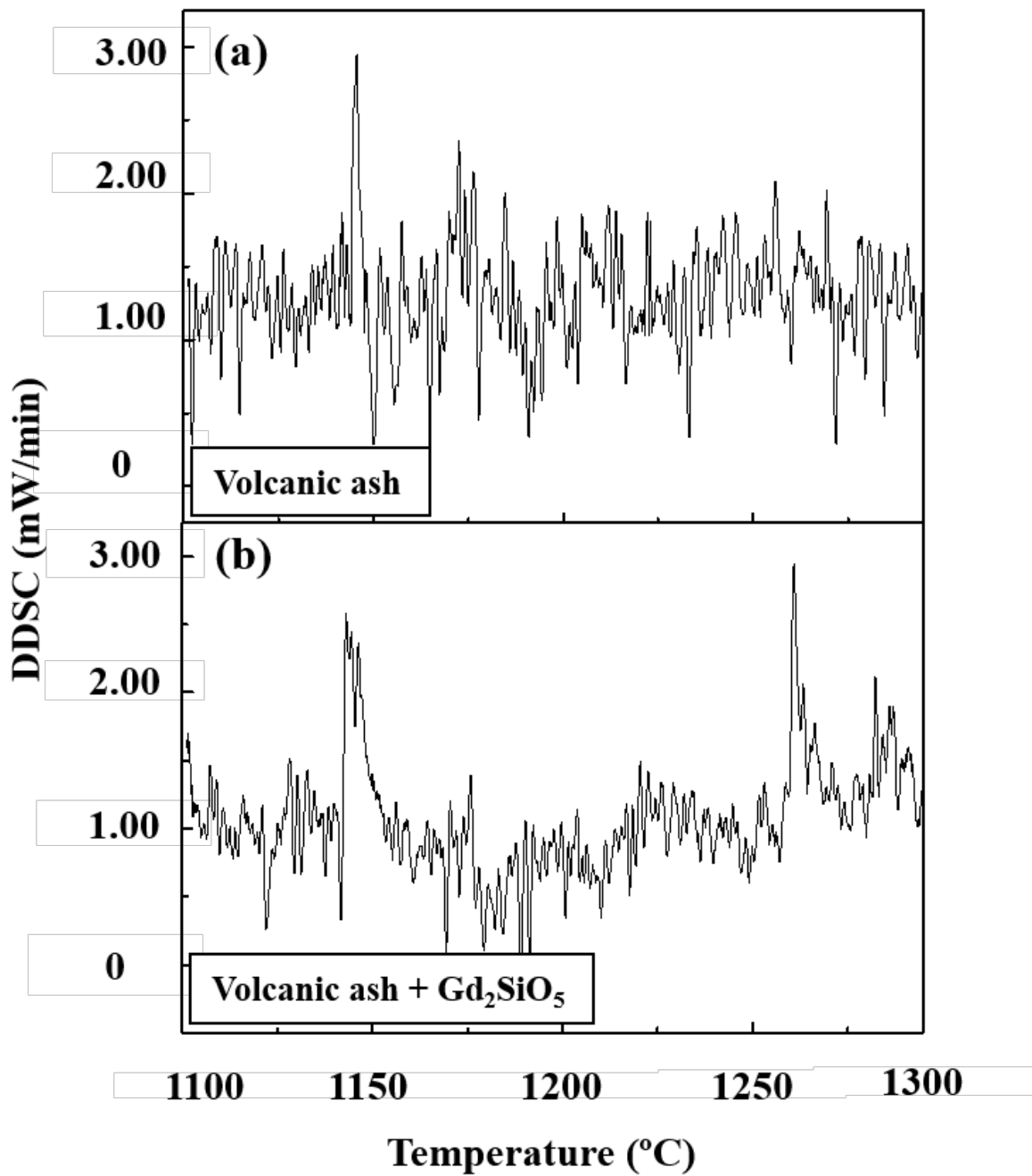


Fig. 13. DDSC results of volcanic ash powder and volcanic ash–Gd<sub>2</sub>SiO<sub>5</sub> (1 : 1 wt.%) mixed powder.

In order to compare the reaction temperature of the volcanic ash and the volcanic ash–Gd<sub>2</sub>SiO<sub>5</sub> mixed powder in Fig. 13 (b), the volcanic ash and Gd<sub>2</sub>SiO<sub>5</sub> were measured at 1 : 1

wt.% after stirring. The sharp exothermal peak appeared at 1140°C and another sharp exothermal peak at 1270°C. The peak at 1140°C shows the melting point of volcanic ash, and the peak below 1270°C is the melting point of the volcanic ash–Gd<sub>2</sub>SiO<sub>5</sub> mixed powder in Fig. 13 (b). As a high-temperature-applicable material, it exhibits stable thermodynamic properties.

### 2.3.2. High-Temperature Corrosion of Sintered Gd<sub>2</sub>SiO<sub>5</sub> with Volcanic Ash

Fig. 14 represents (a) 2 h, (b) 12 h, and (c) 48 h low magnification images after heat treatment at 1400°C. The exact depth behavior of the reaction layer can be identified in the high-magnification pictures at (d) 2 h, (e) 12 h, and (f) 48 h in Fig. 14. It is found that the behavior in the microstructure of the Gd<sub>2</sub>SiO<sub>5</sub> was significant near the volcanic ash and Gd<sub>2</sub>SiO<sub>5</sub> interface, and the thickness of the area affected by volcanic ash increased with increasing exposure time. This region is referred as the “reaction area” in this work. It can be seen that the volcanic ash melts into sintered Gd<sub>2</sub>SiO<sub>5</sub> at a high temperature of 1400°C to form a reaction area. The volcanic ash and Gd<sub>2</sub>SiO<sub>5</sub> reaction area were found to be deepest at (f) 48 h. In the reaction area, there appears some elongated morphology of grains.

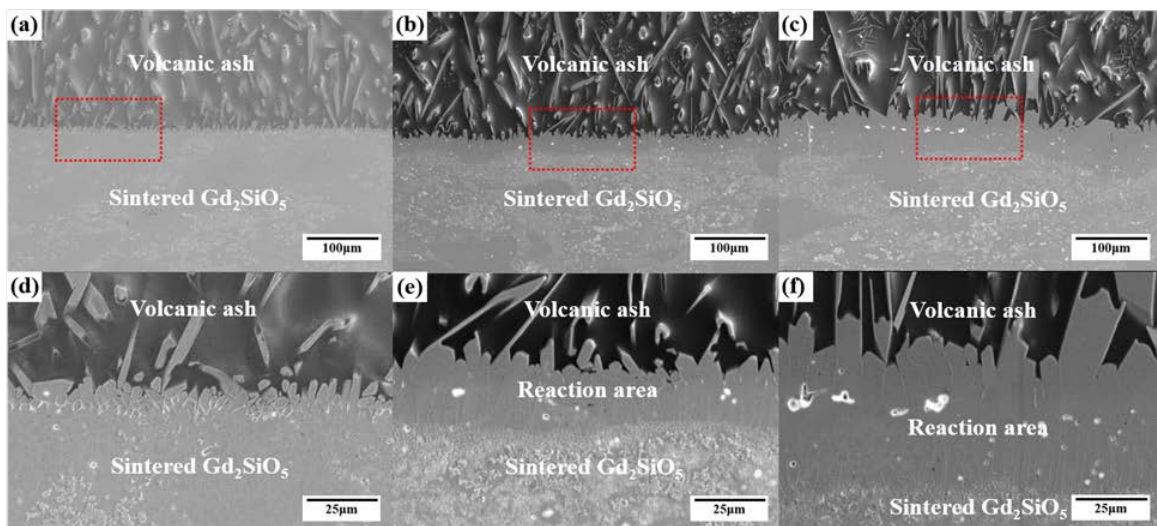


Fig. 14. SEM images of a cross section after heat treatment at 1400°C with volcanic ash: (a), (d) 2 h; (b), (e) 12 h; and (c), (f) 48 h.

Fig. 15 shows SEM images of the sample of  $Gd_2SiO_5$  coated with volcanic ash sintered at  $1400^\circ C$  for 12 h. EDS analysis detected Gd, which is a sintered  $Gd_2SiO_5$ , and Si, Al, Mg, Ca, and Fe, which are volcanic ash components. Particularly, the volcanic ash component Si, Ca accumulated on the surface of the sintered  $Gd_2SiO_5$  and partially melted to react. The elongated morphology of grains observed in the reaction area is thicker due to the increase in heat-treat time as the ash dissolves.

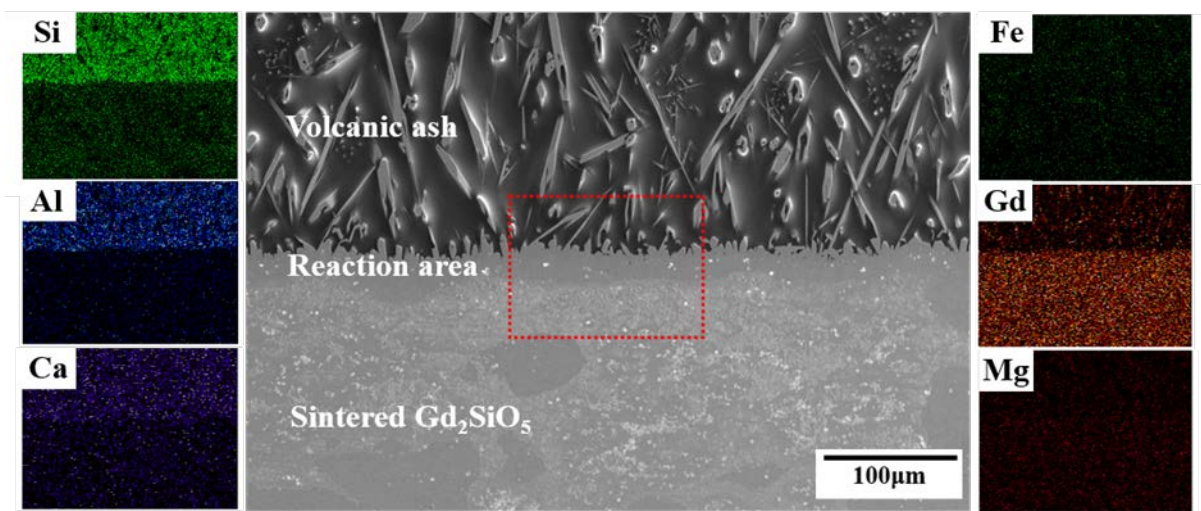


Fig. 15. EDS mapping results of heat-treated  $Gd_2SiO_5$  at  $1400^\circ C$  for 12 h with volcanic ash.

Fig. 16 shows a high-magnification SEM photograph of the microstructure of the same sample indicated as the red area in Fig. 15. In order to confirm the boundary of the reaction area, EDS point analysis were performed on parts A, B, and C. Table 4 shows the results of the EDS point analysis on parts A, B, and C of Fig. 16. The volcanic ash elements (Si, Al, Fe, Mg, Ca, and Na) and O were detected at point A in Fig. 16, indicating that the point A was filled with volcanic ash. The volcanic ash melted at a high temperature and penetrated sintered  $Gd_2SiO_5$  to form a reaction area. Si, O, Ca and Gd components (point B) were detected in the reaction area. This result suggests that there was a difference in composition between the

reaction area and the sintered  $Gd_2SiO_5$  area. Also, the components Gd, Si, and O of the sintered  $Gd_2SiO_5$  were detected at point C.

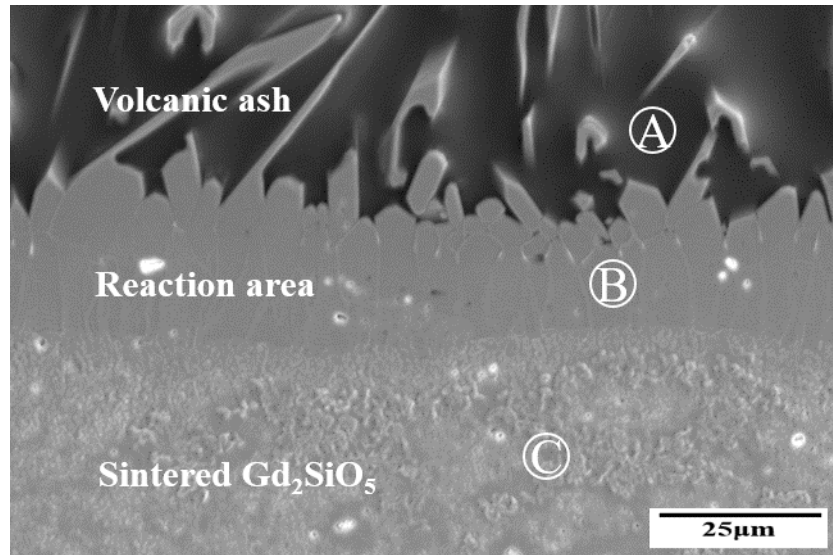


Fig. 16. SEM images of heat-treated  $Gd_2SiO_5$  at  $1400^\circ C$  for 12 h with volcanic ash of the red area in Fig. 15.

Table 4. Normalized elemental ratio (at.%) at points A, B, and C of Fig. 16 were measured using EDS point analysis.

Elements	O	Na	Mg	Al	Si	Ca	Fe	Gd	Total
Point A	53.25	2.77	1.67	9.12	23.79	7.47	1.93	0	100.00
Point B	52.48	0	0	0	19.20	5.31	0	23.01	100.00
Point C	50.76	0	0	0	15.56	0	0	33.68	100.00

Fig. 17 is a SEM image of sintered  $Gd_2SiO_5$  heat-treated at  $1400^\circ C$  for 48 h coated with volcanic ash analyzed using EDS mapping analysis. Si, Al, Mg, Ca, and Fe of volcanic ash components and Gd were detected as a result of the EDS mapping analysis. As previously

discussed, the reaction area and thickness of elongated grains increased with increasing exposure time. According to the results of the EDS mapping analysis, it is possible to confirm Ca contained in the reaction area. According to another study [28], RE-apatite production in CAS melts was analyzed for rare earth elements. In particular, it was concluded that the Gd element forms apatite from short-time interactions and is advantageous for rare earths with a larger ionic radius. It has been reported that molten CAS affects RE-apatite nucleation and crystal growth. As time increased, the reaction area showed the growth of  $\text{Ca}_2\text{Gd}_8(\text{SiO}_4)_6\text{O}_2$  grains vertically at the interface of the molten volcanic ash. This result explains the differences in reaction area and thickness of  $\text{Ca}_2\text{Gd}_8(\text{SiO}_4)_6\text{O}_2$  grains observed in the reaction areas of Fig. 15 and Fig. 17.

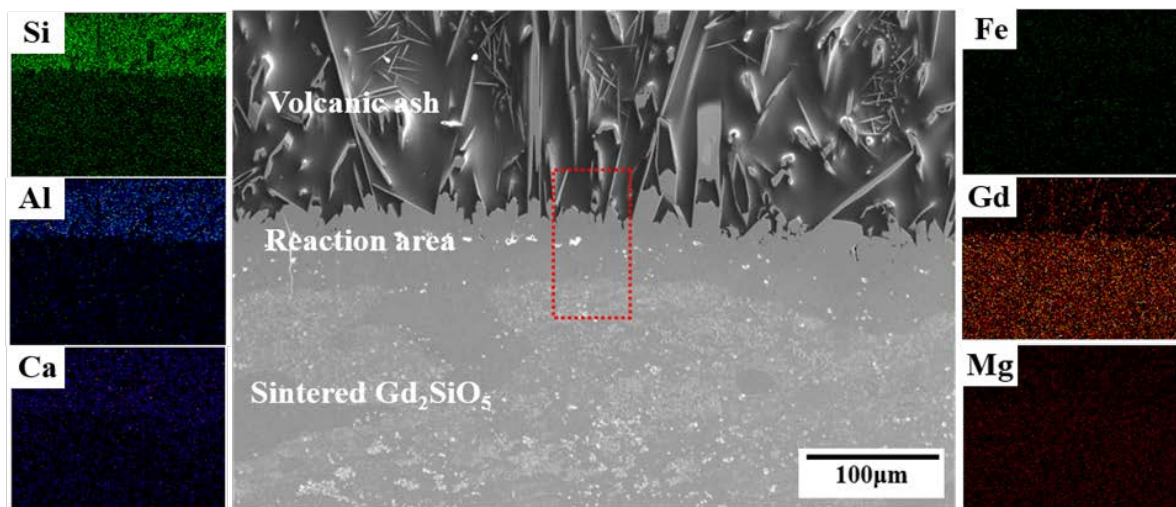


Fig. 17. EDS mapping results of heat-treated  $\text{Gd}_2\text{SiO}_5$  at 1400°C for 48 h with volcanic ash.

To investigate the formation behavior of the reaction area, an EDS line analysis of  $\text{Gd}_2\text{SiO}_5$  heat treated at 1400°C for 48 h with volcanic ash has been carried out, and the results are shown in Fig. 18. Fig. 18 (a) is a cross-sectional SEM image of the red area in Fig. 17, divided into volcanic ash, reaction area, and sintered  $\text{Gd}_2\text{SiO}_5$ . Fig. 18 (b) is a graph showing the components of the line analysis using EDS. Line analysis can be used to identify the elemental

components constituting each region. In addition, EDS results show the distribution of each element, Gd, Si, Fe, Ca, Mg, Na, Al, and O from the volcanic ash to the sintered  $\text{Gd}_2\text{SiO}_5$ . The Ca component, one of the volcanic ash components, is clearly observed in the reaction area. The Gd element increased as the line moved from the volcanic ash region to the sintered  $\text{Gd}_2\text{SiO}_5$ . In addition, the depth of the reaction area was found to be about 50  $\mu\text{m}$  deeper than the reaction area after heat treatments of 2 h and 12 h.

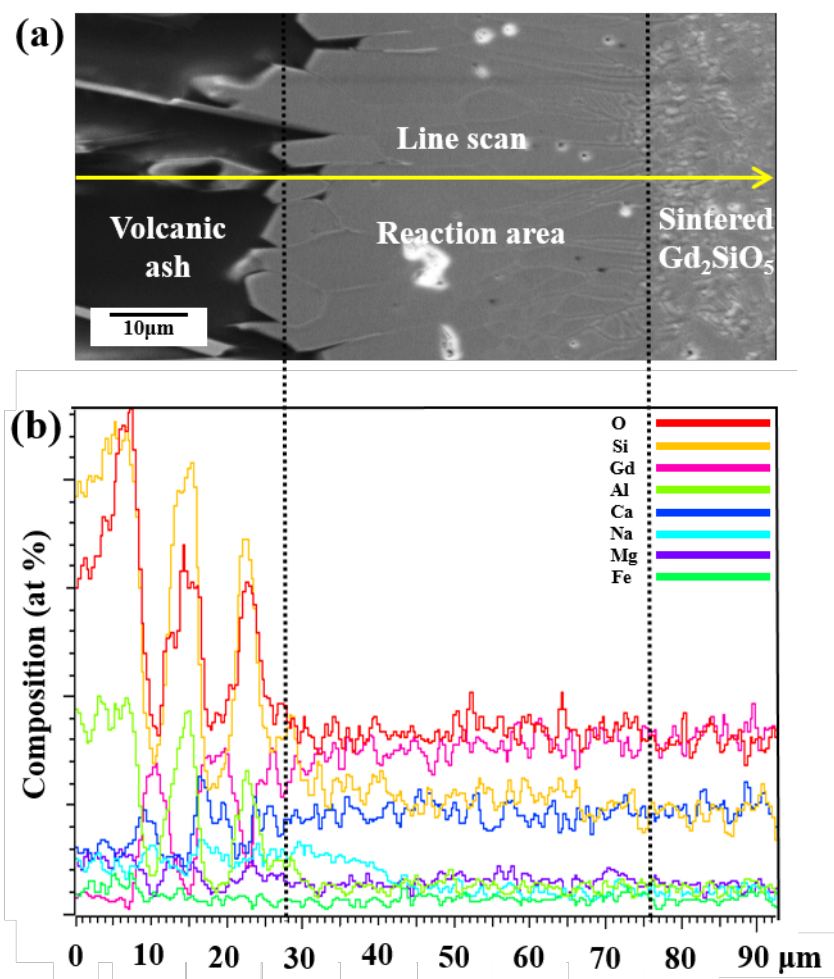


Fig. 18. Results by compositional line analysis of heat-treated  $\text{Gd}_2\text{SiO}_5$  at  $1400^\circ\text{C}$  for 48 h with volcanic ash: (a) cross sectional SEM image of the specimen and analyzed part of the red area in Fig. 17 and (b) result of compositional line analysis.

Fig. 19 shows the result of the HT-XRD pattern that can confirm the phase transition at high temperatures. To analyze the dynamic reaction process between sintered  $\text{Gd}_2\text{SiO}_5$  and molten volcanic ash, HT-XRD can be used to determine the temperature at which the reaction occurs [21]. The reactions occur at those temperatures at which phase transitions or chemical reactions occur. Because reactions occurred at around  $1140^\circ\text{C}$  and  $1270^\circ\text{C}$ , as indicated by DDSC analysis as shown in Fig. 13, the reaction phase was evaluated at each temperature using HT-XRD from  $1100^\circ\text{C}$  to  $1400^\circ\text{C}$ . In addition, since the phase change may occur during cooling in response to the viscosity of the melt during cooling, the room temperature ( $25^\circ\text{C}$ ) state after cooling was evaluated. Thus, it is necessary to investigate the dynamic reaction process of molten volcanic ash, which acts with sintered  $\text{Gd}_2\text{SiO}_5$ ; thereafter, the sintered  $\text{Gd}_2\text{SiO}_5$  and the volcanic ash mixing powder were continuously heated from room temperature to  $1400^\circ\text{C}$  to observe the reaction between the molten volcanic ash and the sintered  $\text{Gd}_2\text{SiO}_5$ .

According to the HT-XRD results,  $\text{Gd}_2\text{SiO}_5$  and  $\text{Gd}_{4.67}\text{Si}_3\text{O}_{13}$  were observed in Fig. 19 (a) at  $25^\circ\text{C}$ . In addition, a peak of  $\text{NaAlSi}_3\text{O}_8$  (albite) and  $\text{Ca}_2(\text{Al}_{0.46}\text{Mg}_{0.54})(\text{Al}_{0.46}\text{Si}_{1.54})\text{O}_7$  (melilite) containing a volcanic ash component was observed. The crystal phases in Fig. 19 (b) at  $1100^\circ\text{C}$  and Fig. 19 (c) at  $1200^\circ\text{C}$  are the same as those at  $25^\circ\text{C}$ . As shown in Fig. 19 (d) and (e), the peak on  $\text{NaAlSi}_3\text{O}_8$  (albite) and  $\text{Ca}_2(\text{Al}_{0.46}\text{Mg}_{0.54})(\text{Al}_{0.46}\text{Si}_{1.54})\text{O}_7$  (melilite) disappeared when the temperature rose to  $1300^\circ\text{C}$  and  $1400^\circ\text{C}$ , respectively. On the other hand, a  $\text{Ca}_2\text{Gd}_8(\text{SiO}_4)_6\text{O}_2$  phase was observed. The  $\text{Ca}_2\text{Gd}_8(\text{SiO}_4)_6\text{O}_2$  phase formed by the reaction of  $\text{Gd}_2\text{SiO}_5$  and ash acts as a protective layer against attack by molten ash. Other studies [18] suggested that RE (La and Gd) zirconates show excellent resistance to CMAS with components similar to volcanic ash, melt vigorously and rapidly form calcium-rich phases to prevent further volcanic ash infiltration. According to related study [24], it was confirmed by XRD analysis that  $\text{Ca}_2\text{Gd}_8(\text{SiO}_4)_6\text{O}_2$  phase was generated by reaction of  $\text{Gd}_2\text{SiO}_5$ -CMAS at high temperature. The reason  $\text{Ca}_2\text{Gd}_8(\text{SiO}_4)_6\text{O}_2$  phase is formed is the main cause of the Ca component in CMAS.

In contrast, another study [16] reported that the  $\text{Gd}_2\text{SiO}_5$  phase changes only to the  $\text{Gd}_{4.67}\text{Si}_3\text{O}_{13}$  phase through high-temperature water vapor corrosion behavior. The same effect was not reflected due to effects of volcanic ash in this study. A strong Pt peak from a sample holder was also observed. These results indicate that the volcanic ash melted, and the incident X-rays penetrated the liquid and reached the Pt holder. The melting point of the second peak was confirmed by DDSC in Fig. 13 (b). It was analyzed that there was no phase change during the cooling process in Fig. 19 (f).

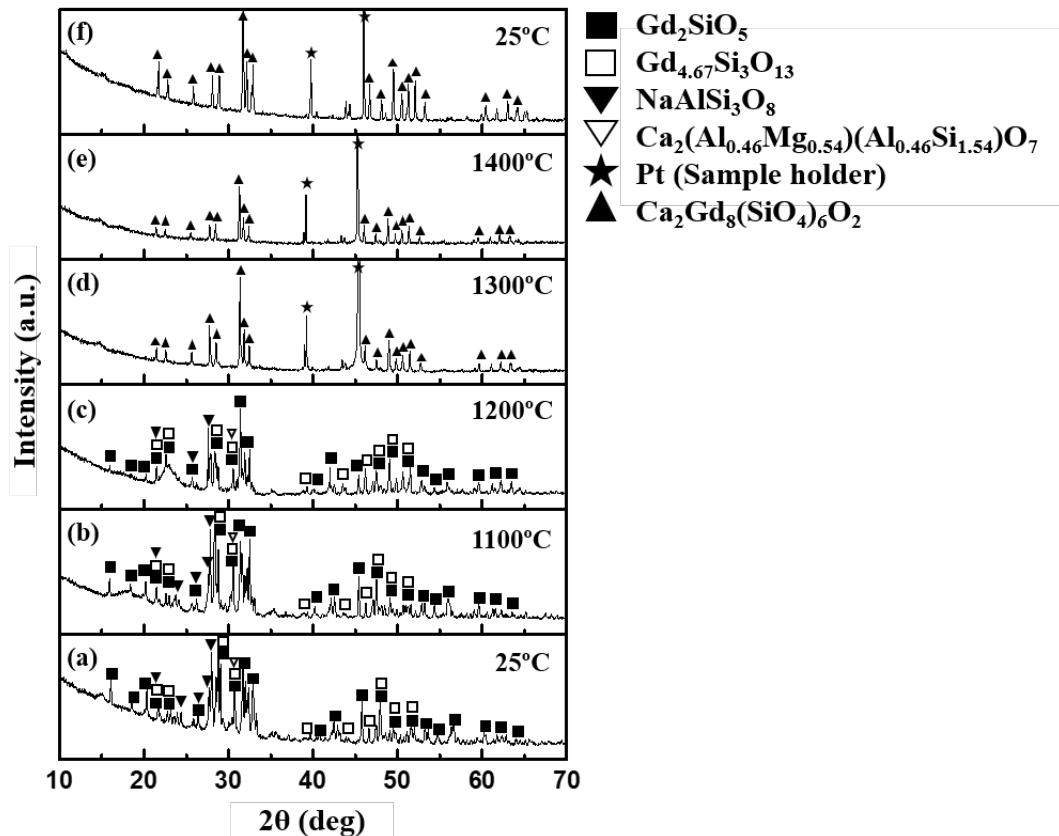


Fig. 19. HT-XRD patterns of mixed volcanic ash– $\text{Gd}_2\text{SiO}_5$  powder (1 : 1 wt.%) during a heating step at (a) 25°C, (b) 1100°C, (c) 1200°C, (d) 1300°C, (e) 1400°C, and a cooling step at (f) 25°C.

Fig. 20 is a graph showing the depth of the reaction area of volcanic ash and  $\text{Gd}_2\text{SiO}_5$  with

2 h, 12 h, and 48 h of heat treatment at 1400°C. The penetration depth after reaction times of 2 h, 12 h, and 48 h were calculated to be about 5, 18, and 45  $\mu\text{m}$ , respectively. In other words, according to the EDS point analysis in Table 4, the penetration of the reaction area grew 9 times from 2 to 48 h. Therefore, it was concluded that as the corrosion time increases, the molten volcanic ash continues to penetrate into the sintered  $\text{Gd}_2\text{SiO}_5$ .

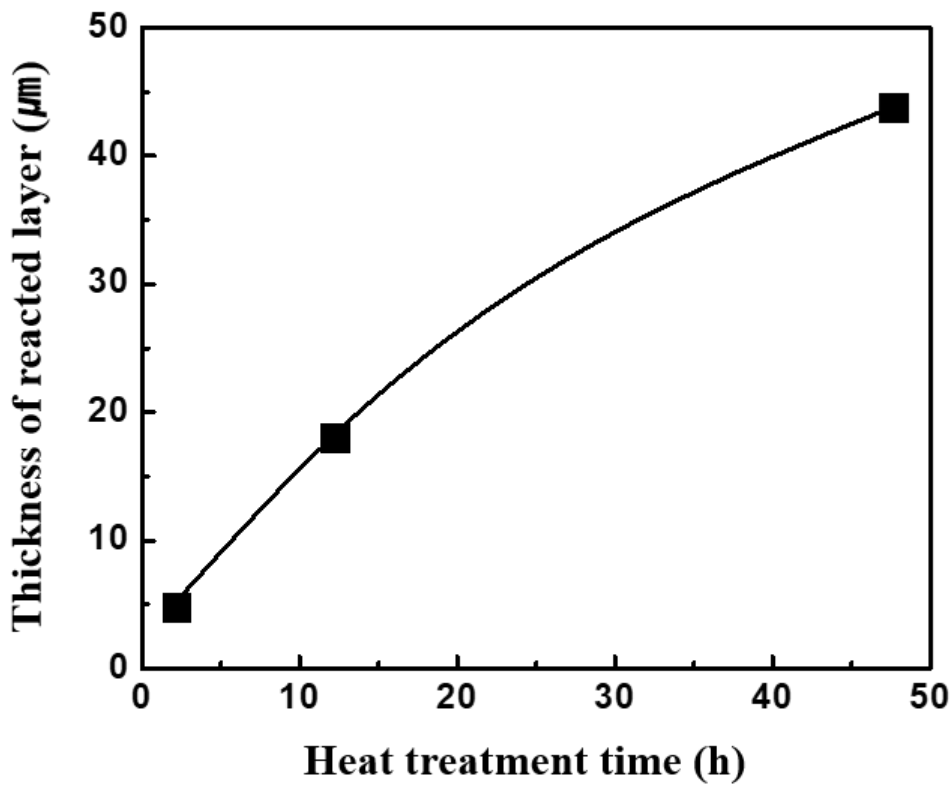


Fig. 20. Thickness of the reacted layer with the heat-treatment time.

In another study [23], dealing with corrosion by heat treatment of volcanic ash and  $\text{Yb}_2\text{SiO}_5$  (smaller RE cation), the depth of the reaction area generated was only about 10  $\mu\text{m}$  at 1400°C for 48 h. However, in this study, it can be confirmed that in the case of  $\text{Gd}_2\text{SiO}_5$  (larger RE cation), a deeper corrosion layer reacted to 45  $\mu\text{m}$  at 1400°C for 48 h.

## 2.4. Conclusions

In this study, sintered  $\text{Gd}_2\text{SiO}_5$  was prepared by the SPS process at  $1400^\circ\text{C}$  for 20 min under a pressure of 60 MPa, and the high-temperature corrosion performance of volcanic ash was evaluated at  $1400^\circ\text{C}$  for 2 h, 12 h, and 48 h. The reaction area between  $\text{Gd}_2\text{SiO}_5$  and molten volcanic ash increased with time due to the attack of molten volcanic ash. The reaction area was found to be deepest at 48 h. This result confirmed through HT-XRD is that the reaction products may melt at  $1300^\circ\text{C}$  or dissolve into the molten volcanic ash. The elongated morphology of  $\text{Ca}_2\text{Gd}_8(\text{SiO}_4)_6\text{O}_2$  grains observed in the reaction area is thought to be thicker due to the increased heat-treatment time as the volcanic ash dissolves. According to the HT-XRD results,  $\text{NaAlSi}_3\text{O}_8$  (albite) and  $\text{Ca}_2(\text{Al}_{0.46}\text{Mg}_{0.54})(\text{Al}_{0.46}\text{Si}_{1.54})\text{O}_7$  (melilite) containing volcanic ash components other than  $\text{Gd}_2\text{SiO}_5$  and  $\text{Gd}_{4.67}\text{Si}_3\text{O}_{13}$  were observed before heat treatment at room temperature. When the temperature increased to a reaction temperature of  $1300^\circ\text{C}$ , the peaks of  $\text{NaAlSi}_3\text{O}_8$  (albite) and  $\text{Ca}_2(\text{Al}_{0.46}\text{Mg}_{0.54})(\text{Al}_{0.46}\text{Si}_{1.54})\text{O}_7$  (melilite) disappeared, and  $\text{Ca}_2\text{Gd}_8(\text{SiO}_4)_6\text{O}_2$ , Pt peak were observed. The  $\text{Ca}_2\text{Gd}_8(\text{SiO}_4)_6\text{O}_2$  phase formed by the reaction of  $\text{Gd}_2\text{SiO}_5$  and volcanic ash acts as a protective layer against attack by molten ash.

## References

- [1] J. Shin, Statement before the subcommittee on space and aeronautics, Committee on Science and Technology, U.S. House of Representatives, May 5, (2010).
- [2] R. Dinius, Statement before the subcommittee on space and aeronautics, Committee on Science and Technology, U.S. House of Representatives, May 5, (2010).
- [3] S. Ramasamy, S.N. Tewari, K.N. Lee, R.T. Bhatt, D.S. Fox, Environmental durability of slurry based mullite–gadolinium silicate EBCs on silicon carbide, *J. Euro. Ceram. Soc.* 31 (2011) 1123–1130.
- [4] R.G. Munro, S.J. Dapkunas, Corrosion characteristics of silicon carbide and silicon nitride, *J. Res. Inst. Stand. Technol.* 98 (1993) 607–631.
- [5] K.N. Lee, D.S. Fox, N.P. Bansal, Rare earth silicate environmental barrier coatings for SiC/SiC composites and Si<sub>3</sub>N<sub>4</sub> ceramics, *J. Eur. Ceram. Soc.* 25 (2005) 1705–1715.
- [6] B.K. Jang, Y. Sakka, Thermophysical properties of porous SiC ceramics fabricated by pressureless sintering, *Adsorp. Sci. Technol.* 8 (2007) 655–659.
- [7] B.K. Jang, Y. Sakka, Influence of microstructure on the thermophysical properties of sintered SiC ceramics, *J. Alloys Compd.* 463 (2008) 493–497.
- [8] Y. Li, P. Xiao, Z. Li, W. Zhou, T. Liensdorf, W. Freudenberg, N. Langhof, W. Krenkel, Tensile fatigue behavior of plain-weave reinforced C<sub>f</sub>/C-SiC composites, *Ceram. Int.* 42 (2016) 6850–6857.
- [9] C. Spatz, N. Langhof, J. Schmidt, W. Krenkel, CMC jackets for metallic pipes—a novel approach to prevent the creep deformation of thermo-mechanically loaded metals, *J. Eur. Ceram. Soc.* 38 (2018) 2954–2960.
- [10] G.D. Girolamo, C. Blasi, L. Pilloni, M. Schioppa, Microstructural and thermal properties of plasma sprayed mullite coatings, *Ceram. Int.* 36 (2010) 1389–1395.

- [11] H. Chen, Y. Gao, Y. Liu, H. Luo, Hydrothermal synthesis of ytterbium silicate nanoparticles, *Inorg. Chem.* 49 (2010) 1942–1946.
- [12] P. Mechnich, W. Braue, U. Schulz, High-Temperature Corrosion of EB-PVD Yttria Partially Stabilized Zirconia Thermal Barrier Coatings with an Artificial Volcanic Ash Overlay, *J. Am. Ceram. Soc.* 94 [3] (2011) 925–931.
- [13] P. Mechnich, W. Braue, Volcanic Ash-Induced Decomposition of EB -PVD  $Gd_2Zr_2O_7$  Thermal Barrier Coatings to Gd-Oxyapatite, Zircon, and Gd, Fe -Zirconolite, *J. Am. Ceram. Soc.* 96 [6] (2013) 1958–1965.
- [14] B.K. Jang, F.J. Feng, K. Suzuta, H. Tanaka, Y. Matsushita, K.S. Lee, S.W. Kim, Y.S. Oh, H.T. Kim, Corrosion behavior of volcanic ash on sintered mullite for environmental barrier coatings, *Ceram. Int.* 43 (2017) 1880–1886.
- [15] B.K. Jang, F.J. Feng, K.S. Lee, E. García, A. Nistal, N. Nagashima, S.W. Kim, Y.S. Oh, H.T. Kim, Thermal behavior and mechanical properties of  $Y_2SiO_5$  environmental barrier coatings after isothermal heat treatment, *Surf. Coat. Technol.* 308 (2016) 24–30.
- [16] N. Al Nasiri, N. Patra, D.D. Jayaseelan, W.E. Lee, Water vapour corrosion of rare earth monosilicates for environmental barrier coating application, *Ceram. Int.* 43 (2017) 7393–7400.
- [17] N. Maier, K.G. Nickel, G. Rixecker, High temperature water vapour corrosion of rare earth disilicates (Y, Yb, Lu) $_2Si_2O_7$  in the presence of  $Al(OH)_3$  impurities, *J. Eur. Ceram. Soc.* 27 (2007) 2705–2713.
- [18] U. Schulz, W. Braue, Degradation of  $La_2Zr_2O_7$  and other novel EB-PVD thermal barrier coatings by CMAS (CaO–MgO– $Al_2O_3$ – $SiO_2$ ) and volcanic ash deposits, *Surf. Coat. Tech.* 235 (2013) 165–173.
- [19] K.I. Lee, L.T. Wu, R.T. Wu, P. Xiao, Mechanisms and mitigation of volcanic ash attack on yttria stabilized zirconia thermal barrier coatings, *Surf. Coat. Tech.* 260 (2014) 68–72.

- [20] W.J. Lee, B.K. Jang, D.S. Lim, Y.S. Oh, S.W. Kim, H.T. Kim, H. Araki, H. Murakami, S. Kuroda, Hot corrosion behavior of plasma sprayed 4 mol%  $\text{Y}_2\text{O}_3$ - $\text{ZrO}_2$  thermal barrier coatings with volcanic ash, *J. Korean Ceram. Soc.* 50 (2013) 353–358.
- [21] Z. Sun, M. Li, Z. Li, Y. Zhou, Hot corrosion of  $\gamma$ - $\text{Y}_2\text{Si}_2\text{O}_7$  in strongly basic  $\text{Na}_2\text{CO}_3$  molten salt environment, *J. Eur. Ceram. Soc.* 28 (1) (2008) 259–265.
- [22] K.M. Grant, S. Krämer, J.P.A. Löfvander, C.G. Levi, CMAS degradation of environmental barrier coatings, *J. Eur. Ceram. Soc.* 202 (2007) 653–657.
- [23] B.K. Jang, H. Tanaka, K. Suzuta, Y. Matsushita, K.S. Lee, F.J. Feng, S. Ueno, Corrosion behavior of volcanic ash and calcium magnesium aluminosilicate on  $\text{Yb}_2\text{SiO}_5$  environmental barrier coatings, *J. Ceram. Soc. Jpn.* 125 [4] (2017) 326–332.
- [24] F. Jiang, L. Cheng, Y. Wang, Hot corrosion of  $\text{RE}_2\text{SiO}_5$  with different cation substitution under calcium–magnesium–aluminosilicate attack, *Ceram. Int.* 43 (2017) 9019–9023.
- [25] C.S. Kwon, S.M. Lee, Y.S. Oh, H.T. Kim B.K. Jang, S.W. Kim, Fabrication and characterization of  $\text{La}_2\text{Zr}_2\text{O}_7/\text{YSZ}$  double-ceramic-layer thermal barrier coatings fabricated by suspension plasma spray, *Journal of the Korean Institute of Surface Engineering*, 48 (2015) 315–321.
- [26] S.J. Kim, S.M. Lee, Y.S. Oh, H.T. Kim B.K. Jang, S.W. Kim, Phase formation and thermal diffusivity of thermal barrier coatings of  $\text{La}_2\text{Zr}_2\text{O}_7$ ,  $(\text{La}_{0.5}\text{Gd}_{0.5})_2\text{Zr}_2\text{O}_7$ ,  $\text{Gd}_2\text{Zr}_2\text{O}_7$  fabricated by suspension plasma spray, *Journal of the Korean Institute of Surface Engineering*, 49 (2016) 604–611.
- [27] B.K. Jang, S.W. Kim, Y.S. Oh, H.T. Kim, High temperature corrosion of  $\text{ZrO}_2$ -4mol% $\text{Y}_2\text{O}_3$  thermal barrier coatings with volcanic ash, *Mater. Sci. Tech. Jpn.* 54 (2017) 128–131.

- [28] F. Perrudin, M.H. Vidal-Sétif, C. Rio, C. Petitjean, P.J. Panteix, M. Vilasi, Influence of rare earth oxides on kinetics and reaction mechanisms in CMAS silicate melts, *J. Eur. Ceram. Soc.* 39 (2019) 4223–4232.

# Chapter 3. High-Temperature Corrosion of $Gd_2SiO_5$ with CMAS for EBCs

## 3.1. Introduction

Research and development were conducted to investigate the effect of actual volcanic ash on EBCs in a high-temperature combustion environment. The accumulation of volcanic ash that reacts chemically to components can cause corrosion of the EBCs, degrading performance and reducing high-temperature capabilities [1–4]. Recently, high-temperature interactions between volcanic ash and artificial calcium-magnesium-aluminosilicate (CMAS) with similar composition have been studied [5–11]. In addition, corrosion resistance to the dissolved salt deteriorates, resulting in EBC and engine-component failure. Therefore, rare earth (RE)–doped silicates, which have very good oxidation resistance and can withstand high temperatures, are attracting attention for this kind of application [12–16].

Rare earth silicates have been applied to EBCs to protect silicon-based ceramics from corrosion [17–19]. They have the advantage of being able to withstand a low thermal expansion coefficient and a temperature of 1400°C for thousands of hours. However, if CMAS stacks up on the surface of a hot part, it can damage the part and shorten its life. For applicable materials, the coating dissolves quickly in molten CMAS while promoting re-precipitation and reactive crystallization. Therefore, it is necessary to apply an EBC of RE silicate for excellent corrosion resistance and thermal and chemical stability [20–23].

Kim et al.[24] conducted a study on the corrosion resistance of volcanic ash to  $Gd_2SiO_5$  at high temperatures. Volcanic ash was melted at a high temperature and reacted with  $Gd_2SiO_5$  to form RE-apatite phase. The main material used for EBCs is Yb. According to Schulz et al. [27], a material with small RE cations (Y, Yb) were found to have excellent resistance to CMAS, as a component similar to volcanic ash. Conversely, it has been proposed that large RE cations

(La) react violently with CMAS dissolution, rapidly forming a crystalline RE apatite step to prevent further CMAS penetration. Therefore, it is possible to study the optimum resistance to the corrosion of RE materials by studying the high-temperature corrosion behavior of  $Gd_2SiO_5$ . According to Krämer et al. [12], CMAS melted at a high temperature reacts with  $Gd_2Zr_2O_7$  to form  $Gd_8Ca_2(SiO_4)_6O_2$  (apatite), with a sealing effect. In order to minimize damage to CMAS penetration,  $Gd_8Ca_2(SiO_4)_6O_2$  (apatite) is formed in a short time through dissolution and recrystallization [12]. Resistance to CMAS plays an important role in the evaluation of a RE material for EBCs due to the effect of the increase in temperature and time on the change in penetration rate and reaction thickness. The purpose of this study is focuses on the high-temperature corrosion behavior of  $Gd_2SiO_5$  and artificial CMAS, and the comparison of the reaction layer formation according to the CaO:SiO<sub>2</sub> ratios (volcanic ash in chapter 2: 0.11, CMAS: 0.73).

## 3. 2. Experimental Procedure

### 3.2.1. Sample Preparation and Heat Treatment

CaO (Japan Wako Pure Chemical Industry), MgO (Japan Wako Pure Chemical Industry), Al<sub>2</sub>O<sub>3</sub> (Japan Kanto Chemical), and SiO<sub>2</sub> (Japan Kanto Chemical) were synthesized to manufacture CMAS. The composition content of the synthesized CMAS is 33CaO-9MgO-13AlO<sub>1.5</sub>-45SiO<sub>2</sub> mol%. Ball milling was performed for 24 h using ZrO<sub>2</sub> balls and ethanol. After the ball-milling process, the suspension was dried at room temperature. The dry powder was treated with two stages of heat treatment, using the Al<sub>2</sub>O<sub>3</sub> crucible. CMAS was first synthesized at 80°C for 10 h, heat treated at 1200°C for 24 h, and then finely and uniformly pulverized.

Gd<sub>2</sub>SiO<sub>5</sub> powder was synthesized by reaction with Gd<sub>2</sub>O<sub>3</sub> (Rare Metallurgical Corporation, Japan) and SiO<sub>2</sub> (Wako Pure Chemical Industries, Japan) powders. The mass fractions of the two powders were prepared in a molar ratio of 1:1. Ball milling, using ZrO<sub>2</sub> balls and ethanol, was performed for 24 h. After ball milling, the suspension was dried at 60°C for 24 h, and the Gd<sub>2</sub>O<sub>3</sub>-SiO<sub>2</sub> mixed powder was put in an Al<sub>2</sub>O<sub>3</sub> crucible and heated to 1400°C to synthesize for 20 h. A graphite mold 30 mm in diameter was placed in a spark plasma sintering (SPS) system (Dr. Sinter 1050, SCM, Japan), and the temperature was raised to 1400°C in a vacuum of 10<sup>-2</sup> Pa at a temperature rate of 10°/min and under 60 MPa of pressure. A Gd<sub>2</sub>SiO<sub>5</sub> sintered body 10 X 5 mm in size and 3 mm thick was cut using a diamond saw. After cutting, it was washed for 5 min in acetone and ethanol using an ultrasonic cleaner. Thereafter, polishing was performed using 9, 3, and 1 μm diamond suspensions.

The process for preparing a hot corrosion specimen is as follows. CMAS was sprayed onto the polished Gd<sub>2</sub>SiO<sub>5</sub> sintered surface using CMAS pastes with a concentration of 40 mg/cm<sup>2</sup> [28–29]. The Gd<sub>2</sub>SiO<sub>5</sub> sintered body sprayed with CMAS was exposed to 1400°C for 2, 12, and 48 h at a rate of 5°C/min. The heat-treated Gd<sub>2</sub>SiO<sub>5</sub> specimen was cut to 5 X 5 mm

using a diamond saw for cross-sectional analysis. Then, the cross section was polished using 9, 3, and 1  $\mu\text{m}$  diamond suspensions. After polishing, it was washed for 5 min with acetone and ethanol using an ultrasonic cleaner.

### 3.2.2. Characterization

The corrosion status of each specimens were analyzed using a scanning electron microscope (SEM S-4300, Hitachi, Ltd., Japan). Energy-dispersive X-ray spectroscopy (EDS) was used to determine the infiltrated component, distribution, and content ratio at 15 kV and at a working distance of 15 mm. Differential scanning calorimetry (DSC6300, Hitachi, Japan) measurements were performed to estimate the reaction temperature of the ash and  $\text{Gd}_2\text{SiO}_5$  under the atmosphere. At room temperature, a homogeneous sample (CMAS:  $\text{Gd}_2\text{SiO}_5 = 1:1$  weight %) for DSC measurement was prepared and stirred in EtOH under argon (Ar) gas flow conditions. To confirm the phase relationship of the CMAS– $\text{Gd}_2\text{SiO}_5$  mixed powder up to 1300°C under air, HT-XRD measurements were carried out using a Rigaku SmartLab 9 kW (Cu  $\text{K}\alpha_1$  radiation:  $\lambda = 1.54056\text{\AA}$ ). The heating rate to the target temperature was 10°C/min. Intensity measurement conditions are in the  $2\theta$  range of 20–65°, with a scan speed of 1°/min, and a scan step of 0.02°/min.

### 3.3. Results and Discussion

#### 3.3.1. Characterization of CMAS

Fig. 21 compares the differential scanning calorimetry (DSC) results of CMAS powder and CMAS–Gd<sub>2</sub>SiO<sub>5</sub> mixed powder. According to Mohamed et al. [21], reported that the endothermic peak of the solid-solid transition ( $T_{\text{trans}}$ ) occurred before the glass transition ( $T_g$ ) caused an endothermic peak during typical DSC curve. Morelli et al. [6], also confirmed that a solid-solid transition ( $T_{\text{trans}}$ ) appeared before the glass transition ( $T_g$ ) in the DSC analysis of CMAS. In the current study, the endothermic peak appearing around 250°C is considered to be a solid-solid transition ( $T_{\text{trans}}$ ).

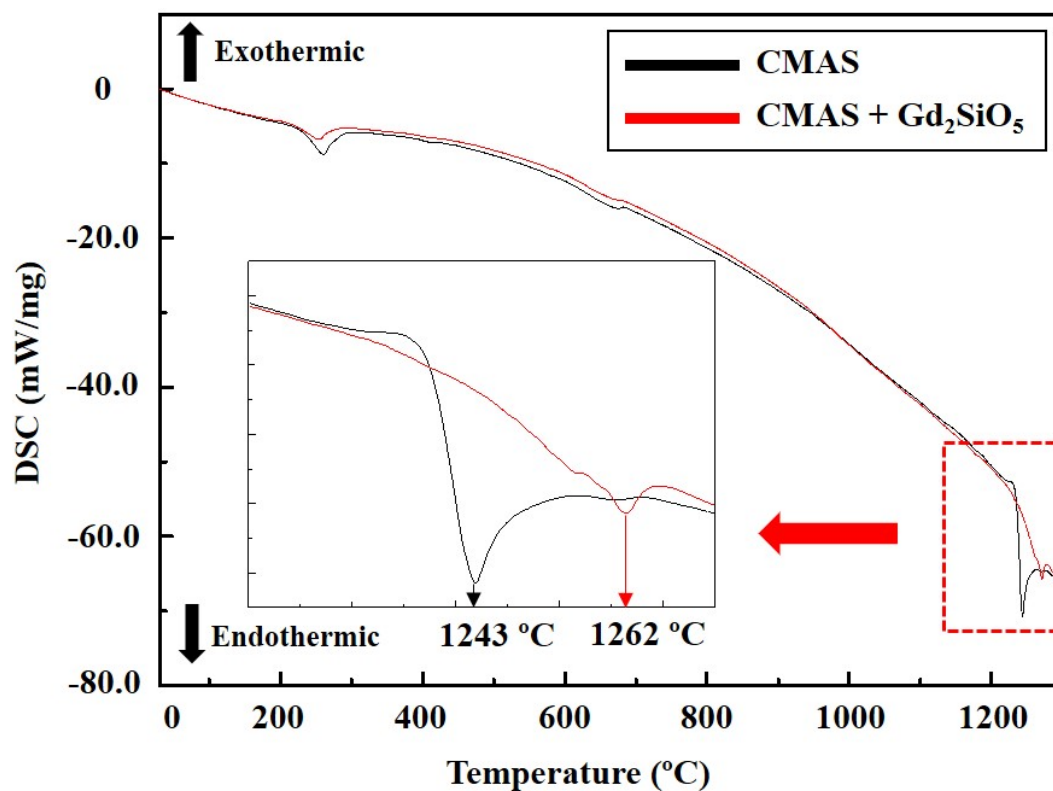


Fig. 21. Comparison of DSC results of CMAS powder and CMAS + Gd<sub>2</sub>SiO<sub>5</sub> powder.

Also, according to Zaleski et al. [22], melting and recrystallization behavior was confirmed according to the composition of CMAS. The glass transition ( $T_g$ ) of CMAS

consisting of a total of 10 components was analyzed from 709°C to 807°C. The results of the current study show a small change, consistent with a glass transition ( $T_g$ ) of about 700°C, according to the DSC curve. As reported previously [24], the endothermic and exothermic temperatures were analyzed to set the target heat treatment temperature and phase change. A sharp endothermic peak for CMAS was observed at 1243°C. This can be seen as the melting point of CMAS powder. In order to compare the melting point of CMAS and the CMAS–Gd<sub>2</sub>SiO<sub>5</sub> mixed powder, CMAS and Gd<sub>2</sub>SiO<sub>5</sub> at a ratio of 1:1 were stirred to prepare the powder. The CMAS–Gd<sub>2</sub>SiO<sub>5</sub> mixed powder had an abrupt endothermic peak at 1262°C. This suggests that the peak is the reaction temperature of the CMAS–Gd<sub>2</sub>SiO<sub>5</sub> mixed powder. DSC analysis confirmed that CMAS powder and CMAS–Gd<sub>2</sub>SiO<sub>5</sub> melted at about 1300°C.

### 3.3.2. High-Temperature Corrosion of Sintered Gd<sub>2</sub>SiO<sub>5</sub> with CMAS

Fig. 22 is a microstructure SEM photograph of a cross section of sintered Gd<sub>2</sub>SiO<sub>5</sub> after CMAS corrosion at 1400°C for 2, 12, and 48 h. In (a) 2 h, (b) 12 h, and (c) 48 h, it was confirmed that CMAS partially melted to form a reaction area with sintered Gd<sub>2</sub>SiO<sub>5</sub>.

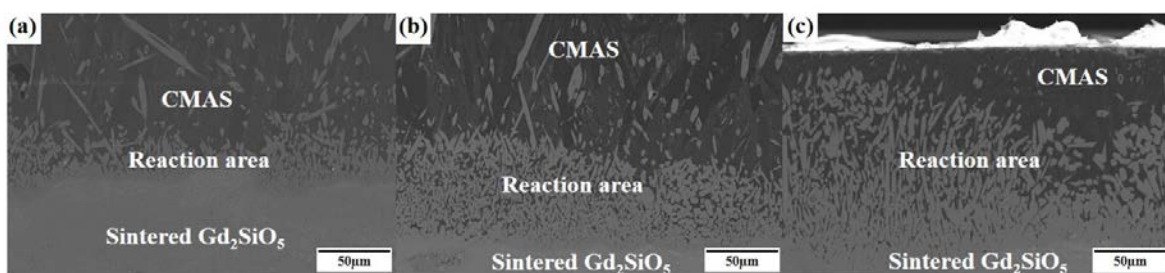


Fig. 22. SEM images of cross section after CMAS corrosion at 1400°C: (a) CMAS-2 h, (b) CMAS-12 h, and (c) CMAS-48 h.

In addition, it was confirmed that the CMAS and Gd<sub>2</sub>SiO<sub>5</sub> reaction regions were deepest at 48 h. The depth of the reaction area formed in this way increases as the heat treatment time

increases. As the CMAS melts, it reacts with  $Gd_2SiO_5$ , and a new phase is observed, showing a needle-like morphology. As time increases, the needle morphology shows that the CMAS– $Gd_2SiO_5$  reaction area is composed of a reactive layer that grows vertically thinner toward the CMAS melt.

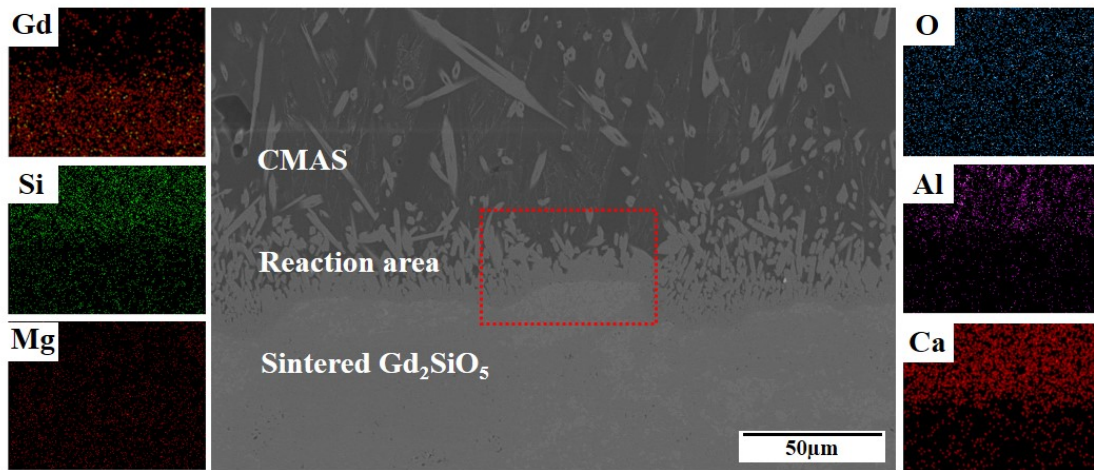


Fig. 23. EDS element mapping of cross-sectional results of sintered  $Gd_2SiO_5$  at  $1400^{\circ}C$  for 2 h with CMAS.

Fig. 23 is a microstructure SEM photograph of the cross section of sintered  $Gd_2SiO_5$  heat treated for 2 h with CMAS. In addition, component analysis results were obtained using EDS mapping. Sintered  $Gd_2SiO_5$  main components Gd, Si, and O and CMAS components Ca, Mg, Al, and Si were detected. Ca and Si, which are components of CMAS, were seen to accumulate on the surface of the sintered  $Gd_2SiO_5$ , partially melt, and react with the sintered  $Gd_2SiO_5$  to form a reaction area. It was found to grow vertically due to recrystallization at the interface of the CMAS melt. According to Jiang et al. [20], a corrosion mechanism based on reaction crystallization was reported that demonstrates the details of the  $RE_2SiO_5$  corrosion process due to CMAS. Some  $RE_2SiO_5$  particles interact with  $SiO_2$  in CMAS to form  $RE_2Si_2O_7$ . In addition, Ca RE silicates reportedly have been produced by interacting with Ca. As an additional point,

the reaction area and the sintered  $\text{Gd}_2\text{SiO}_5$  in the red area have different morphology. According to Wolf et al. [4], these phenomena are considered areas with a suitable mixture, and incomplete degradation can be the cause of this agglomeration. It was observed that the agglomeration area also extends to the pellet interface. Wolf et al. [4], reported that the average thickness of the reaction area of Yb monosilicate and Yb disilicate was thinner than that of the pure Yb monosilicate sample.

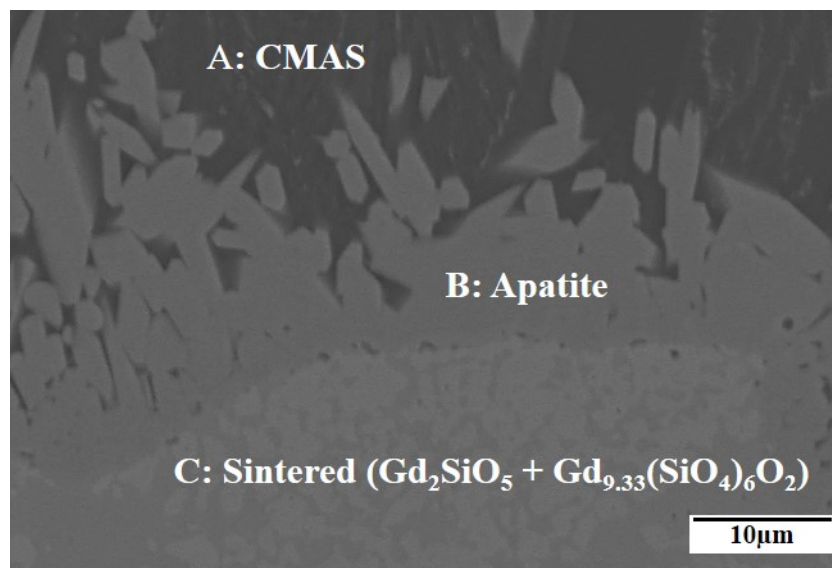


Fig. 24. High magnification of SEM images of the red area in Fig. 23.

Fig. 24 is a SEM photograph showing the red area of Fig. 23 at high magnification after the sintered  $\text{Gd}_2\text{SiO}_5$  coated with CMAS was heat treated at  $1400^\circ\text{C}$  for 2 h. In order to confirm the phase distribution through component analysis of the reaction region, EDS point analysis were performed on parts A, B, and C. Table 5 shows the results of EDS point analysis of chemical composition in the cross section of sintered  $\text{Gd}_2\text{SiO}_5$  with CMAS at parts A, B, and C of Fig. 24. O, Mg, Al, Si, Ca, and Gd were detected at part A (CMAS). Component analysis confirms the presence of CMAS. Sleeper. [31], reported on the thermochemistry of CMAS and  $\text{Ca}_2\text{Y}_8(\text{SiO}_4)_6\text{O}_2$  (apatite).

Table 5. EDS point analysis of the chemical composition of the cross section with CMAS at parts A, B, and C of Fig. 24.

	(at%)					
Element	O	Mg	Al	Si	Ca	Gd
A: CMAS	51.3 (±0.60)	3.1 (±0.28)	4.63 (±0.65)	25.64 (±1.23)	11.85 (±1.58)	3.48 (±0.89)
B: Apatite	48.01 (±0.41)	0	0	19.76 (±0.47)	5.47 (±0.98)	26.76 (±1.98)
C: Sintered (Gd <sub>2</sub> SiO <sub>5</sub> + Gd <sub>9.33</sub> (SiO <sub>4</sub> ) <sub>6</sub> O <sub>2</sub> )	46.52 (±4.77)	0	0	20.02 (±1.45)	0	33.46 (±4.76)

Apatite–CMAS reaction confirms that a small amount of RE (Y) is contained in the amorphous region. At part B (Apatite), Gd, O, Si, and Ca components were detected; Mg and Al components were not detected. This means that CMAS melts at a high temperature and penetrates into sintered Gd<sub>2</sub>SiO<sub>5</sub> to form a reaction area. Analyzing the content of the reaction layer, it can be seen that Gd<sub>2</sub>SiO<sub>5</sub> and Ca components of CMAS reacted to form Ca<sub>2</sub>Gd<sub>8</sub>(SiO<sub>4</sub>)<sub>6</sub>O<sub>2</sub> (apatite). Jang et al. [18] evaluated the corrosion properties of Yb<sub>2</sub>SiO<sub>5</sub> and CMAS at high temperatures. Similar results showed that CMAS reacted more easily and violently with Yb<sub>2</sub>SiO<sub>5</sub> due to the high concentration of caustic element Ca, resulting in the rapid growth of the Ca<sub>2</sub>Yb<sub>8</sub>(SiO<sub>4</sub>)<sub>6</sub>O<sub>2</sub> (apatite) reactant. Part C is considered a mixed area of Gd<sub>2</sub>SiO<sub>5</sub> and Gd<sub>9.33</sub>(SiO<sub>4</sub>)<sub>6</sub>O<sub>2</sub>. The needle-shaped Gd<sub>8</sub>Ca<sub>2</sub>(SiO<sub>4</sub>)<sub>6</sub>O<sub>2</sub> (apatite) thickness located on the mixed of Gd<sub>9.33</sub>(SiO<sub>4</sub>)<sub>6</sub>O<sub>2</sub> and Gd<sub>2</sub>SiO<sub>5</sub> area was thinner than that of the pure Gd<sub>2</sub>SiO<sub>5</sub> area. According to Wolf et al. [4], a mixture of Yb monosilicate and disilicate were studied for resistance to CMAS. Their results showed that the thickness of the needle-shaped apatite was thin, but the fringe was thicker where the silicate mixture was uniformly mixed. In addition,

the average thickness of the reaction area appeared to be thinner than the reaction layer over the pure monosilicate sample.

Fig. 25 shows an EDS element mapping of the cross-sectional results of  $Gd_2SiO_5$  heat treated at  $1400^\circ C$  for 12 h with CMAS. Sintered  $Gd_2SiO_5$  main components Gd, Si, and O and CMAS components Ca, Mg, Al, and Si were detected using EDS mapping to obtain a component analysis result. As shown in Fig. 23 (sample heat treated for 2 h), CMAS components Ca and Si partially melted on the sintered  $Gd_2SiO_5$  surface to create a reaction area. Recrystallization at the interface of the CMAS melt enabled grains of  $Ca_2Gd_8(SiO_4)_6O_2$  (apatite) to grow vertically. After 12 h, CMAS was melted on the surface of the sintered  $Gd_2SiO_5$  and penetrated into the sintered  $Gd_2SiO_5$  to create a reaction area. The depth of the reaction area increased with increasing exposure time. In addition, the result of the analysis of the Al component in EDS mapping (Fig. 25) confirmed crystallization in the residual CMAS.

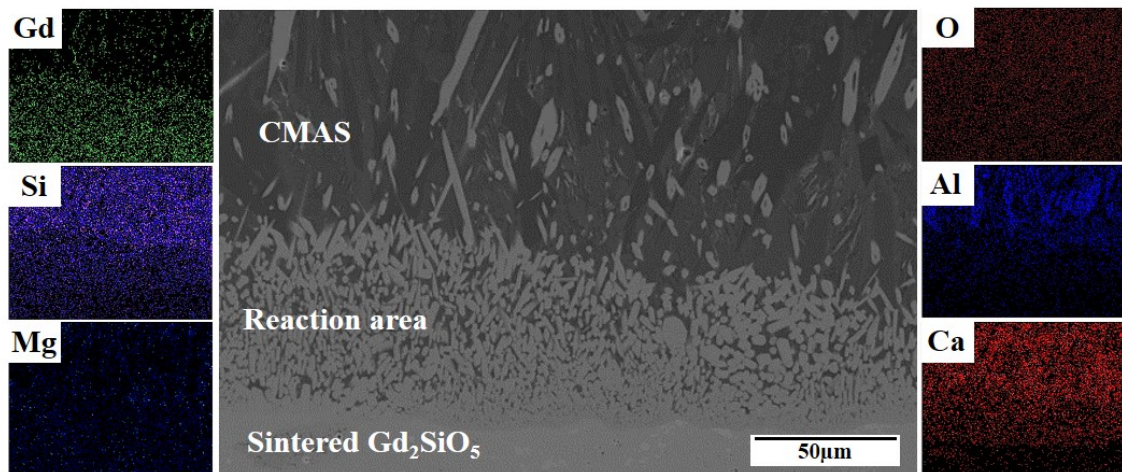


Fig. 25. EDS element mapping of cross-sectional results of sintered  $Gd_2SiO_5$  at  $1400^\circ C$  for 12 h with CMAS.

In addition, the anorthite ( $CaAl_2Si_2O_8$ ) phase was analyzed as shown in the result HT-XRD analysis at  $25^\circ C$ . As a result, the needle-shaped  $CaAl_2Si_2O_8$  phase was analyzed in the

remaining CMAS area. In addition, it was reported that the  $\text{CaAl}_2\text{Si}_2\text{O}_8$  region maintained almost the same atomic ratio of the CMAS mixture ( $\text{Ca}:\text{Mg}:\text{Al}:\text{Si} = 33:9:13:45$  in mol.%).

Fig. 26 (a) shows an EDS linear scan of cross sections of  $\text{Gd}_2\text{SiO}_5$  heat treated at  $1400^\circ\text{C}$  for 12 h with CMAS, a cross-sectional SEM image divided into three parts, a reaction area, and sintered  $\text{Gd}_2\text{SiO}_5$ . Fig. 26 (b) is a graph showing the components of the line analysis using EDS. Line analysis can be used to identify the distribution of each element—Gd, Si, and Ca—from the CMAS to the sintered  $\text{Gd}_2\text{SiO}_5$ . CMAS components Ca and Si are clearly observed in the reaction area. The Gd element increased as the line moved from the CMAS area to the sintered  $\text{Gd}_2\text{SiO}_5$ .

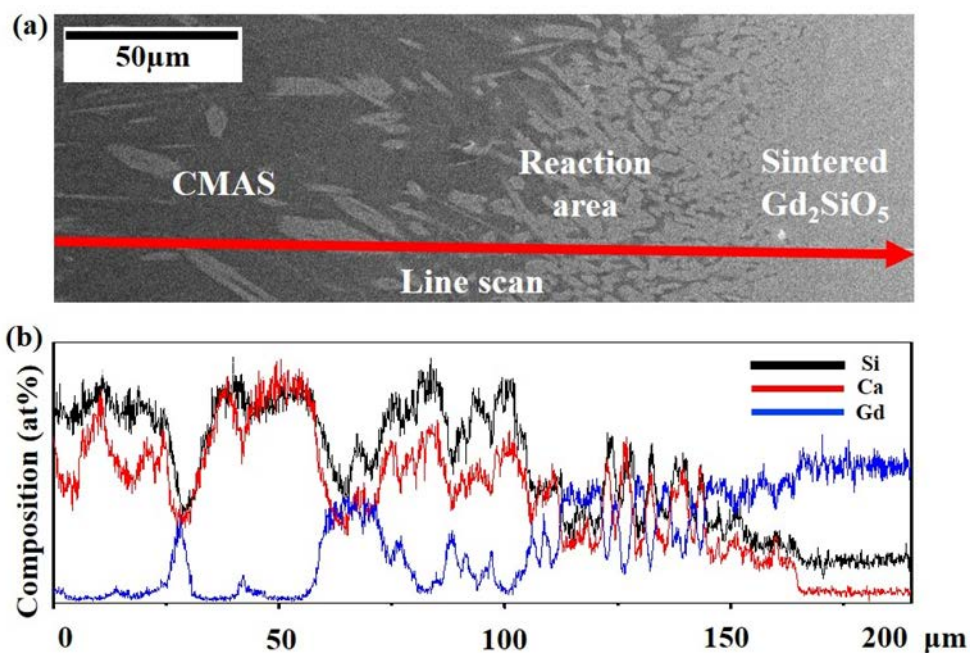


Fig. 26. EDS linear scan of cross sections of sintered  $\text{Gd}_2\text{SiO}_5$  after CMAS corrosion at  $1400^\circ\text{C}$  for 12 h. (a) SEM image of the result by CMAS of heat-treated  $\text{Gd}_2\text{SiO}_5$  and (b) result of the compositional red line analysis in (a).

Fig. 27 shows the results obtained by using a HT-XRD to analyze the phase change occurring at high temperatures in the reaction of  $\text{Gd}_2\text{SiO}_5$  and CMAS. As described above by

DSC analysis in Fig. 21, the temperature at which  $\text{Gd}_2\text{SiO}_5$  and CMAS react is  $1262^\circ\text{C}$ . Therefore, the phase relationships were identified using HT-XRD intensity measurements at  $25^\circ\text{C}$ ,  $1100^\circ\text{C}$ ,  $1200^\circ\text{C}$ ,  $1300^\circ\text{C}$ , and  $1400^\circ\text{C}$ . In addition, after a reaction occurs at a high temperature, phase change may occur in response to the viscosity of the melt of  $\text{Gd}_2\text{SiO}_5$  and CMAS during the cooling step, so the room temperature ( $25^\circ\text{C}$ ) state after cooling was also analyzed. By comparing these data, the reaction process of sintered  $\text{Gd}_2\text{SiO}_5$  and CMAS was confirmed. Based on the HT-XRD results, the phase change of  $\text{Gd}_2\text{SiO}_5$  powder was analyzed at  $25^\circ\text{C}$  and  $1300^\circ\text{C}$  in Fig. 27 (a), (b). It was confirmed that there was no phase change even at a high temperature of  $1300^\circ\text{C}$  above the melting point of CMAS. Fig. 27 (c) shows the peaks of  $\text{CaSiO}_3$ ,  $\text{Ca}_2\text{MgSi}_2\text{O}_7$ , and  $\text{CaAl}_2\text{Si}_2\text{O}_8$ , which are components of CMAS;  $\text{Gd}_2\text{SiO}_5$ , and  $\text{Gd}_{9.33}(\text{SiO}_4)_6\text{O}_2$  at  $25^\circ\text{C}$ . According to Jang et al. [22],  $\text{Ca}_2\text{MgSi}_2\text{O}_7$ ,  $\text{CaAl}_2\text{Si}_2\text{O}_8$ , and  $\text{CaSiO}_3$ , which are observed at  $25^\circ\text{C}$ , are representative phases of CMAS.

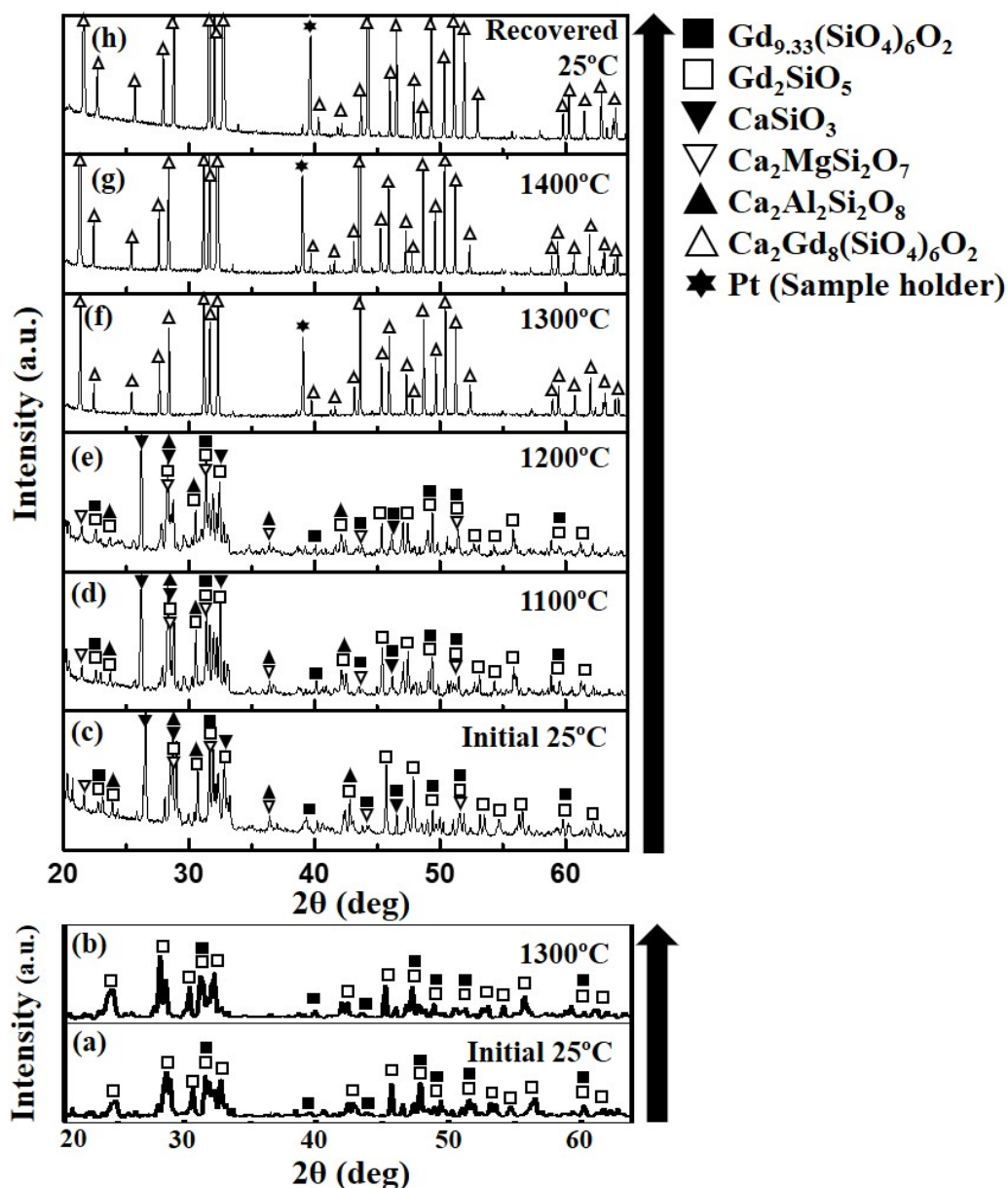
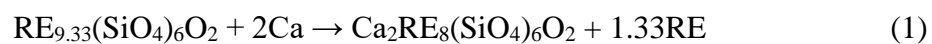


Fig. 27. HT-XRD patterns of  $Gd_2SiO_5$  powder (a) 25°C, (b) 1300°C and CMAS –  $Gd_2SiO_5$  mixed powder (1 : 1 wt.%). From heating step at (c) 25°C, (d) 1100°C, (e) 1200°C, (f) 1300°C, and (g) 1400°C and from cooling step at (h) 25°C.

The reaction between  $RE_2SiO_5$  and CMAS is dominant during the corrosion process due to violent corrosion by CMAS at short residence times. In Fig. 27 (d) 1100°C and 27 (e) 1200°C, the crystal phases are the same as at 25°C and are  $Gd_2SiO_5$ ,  $Gd_{9.33}(SiO_4)_6O_2$ ,  $CaSiO_3$ ,  $CaAl_2Si_2O_8$ , and  $Ca_2MgSi_2O_7$ . In Fig. 27 (f) 1300°C and (g) 1400°C, the  $Gd_2SiO_5$ ,  $CaSiO_3$ ,

CaAl<sub>2</sub>Si<sub>2</sub>O<sub>8</sub>, and Ca<sub>2</sub>MgSi<sub>2</sub>O<sub>7</sub> peaks have disappeared. A sharp Pt peak was also analyzed in a sample holder. These results indicate that incident X-rays penetrated the liquid and reached the Pt holder. After cooling, Fig. 27 (h) shows that the 25°C phase change did not occur. Fig. 21 shows that the melting point of the peak was confirmed by DSC. Gd<sub>2</sub>SiO<sub>5</sub> and CMAS melted and reacted because the reaction temperature was above 1262°C. The reaction produced Ca<sub>2</sub>Gd<sub>8</sub>(SiO<sub>4</sub>)<sub>6</sub>O<sub>2</sub>. Krämer et al. [25], suggested that RE (La and Gd) zirconate reacts with CMAS to actively dissolve and rapidly form a calcium-rich phase to prevent further CMAS infiltration. Krämer et al. [25], obtained similar results as were previously mentioned, confirming that CMAS and Gd<sub>2</sub>SiO<sub>5</sub> react at a high temperature to produce Ca<sub>2</sub>Gd<sub>8</sub>(SiO<sub>4</sub>)<sub>6</sub>O<sub>2</sub> (apatite). Drexler et al. [26], reported that Gd<sub>2</sub>Zr<sub>2</sub>O<sub>7</sub> reacts with molten CMAS, resulting in the formation of a crystalline Ca<sub>2</sub>Gd<sub>8</sub>(SiO<sub>4</sub>)<sub>6</sub>O<sub>2</sub> (apatite) phase at the interface that prevents further infiltration of molten CMAS in the coating.

Fig. 28 shows a ternary phase diagram of CaO-SiO<sub>2</sub>-GdO<sub>1.5</sub> at 1400°C [3,28]. Since Al<sub>2</sub>O<sub>3</sub> and MgO exist among CMAS components, the liquid area of CMAS needs to be enlarged so that the corresponding liquid area is widened. It can be seen from the phase diagram that (a) CMAS dissolves and re-precipitates (b) Gd<sub>2</sub>SiO<sub>5</sub> and (c) Gd<sub>9.33</sub>(SiO<sub>4</sub>)<sub>6</sub>O<sub>2</sub> and forms (d) Gd<sub>8</sub>Ca<sub>2</sub>(SiO<sub>4</sub>)<sub>6</sub>O<sub>2</sub> (apatite). As shown in Fig. 21, when the temperature rises, CMAS reacts with Gd<sub>2</sub>SiO<sub>5</sub> and infiltrates at 1262°C. Zhang et al. [28], presented similar results. Another possibility for the formation of the RE<sub>8</sub>Ca<sub>2</sub>(SiO<sub>4</sub>)<sub>6</sub>O<sub>2</sub> layer is the direct diffusion of RE and Si from RE<sub>9.33</sub>(SiO<sub>4</sub>)<sub>6</sub>O<sub>2</sub> (RE-apatite) grains to the CMAS glass and the counter diffusion of Ca from the CMAS melt to RE-apatite. The reverse diffusion and related reactions of the equation are represented by Eq. (1) [28].





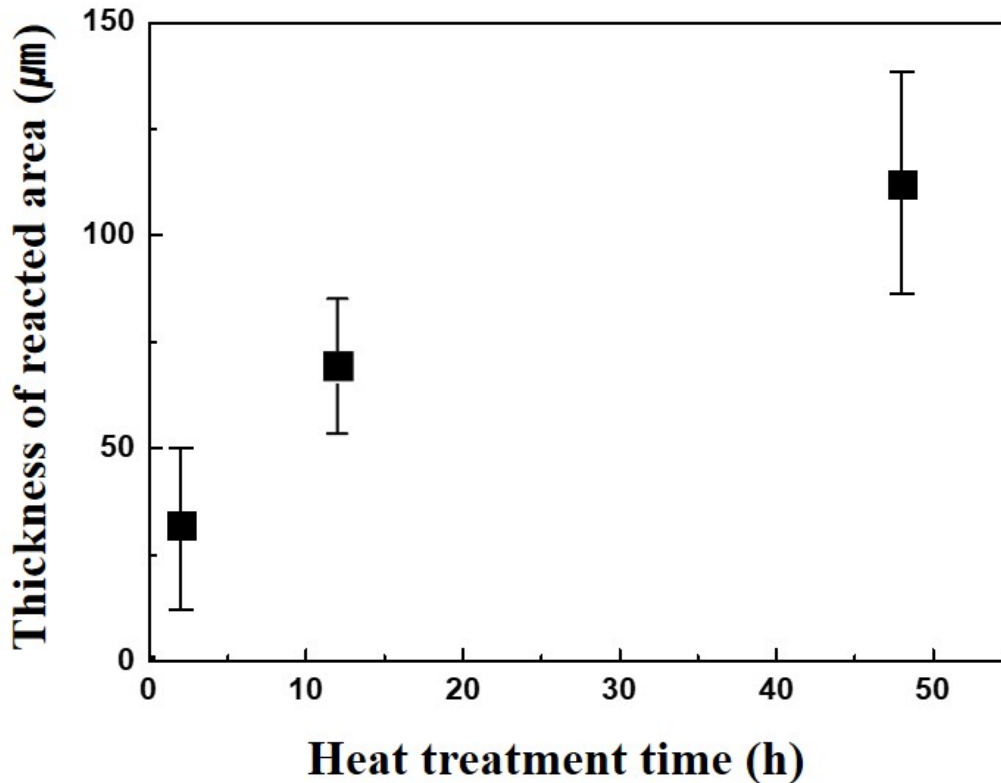


Fig. 29. Thickness of the reacted area for sintered  $\text{Gd}_2\text{SiO}_5$  ( $\text{Gd}_{9.33}(\text{SiO}_4)_6\text{O}_2$ ) as a function of heat treatment times at  $1400^\circ\text{C}$ .

Thus, with increasing corrosion time, it appears that molten CMAS reacts with the sintered  $\text{Gd}_2\text{SiO}_5$  ( $\text{Gd}_{9.33}(\text{SiO}_4)_6\text{O}_2$ ) to produce  $\text{Ca}_2\text{Gd}_8(\text{SiO}_4)_6\text{O}_2$ . According to Kim et al. [24], high-temperature corrosiveness between  $\text{Gd}_2\text{SiO}_5$  and volcanic ash at  $1400^\circ\text{C}$  were evaluated over time (2, 12, and 48 h). In the case of volcanic ash, the reaction areas have been reported as 5, 18, and  $45 \mu\text{m}$ . As compared to CMAS at 48 h, about 3 times as much apatite was formed. The main corrosion factor is Ca, and it is thought that the Ca content of CMAS is higher than that of volcanic ash, and more of the  $\text{Ca}_2\text{Gd}_8(\text{SiO}_4)_6\text{O}_2$  (apatite) phase is formed by reacting with  $\text{Gd}_2\text{SiO}_5$ . Wolf et al. [4] reported resistance to CMAS for  $\text{Yb}_2\text{SiO}_5$  and  $\text{Y}_2\text{SiO}_5$  at the same temperature ( $1400^\circ\text{C}$ ). Different amounts of CMAS are applied. However, after the high-temperature test,  $\text{Yb}_2\text{SiO}_5$  was  $43 \mu\text{m}$ , and  $\text{Y}_2\text{SiO}_5$  was  $88 \mu\text{m}$ . This represents a lower retreat

of  $\text{Yb}_2\text{SiO}_5$  against CMAS attacks as compared to that of  $\text{Yb}_2\text{SiO}_5$ . Turcer et al. [5] evaluated the reaction-recrystallization of apatite to molten CMAS,  $\beta\text{-Yb}_2\text{Si}_2\text{O}_7$ , and  $\beta\text{-Sc}_2\text{Si}_2\text{O}_7$  and that it was minimized in  $\beta\text{-Yb}_2\text{Si}_2\text{O}_7$  and not analyzed in  $\beta\text{-Sc}_2\text{Si}_2\text{O}_7$ . This is consistent with the report that  $\text{Yb}^{3+}$  (0.985 Å), which has a larger ionic radius than  $\text{Sc}^{3+}$  (0.870 Å), provides a more reactive driving force for Ca. As compared with  $\text{Gd}^{3+}$  (1.05 Å), the theory that the thickness of the reaction layer (apatite) becomes thicker as the size of ions increases is supported. In CMAS combined with a larger  $\text{RE}^{3+}$  cation size, an increased reaction to higher CaO:SiO<sub>2</sub> ratios resulted in a change in apatite formation. Gd formed apatite at a low CaO:SiO<sub>2</sub> ratio. In other words, the ability of  $\text{Gd}^{3+}$  cations to stabilize apatite melts to a lower CaO concentration than that of  $\text{Dy}^{3+}$  or  $\text{Nd}^{3+}$ , indicating that there is an optimal cation size range for larger RE cations where apatite formation is preferred.

Fig. 30 shows a schematic diagram of the corrosion mechanism for reaction crystallization between sintered  $\text{Gd}_2\text{SiO}_5$  ( $\text{Gd}_{9.33}(\text{SiO}_4)_6\text{O}_2$ ) and CMAS (Fig. 30 (a)). At a corrosion temperature of 1300°C higher than the melting temperature of CMAS, CMAS melts and penetrates into the sintered  $\text{Gd}_2\text{SiO}_5$  ( $\text{Gd}_{9.33}(\text{SiO}_4)_6\text{O}_2$ ), creating a reaction area (Fig. 30 (b)). This change induces a reaction area at the interface, and the reaction product crystallizes from the melted CMAS at a high temperature. As time increases, the molten CMAS penetrates into the sintered  $\text{Gd}_2\text{SiO}_5$  ( $\text{Gd}_{9.33}(\text{SiO}_4)_6\text{O}_2$ ), and the reaction area deepens (Fig. 30 (c)). When sintered  $\text{Gd}_2\text{SiO}_5$  ( $\text{Gd}_{9.33}(\text{SiO}_4)_6\text{O}_2$ ) and CMAS react,  $\text{Ca}_2\text{Gd}_8(\text{SiO}_4)_6\text{O}_2$  is produced, and growth occurs in the vertical direction in a needle morphology (Fig. 30 (d)). This is the result as shown in Fig. 24 (part C), where the thickness of the reaction area above the mixed area of  $\text{Gd}_{9.33}(\text{SiO}_4)_6\text{O}_2$  and  $\text{Gd}_2\text{SiO}_5$  is thinner than that of the reaction area above the pure  $\text{Gd}_2\text{SiO}_5$  area.

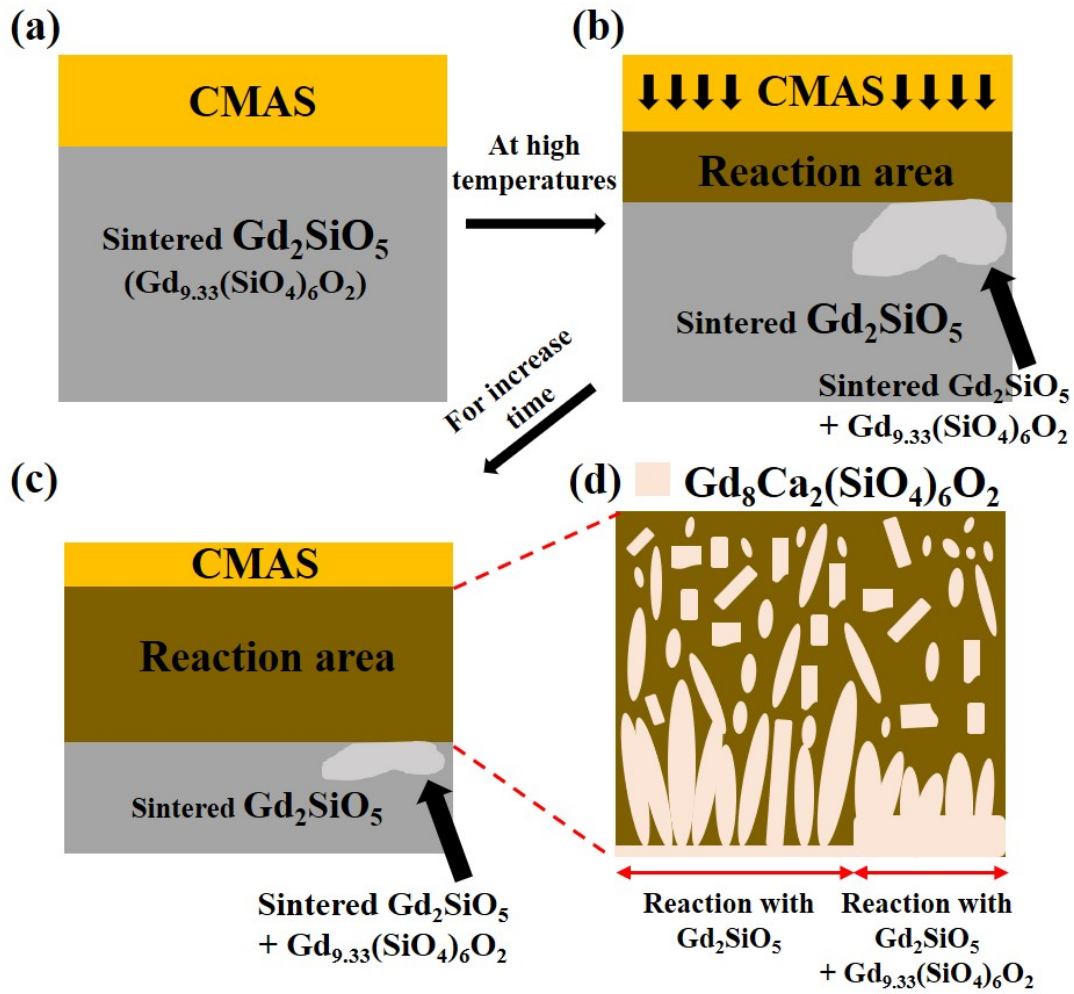


Fig. 30. A schematic illustration of the mechanism of CMAS corrosion on sintered  $\text{Gd}_2\text{SiO}_5$  ( $\text{Gd}_{9.33}(\text{SiO}_4)_6\text{O}_2$ ) at  $1400^\circ\text{C}$ : (a) the initial condition, (b) formation of the reaction area between CMAS and sintered  $\text{Gd}_2\text{SiO}_5$  ( $\text{Gd}_{9.33}(\text{SiO}_4)_6\text{O}_2$ ), (c) formation of the reaction area and sintered  $\text{Gd}_2\text{SiO}_5$  ( $\text{Gd}_{9.33}(\text{SiO}_4)_6\text{O}_2$ ), (d) morphology of the reaction area.

The corrosion mechanism with the infiltration time and viscosity of melted CMAS can be explained as follows. The viscosity ( $\eta$ ) of the CMAS composition used in the current study has been previously reported [29–33]. The viscosity value of CMAS glass was previously calculated by Giordano et al. [32] and Fluegel. [33] To evaluate the accuracy of the predicted values in the two models, Wiesner [29] used temperatures of  $1215^\circ\text{C}$  to  $1519^\circ\text{C}$ . The calculated

viscosity value was closer to that of Fluegel [33] than of Giordano et al.[32] Since the composition of CMAS was slightly different from that in the current study, it was calculated using the viscosity of Wiesner et al. [29], who estimated that the viscosity value for Eq. (2) as the viscosity result for CMAS is based on a global statistical approach. Although it is not possible to calculate the exact infiltration value, the approximate infiltration time can be calculated through Equations 2 and 3.

$$\log\eta(\text{Pa.s}) = -3.25 + 4418/(T-375) \quad (2)$$

By considering the capillary reaction and ignoring CMAS crystallization and/or other thermochemical interactions with the sintered body, the time (t) required for the melted CMAS to penetrate the sintered  $\text{Gd}_2\text{SiO}_5$  with a thickness (L) of 3 mm is determined using Eq. (3) [31,34,35].

$$t \sim \left[ \frac{K_t}{8D_c} \left( \frac{1-\omega}{\omega} \right)^2 L^2 \right] \frac{\eta}{\sigma_{LV}} \quad (3)$$

Table 6. Parameters used to calculate CMAS infiltration times from Eq. (3)

Parameter	Value
Substrate thickness (L)	3mm
Tortuosity ( $k_t$ )	3
Capillary diameter ( $D_c$ )	1 $\mu\text{m}$
Pore fraction ( $\omega$ )	0.1
Surface tension ( $\sigma_{LV}$ )	0.4 J/m <sup>2</sup>

The CMAS infiltration time could then be calculated using Eq. (3) in Table 6: the tortuosity ( $K_t$ ) value was  $\sim 3$  [31], and the capillary diameter ( $D_c$ ) was 1  $\mu\text{m}$ .  $\omega \sim 0.1$  was the pore fraction

open to flow, and the surface tension ( $\sigma_{LV}$ ) was estimated as  $\sim 0.4 \text{ J/m}^2$  [31,36], which was calculated using an approach for silicate glass melts at  $1400^\circ\text{C}$ , as shown in Table 7 [31,36], and was comparable to a  $\sigma_{LV}$  value for a different CMAS composition [31].

Table 7. Viscosity of CMAS from Eq. (2) and calculated times for CMAS melt to infiltrate sintered  $\text{Gd}_2\text{SiO}_5$  using Eq. (3) at  $1215^\circ\text{C}$ – $1519^\circ\text{C}$ .

Temperature ( $^\circ\text{C}$ )	Viscosity, $\eta$ (Pa.s)			Infiltration time, $t$ (min)
	Giordano et al. [32]	Fluegel [33]	Wiesner et al. [29]	
1215	1623	100.7	75.5	860
1318	299.8	26.9	19.5	222
1411	84.0	10.2	7.1	80
1519	24.1	4.04	3.3	37

Surface tension values are expected to vary slightly depending on the temperature. The  $\sigma_{LV}$  value does not change significantly with the temperatures evaluated in this study. As illustrated in Table 7, the viscosity of CMAS decreases as the temperature increases from  $1215^\circ\text{C}$  to  $1519^\circ\text{C}$ . Penetration is very fast due to the lowered viscosity of CMAS. Consequently, the higher the temperature, the faster the Ca component reacts with the sintered  $\text{Gd}_2\text{SiO}_5$  to form the  $\text{Ca}_2\text{Gd}_8(\text{SiO}_4)_6\text{O}_2$  (apatite) phase. The contact angle between CMAS melt and bulk ceramic reflects their wettability, the larger the contact angle, the worse the wettability and the smaller the contact area [37]. According to B. Yin et al. [38], the stable contact angle of a CMAS droplet on the TBC increased with increase in the surface roughness. The stable contact angle was proportional to the square of the roughness. As the surface roughness increased, the CMAS droplet must overcome a higher surface energy in order to spread, resulting in a decrease in the

spreading rate and spreading distance. As the temperature further increased beyond the melting point, the viscosity and contact angle continued to decrease, but at a slower rate. According to R. Kumar [39], penetration by CMAS of various viscosities has been reported through the following equation (4) that CMAS viscosity plays a decisive role in the penetration depth in units of time in the coating layer.

$$L^2 = \frac{\gamma D t \cos(\theta)}{4\eta} \quad (4)$$

where, L = depth of infiltration at a time t,  $\gamma$  = surface tension of CMAS melt, D = diameter of the cracks, t = time for infiltration,  $\cos(\theta)$  = Contact angle,  $\eta$  = dynamic viscosity

CMAS with a lower viscosity penetrates the coating more easily, while CMAS with a higher viscosity has less penetration into the coating.

### 3.4. Conclusions

In this study, the high-temperature corrosion behavior of CMAS on sintered  $\text{Gd}_2\text{SiO}_5$  was performed at  $1400^\circ\text{C}$  for 2, 12, and 48 h. Due to the attack of the dissolved CMAS, it reacted with the sintered  $\text{Gd}_2\text{SiO}_5$ , and the heat treatment time and the reaction area increased. The vertically elongated needle morphology of the  $\text{Ca}_2\text{Gd}_8(\text{SiO}_4)_6\text{O}_2$  particles analyzed in the reaction area became thicker with increasing heat treatment time as the CMAS was dissolved. From the HT-XRD analysis results, it can be confirmed that CMAS dissolves at  $1300^\circ\text{C}$  to react with sintered  $\text{Gd}_2\text{SiO}_5$ . Additionally, the reaction temperature of CMAS and  $\text{Gd}_2\text{SiO}_5$  was found to be the same as the result by DSC analysis— $1262^\circ\text{C}$  or higher. Representative  $\text{CaSiO}_3$ ,  $\text{CaAl}_2\text{Si}_2\text{O}_8$ , and  $\text{Ca}_2\text{MgSi}_2\text{O}_7$  phases from CMAS were analyzed at  $25^\circ\text{C}$ . In addition,  $\text{Gd}_2\text{SiO}_5$  and  $\text{Gd}_{9.33}(\text{SiO}_4)_6\text{O}_2$  phases were analyzed. However, when the temperature rose to  $1300^\circ\text{C}$ , the peaks of  $\text{CaSiO}_3$ ,  $\text{CaAl}_2\text{Si}_2\text{O}_8$ , and  $\text{Ca}_2\text{MgSi}_2\text{O}_7$  disappeared, and peaks of  $\text{Ca}_2\text{Gd}_8(\text{SiO}_4)_6\text{O}_2$  were observed. This confirmed that CMAS melted at  $1300^\circ\text{C}$ , and as the CMAS reacted with  $\text{Gd}_2\text{SiO}_5$  ( $\text{Gd}_{9.33}(\text{SiO}_4)_6\text{O}_2$ ) and,  $\text{Ca}_2\text{Gd}_8(\text{SiO}_4)_6\text{O}_2$  formed as the Ca component of CMAS was consumed. The  $\text{Ca}_2\text{Gd}_8(\text{SiO}_4)_6\text{O}_2$  produced by this procedure appears to prevent the further penetration of dissolved CMAS at the interface.

## References

- [1] V.L. Wiesner, D. Scales, N.S. Johnson, B.J. Harder, A. Garg, N.P. Bansal, Calcium–magnesium aluminosilicate (CMAS) interactions with ytterbium silicate environmental barrier coating material at elevated temperatures, *Ceram Int.* (2020) 16733–16742.
- [2] N.A. Nasiri, N. Patra, D.D. Jayaseelan, W.E. Lee, Water vapour corrosion of rare earth monosilicates for environmental barrier coating application, *Ceram. Int.* 43 (2017) 7393–7400.
- [3] D.L. Poerschke, R.W. Jackson, C.G. Levi, Silicate deposit degradation of engineered coatings in gas turbines: progress toward models and materials solutions, *Ann. Rev. Mater. Res.* 47 (2017) 297–330.
- [4] D.L. Poerschke, J.H. Shaw, N. Verma, F.W. Zok, C.G. Levi, Interaction of yttrium disilicates environmental barrier coatings with calcium-magnesium-iron alumino-silicate melts, *Acta Mater.* 145 (2018) 451–461.
- [5] K.M. Grant, S. Krämer, G.G.E. Seward, C.G. Levi, Calcium-magnesium alumino-silicate interaction with yttrium monosilicate environmental barrier coatings, *J. Am. Ceram. Soc.* 93 (2010) 3504–3511.
- [6] C.G. Levi, J.W. Hutchinson, M.H. Vidal-Setif, C.A. Johnson, Environmental degradation of thermal-barrier coatings by molten deposits, *MRS Bull.* (2012) 932–941.
- [7] D.L. Poerschke, C.G. Levi, Phase equilibria in the calcia-gadolinia-silica system, *J. Alloys. Compd.* 695 (2017) 1397–1404.
- [8] M. Wolf, D.E. Mack, O. Guillon, R. Vaßen, Resistance of pure and mixed rare earth silicates against calciummagnesium-aluminosilicate (CMAS): A comparative study, *J. Am. Ceram. Soc.* 103 (2020) 7056–7071.
- [9] L.R. Turcer, A.R. Krause, H.F. Garces, L. Zhang, N.P. Padture, Environmental-barrier coating ceramics for resistance against attack by molten calcia-magnesia-aluminosilicate

- (CMAS) glass: Part II,  $\beta$ -Yb<sub>2</sub>Si<sub>2</sub>O<sub>7</sub> and  $\beta$ -Sc<sub>2</sub>Si<sub>2</sub>O<sub>7</sub>, *J. Eur. Ceram. Soc.* 38 (2018) 3914–24.
- [10] S. Morelli, V. Testa, G. Bolelli, O. Ligabue, E. Molinari, N. Antolotti, L. Lusvarghi, CMAS corrosion of YSZ thermal barrier coatings obtained by different thermal spray processes, *J. Eur. Ceram. Soc.* 40 (2020) 4084–4100.
- [11] P. Mechnich, W. Braue, Volcanic ash-induced decomposition of EB-PVD Gd<sub>2</sub>Zr<sub>2</sub>O<sub>7</sub> thermal barrier coatings to Gd-Oxyapatite, Zircon, and Gd, Fe-Zirconolite, *J. Am. Ceram. Soc.* 96 (2013) 1958–1965.
- [12] S. Krämer, J. Yang, C.G. Levi, Infiltration-inhibiting reaction of gadolinium zirconate thermal barrier coatings with CMAS melts, *J. Am. Ceram. Soc.* 91 (2008) 576–583.
- [13] N.A. Nasiri, N. Patra, D. Horlait, D.D. Jayaseelan, W.E. Lee, Thermal properties of rare-earth monosilicates for EBC on Si-based ceramic composites, *J. Am. Ceram. Soc.* 99 (2016) 589–596.
- [14] H.B. Zha, B.T. Richards, C.G. Levi, H.N.G. Wadley, Molten silicate reactions with plasma sprayed ytterbium silicate coatings, *Surf. Coat. Technol.* 288 (2016) 151–162.
- [15] W.D. Summers, D.L. Poerschke, A.A. Taylor, A.R. Ericks, C.G. Levi, F.W. Zok, Reactions of molten silicate deposits with yttrium monosilicate, *J. Am. Ceram. Soc.* 103 (2020) 2919–2932.
- [16] B.K. Jang, F.J. Feng, K. Suzuta, H. Tanaka, Y. Matsushita, K.S. Lee, S.W. Kim, Y.S. Oh, H.T. Kim., Corrosion behavior of volcanic ash on sintered mullite for environmental barrier coatings, *Ceram. Int.* 43 (2017) 1880–1886.
- [17] K.M. Grant, S. Krämer, J.P.A. Löfvander, C.G. Levi, CMAS degradation of environmental barrier coatings, *J. Eur. Ceram. Soc.* 202 (2007) 653–657.

- [18] B.K. Jang, F.J. Feng, K. Suzuta, H. Tanaka, Y. Matsushita, K.S. Lee, S. Ueno, Corrosion behavior of volcanic ash and calcium magnesium aluminosilicate on  $\text{Yb}_2\text{SiO}_5$  environmental barrier coatings, *J. Ceram. Soc. Jpn.* 125 (2017) 326–332.
- [19] F. Stolzenburg, M.T. Johnson, K.N. Lee, N.S. Jacobson, K.T. Faber, The interaction of calcium–magnesium–aluminosilicate with ytterbium silicate environmental barrier materials. *Surf. Coat. Technol* 284 (2015) 44–50.
- [20] F. Jiang, L. Cheng, Y. Wang, Hot corrosion of  $\text{RE}_2\text{SiO}_5$  with different cation substitution under calcium–magnesium–aluminosilicate attack, *Ceram. Int.* 43 (2017) 9019–9023.
- [21] A.E. Mohamed, M.K. Thomas, A review on differential scanning calorimetry technique and its importance in the field of energetic materials, *Physical Sciences Reviews.* 3 (2018) 20170103.
- [22] E.M. Zaleski, C. Ensslen, C.G. Levi, Melting and crystallization of silicate systems relevant to thermal barrier coating damage, 98 (2015) 1642–1649.
- [23] B.K. Jang, F.J. Feng, K.S. Lee, E. García, A. Nistal, N. Nagashima, S.W. Kim, Y.S. Oh, H.T. Kim, Thermal behavior and mechanical properties of  $\text{Y}_2\text{SiO}_5$  environmental barrier coatings after isothermal heat treatment, *Surf. Coat. Technol.* 308 (2016) 24–30.
- [24] S.H. Kim, B.N. Kim, N. Nagashima, Y. Matsushita, B.K. Jang, High-temperature corrosion of spark plasma sintered  $\text{Gd}_2\text{SiO}_5$  with volcanic ash for environmental barrier coatings, *J. Eur. Ceram. Soc.* 41 (2020) 3161–3166.
- [25] S. Krämer, J. Yang, C.G. Levi, Infiltration-inhibiting reaction of gadolinium zirconate thermal barrier coatings with CMAS melts, *J. Am. Ceram. Soc.* 91 (2010) 576–583.
- [26] J.M. Drexler, C.H. Chen, A.D. Gledhill, K. Shinoda, S. Sampath, N.P. Padture, Plasma sprayed gadolinium zirconate thermal barrier coatings that are resistant to damage by molten Ca-Mg-Al-silicate glass, *Surf. Coat. Technol.* 206 (2012) 3911–3916.

- [27] U. Schulz, W. Braue, Degradation of  $\text{La}_2\text{Zr}_2\text{O}_7$  and other novel EB-PVD thermal barrier coatings by CMAS ( $\text{CaO-MgO-Al}_2\text{O}_3\text{-SiO}_2$ ) and volcanic ash deposits, *Surf. Coat. Tech.* 235 (2013) 65–73.
- [28] H. Zhang, J. Lu, X. Shan, D. Wu, X. Zhao, F. Guo, P. Xiao, A promising molten silicate resistant material: rare-earth oxy-apatite  $\text{RE}_{9.33}(\text{SiO}_4)_6\text{O}_2$  (RE=Gd, Nd or La), *J. Eur. Ceram. Soc.* 40 (2020) 5380–5390.
- [29] V.L. Wiesner, U.K. Vempati, N.P. Bansal, High temperature viscosity of calcium-magnesium-aluminosilicate glass from synthetic sand, *Scrip Mater.* 124 (2016) 189–192.
- [30] V.L. Wiesner, N.P. Bansal, Mechanical and thermal properties of calcium–magnesium-aluminosilicate (CMAS) glass, *J. Eur. Ceram. Soc.* 35 (2015) 2907–2914.
- [31] J. Sleeper, A. Garg, V.L. Wiesner, N.P. Bansal, Thermochemical interactions between CMAS and  $\text{Ca}_2\text{Y}_8(\text{SiO}_4)_6\text{O}_2$  apatite environmental barrier coating material, *J. Eur. Ceram. Soc.* 39 (2019) 5380–5390.
- [32] D. Giordano, J.K. Russell, D.B. Dingwell, Viscosity of magmatic liquids: A model, *Earth Planet, Sci Lett.* 271 (2008) 123–134.
- [33] A. Fluegel, Glass viscosity calculation based on a global statistical modelling approach, *Glass Technol. Eur. J. Glass Sci. Technol. Part A* 48 (2007) 13–30.
- [34] D.R. Poirier, G.H. Geiger, *Transport phenomena in materials processing*, Minerals: Met Mater Soc; (1994).
- [35] S. Krämer, J. Yang, C.G. Levi, C.A. Johnson, Thermochemical interaction of thermal barrier coatings with molten  $\text{CaO-MgO-Al}_2\text{O}_3\text{-SiO}_2$ (CMAS) deposits, *J. Am. Ceram. Soc.* 89 (2006) 3167–75.
- [36] A. Kucuk, A. Clare, L. Jones, An estimation of the surface tension for silicate glass melts at  $1400^\circ\text{C}$  using statistical analysis, *Glass Technol.* 40 (1999) 149–153.

- [37] H. Li, Y. Yu, B. Fang, P. Xiao, W. Li, S. Wang, High temperature behavior of  $\text{HfSiO}_4$  subjected to calcium-magnesium-alumina-silicate (CMAS) and high-velocity water vapor, *J. Eur. Ceram. Soc.* 43 (2023) 621–628.
- [38] R. Kumar, S. Rommel, C. Jiang, E.H. Jordan, Effect of CMAS viscosity on the infiltration depth in thermal barrier coatings of different microstructures, *Surf. Coat. Technol.* 432 (2022) 128039.
- [39] B. Yin, M. Sun, W. Zhu, L. Yang, Y. Zhou, Wetting and spreading behaviour of molten CMAS towards thermal barrier coatings and its influencing factors, *Results in Physics.* 26 (2021) 104365.

# Chapter 4. High-Temperature Corrosion of $\text{Gd}_2\text{Si}_2\text{O}_7$ with CMAS for EBCs

## 4.1. Introduction

Environmental barrier coatings (EBCs) are required to resist corrosion by silica-based particles (sand and, ash) in high temperature combustion environments and prevent their reaction with water vapor. In particular, high-temperature corrosion of EBC by molten silicate deposits known as calcia-magnesia-alumina-silica (CMAS) during gas turbine engine operation in high-temperature combustion environments is a significant problem [1–10]. Molten CMAS glass is precipitated on EBCs at elevated temperatures ( $>1200^\circ\text{C}$ ), to study coating deterioration.

Rare earth (RE) silicates are being used as promising EBC materials owing to their low  $\text{SiO}_2$  activity and excellent high-temperature capability. In general, RE silicates are classified as monosilicates ( $\text{RE}_2\text{SiO}_5$ ) or disilicates ( $\text{RE}_2\text{Si}_2\text{O}_7$ ) [9,11].  $\text{RE}_2\text{SiO}_5$  is converted to  $\text{RE}_2\text{Si}_2\text{O}_7$  upon reaction with CMAS. This phase change-induced stress can affect the cracking and delamination of the EBCs. However, when  $\text{RE}_2\text{Si}_2\text{O}_7$  reacts with CMAS, it remains chemically stable without phase change [12]. Most studies on the high-temperature corrosion behavior of RE disilicate and CMAS have focused on the reaction between  $(\text{Y},\text{Yb})_2\text{Si}_2\text{O}_7$  and CMAS glass [11]. Several families have promising properties and are classified as RE silicates. Among them, silicates of such as scandium (Sc), lutetium (Lu), ytterbium (Yb), yttrium (Y) and erbium (Er) that have been studied as suitable candidates [13].

Gadolinium (Gd) was also investigated as an EBCs candidate material owing to its high-temperature corrosion behavior. Table 8 shows various studies on gadolinium silicates and CMAS as a function of temperature,  $\text{CaO}:\text{SiO}_2$  ratios and heat-treatment time.

Table 8. Experimental conditions (temperature, CaO:SiO<sub>2</sub> ratios, and heat-treatment time) from previous studies on CMAS.

References	Temp. (°C)	CaO:SiO <sub>2</sub> ratios	CMAS quantity (mg/cm <sup>2</sup> )	Time (h)	RE material
Stokes et al. [3]	1400	0.635 0.478 0.277 0.096	50:50 mol% (RE:CMAS)	1	Gd <sub>2</sub> Si <sub>2</sub> O <sub>7</sub>
Jang et al. [9]	1400	0.73	40	2, 12, 48	Yb <sub>2</sub> SiO <sub>5</sub>
Kim et al. [14]	1400	0.73	40	2, 12, 48	Gd <sub>2</sub> SiO <sub>5</sub>
Kim et al. [15]	1400	0.11	40 (VA)	2, 12, 48	Gd <sub>2</sub> SiO <sub>5</sub>
Liu et al. [16]	1400	0.73	31.4	10	Gd <sub>2</sub> Si <sub>2</sub> O <sub>7</sub>
Zhang et al. [17]	1300	0.73	20	10 min, 4, 8, 24	Gd <sub>9.33</sub> (SiO <sub>4</sub> ) <sub>6</sub> O <sub>2</sub>

VA: Volcanic ash

A study of the high-temperature corrosion behavior of RE silicates and CMAS should consider several details. In previous studies, the high-temperature corrosion behavior of Gd<sub>2</sub>SiO<sub>5</sub> with CMAS [14] and Gd<sub>2</sub>SiO<sub>5</sub> with volcanic ash [15] have been studied. It was confirmed that CMAS (0.73) with a high CaO:SiO<sub>2</sub> ratio formed a thicker reaction layer than volcanic ash (0.11). Liu et al. [16] evaluated the high-temperature corrosion behavior of Gd<sub>2</sub>Si<sub>2</sub>O<sub>7</sub> after heat-treatment at 1400°C for 10 h. Zhang et al. [17] performed a high-temperature corrosion evaluation for Gd<sub>9.33</sub>(SiO<sub>4</sub>)<sub>6</sub>O<sub>2</sub> and CMAS at 1300°C for 24 h.

However, the high-temperature corrosion behavior of Gd<sub>2</sub>Si<sub>2</sub>O<sub>7</sub> and CMAS has rarely been reported for long-term isothermal heat-treatment. The purpose of this study was to evaluate the suitability of Gd<sub>2</sub>Si<sub>2</sub>O<sub>7</sub> as an EBCs material by investigating the chemical and microstructural

changes caused by the chemical reaction of  $\text{Gd}_2\text{Si}_2\text{O}_7$  with CMAS at high temperature for a long time. Specifically, identify the reaction products formed by sintered  $\text{Gd}_2\text{Si}_2\text{O}_7$  and CMAS at high temperature, and analyzed the thickness and width of apatite over time. In addition, the main purpose of this study is focuses on the high-temperature corrosion behavior of  $\text{Gd}_2\text{Si}_2\text{O}_7$  and CMAS, and the comparison of reaction layer formation between  $\text{RE}_2\text{SiO}_5$  ( $\text{Gd}_2\text{SiO}_5$  in chapter 3) and  $\text{RE}_2\text{Si}_2\text{O}_7$  ( $\text{Gd}_2\text{Si}_2\text{O}_7$ ).

## 4.2. Experimental

### 4.2.1. Sample Fabrication

Gd<sub>2</sub>O<sub>3</sub> (Rare Metallurgical Corporation, Japan) and SiO<sub>2</sub> (Wako Pure Chemical Industries Ltd., Japan) powders were used to prepare Gd<sub>2</sub>Si<sub>2</sub>O<sub>7</sub>. The mixed Gd<sub>2</sub>O<sub>3</sub>-2SiO<sub>2</sub> powder was ball milled using 5 mm diameter YSZ balls in EtOH for 24 h. The mixed Gd<sub>2</sub>O<sub>3</sub>-SiO<sub>2</sub> powder was then dried in an oven at 80°C for 24 h and then heated at 1400°C for 20 h to form Gd<sub>2</sub>Si<sub>2</sub>O<sub>7</sub>. The synthesized Gd<sub>2</sub>Si<sub>2</sub>O<sub>7</sub> powder was then transferred into a graphite mold with a diameter of 30 mm and spark plasma sintered (Dr. Sinter 1050, Sumitomo Coal Mining Co., Ltd., Japan) under a pressure of 60 MPa in a vacuum of 10<sup>-2</sup> at 1400°C for 20 min, heated at 10°C/min. The CMAS (33CaO-9MgO-13AlO<sub>1.5</sub>-45SiO<sub>2</sub> mol%) powders used for high-temperature corrosion were fabricated using the same manufacturing method as in our previous study [12,14].

The sintered Gd<sub>2</sub>Si<sub>2</sub>O<sub>7</sub> was cut into 10 mm × 5 mm × ~3 mm using a diamond saw. After cutting, the surface of the specimens were sequentially polished with 9, 3, and 1 μm diamond suspensions. Specimens for high-temperature corrosion experiments were prepared by attaching CMAS paste (prepared by ultrasonic dispersion in EtOH) to the surface of each Gd<sub>2</sub>Si<sub>2</sub>O<sub>7</sub> specimen under a load of 40 mg/cm<sup>2</sup>. The individual specimens were annealed at 1400°C at a heating rate of 5°C/min for 0.5, 2, 12, 48 or 100 h, followed by furnace cooling to room temperature. After the heat treatment, the specimen was cut into 5 × 5 × 3 mm cross-sections for analysis of the cross-section of the reaction layer. Sections of the specimens were polished successively using 9, 3, and 1 μm diamond suspensions and then ultrasonically cleaned with acetone and EtOH for 5 min.

### 4.2.2. Characterization

The changes in the microstructure and reaction layer during the high-temperature corrosion of sintered  $\text{Gd}_2\text{Si}_2\text{O}_7$  were observed using a scanning electron microscope (SEM, Hitachi S-4300). A beam voltage of 15 kV and working distance of 15 mm were used for energy-dispersive X-ray spectroscopy (EDS) measurements to determine the element ratios (compositions) of the specimen cross-section. High-temperature X-ray diffraction (HT-XRD) data were collected using a Rigaku Smart Lab diffractometer with  $\text{Cu K}\alpha_1$  radiation ( $\lambda = 1.54056 \text{ \AA}$ ) to examine the phase evolution of the high-temperature reaction of  $\text{Gd}_2\text{Si}_2\text{O}_7$  and CMAS powders from room temperature ( $25^\circ\text{C}$ ) up to  $1300^\circ\text{C}$  at a heating rate of  $10^\circ\text{C}/\text{min}$ . The phase of  $\text{Gd}_2\text{Si}_2\text{O}_7$  powders was investigated at  $25^\circ\text{C}$ . Intensity measurements were performed over a  $2\theta$  range of  $20\text{--}60^\circ$  using a scan step of  $0.02^\circ/\text{min}$  and a scan speed of  $1^\circ/\text{min}$ . The apatite width was determined, as an average of five measurements in units of  $50 \mu\text{m}$  from the interface between the sintered  $\text{Gd}_2\text{Si}_2\text{O}_7$  and apatite.

### 4.3. Results and Discussion

#### 4.3.1. Characterization of Sintered $Gd_2Si_2O_7$

Fig. 31 (a) shows the SEM micrograph of the sintered  $Gd_2Si_2O_7$  and (b) the XRD pattern of the  $Gd_2Si_2O_7$  powders at room temperature (initial measurement data for HT-XRD measurements). The average grain size of the sintered  $Gd_2Si_2O_7$  was approximately 8.4  $\mu m$ . The porosity was 5.7% and the relative density was 94.3%, as shown in Fig. 31 (a). Fig. 31 (b) shows the XRD pattern of the obtained  $Gd_2Si_2O_7$  powders, and the  $Gd_2Si_2O_7$  peaks were clearly identified was analyzed at room temperature.

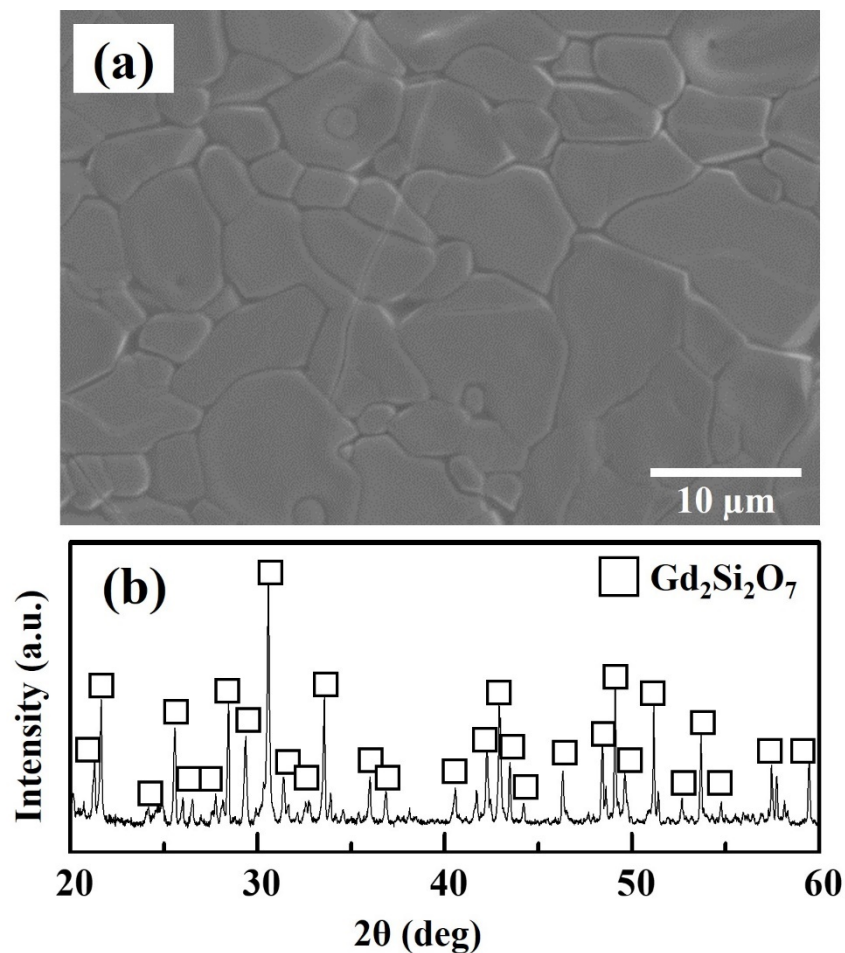


Fig. 31. (a) SEM micrograph of a thermally-etched sintered  $Gd_2Si_2O_7$  and (b) HT-XRD results of  $Gd_2Si_2O_7$  powder.

This confirms that the mixed  $\text{Gd}_2\text{O}_3\text{-2SiO}_2$  powder was completely synthesized before the CMAS high-temperature reaction to complete the  $\text{Gd}_2\text{Si}_2\text{O}_7$  powder. This result is consistent with the XRD results for  $\text{Gd}_2\text{Si}_2\text{O}_7$  in the reported research [16].

#### 4.3.2. High-Temperature Corrosion Behavior

Fig. 32 shows the HT-XRD pattern of the mixed CMAS/ $\text{Gd}_2\text{Si}_2\text{O}_7$  powder from 25 to 1300°C. The melting point ( $T_m$ ) of the CMAS powder was confirmed to be 1243°C in our previous study [12]. Thus, based on  $T_m$  the CMAS powder, HT-XRD was performed up to 1300°C and at room temperature before and after the heat treatment. Fig. 32 (a) shows the HT-XRD pattern of the mixed CMAS/ $\text{Gd}_2\text{Si}_2\text{O}_7$  powder measured at 25°C before heat treatment. The XRD results corresponding to  $\text{Gd}_2\text{Si}_2\text{O}_7$ ,  $\text{CaSiO}_3$ ,  $\text{Ca}_2\text{MgSi}_2\text{O}_7$ , and  $\text{CaAl}_2\text{Si}_2\text{O}_8$  were analyzed. Figs. 32 (b) - (c) show no change in the phase set up to 1200°C. However, CMAS reacted with  $\text{Gd}_2\text{Si}_2\text{O}_7$  and the peak corresponding to  $\text{Ca}_2\text{Gd}_8(\text{SiO}_4)_6\text{O}_2$  was observed at 1300°C in Fig. 32 (d). The XRD pattern of  $\text{Ca}_2\text{Gd}_8(\text{SiO}_4)_6\text{O}_2$  at 1300°C confirmed the high-temperature reaction of  $\text{Gd}_2\text{SiO}_5$  and CMAS reported in our previous study [14], which was the same as the  $\text{Ca}_2\text{Gd}_8(\text{SiO}_4)_6\text{O}_2$  pattern in the present study. Even after cooling, the peak of the  $\text{Ca}_2\text{Gd}_8(\text{SiO}_4)_6\text{O}_2$  phase was observed, as shown in Fig. 32 (e).

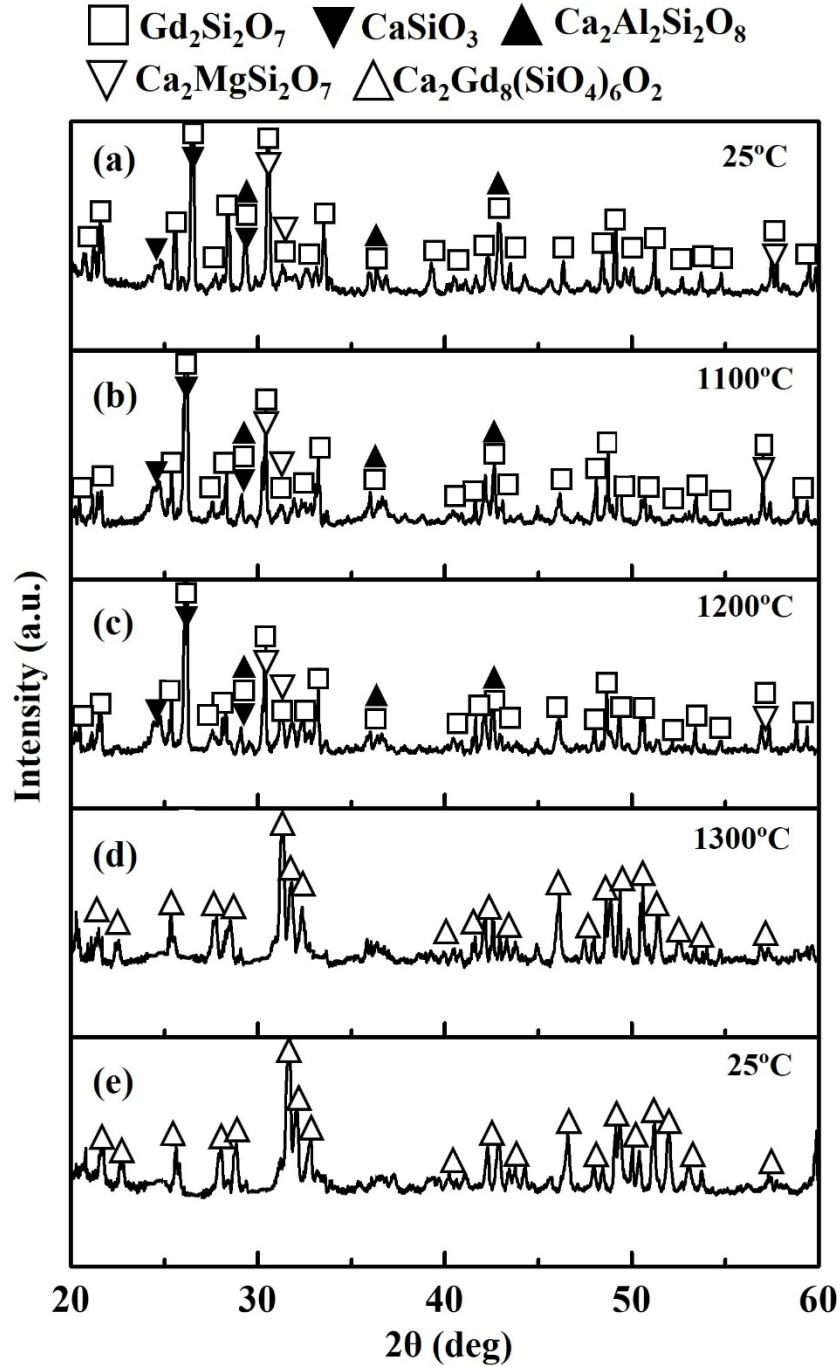


Fig. 32. HT-XRD patterns of mixed CMAS +  $\text{Gd}_2\text{Si}_2\text{O}_7$  powder (1 : 1 wt.%): at (a) 25°C, (b) 1100°C, (c) 1200°C, (d) 1300°C, and during cooling at (e) 25°C.

Fig. 33 shows a cross-sectional SEM micrograph of  $\text{Gd}_2\text{Si}_2\text{O}_7$  coated with CMAS after heat treatment at 1400 °C for (a) 0.5, (b) 2, (c) 12, (d) 48, and (e) 100 h. The formation of a reaction layer at the interface between molten CMAS and  $\text{Gd}_2\text{Si}_2\text{O}_7$  after heat treatment is

shown in Figs. 33 (a) - (e). As the heat-treatment time increased, the thickness of the reaction layer increased, and the reaction layer grew vertically.

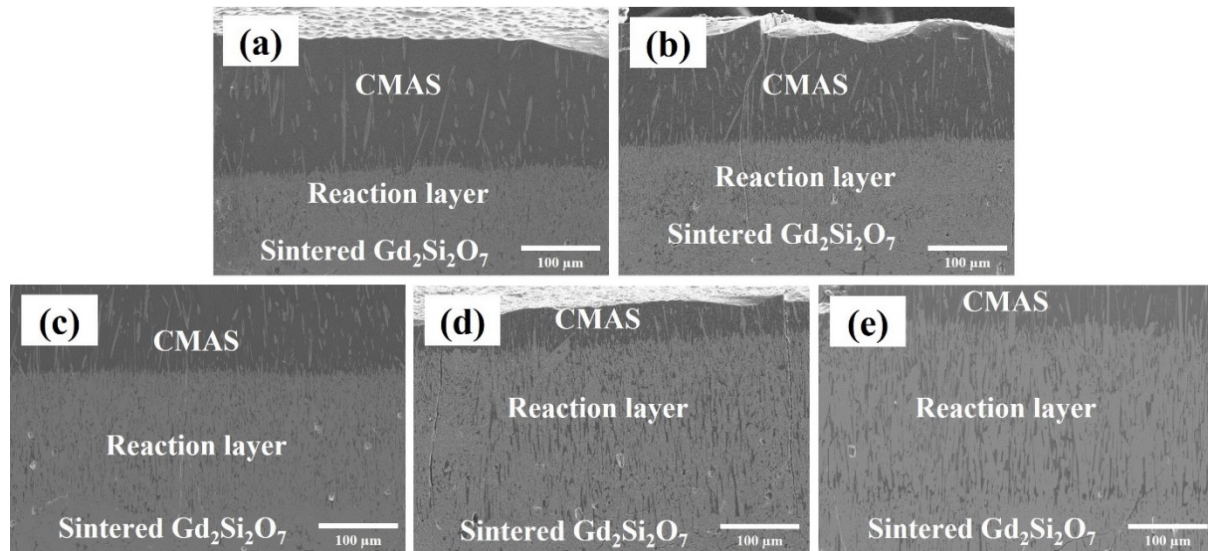


Fig. 33. Cross-sectional SEM micrograph of sintered  $Gd_2Si_2O_7$  after the interaction with CMAS at  $1400^\circ C$ : for (a) 0.5 h, (b) 2 h, (c) 12 h, (d) 48 h, and (e) 100 h.

Fig. 34 (a) shows the SEM micrograph of the reaction of  $Gd_2Si_2O_7$  with CMAS after heat treatment at  $1400^\circ C$  for 2 h. Fig. 34 (a) shows CMAS,  $Ca_2Gd_8(SiO_4)_6O_2$ , and sintered  $Gd_2Si_2O_7$ . Fig. 34 (b) shows the results of the EDS line analysis along the yellow line in Fig. 34 (a). Si, Ca, and O down to approximately  $50 \mu m$  were analyzed in the CMAS region. In addition, Si, O, Ca, and Gd, which are components of  $Ca_2Gd_8(SiO_4)_6O_2$ , were detected in the region from approximately  $50$  to  $200 \mu m$ . Finally, the region after  $250 \mu m$  is considered to be sintered  $Gd_2Si_2O_7$  because Si, O, and Gd, but not except Ca, were detected.

Stokes et al. [3] used image analysis for studying the reactions of  $Dy_2Si_2O_7$ ,  $Gd_2Si_2O_7$ , and  $Nd_2Si_2O_7$  with CMAS with four CaO:SiO<sub>2</sub> ratios (0.635, 0.478, 0.277, and 0.098, respectively) and quantified the change in the circularity ( $C$ ) of the sediment morphology using Equation (1). where  $A$  is the area and  $P$  is the perimeter.

$$C = \frac{4\pi A}{P^2} \quad (1)$$

Lower circularity occurred more frequently in the reaction with CMAS with a CaO:SiO<sub>2</sub> ratio (0.635) and most of the elongated precipitates had values of approximately 0.4. The reaction with CMAS with CaO:SiO<sub>2</sub> ratios (0.478 and 0.277) produced a similar precipitate morphology and the circularity increased to a maximum of ~0.75. This suggests that the aspect ratio of the sediment decreased. In addition, although circularity significantly changed depending on the CMAS composition, there was no apparent trend in these analyses to indicate differences in morphology between the RE species. In our previous study [12], it can be confirmed that there were no differences in the apatite morphology for different RE species. The apatite form and elongated needle shape formed in Er<sub>2</sub>Si<sub>2</sub>O<sub>7</sub> under the same conditions (CaO:SiO<sub>2</sub> ratios, temperature, and time) were analyzed. In the present study, because the CaO:SiO<sub>2</sub> ratio was 0.73, an elongated precipitate with smaller circularity than the precipitate generated at 0.635 was observed.

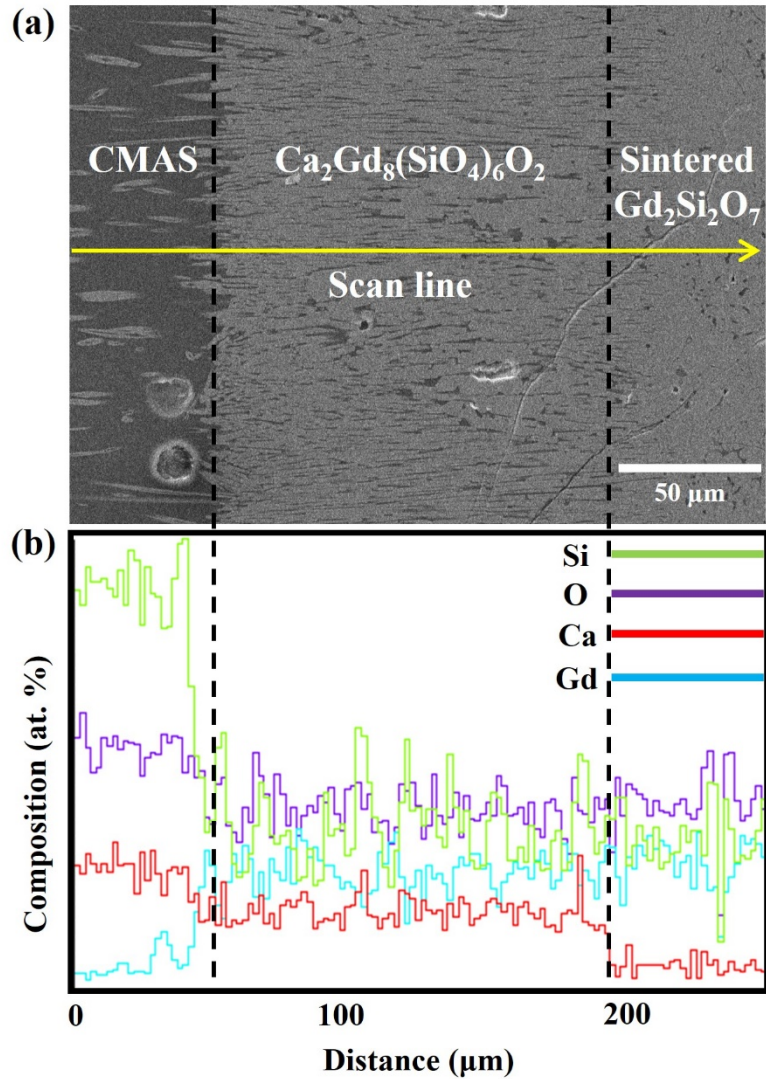


Fig. 34. SEM micrograph of sintered  $\text{Gd}_2\text{Si}_2\text{O}_7$  after the interaction with CMAS at  $1400^\circ\text{C}$  for 2 h: (a) cross-sectional SEM micrograph of CMAS,  $\text{Ca}_2\text{Gd}_8(\text{SiO}_4)_6\text{O}_2$ , and sintered  $\text{Gd}_2\text{Si}_2\text{O}_7$ , (b) EDS line analysis results for the region shown with the yellow arrow.

Fig. 35 shows the EDS mapping results of the sintered  $\text{Gd}_2\text{Si}_2\text{O}_7$  cross-sections coated with CMAS after the heat treatment at  $1400^\circ\text{C}$  for 12 h. The measurements were distinguished for the following regions CMAS, reaction layer and sintered  $\text{Gd}_2\text{Si}_2\text{O}_7$ . The results were the same as the EDS line analysis result, and Ca, Si, Al, and O, which are the main components, were detected in the CMAS area. Subsequently, Ca content was analyzed up to the reaction layer. Ca, Si, Gd, and O were detected in the reaction layer, confirming the presence of

$\text{Ca}_2\text{Gd}_8(\text{SiO}_4)_6\text{O}_2$ . This is consistent with the HT-XRD results showing the formation of  $\text{Ca}_2\text{Gd}_8(\text{SiO}_4)_6\text{O}_2$  in Fig. 32.

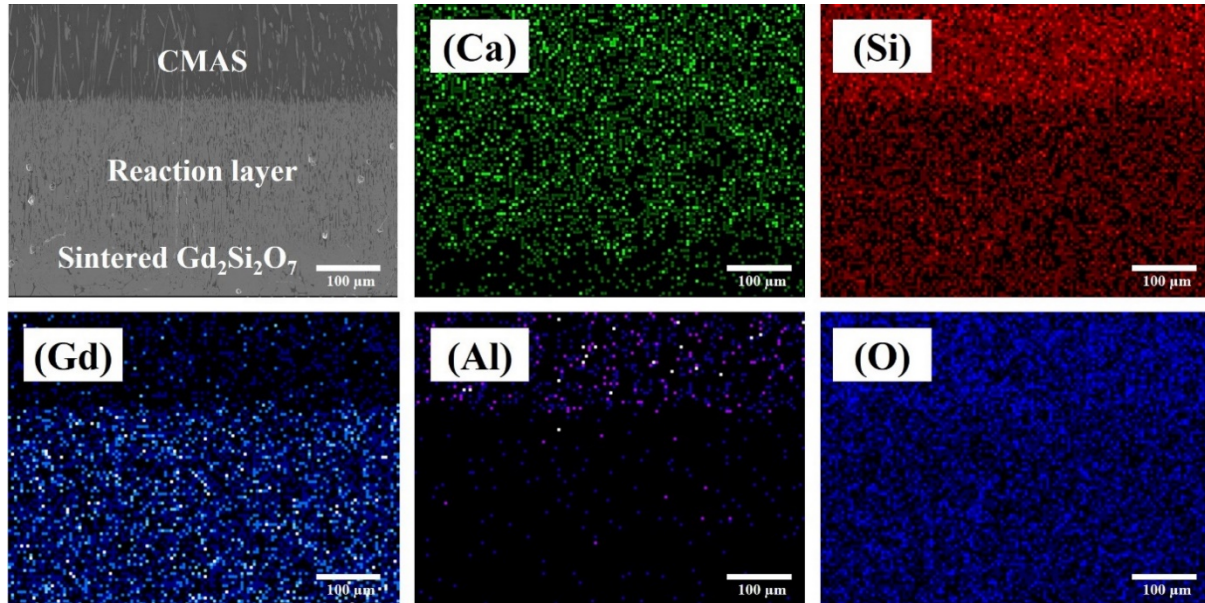


Fig. 35. EDS map (Ca, Si, Al, O, and Gd) of sintered  $\text{Gd}_2\text{Si}_2\text{O}_7$  after the interaction with CMAS at  $1400^\circ\text{C}$  for 12 h.

Fig. 36 (a) shows a low-magnification SEM micrograph of the sintered  $\text{Gd}_2\text{Si}_2\text{O}_7$  cross-section coated with CMAS after heat treatment at  $1400^\circ\text{C}$  for 12 h. Fig. 36 (b) shows a high magnification SEM micrograph of the yellow box in Fig. 36 (a). A, B, C, and D in Fig. 36 (b) show the EDS point analysis areas. Table 9 presents the results of the EDS point analysis for areas A, B, C, and D in Fig. 36 (b). Gd, Mg, Al, Si, Ca, and O were detected in parts A and B. Based on the detected elements, A and B were considered to be CMAS glass. Approximately 2% of Gd was detected in the CMAS glass, similar to apatite  $\text{Ca}_2\text{Y}_8(\text{SiO}_4)_6\text{O}_2$  in contact with CMAS at  $1200\text{--}1500^\circ\text{C}$ , with small amounts of yttrium detected in the melt [18]. Gd, Si, Ca, and O were detected in parts C and D, these parts were considered to be apatite. This shows that Ca is the major CMAS component that contributes to apatite crystallization. Zhao et al.

[19] reported that the Ca concentration of the CMAS melt decreases with increasing reaction time. The high-temperature reactions of  $\text{Yb}_2\text{Si}_2\text{O}_7$  and CMAS were investigated at  $1300^\circ\text{C}$  for 200 h. Faster Ca loss at the beginning of the reaction with respect to the Ca concentration of the CMAS melt, affected the formation of a continuous apatite layer. In our previous study, it was also confirmed that the Ca concentration initially decreased in the high-temperature reaction of  $\text{Er}_2\text{Si}_2\text{O}_7$  and CMAS [12].

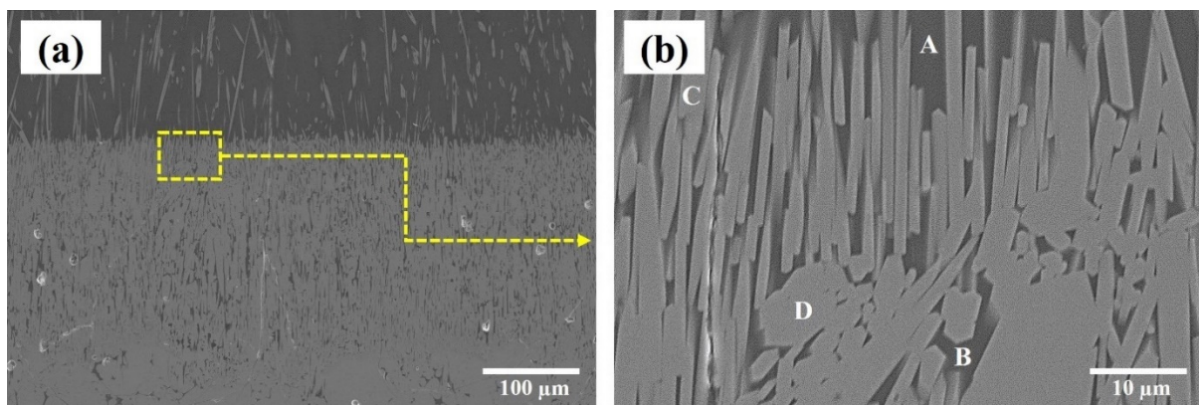


Fig. 36. (a) Low- and (b) cross-sectional SEM micrographs of sintered  $\text{Gd}_2\text{Si}_2\text{O}_7$  after the interaction with CMAS at  $1400^\circ\text{C}$  for 12 h: parts A, B (CMAS), and C, D (reaction region).

Table 9. The average compositions (at.%) of the cross-section with CMAS at parts A, B, C and D in Fig. 36 (b).

Elements	Gd	Mg	Al	Si	Ca	O
Part A	3.36	2.30	5.33	21.02	5.71	62.28
Part B	3.66	1.89	4.69	20.29	5.86	63.61
Part C	16.48	0	0	16.93	3.95	62.64
Part D	17.12	0	0	16.41	3.96	62.51

Fig. 37 shows the average thickness of the reaction layer according to the increase in the reaction time with CMAS and  $Gd_2Si_2O_7$  after heat treatment at  $1400^\circ C$ . Additionally, the average thickness of the reaction layers of  $Gd_2SiO_5$  and ash [15], and  $Gd_2SiO_5$  and CMAS [14] after the heat treatment at  $1400^\circ C$  are shown, as reported in our previous study. As a result of the reaction between CMAS and  $Gd_2Si_2O_7$ , the thickness of the reaction layer increased to approximately 98, 145, 211, 306, and 315  $\mu m$  after 0.5, 2, 12, 48, and 100 h, respectively. In addition, the CMAS and  $Gd_2SiO_5$  reaction layers measured 25, 70, and 120  $\mu m$  at 2, 12, and 48 h, respectively, in a previous study [14]. The volcanic ash and  $Gd_2SiO_5$  reaction layers had a thickness of 5, 18, and 45  $\mu m$  at 2, 12, and 48 h, respectively [15]. According to the change in time, the thickness of the reaction layer was divided into regions I, II, and III, as shown in Fig. 37.

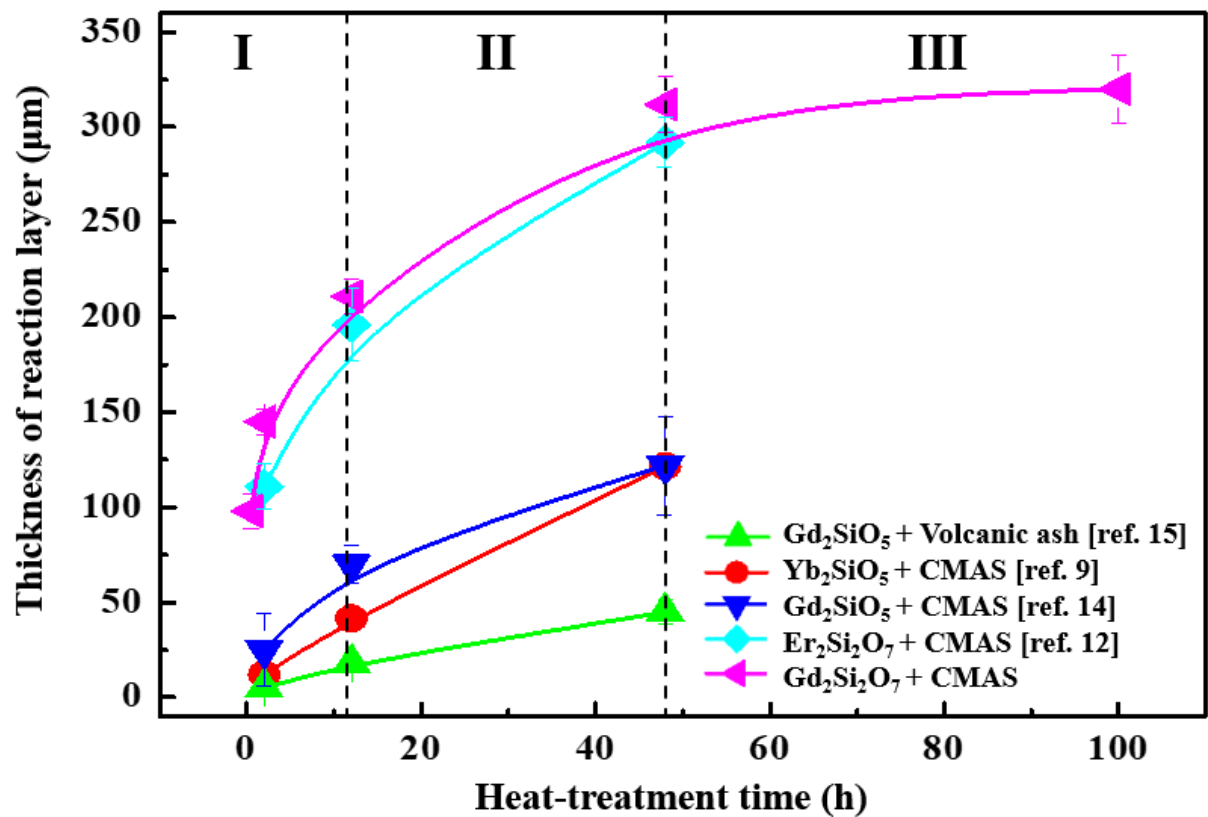


Fig. 37. Average thickness of reaction layer at  $1400^\circ C$  as a function of heat-treatment time.

A relatively fast reaction layer was formed relatively fast in region I and further increased in thickness; it was confirmed that the thickness of the reaction layer formation from regions II to III were slower than that in region I. Perrudin et al. [20] reported a study on the crystal growth of apatite. The high-temperature reaction of  $\text{RE}_2\text{O}_3$  (RE = Yb, Dy, Gd, Sm, Nd) with CMAS was evaluated at  $1200^\circ\text{C}$ . After heat treatment for 5 min, apatite crystal growth was observed throughout the RE. Owing to the short interaction time between  $\text{RE}_2\text{O}_3$  and CMAS, apatite formation develops in RE elements with large ionic radii. The thickness of the reaction layer in regions I, II, and III increases with time, and the curves have the form of a parabolas. Wiesner et al. [21], annealed 80 wt.%  $\text{Y}_2\text{Si}_2\text{O}_7$  and 20 wt.% CMAS pellets from 1200 to  $1500^\circ\text{C}$  for 20 h and confirmed that the average amount of CaO in the CMAS melt decreases with increasing temperature. They also found that the apatite reaction stop when calcium is depleted from the CMAS melt at the  $\text{Y}_2\text{Si}_2\text{O}_7$  interface with the CMAS. In our previous study [12], the concentration of Ca in a CMAS melt decreased with increasing time and temperature. The Ca content of the molten CMAS after heat treatment decreased from 6.54 to 4.26 at.% with the increase in reaction time from 2 to 48 h. This result is consistent with the Ca content of molten CMAS consumed during the crystallization of apatite. In other words, the rate of increase in the thickness of the reaction layer increased with time.

Using the results in Fig. 37, we determined the high-temperature corrosion behavior of Gd-silicate in the three previous results. First, CMAS had a stronger effect on the reaction layer formation than volcanic ash because CMAS (0.73) has a higher CaO:SiO<sub>2</sub> ratio than volcanic ash (0.11). The content of Ca had the strongest effect on the formation of apatite. Second, the thickness and width of the reaction layer increased with time. The apatite widths are shown in Fig. 38. Third,  $\text{RE}_2\text{Si}_2\text{O}_7$  had a stronger effect on the reaction layer formation than  $\text{RE}_2\text{SiO}_5$ . Wolf et al. [11], reported consistently lower apatite production in monosilicate than in disilicate as a result of the CMAS interaction with (Y,Yb) monosilicate and (Y,Yb) disilicate. Disilicate

has been reported to consume CaO in the CMAS melt to produce apatite while simultaneously releasing SiO<sub>2</sub>. However, in the case of monosilicate, the precipitation of apatite consumes SiO<sub>2</sub> and CaO in the CMAS melting. Therefore, Ca<sup>2+</sup> is depleted more rapidly and the amount of apatite produced by monosilicate decreases [22].

Stokes et al. [3] analyzed the interaction between RE-disilicate (RE<sub>2</sub>Si<sub>2</sub>O<sub>7</sub>, RE = Er, Dy, Gd, Nd) and four CMAS compositions at 1400°C. RE disilicates were dissolved by CMAS, resulting in mainly Ca-RE apatite type silicate crystallization, which was dependent on the RE cation size and amount of CaO present. Increased reactivity was observed for larger RE<sup>3+</sup> cation sizes and higher CaO:SiO<sub>2</sub> ratios. Our previous study investigated the high-temperature reaction between Er<sub>2</sub>Si<sub>2</sub>O<sub>7</sub> and CMAS [12]. Gd (1.107 Å) [23] forms thicker apatite due to its larger cation size than Er (1.004 Å) [34]. The same results were obtained for monosilicate. Gd (1.107 Å) [23], which has a larger cation size than Yb (0.985 Å) [11], forms a thicker reaction layer. Under the same conditions (temperature, time, and CaO:SiO<sub>2</sub> ratio), the reaction layer in the case of Gd<sub>2</sub>SiO<sub>5</sub> and CMAS is thicker than that for Yb<sub>2</sub>SiO<sub>5</sub> [9] and CMAS.

In other words, it was confirmed that the apatite formation decreased as the difference in Ca<sup>2+</sup> radius increased. Tian et al. [25], reported that RE<sub>2</sub>SiO<sub>5</sub> (RE=Tm, Yb, Lu) exhibits strong resistance to CMAS corrosion. As the RE cation size decreases, the reaction layer thickness also decreases because the enthalpy of formation of RE silicate apatite becomes more endothermic with decreasing RE cation size [25].

G. Cao et al. discussed the growth mechanism of the reaction layer of (Y<sub>1-x</sub>Yb<sub>x</sub>)<sub>2</sub>SiO<sub>5</sub> and CMAS [26]. The average growth rate of the apatite layer was investigated at 1573 K as a function of corrosion time, and the measured thickness of apatite increased rapidly between 4 and 16 h. However, the growth rate decreased and the increase in the thickness of the apatite decreased after 16 h.

$$\eta = \frac{K_B T}{D \lambda} \quad (2)$$

According to the Einstein-Stokes equation (2), the diffusion coefficient  $D$  increases with decreasing viscosity  $\eta$ .  $K_B$  is the Boltzmann constant,  $T$  is the temperature, and  $\lambda$  is the ion diffusion step [27]. It has also been reported that rare earth oxides dissolved in the melt increase the diffusion rate of the melt surrounding the apatite and decrease the viscosity of the melt surrounding the apatite [26]. In other words, as the RE content of the melt increases, the viscosity decreases and the diffusion coefficient increases, so the reactants CaO and SiO<sub>2</sub> can be transported faster. However, as time increases, CaO is depleted from the melt, and the growth rate of apatite is reduced. In our previous study, as the time increased from 2 h to 48 h, the Ca content in the melt decreased from 6.54% to 4.26%, and the growth rate of apatite decreased [12]. As shown in Fig. 37, the thickness of apatite increased up to 48 h in the reaction between Gd<sub>2</sub>Si<sub>2</sub>O<sub>7</sub> and CMAS, but the thickness increase rate of apatite gradually decreased until 100 h.

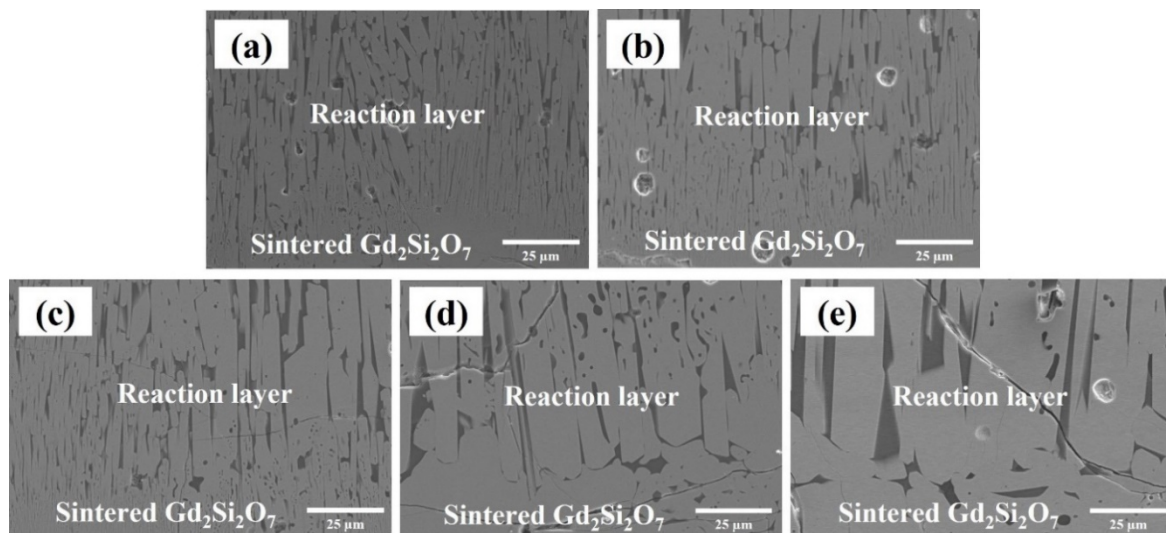


Fig. 38. Cross-sectional SEM micrograph of sintered Gd<sub>2</sub>Si<sub>2</sub>O<sub>7</sub> after the interaction with CMAS at 1400°C: for (a) 0.5 h, (b) 2 h, (c) 12 h, (d) 48 h, and (e) 100 h.

Fig. 38 shows SEM micrograph of the cross-section of sintered  $\text{Gd}_2\text{Si}_2\text{O}_7$  with CMAS for (a) 0.5, (b) 2, (c) 12, (d) 48, (e) 100 h at  $1400^\circ\text{C}$ . The thickness of the apatite increases with the heat-treatment time. The width of apatite after 0.5 h heat treatment is narrower than that of apatite after 100 h heat treatment. The sintered  $\text{Gd}_2\text{Si}_2\text{O}_7$  and the reaction layer boundaries appear as vertically grown dense layers. Thus, the penetration of the molten CMAS was confirmed. This reaction layer was identified as  $\text{Ca}_2\text{Gd}_8(\text{SiO}_4)_6\text{O}_2$  formed in the reaction of CMAS with  $\text{Gd}_2\text{Si}_2\text{O}_7$ . vertical (Fig. 33) cracks and horizontal cracks (Fig. 38) were observed in the SEM micrographs of the sintered  $\text{Gd}_2\text{Si}_2\text{O}_7$ . In particular, high-temperature reactions produce apatite with inconsistent coefficients of thermal expansion (CTE). The possibility of cracking and fracturing is caused by the CTE mismatch between apatite and the composite. That is, cooling owing to the difference in CTE of CMAS ( $9.8 \times 10^{-6}/\text{K}^{-1}$ ) [38], induces stress in the sintered  $\delta\text{-Gd}_2\text{Si}_2\text{O}_7$  ( $7.3 \times 10^{-6}/\text{K}^{-1}$ ) [29]. Lee et al. [30] reported that the CTE mismatch is the cause of vertical cracking. Additionally, it was reported that as TGO with  $\text{SiO}_2$  chemistry grows, horizontal cracks coalesce and lead to EBCs fracture. However, after reacting at  $1400^\circ\text{C}$  for 100 h, vertical (Fig. 33) cracks and horizontal cracks (Fig. 38) were found, but no interfacial delamination occurred in this study.

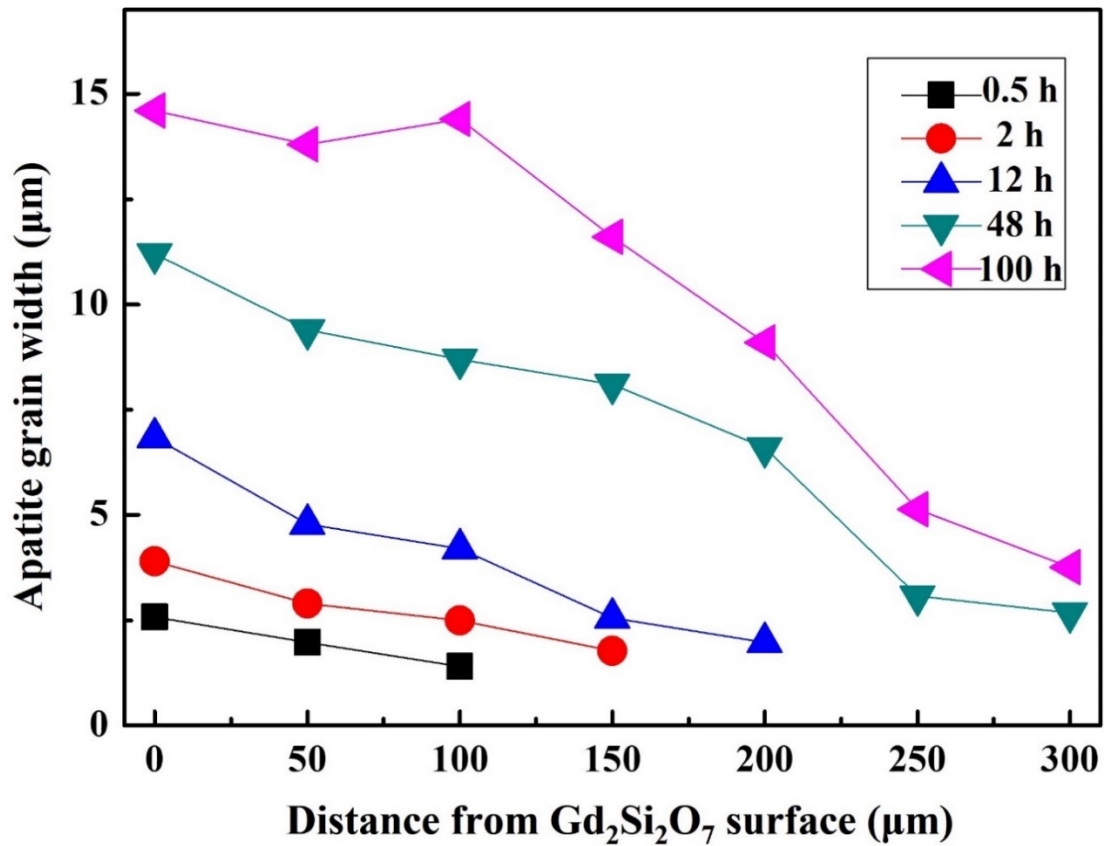


Fig. 39. The average grain size as a function of the distance from the Gd<sub>2</sub>Si<sub>2</sub>O<sub>7</sub> surface for different heat-treatment time.

Fig. 39 shows the correlation between the average width of apatite and the distance from the surface of the sintered Gd<sub>2</sub>Si<sub>2</sub>O<sub>7</sub> for different heat-treatment times. The width of apatite increases to 2.6, 3.9, 6.8, 11.2, and 14.6 µm at 0.5, 2, 12, 48, and 100 h, respectively. As the height increases from the surface of the sintered Gd<sub>2</sub>Si<sub>2</sub>O<sub>7</sub>, the width of the apatite decreases. The increased thickness of apatite prevents the penetration of molten CMAS. However, an excessive increase in the thickness of apatite by molten CMAS leads to the mismatch of CTE with EBC materials and non-uniform mechanical properties [31]. As a result, excessive apatite production adversely affects the EBC lifespan. Therefore, the design of EBC materials based on the formation of an appropriate apatite layer is required. We investigated the effects of time, temperature, Ca concentration, monosilicate (RE<sub>2</sub>SiO<sub>5</sub>) and disilicate (RE<sub>2</sub>Si<sub>2</sub>O<sub>7</sub>) on the high-

temperature corrosion behavior based on previous studies on Gd silicate [14, 15]. In addition, the effects of CMAS and high-temperature corrosion behavior on the cation size of the RE were investigated using through Er (1.004 Å) [24] disilicate and Gd (1.107 Å) [23] disilicate in the present study. In this and our previous studies [12, 14, 15], the parameters affecting the reaction layer were analyzed as follows. The thickness of the reaction layer increased with an increase in the CaO:SiO<sub>2</sub> ratio, cation size, and time. In addition, it was confirmed that the reaction layer was thicker in disilicate than in monosilicate. The results of this study will enable the design of EBC materials based on the formation of appropriate apatite layers of various RE-silicates.

#### 4.4. Conclusions

In this study, high-temperature corrosion behavior of CMAS-coated sintered  $\text{Gd}_2\text{Si}_2\text{O}_7$  was investigated at 1400°C for 0.5, 2, 12, 48, and 100 h to evaluate their suitability as EBC materials. XRD results showed the presence of  $\text{Gd}_2\text{Si}_2\text{O}_7$ ,  $\text{CaSiO}_3$ ,  $\text{CaAl}_2\text{Si}_2\text{O}_8$  and  $\text{Ca}_2\text{MgSi}_2\text{O}_7$  phases from 25 to 1200°C, but at 1300°C a phase change occurred. This indicates that CMAS melted at approximately 1300°C and reacted with  $\text{Gd}_2\text{Si}_2\text{O}_7$  to form an apatite phase. The  $\text{Ca}_2\text{Gd}_8(\text{SiO}_4)_6\text{O}_2$  (apatite) phase formed in the reaction between molten CMAS and  $\text{Gd}_2\text{Si}_2\text{O}_7$ , was analyzed using HT-XRD at 1300°C. As the heat-treatment time increased, the thickness of the reaction layer increased because of the reaction between CMAS and sintered  $\text{Gd}_2\text{Si}_2\text{O}_7$ , and the reaction layer grew vertically at the  $\text{Gd}_2\text{Si}_2\text{O}_7$  interface. With the extension of the reaction time from 0.5 to 100 h, the thickness of the reaction layer increased from approximately 98 to 315  $\mu\text{m}$ . The thickness of the reaction layer was found to increase in the form of a parabola. The width of the apatite increased from 2.6 to 14.6  $\mu\text{m}$  with increasing time from 0.5 to 100 h, respectively. At the same time, the width of the apatite decreased with increasing thickness on the surface of the sintered  $\text{Gd}_2\text{Si}_2\text{O}_7$ . The thickness of the reaction layer increased with an increase in the  $\text{CaO}:\text{SiO}_2$  ratios, cation size, and time. In addition, it was confirmed that the reaction layer was thicker in disilicate than in monosilicate.

## References

- [1] G. Costa, B.J. Harder, N.P. Bansal, B.A. Kowalski, J.L. Stokes, Thermochemistry of calcium rare-earth silicate oxyapatites, *J. Am. Ceram. Soc.* 00 (2019) 1–8.
- [2] J.L. Stokes, B.J. Harder, V.L. Wiesner, D.E. Wolfe, High-temperature thermochemical interactions of molten silicates with  $\text{Yb}_2\text{Si}_2\text{O}_7$  and  $\text{Y}_2\text{Si}_2\text{O}_7$  environmental barrier coating materials, *J. Eur. Ceram. Soc.* 39 (2019) 5059–5067.
- [3] J.L. Stokes, B.J. Harder, V.L. Wiesner, D.E. Wolfe, Effects of crystal structure and cation size on molten silicate reactivity with environmental barrier coating materials, *J. Am. Ceram. Soc.* 103 (2020) 622–634.
- [4] Z. Tian, X. Ren, Y. Lei, L. Zheng, W. Geng, J. Wang, Corrosion of  $\text{RE}_2\text{Si}_2\text{O}_7$  (RE=Y, Yb, and Lu) environmental barrier coating materials by molten calcium-magnesium-alumino-silicate glass at high temperatures, *J. Eur. Ceram. Soc.* 39 (2019) 4245–4254.
- [5] H. Yang, Y. Zhang, Y. Li, X. Huang, Y. Liu, In situ observation of environmental barrier coating against calcium–magnesium–alumina–silicate attack at elevated temperature, *Int. J. Appl. Ceram. Technol.* 18 (2021) 1281–1287.
- [6] P. Mechnich, W. Braue, U. Schulz, High-temperature corrosion of EB-PVD yttria partially stabilized zirconia thermal barrier coatings with an artificial volcanic ash overlay, *J. Am. Ceram. Soc.* 94 (2011) 925–931.
- [7] P. Mechnich, W. Braue, Volcanic ash-induced decomposition of EB-PVD  $\text{Gd}_2\text{Zr}_2\text{O}_7$  thermal barrier coatings to Gd-Oxyapatite, Zircon, and Gd, Fe-Zirconolite, *J. Am. Ceram. Soc.* 96 (2013) 1958–1965.
- [8] B.S. Kim, B.-K. Jang, F.J. Feng, K. Suzuta, H. Tanaka, Y. Matsushita, K.S. Lee, Y.-S. Oh, H.-T. Kim, Corrosion behavior of volcanic ash on sintered mullite for environmental barrier coatings, *Ceram. Int.* 43 (2017) 1880–1886.

- [9] B.-K. Jang, F.J. Feng, K. Suzuta, H. Tanaka, Y. Matsushita, K.S. Lee, S. Ueno, Corrosion behavior of volcanic ash and calcium magnesium aluminosilicate on  $\text{Yb}_2\text{SiO}_5$  environmental barrier coatings, *J. Ceram. Soc. Jpn.* 125[4] (2017) 326–332.
- [10] L.R. Turcer, A.R. Krause, H.F. Garces, L. Zhang, N.P. Padture, Environmental-barrier coating ceramics for resistance against attack by molten calcia-magnesia-aluminosilicate (CMAS) glass: Part II,  $\beta\text{-Yb}_2\text{Si}_2\text{O}_7$  and  $\beta\text{-Sc}_2\text{Si}_2\text{O}_7$ , *J. Eur. Ceram. Soc.* 38 (2018) 3914–3924.
- [11] M. Wolf, D.E. Mack, O. Guillon, R. Vaßen, Resistance of pure and mixed rare earth silicates against calcium-magnesium-aluminosilicate (CMAS): A comparative study, *J. Am. Ceram. Soc.* 103 (2020) 7056–7071.
- [12] S.H. Kim, C.A.J. Fisher, N. Nagashima, Y. Matsushita, B.K. Jang, Reaction between environmental barrier coatings material  $\text{Er}_2\text{Si}_2\text{O}_7$  and a calcia-magnesia-alumina-silica melt, *Ceram. Int.* 48 (2022) 17369–17375.
- [13] K.N. Lee, D.S. Fox, N.P. Bansal, Rare earth silicate environmental barrier coatings for SiC/SiC composites and  $\text{Si}_3\text{N}_4$  ceramics, *J. Eur. Ceram. Soc.* 25 (2005) 1705–1715.
- [14] S.H. Kim, N. Nagashima, Y. Matsushita, B.N. Kim, B.K. Jang, Corrosion behavior of calcium-magnesium-aluminosilicate (CMAS) on sintered  $\text{Gd}_2\text{SiO}_5$  for environmental barrier coatings, *J. Am. Ceram. Soc.* 104 (2021) 3119–3129.
- [15] S.H. Kim, B.N. Kim, N. Nagashima, Y. Matsushita, B.K. Jang, High-temperature corrosion of spark plasma sintered  $\text{Gd}_2\text{SiO}_5$  with volcanic ash for environmental barrier coatings, *J. Eur. Ceram. Soc.* 41 (2021) 3161–3166.
- [16] J. Liu, L. Zhang, Q. Liu, L. Cheng, Y. Wang, Calcium–magnesium–aluminosilicate corrosion behaviors of rare-earth disilicates at  $1400^\circ\text{C}$ , *J. Am. Ceram. Soc.* 33 (2013) 3419–3428.

- [17] H. Zhang, J. Lu, X. Shan, D. Wu, X. Zhao, F. Guo, P. Xiao, A promising molten silicate resistant material: Rare-earth oxy-apatite  $\text{RE}_{9.33}(\text{SiO}_4)_6\text{O}_2$  (RE = Gd, Nd or La), *J. Eur. Ceram. Soc.* 40 (2020) 4101–4110.
- [18] J. Sleeper, A. Garg, V.L. Wiesner, N.P. Bansal, Thermochemical interactions between CMAS and  $\text{Ca}_2\text{Y}_8(\text{SiO}_4)_6\text{O}_2$  apatite environmental barrier coating material, *J. Eur. Ceram. Soc.* 39 (2019) 5380–5390.
- [19] H. Zhao, B.T. Richards, C.G. Levi, H.N.G. Wadley, Molten silicate reactions with plasma sprayed ytterbium silicate coatings, *Surf. Coat. Technol.* 288 (2016) 151–162.
- [20] F. Perrudin, M.H. Vidal-Setif, C. Rio, C. Petitjean, P.J. Panteix, M. Vilasi, Influence of rare earth oxides on kinetics and reaction mechanisms in CMAS silicate melts, *J. Eur. Ceram. Soc.* 39 (2019) 4223–4232.
- [21] V.L. Wiesner, B.J. Harder, N.P. Bansal, High-temperature interactions of desert sand CMAS glass with yttrium disilicate environmental barrier coating material, *Ceram. Int.* 44 (2018) 22738–22743.
- [22] D.L. Poerschke, R.W. Jackson, C.G. Levi, Silicate deposit degradation of engineered coatings in gas turbines: progress toward models and materials solutions, *Annual Rev. Mater. Res.* 47 (2017) 297–330.
- [23] R.D. Shannon, Revised effective ionic radii and systematic studies of interatomic distances in halides and chalcogenides, *Acta Crystallogr. A* 32(5) (1976) 751–767.
- [24] S. Welinski, C.W. Thiel, J. Dajczgewand, A. Ferrier, R.L. Cone, R.M. Macfarlane, T. Chanelière, A. Louchet-Chauvet, P. Goldner, Effects of disorder on optical and electron spin linewidths in  $\text{Er}^{3+}$ ,  $\text{Sc}^{3+}:\text{Y}_2\text{SiO}_5$ , *Opt. Mater.* 63 (2017) 69–75.
- [25] Z. Tian, J. Zhang, L. Zheng, W. Hu, X. Ren, Y. Lei, J. Wang, General trend on the phase stability and corrosion resistance of rare earth monosilicates to molten calcium–magnesium–aluminosilicate at 1300°C, *Corros. Sci.* 148 (2019) 281–292.

- [26] G. Cao, Y.H. Wang, Z.Y. Ding, H.L. Yang, Z.G. Liu, J.H. Ouyang, Y.M. Wang, Y.J. Wang, Tunable corrosion resistance of rare-earth monosilicate to molten calcia-magnesia-aluminosilicate glass by RE-doping strategy, *Corros. Sci.* 202 (2022) 110319.
- [27] T. Wu, S.P. He, Y.J. Liang, Q. Wang, Molecular dynamics simulation of the structure and properties for the CaO-SiO<sub>2</sub> and CaO-Al<sub>2</sub>O<sub>3</sub> systems, *J. Non-Cryst. Solids* 411 (2015) 145–151.
- [28] N.P. Bansal, S.R. Choi, Properties of CMAS glass from desert sand, *Ceram. Int.* 41 (2015) 3901–3909.
- [29] A.J. Fernandez-Carrion, M. Allix, A.I. Becerro, Thermal Expansion of Rare-Earth Pyrosilicates, *J. Am. Ceram. Soc.* 96 [7] (2013) 2298–2305.
- [30] K.N. Lee, D.L. Waters, B.J. Puleo, A. Garg, W.D. Jennings, G. Costa, D.E. Sacksteder, Development of oxide-based High temperature environmental barrier coatings for ceramic matrix composites via the slurry process, *J. Eur. Ceram. Soc.* 41 (2021) 1639–1653.
- [31] L.R. Turcer, N.P. Padture, Towards multifunctional thermal environmental barrier coatings (TEBCs) based on rare-earth pyrosilicate solid-solution ceramics, *Scr. Mater.* 154 (2018) 111–117.

## Chapter 5. High-Temperature Corrosion of $\text{Er}_2\text{Si}_2\text{O}_7$ with CMAS for EBCs

### 5.1. Introduction

Rare earth (RE) silicates ( $\text{RE}_2\text{SiO}_5$  and  $\text{RE}_2\text{Si}_2\text{O}_7$ ) have been proposed as a class of promising environmental barrier coatings (EBCs) materials, and many studies investigating their high-temperature corrosion properties to molten CMAS deposits have been reported in recent years [1–10]. RE silicates exhibit many attractive properties such as low coefficients of thermal expansion (CTE), good chemical stability, and good adhesion to SiC. The disilicates ( $\text{RE}_2\text{Si}_2\text{O}_7$ ) are thermochemically compatible with  $\text{SiO}_2$  and have CTEs more similar to that of SiC than do the monosilicates ( $\text{RE}_2\text{SiO}_5$ ) [11]. The unique stable polymorph in  $\text{RE}_2\text{Si}_2\text{O}_7$  compounds with small  $\text{RE}^{3+}$  cations is  $\beta\text{-RE}_2\text{Si}_2\text{O}_7$ , and  $\beta\text{-RE}_2\text{Si}_2\text{O}_7$  compounds exhibit the closest CTE to that of SiC. In particular,  $\beta\text{-Er}_2\text{Si}_2\text{O}_7$  shows excellent compatibility with SiC, as its CTE of  $3.9 \times 10^{-6} \text{ K}^{-1}$  is close to that of SiC ( $4\text{--}5.5 \times 10^{-6} \text{ K}^{-1}$ ) [12].  $\text{Er}_2\text{Si}_2\text{O}_7$  is also known to be a refractory silicate with a melting temperature of  $\sim 1800^\circ\text{C}$  [13] and excellent high-temperature oxidation resistance. These properties make  $\text{Er}_2\text{Si}_2\text{O}_7$  a promising material for use as an EBCs in harsh environments.

Most previous studies of the high-temperature corrosion behavior of RE disilicates have focused on the reaction between  $(\text{Y},\text{Yb})_2\text{Si}_2\text{O}_7$  compounds and CMAS glasses. Stokes et al. examined the thermochemical behavior of  $\text{Y}_2\text{Si}_2\text{O}_7$  and  $\text{Yb}_2\text{Si}_2\text{O}_7$  using three CMAS compositions [2]. In another study, the thermochemical interactions with different  $\text{CaO}:\text{SiO}_2$  ratios for four RE-disilicates ( $\text{RE}_2\text{Si}_2\text{O}_7$ , RE = Er, Dy, Gd, and Nd) were investigated [3]. In contrast, to the best of our knowledge, the isothermal heat-treatment chemical reaction between  $\text{Er}_2\text{Si}_2\text{O}_7$  and CMAS requires further investigation. In this study, we focus on the high-temperature corrosion behavior of  $\text{Er}_2\text{Si}_2\text{O}_7$  with CMAS as a function of time, and the

comparison of the reaction layer formation according to the ionic radius (Gd (1.107 Å in chapter 4) and Er (1.004 Å)).

## 5.2. Experimental Procedure

### 5.2.1. Sample Preparation

CMAS powder of composition  $33\text{CaO}-9\text{MgO}-13\text{AlO}_{1.5}-45\text{SiO}_2$  mol% was prepared from reagents CaO (Wako Pure Chemical Industry Ltd., Japan), MgO (Wako Pure Chemical Industry Ltd., Japan),  $\text{Al}_2\text{O}_3$  (Kanto Chemical Co., Inc., Japan), and  $\text{SiO}_2$  (Kanto Chemical Co., Inc., Japan). To obtain a homogeneous mixture, ball milling of the reagents in ethanol (EtOH) was performed for 24 h using yttria-stabilized zirconia (YSZ) balls at room temperature. The resulting suspension was dried at room temperature and then heated in an alumina crucible to  $80^\circ\text{C}$  for 10 h. Next, the dried powder was heat-treated at  $1200^\circ\text{C}$  for 24 h and then finely and uniformly crushed in an agate mortar and pestle after furnace cooling to room temperature. Our previous work used with the same  $33\text{CaO}-9\text{MgO}-13\text{AlO}_{1.5}-45\text{SiO}_2$  mol% composition for both  $\text{Yb}_2\text{SiO}_5$  and  $\text{Gd}_2\text{SiO}_5$  at the same temperature of  $1400^\circ\text{C}$  and for the same time (2, 12, and 48 h) to evaluate the high-temperature corrosion behavior [14,15]. In another study, the high-temperature corrosion behaviors of seven rare-earth RE disilicates ( $\text{RE}_2\text{Si}_2\text{O}_7$ , RE = Yb, Lu, La, Gd, Eu, Sc, and Y) were evaluated using the same CMAS composition [16].

$\text{Er}_2\text{O}_3$  (Wako Pure Chemical Industry Ltd., Japan) and  $\text{SiO}_2$  (Wako Pure Chemical Industries Ltd., Japan) powders were used to prepare the  $\text{Er}_2\text{Si}_2\text{O}_7$ . First, ball milling of the two reagents were performed using 5-mm diameter YSZ balls in EtOH for 24 h. Then, the mixed  $\text{Er}_2\text{O}_3$ - $\text{SiO}_2$  powder was dried at  $60^\circ\text{C}$  for 24 h in a drying oven before being heated to  $1400^\circ\text{C}$  for 20 h to form  $\text{Er}_2\text{Si}_2\text{O}_7$ . The  $\text{Er}_2\text{Si}_2\text{O}_7$  powder was then poured into a 30 mm diameter graphite mold and spark-plasma sintered (Dr. Sinter 1050, Sumitomo Coal Mining Co., Ltd., Japan) under a pressure of 60 MPa in a vacuum of  $10^{-2}$  Pa at  $1400^\circ\text{C}$  for 20 min using a heating rate of  $10^\circ/\text{min}$ .

The sintered  $\text{Er}_2\text{Si}_2\text{O}_7$  pellets were cut into  $10\text{ mm} \times 5\text{ mm} \times \sim 3\text{ mm}$  bars using a diamond saw. After cutting, the samples were ultrasonically cleaned with acetone and EtOH for 5 min,

and then polished using 9, 3, and 1  $\mu\text{m}$  diamond suspensions in succession. Specimens for the corrosion experiments were prepared by attaching CMAS paste (prepared by ultrasonic dispersion in EtOH) to the surface of each  $\text{Er}_2\text{Si}_2\text{O}_7$  bar with a loading of  $40\text{ mg/cm}^2$ . Individual specimens were exposed to  $1400^\circ\text{C}$  at a heating rate of  $5^\circ\text{C/min}$  for 2, 12, or 48 h, before being furnace-cooled to room temperature. After heat-treatment, the specimens were cut into  $5 \times 5\text{ mm}^2$  sections for cross-sectional analysis. The cross sections were polished successively using 9, 3, and 1  $\mu\text{m}$  diamond suspensions and then cleaned ultrasonically with acetone and EtOH for 5 min.

### 5.2.2. High-Temperature Corrosion Behavior

The changes in particle morphology during the high-temperature corrosion of  $\text{Er}_2\text{Si}_2\text{O}_7$  were observed using scanning electron microscopy (SEM) with an S-4300 SEM microscope (Hitachi Ltd., Japan). A beam voltage of 15 kV and working distance of 15 mm were used for energy-dispersive X-ray spectroscopy (EDS) measurements to determine the element ratios (compositions) in different regions of the cross-sectioned specimens. In addition, the melting temperature was determined using differential scanning calorimetry (DSC) on with a DSC6300 calorimeter (Hitachi Ltd., Japan). DSC measurements were performed on a mixed powder of CMAS/ $\text{Er}_2\text{Si}_2\text{O}_7$  (1:1 wt. %) up to and exceeding the reaction temperature in air to a maximum temperature of  $1300^\circ\text{C}$ . The mixed powder was stirred in EtOH under flowing Ar gas. High-temperature X-ray diffraction (HT-XRD) was performed with Cu  $K\alpha_1$  radiation ( $\lambda = 1.54056\text{ \AA}$ ) in air using a Smart Lab (Rigaku Co., Japan) diffractometer to examine the phase evolution of the powder from  $25^\circ\text{C}$  up to  $1400^\circ\text{C}$  at a heating rate of  $10^\circ\text{C/min}$ . Measurements were taken over a  $2\theta$  range of  $20\text{--}60^\circ$ , with a scan step of  $0.02^\circ/\text{min}$  and a scan speed of  $1^\circ/\text{min}$ .

### 5.3. Results and Discussion

#### 5.3.1. Characterization of CMAS

Fig. 40 shows dynamic differential scanning calorimetry (DDSC) measurements taken of (a) CMAS powder and (b) mixed CMAS/ $\text{Er}_2\text{Si}_2\text{O}_7$  (1:1 wt.%) powder.

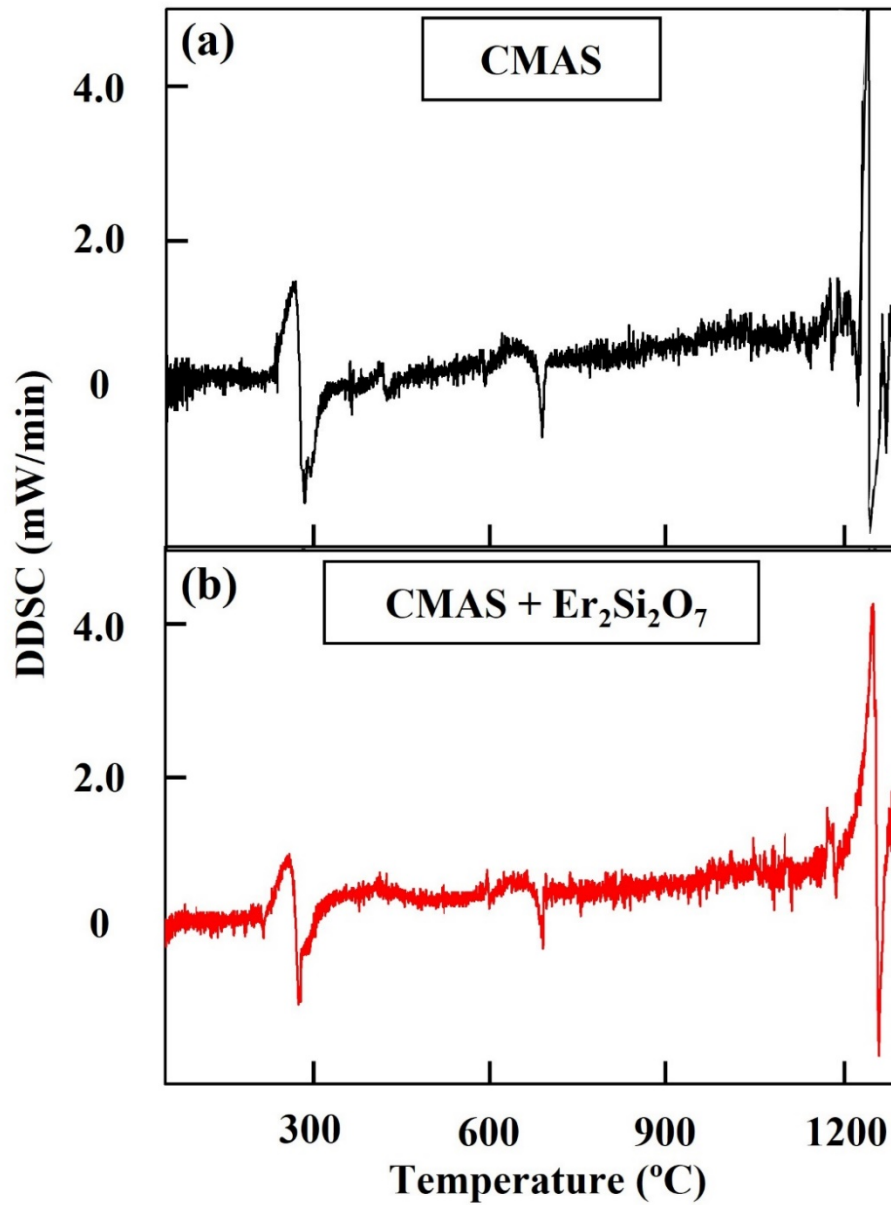


Fig. 40. DDSC results of (a) CMAS powder and (b) mixed CMAS/ $\text{Er}_2\text{Si}_2\text{O}_7$  (1:1 wt.%) powder.

DDSC corresponds to the differential of DSC and is designed to simplify analysis of the variations in DSC. That is, the DDSC takes the maximum value at the inflection point that conforms to the melting point initiation temperature in the DSC. In general, chemical reactions and phase transitions occur at temperatures at which endothermic and exothermic reactions occur. The peak appearing about 300°C is the peak of the solid-solid transition ( $T_{\text{trans}}$ ) in Fig. 40. It has been reported that the  $T_{\text{trans}}$  occurs before the glass transition ( $T_g$ ) in a typical DSC curve [17,18]. Therefore, it shows a change consistent with the  $T_{\text{trans}}$  at approximately 300°C.  $T_g$  occurred at the inflection point in the curve at approximately 700°C, which is in good agreement with the  $T_g$  values for CMAS reported in the literature, approximately 700°C depending on the composition [19]. A sharp peak for CMAS powder was observed at 1243°C in Fig. 40 (a) [15]. The sharp peak at approximately 1258°C indicates the melting temperature ( $T_m$ ), and likely corresponds to the maximum of the reaction between CMAS and  $\text{Er}_2\text{Si}_2\text{O}_7$  in Fig. 40 (b). This  $T_m$  value was used to select the heat-treatment temperatures used for corrosion tests of CMAS-coated  $\text{Er}_2\text{Si}_2\text{O}_7$  [20–22].

### 5.3.2. High-Temperature Corrosion Behavior

Fig. 41 shows the SEM image of the (a) surface and (b) cross-sectional of sintered  $\text{Er}_2\text{Si}_2\text{O}_7$  and (c) the XRD patterns of  $\text{Er}_2\text{Si}_2\text{O}_7$  powder. The average grain size of the sintered  $\text{Er}_2\text{Si}_2\text{O}_7$  before the CMAS reaction was  $\sim 2.1 \mu\text{m}$ . In addition, the porosity was measured to be 3.6%, and the relative density was 96.4%, as shown in Figs.41 (a), (b). Fig. 41 (c) shows the results of the synthesis of the  $\text{Er}_2\text{O}_3\text{-SiO}_2$  powder, and the  $\text{Er}_2\text{Si}_2\text{O}_7$  peak was analyzed at room temperature. This confirms that the  $\text{Er}_2\text{O}_3\text{-SiO}_2$  powder was completely synthesized to  $\text{Er}_2\text{Si}_2\text{O}_7$  powder before the CMAS high-temperature reaction.

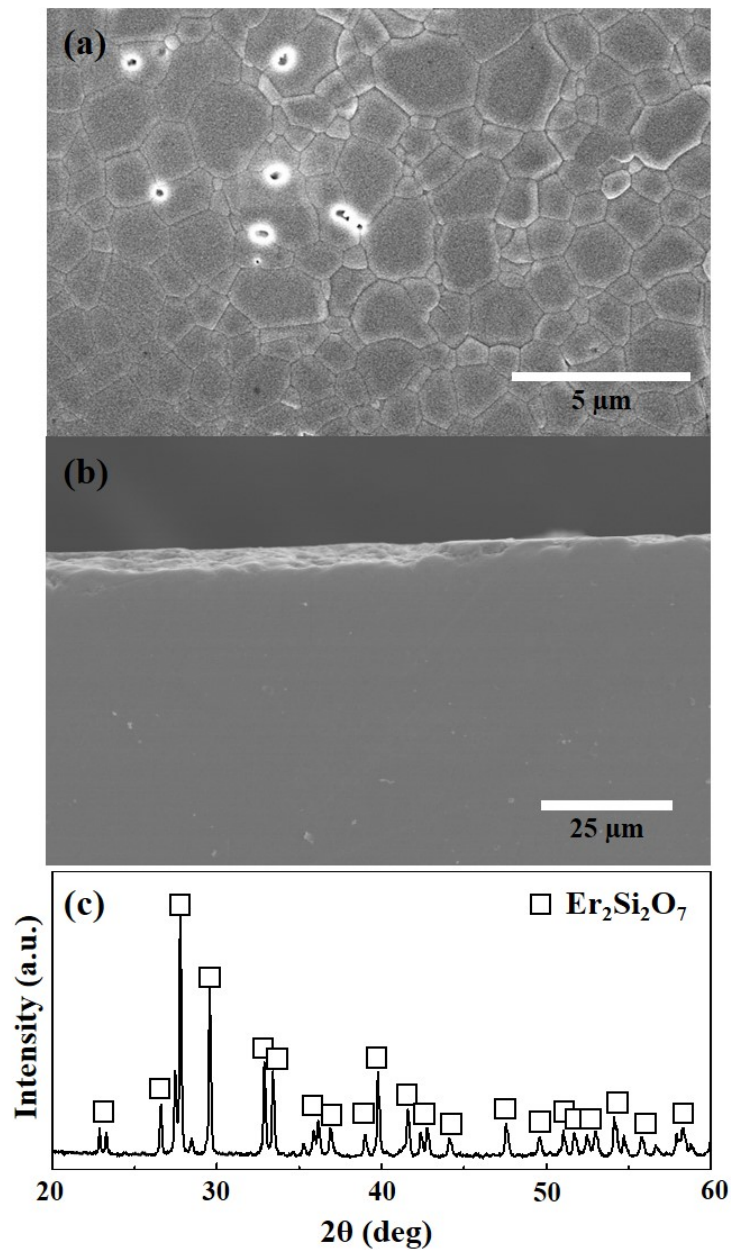


Fig. 41. Results of SEM images of (a) surface and (b) cross-section of sintered  $\text{Er}_2\text{Si}_2\text{O}_7$ , (c) XRD patterns on  $\text{Er}_2\text{Si}_2\text{O}_7$  powder.

Fig. 42 shows the HT-XRD patterns of the mixed CMAS/ $\text{Er}_2\text{Si}_2\text{O}_7$  powder at different temperatures. Because the  $T_m$  of the powder was determined to be approximately  $1258^\circ\text{C}$  (Fig. 40), HT-XRD measurements were performed at temperatures close to this value up to a maximum value of  $1400^\circ\text{C}$ , as well as at room temperature before and after heat treatment. Fig. 42 (a) shows the HT-XRD spectrum of the mixed CMAS/ $\text{Er}_2\text{Si}_2\text{O}_7$  powder measured at  $25^\circ\text{C}$

before high-temperature heat treatment. Peaks corresponding to  $\beta$ - $\text{Er}_2\text{Si}_2\text{O}_7$ ,  $\text{CaSiO}_3$ ,  $\text{Ca}_2\text{MgSi}_2\text{O}_7$ , and  $\text{CaAl}_2\text{Si}_2\text{O}_8$  were also identified.  $\beta$ - $\text{Er}_2\text{Si}_2\text{O}_7$  has the cell parameters  $a = 6.8496 \text{ \AA}$ ,  $b = 8.9403 \text{ \AA}$ ,  $c = 4.7214 \text{ \AA}$ ,  $\alpha = 90^\circ$ ,  $\beta = 101.728^\circ$ , and  $\gamma = 90^\circ$  [12]. Figs. 42 (b)–(c) show that no changes in the phase assemblage occurred up to  $1200^\circ\text{C}$ .

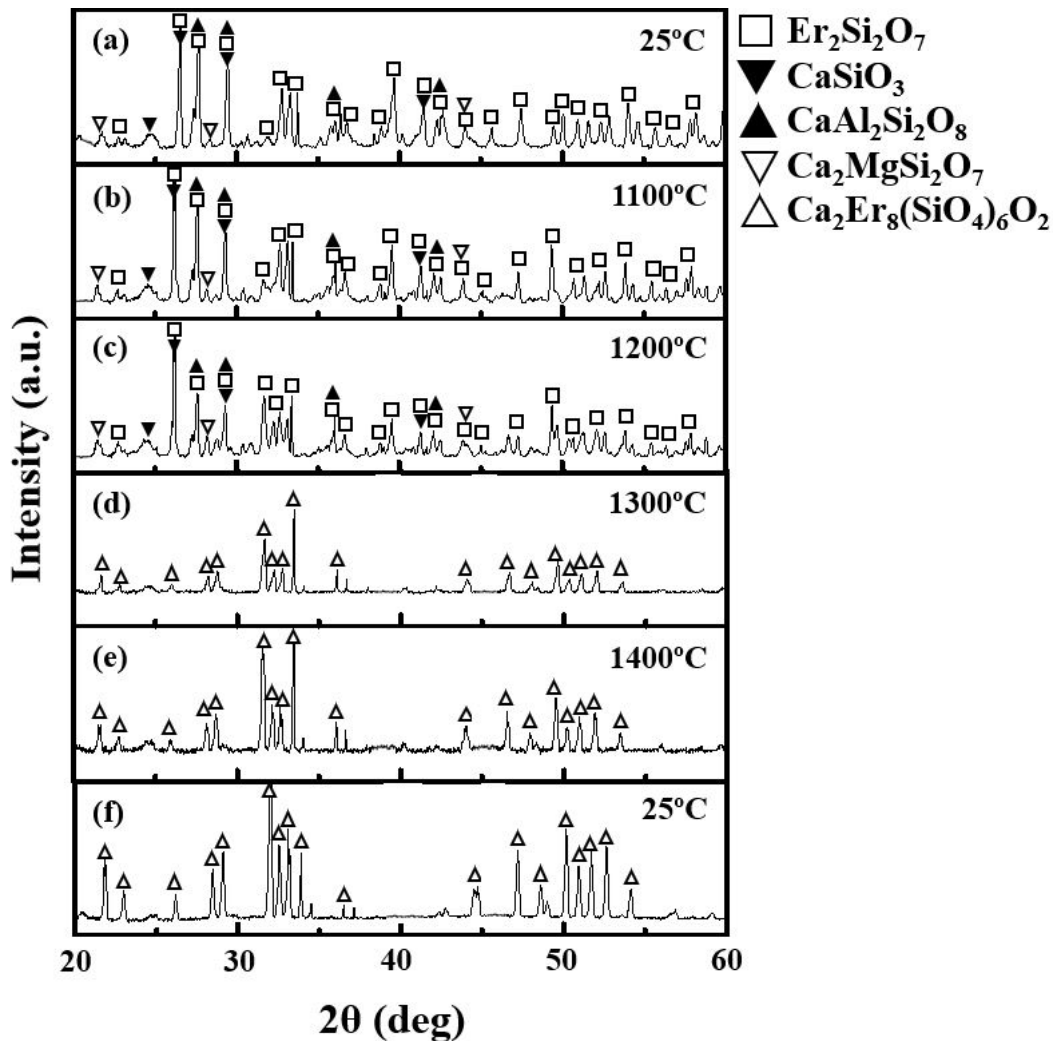


Fig. 42. HT-XRD spectra of mixed CMAS/ $\text{Er}_2\text{Si}_2\text{O}_7$  powders (1:1 wt.%) at different temperatures: (a)  $25^\circ\text{C}$  before heat-treatment, (b)  $1100^\circ\text{C}$ , (c)  $1200^\circ\text{C}$ , (d)  $1300^\circ\text{C}$ , (e)  $1400^\circ\text{C}$ , and (f) after cooling back to  $25^\circ\text{C}$ .

However, Fig. 42 (d) shows that CMAS had reacted with  $\text{Er}_2\text{Si}_2\text{O}_7$  at  $1300^\circ\text{C}$ , with peaks corresponding to  $\text{Ca}_2\text{Er}_8(\text{SiO}_4)_6\text{O}_2$  appearing in the spectra at 1300 and  $1400^\circ\text{C}$  (Figs. 42 (d)

and (e)). The XRD pattern of  $\text{Ca}_2\text{Er}_8(\text{SiO}_4)_6\text{O}_2$  reported in another study is confirmed to be identical to the  $\text{Ca}_2\text{Er}_8(\text{SiO}_4)_6\text{O}_2$  pattern in Figs. 42 (d), (e) and (f). Furthermore,  $\text{Ca}_2\text{Er}_8(\text{SiO}_4)_6\text{O}_2$  having cell parameters  $a = b = 9.3291 \text{ \AA}$ ,  $c = 6.7575 \text{ \AA}$ ,  $\alpha = \beta = 90^\circ$ , and  $\gamma = 120^\circ$ . The peaks of the major components of the CMAS powder, viz.  $\text{CaSiO}_3$ ,  $\text{Ca}_2\text{MgSi}_2\text{O}_7$ , and  $\text{CaAl}_2\text{Si}_2\text{O}_8$ , also disappeared at  $1300^\circ\text{C}$ , even after cooling, peaks from the  $\text{Ca}_2\text{Er}_8(\text{SiO}_4)_6\text{O}_2$  phase remained, as shown in Fig. 42 (f).

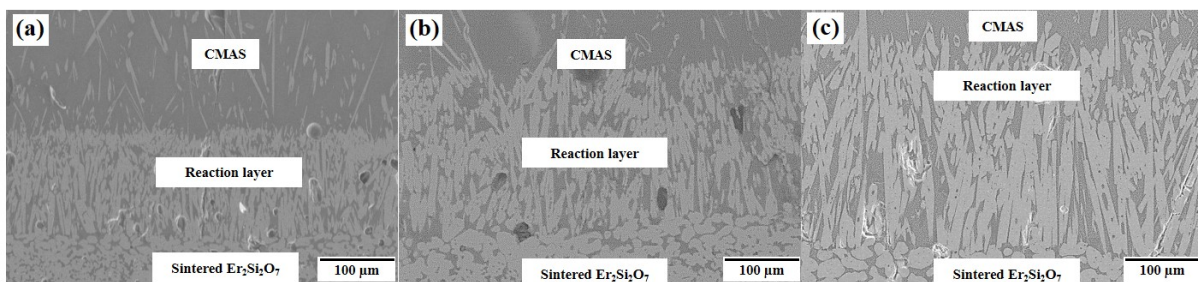


Fig. 43. Cross-sectional SEM images of sintered  $\text{Er}_2\text{Si}_2\text{O}_7$  after exposure to CMAS at  $1400^\circ\text{C}$  for heat-treatment times of (a) 2 h, (b) 12 h, and (c) 48 h.

Fig. 43 shows cross-sectional SEM images of CMAS-coated  $\text{Er}_2\text{Si}_2\text{O}_7$  after the heat treatment at  $1400^\circ\text{C}$  for (a) 2, (b) 12, and (c) 48 h. Reaction layers can be seen to have formed between the CMAS and  $\text{Er}_2\text{Si}_2\text{O}_7$  in each case. The thickness of the reaction layer was observed to increase with heat-treatment time, Apatite particles grew with an elongated, shard-like morphology from the surface of each sintered  $\text{Er}_2\text{Si}_2\text{O}_7$  into the molten CMAS layer, their number and lengths and widths increasing with increasing exposure time. A plot of the average thickness of the reaction layer with increasing time is presented in Fig. 44. These results are similar to those reported for  $\text{Yb}_2\text{Si}_2\text{O}_7$  exposed to molten CMAS for 250 h, that is, a  $\text{Ca}_2\text{Yb}_8(\text{SiO}_4)_6\text{O}_2$  grew between the two phases with elongated and fragmentary particles [11]. We previously also reported that the thickness of the reaction layer between  $\text{Yb}_2\text{SiO}_5$  and CMAS increases with time in a similar manner [14]. X. Zhong [23] investigated, ytterbium

silicate coatings with different contents of  $\text{Yb}_2\text{O}_3$ ,  $\text{Yb}_2\text{SiO}_5$ , and  $\text{Yb}_2\text{Si}_2\text{O}_7$  were investigated for corrosion resistance to CMAS melting at  $1400^\circ\text{C}$  for 25, 50, and 100 h. The CMAS composition was performed with  $33\text{CaO}-10\text{MgO}-13\text{AlO}_{1.5}-44\text{SiO}_2$  similar to that of the present study. It was reported that this reaction consumes CaO and produces approximately the same amount of  $\text{SiO}_2$ , and the dissolution-precipitation process continues until CaO is depleted in the CMAS melt. In particular, a continuous increase in the reaction layer was confirmed as the time increased up to 100 h. In the present study, the reaction time was only 48 h, which was sufficient to show that the apatite particles grew rapidly. Additionally, we plan to evaluate the high-temperature corrosion behavior by performing with an exposure time of 100 h or more.

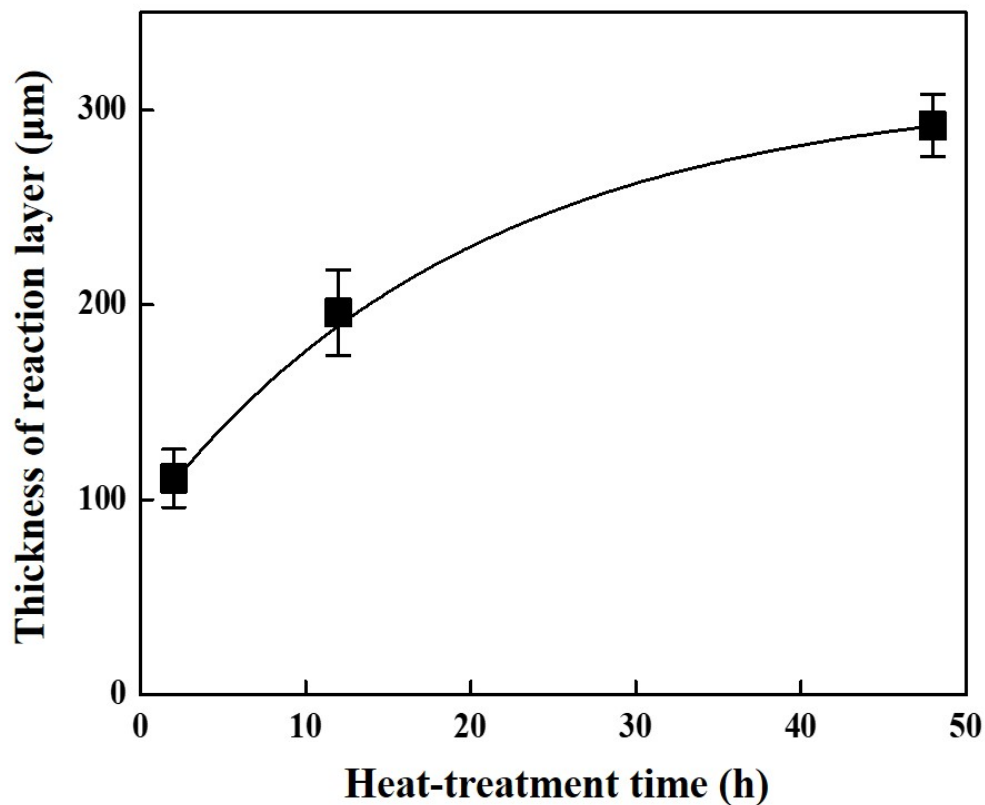


Fig. 44. Average thickness of the reaction layer between CMAS and  $\text{Er}_2\text{Si}_2\text{O}_7$  at  $1400^\circ\text{C}$  as a function of heat-treatment time.

Fig. 45 shows the EDS maps of the cross-sections of CMAS-coated  $\text{Er}_2\text{Si}_2\text{O}_7$  after heat treatment for 48 h. Measurements were taken from regions A (CMAS), B (reaction layer), and C (sintered  $\text{Er}_2\text{Si}_2\text{O}_7$ ). Ca, Si, and Er were detected in the reaction layer, consistent with the HT-XRD results in Fig. 42, which show the formation of  $\text{Ca}_2\text{Er}_8(\text{SiO}_4)_6\text{O}_2$ . Si, O, and Er, but not Ca, were detected in region C.

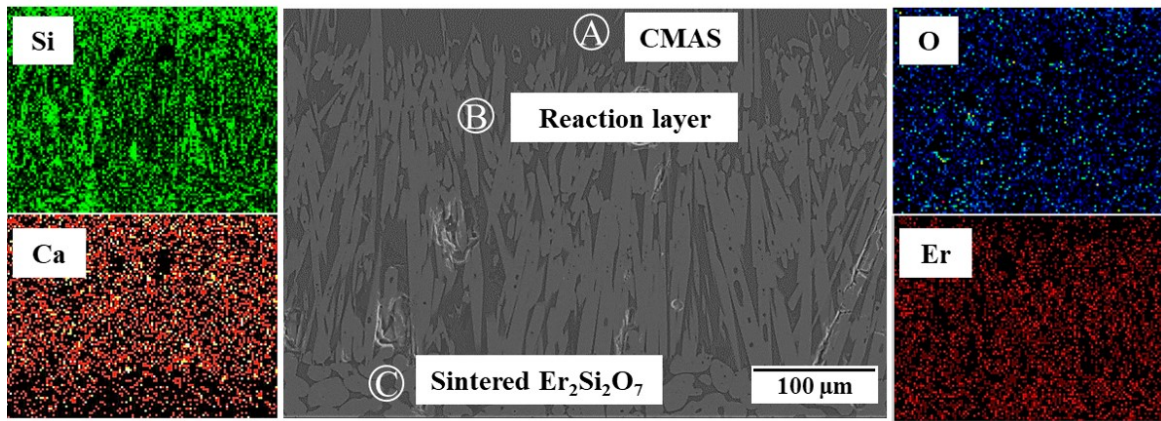


Fig. 45. EDS maps of elements Si, Ca, O, and Er in sintered  $\text{Er}_2\text{Si}_2\text{O}_7$  after contact with CMAS at  $1400^\circ\text{C}$  for 48 h: Regions A, B, and C correspond to CMAS, reaction product, and  $\text{Er}_2\text{Si}_2\text{O}_7$  regions, respectively.

Table 10. Average concentrations of chemical elements (at.%) in regions A, B, and C of a  $\beta$ - $\text{Er}_2\text{Si}_2\text{O}_7$  compact coated with molten CMAS after a heat treatment at  $1400^\circ\text{C}$  for 48 h as determined from the EDS maps in Fig. 45.

Elements	Er	Mg	Al	Si	Ca	O
Region A	2.37	1.81	4.57	22.99	4.26	64.00
Region B	15.36	0	0	18.42	4.08	62.14
Region C	17.76	0	0	17.93	0	64.31

Table 10 lists the quantitative results of the EDS point analysis for the three regions in Fig. 45. These results show that Ca is the main CMAS component contributing to apatite crystallization, with Mg and Al confined to the CMAS layer. A small amount of Er was detected in the CMAS glass, similar to that was observed in the case of apatite  $\text{Ca}_2\text{Y}_8(\text{SiO}_4)_6\text{O}_2$  in contact with CMAS between 1200 and 1500°C, in which a small amount of yttrium was detected in the melt [24]. We thus conclude that the apatite phase is composed of  $\text{Ca}_2\text{Er}_8(\text{SiO}_4)_6\text{O}_2$ , formed by a dissolution-precipitation process on the CMAS side of the interface between  $\text{Er}_2\text{Si}_2\text{O}_7$  and CMAS when heated to temperatures higher than 1258°C. Summers et al. [25], investigated the high-temperature corrosion behavior of yttrium disilicate ( $\text{Y}_2\text{Si}_2\text{O}_7$ ) in contact with CMAS by varying the Ca:Si ratio. Apatite was formed at Ca:Si ratios of 0.72 and 0.33, but not at 0.14. They concluded that the minimum Ca:Si ratio for forming the apatite phase at 1400°C was  $0.27 \pm 0.02$  [25]. Stokes et al. [3], investigated the interaction of  $\text{Er}_2\text{Si}_2\text{O}_7$  with CMAS melts at various CaO:SiO<sub>2</sub> ratios at 1400°C for 1 h. As a result, as the CaO content decreased, apatite formation decreased. In this study, we focused on the effect of isothermal treatment at 1400°C on apatite formation. Similarly, in our earlier examination of the high-temperature corrosion behavior of  $\text{Yb}_2\text{SiO}_5$  as a function of heat-treatment time, we used a CMAS melt with a Ca:Si ratio of 0.73 [14]. We found that the thickness of the  $\text{Ca}_2\text{Yb}_8(\text{SiO}_4)_6\text{O}_2$  layer grew to 12.2, 41.5, and 121.7 μm after 2, 12, and 48 h, respectively, at 1400°C. In this study we chose to use the same Ca:Si ratio of 0.73 in the expectation that it would also be sufficient to form apatite in contact with Er disilicate. Our SEM observations show that the reaction layer grew more than twice as fast as it did in the case of  $\text{Yb}_2\text{SiO}_5$ .

Several studies have examined the reaction of RE silicates with CMAS as a function of the RE ionic radius. For example, in the case of  $\beta\text{-Yb}_2\text{Si}_2\text{O}_7$ , a small amount of apatite  $\text{Ca}_2\text{Yb}_8(\text{SiO}_4)_6\text{O}_2$  formed in contact with CMAS at 1500°C as a product of reaction-crystallization, unlike in the case of  $\beta\text{-Sc}_2\text{Si}_2\text{O}_7$ , where no apatite was detected [10]. It has been

suggested that  $\text{Yb}^{3+}$  (0.985 Å) has a stronger affinity for Ca than  $\text{Sc}^{3+}$  (0.870 Å) because of its larger ionic radius, which provides a stronger driving force for the crystallization of apatite from the melt [10].  $\text{Er}^{3+}$  (1.004 Å) [36] is larger than  $\text{Yb}^{3+}$  (0.985 Å) [10], suggesting that Er forms apatite more readily than does Yb.

Fig. 46 shows a plot of the average element concentrations (at. %) of molten CMAS near the reaction zone after heat treatment for 2, 12, and 48 h. As the reaction time increased, the Si content increased slightly, whereas the Mg, Er, and Al concentrations remained constant. In contrast, Ca content decreased from 6.54 to 4.26 at.% with increasing reaction time.

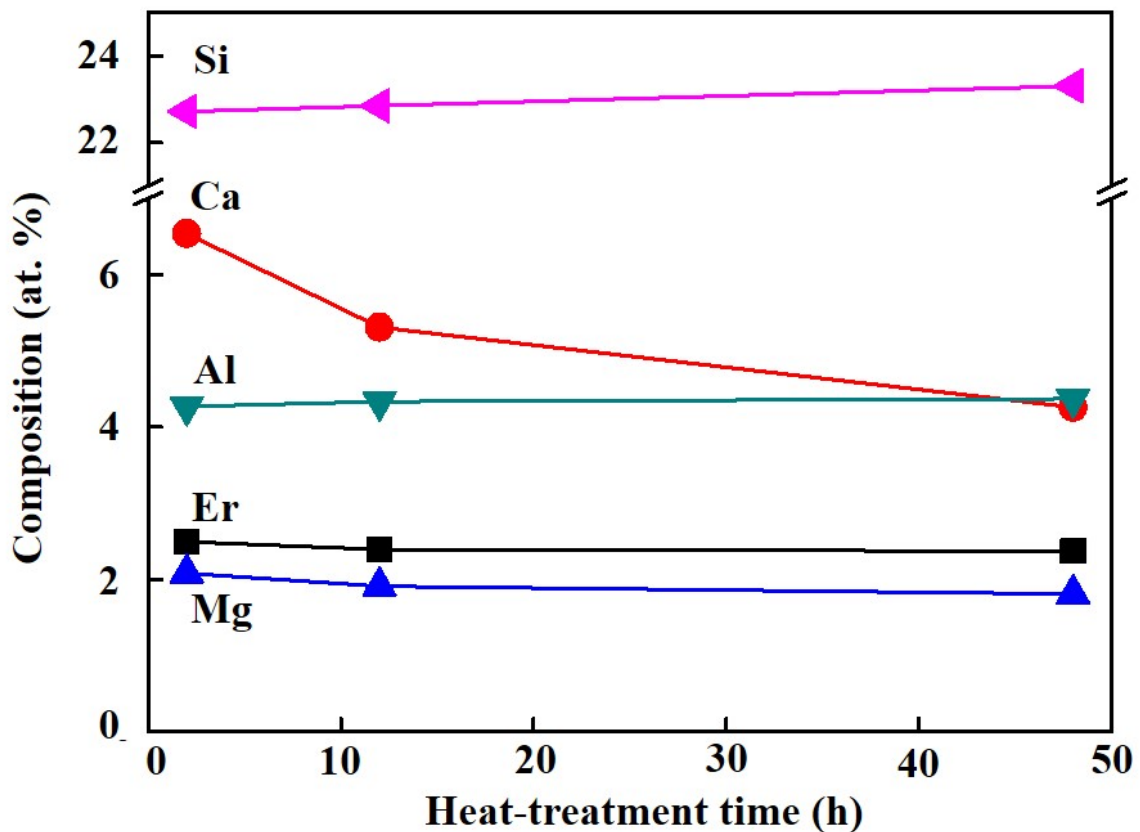


Fig. 46. Average concentrations (at.%) of elements in molten CMAS near the reaction layer as a function of heat-treatment time.

This indicates that the Ca component of molten CMAS is gradually depleted as the apatite phase crystallizes and grows, consistent with a previous study reporting that CaO is consumed from the melt during the formation of apatite [8]. H. Zhao [11] reported, the reaction between  $\text{Yb}_2\text{Si}_2\text{O}_7$  and CMAS at  $1300^\circ\text{C}$  for 200 h. The thickness of the apatite layer converted to approximately parabolic dynamics after 5–10 h of CMAS exposure. It has been reported that the Ca concentration of the CMAS melt decreases with increasing reaction time and is accompanied by an increase in the Si concentration. In addition, the initial rapid Ca loss coincided with the time required to form a continuous apatite layer. The present study suggests a change in elemental concentration with time, however, the effect of temperature also influences the change in concentration. In a study by V.L. Wiesner et al. [27], pellets made of 80 wt%  $\text{Y}_2\text{Si}_2\text{O}_7$  powder and 20 wt% CMAS glass powder were heat-treated in air at 1200, 1300, 1400, and  $1500^\circ\text{C}$  for 20 h. In particular, these researchers commonly reported a stable state at approximately  $218\ \mu\text{m}$  after 20 h exposure at 1400 and  $1500^\circ\text{C}$ . The inability of the reaction layer to continue increasing in thickness at temperatures above  $1400^\circ\text{C}$  is likely a result of calcium depletion in the melt, meaning that an equilibrium CaO concentration has been reached.

Fig. 47 (a) shows a high-magnification SEM image of the interface between sintered  $\text{Er}_2\text{Si}_2\text{O}_7$  and the reaction layer after exposure to CMAS at  $1400^\circ\text{C}$  for 48 h. Fig. 47 (a) shows the results of EDS line analysis along the yellow line. Si and Er were detected in the grains in region A, which is consistent with them the presence of  $\text{Er}_2\text{Si}_2\text{O}_7$ . However, the strong Ca and Si peaks detected at  $9\ \mu\text{m}$ , suggest that molten CMAS penetrated the pores of the sintered  $\text{Er}_2\text{Si}_2\text{O}_7$ . Si, Er, and Ca were detected in the grains in region B, which is consistent with the composition of  $\text{Ca}_2\text{Er}_8(\text{SiO}_4)_6\text{O}_2$ .

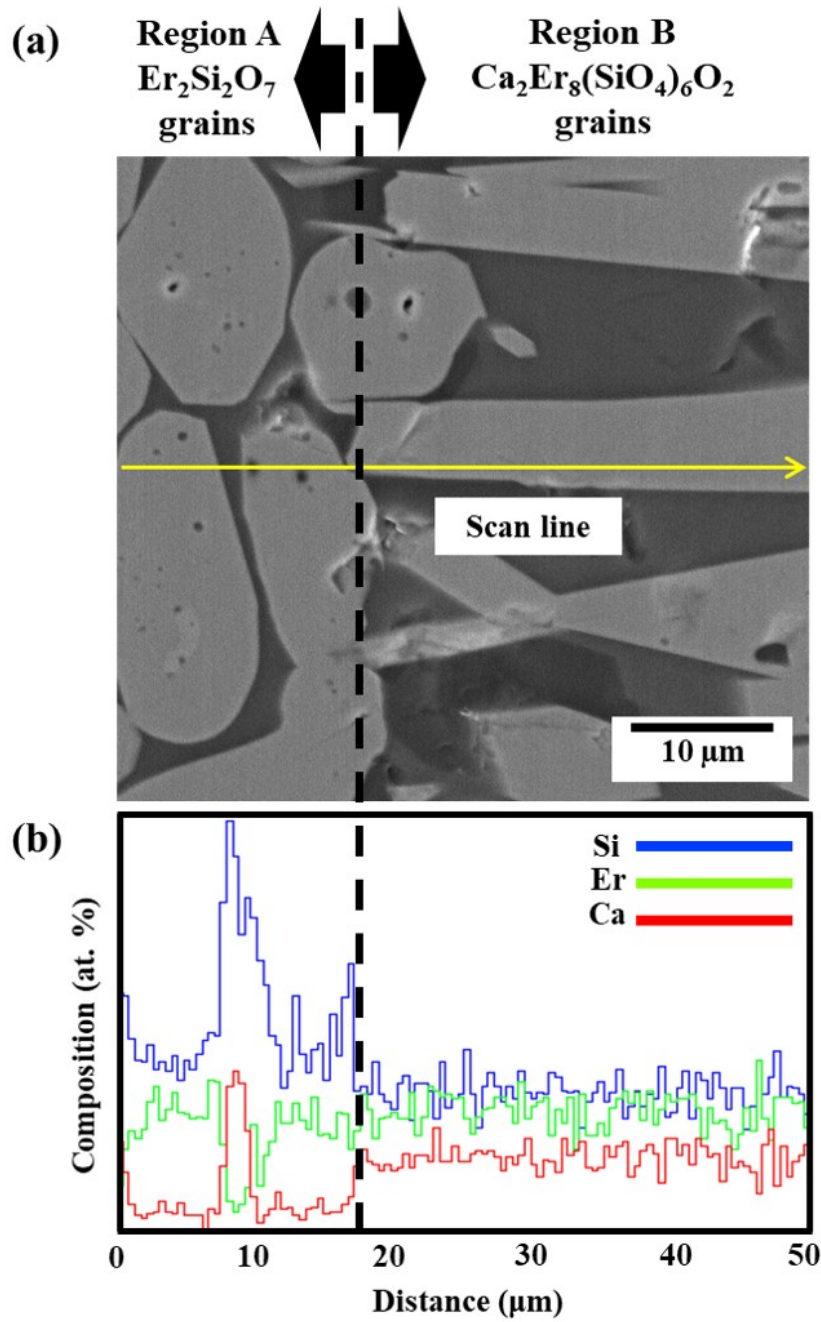
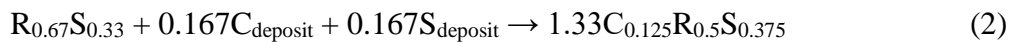
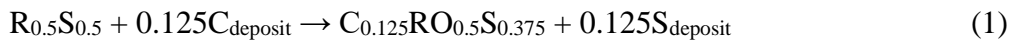


Fig. 47. (a) High-magnification SEM image of sintered  $\text{Er}_2\text{Si}_2\text{O}_7$  after exposure to CMAS at  $1400^\circ\text{C}$  for 48 h showing  $\text{Er}_2\text{Si}_2\text{O}_7$  grains and  $\text{Ca}_2\text{Er}_8(\text{SiO}_4)_6\text{O}_2$  grains; (b) EDS line measurements taken along the yellow scan line in (a).

Sleeper et al. [24], reported that the formation of the apatite interfacial layer at high temperatures may not prevent the penetration of molten CMAS. In their study of

$\text{Ca}_2\text{Y}_8(\text{SiO}_4)_6\text{O}_2$  apatite in contact with CMAS, it was observed that molten CMAS penetrates into the pores and grain boundaries of the sintered compact more rapidly at  $1500^\circ\text{C}$  than at  $1400^\circ\text{C}$  owing to the decrease in viscosity at the lower temperatures. It has been reported that apatite appears to be an effective EBCs material to prevent the penetration of CMAS at temperatures up to  $1200^\circ\text{C}$ , but at higher temperatures, it may not [24]. We also recently showed that low-viscosity CMAS rapidly penetrates  $\text{Gd}_2\text{SiO}_5$  compacts, resulting in the rapid formation of  $\text{Ca}_2\text{Gd}_8(\text{SiO}_4)_6\text{O}_2$  apatite [15]. In another study, Summers et al. investigated the factors affecting the reaction layer between  $\text{Y}_2\text{Si}_2\text{O}_7$  and CMAS melts with different compositions at various temperatures. The recession depth was found to increase faster with increasing time at  $1400^\circ\text{C}$  faster than at  $1300^\circ\text{C}$  [25].

In our recent study of the high-temperature corrosion behavior of  $\text{Gd}_2\text{SiO}_5$  using the same CMAS composition and heating schedule as for  $\text{Er}_2\text{Si}_2\text{O}_7$ , the average thickness of the reaction layer was  $120\ \mu\text{m}$  after 48 h, but for  $\text{Er}_2\text{Si}_2\text{O}_7$  the average thickness was  $292\ \mu\text{m}$  after the same amount of time. This result is consistent with reports that  $\text{RE}_2\text{Si}_2\text{O}_7$  exhibit faster recession when in contact with CMAS than does  $\text{RE}_2\text{SiO}_5$  [28]. Using short-hand chemical notation, Poerschke et al. described the chemical degradation processes of  $\text{RE}_2\text{Si}_2\text{O}_7$  and  $\text{RE}_2\text{SiO}_5$  in contact with CaO in CMAS as follows ( $\text{R} = \text{REO}_{1.5}$ ,  $\text{S} = \text{SiO}_2$ , and  $\text{C} = \text{CaO}$ ) [8]:



According to Equation (1),  $\text{RE}_2\text{Si}_2\text{O}_7$  reacts with CaO in the melt to form the apatite phase, releasing  $\text{SiO}_2$ , whereas Equation (2) indicates that  $\text{RE}_2\text{SiO}_5$  reacts with both CaO and  $\text{SiO}_2$ , with only the apatite phase being produced. This is consistent with reports that the depletion of  $\text{Ca}^{2+}$  proceeds more quickly and the volume of the melt decreases in the case of  $\text{RE}_2\text{SiO}_5$  compounds [8].

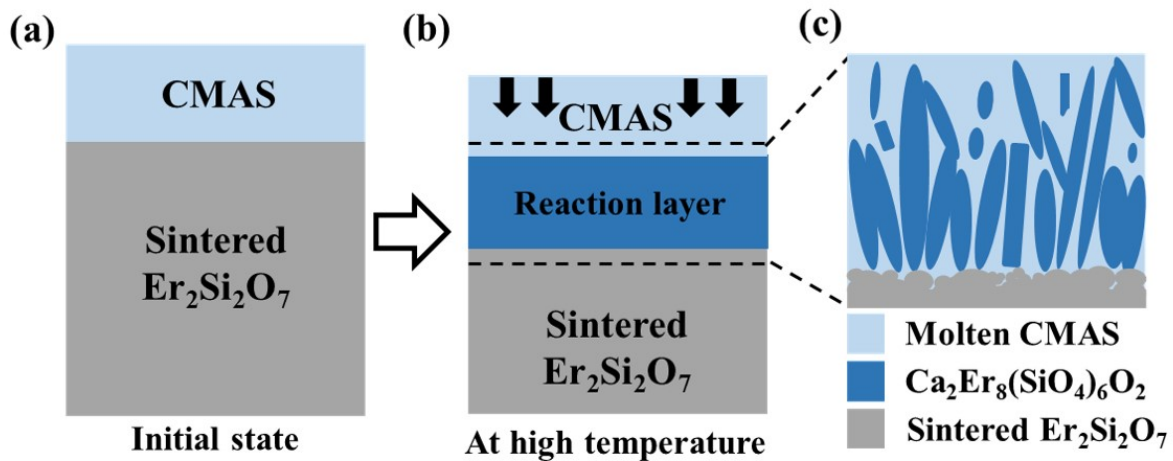


Fig. 48. Schematic illustration of the formation of the reaction layer on sintered  $\text{Er}_2\text{Si}_2\text{O}_7$  in contact with CMAS: (a) initial state, (b) formation of reaction layer between CMAS and  $\text{Er}_2\text{Si}_2\text{O}_7$  at high temperature, and (c) a magnified view of the reaction layer showing the particle morphologies.

Fig. 48 shows a schematic of the interface between  $\text{Er}_2\text{Si}_2\text{O}_7$  and CMAS before (a) and after (b) heat treatment. A magnified view of the reaction layer containing  $\text{Ca}_2\text{Er}_8(\text{SiO}_4)_6\text{O}_2$  is shown in Fig. 48 (c). The  $\text{Ca}_2\text{Er}_8(\text{SiO}_4)_6\text{O}_2$  crystallites were shard-like and oriented more-or-less perpendicular to the  $\text{Er}_2\text{Si}_2\text{O}_7$  surface. The  $\text{Ca}_2\text{Er}_8(\text{SiO}_4)_6\text{O}_2$  grains grew in length and width with increasing time at  $1400^\circ\text{C}$ . A comparison with results from similar measurements of other  $\text{RE}_2\text{Si}_2\text{O}_7$  compounds suggests that the  $\text{Ca}_2\text{RE}_8(\text{SiO}_4)_6\text{O}_2$  phase forms more readily with larger RE cations than with smaller RE cations, at a higher Ca content in the CMAS melt, and at higher temperature (which lowers the viscosity).

J.L. Stokes et al.[3] reported the effect of cationic radius on apatite formation. Because all of these RE cations are expected to be trivalent, theoretically at constant CaO content, equivalent stoichiometries of Ca-RE apatite should be formed in the case of equivalent substitution of  $\text{RE}^{3+}$  between the three.  $\text{Ca}^{2+}$ ,  $\text{Dy}^{3+}$ ,  $\text{Gd}^{3+}$  and  $\text{Nd}^{3+}$  have approximately cation radii of  $1.18 \text{ \AA}$ ,  $1.083 \text{ \AA}$ ,  $1.107 \text{ \AA}$  and  $1.163 \text{ \AA}$ , respectively.  $\text{Ca}^{2+}$  is  $\sim 9\%$  greater than  $\text{Dy}^{3+}$ .

Since  $\text{Dy}^{3+}$  has the largest size difference from  $\text{Ca}^{2+}$ , the same positioning of  $\text{Ca}^{2+}$  and  $\text{Dy}^{3+}$  can lead to more strain in the structure than when  $\text{Dy}^{3+}$  is at more positions than  $\text{Ca}^{2+}$ . In the latter case, strain can be reduced if there are more cations of the same size in the lattice. Conversely,  $\text{Nd}^{3+}$  is a much larger cation than  $\text{Dy}^{3+}$  and only  $\sim 1.5\%$  smaller than  $\text{Ca}^{2+}$ . Therefore, incorporating  $\text{Nd}^{3+}$  into the 9-coordinated site should not result in much lattice distortion since the size of  $\text{Nd}^{3+}$  is close to that of  $\text{Ca}^{2+}$ . Thus, the case of  $\text{Nd}_2\text{Si}_2\text{O}_7$  producing defect-free apatite may be more energetically favorable for the structure. That is, the closer the ionic radius of  $\text{RE}^{+3}$  is to that of  $\text{Ca}^{2+}$ , the more advantageous it is to form apatite.

Generally, assuming that the thickness of EBCs is  $300\ \mu\text{m}$ , the thickness of the  $\text{Ca}_2\text{RE}_8(\text{SiO}_4)_6\text{O}_2$  phase formed by the reaction of CMAS and sintered  $\text{Er}_2\text{Si}_2\text{O}_7$  in this present study was  $292\ \mu\text{m}$  at  $1400^\circ\text{C}$  for 48 h. It is considered that  $\text{Er}_2\text{Si}_2\text{O}_7$  may not sufficiently protect against CMAS attacks. However, the microstructure of the sintered bodies is different from the microstructure of EBCs, and the factors affecting  $\text{Ca}_2\text{RE}_8(\text{SiO}_4)_6\text{O}_2$  phase formation include time, temperature, concentration of Ca, ionic radius of RE, and viscosity of molten CMAS. Based on the present work, a study of the influence of various factors on corrosion behavior is needed.

#### 5. 4. Conclusions

We investigated the high-temperature corrosion behavior of sintered  $\text{Er}_2\text{Si}_2\text{O}_7$  in contact with CMAS to evaluate its suitability as an EBCs material. Sintered  $\text{Er}_2\text{Si}_2\text{O}_7$  samples were exposed to CMAS at  $1400^\circ\text{C}$  for 2, 12, and 48 h. The DSC analysis revealed that the melting temperature of the mixed CMAS/ $\text{Er}_2\text{Si}_2\text{O}_7$  powder mixture was  $1258^\circ\text{C}$ , indicating that the reaction between the two materials occurs at high temperatures. The reaction between CMAS and  $\text{Er}_2\text{Si}_2\text{O}_7$  was also confirmed from results of HT-XRD, with peaks corresponding to  $\beta$ - $\text{Er}_2\text{Si}_2\text{O}_7$ ,  $\text{CaSiO}_3$ ,  $\text{CaAl}_2\text{Si}_2\text{O}_8$ , and  $\text{Ca}_2\text{MgSi}_2\text{O}_7$  phases present at temperatures up to  $1200^\circ\text{C}$ , but absent at  $1300^\circ\text{C}$ . A  $\text{Ca}_2\text{Er}_8(\text{SiO}_4)_6\text{O}_2$  apatite phase was observed at temperatures of  $1300^\circ\text{C}$  and higher, as a result of the reaction between molten CMAS and  $\text{Er}_2\text{Si}_2\text{O}_7$ . SEM observations showed that shard-like crystallites of  $\text{Ca}_2\text{Er}_8(\text{SiO}_4)_6\text{O}_2$  apatite grew perpendicular to the  $\text{Er}_2\text{Si}_2\text{O}_7$  surface as heat-treatment time was increased, and EDS analysis indicated that the Ca content of the CMAS melt decreased concomitantly. The thickness of the reaction layer increased about three times when the exposure time was increased from 2 h to 48 h.

## References

- [1] B.K. Jang, F.J. Feng, K.S. Lee, E. García, A. Nistal, N. Nagashima, S.W. Kim, Y.S. Oh, H.T. Kim, Thermal behavior and mechanical properties of  $Y_2SiO_5$  environmental barrier coatings after isothermal heat treatment, *Surf. Coat. Technol.* 308 (2016) 24–30.
- [2] J.L. Stokes, B.J. Harder, V.L. Wiesner, D.E. Wolfe, High-temperature thermochemical interactions of molten silicates with  $Yb_2Si_2O_7$  and  $Y_2Si_2O_7$  environmental barrier coating materials, *J. Eur. Ceram. Soc.* 39 (2019) 5059–5067.
- [3] J.L. Stokes, B.J. Harder, V.L. Wiesner, D.E. Wolfe, Effects of crystal structure and cation size on molten silicate reactivity with environmental barrier coating materials, *J. Am. Ceram. Soc.* 103 (2020) 622–634.
- [4] Z. Tian, X. Ren, Y. Lei, L. Zheng, W. Geng, J. Wang, et al, Corrosion of  $RE_2Si_2O_7$  (RE=Y, Yb, and Lu) environmental barrier coating materials by molten calcium-magnesium-alumino-silicate glass at high temperatures, *J. Eur. Ceram. Soc.* 39 (2019) 4245–4254.
- [5] H. Yang, Y. Zhang, Y. Li, X. Huang, Y. Liu, In situ observation of environmental barrier coating against calcium–magnesium–alumina–silicate attack at elevated temperature, *Int. J. Appl. Ceram. Technol.* 18 (2021) 1281–1287.
- [6] P. Mechnich, W. Braue, U. Schulz, High-temperature corrosion of EB-PVD yttria partially stabilized zirconia thermal barrier coatings with an artificial volcanic ash overlay, *J. Am. Ceram. Soc.* 94 (2011) 925–931.
- [7] P. Mechnich, W. Braue, Volcanic ash-induced decomposition of EB-PVD  $Gd_2Zr_2O_7$  thermal barrier coatings to Gd-Oxyapatite, Zircon, and Gd, Fe-Zirconolite, *J. Am. Ceram. Soc.* 96 (2013) 1958–1965.

- [8] D.L. Poerschke, R.W. Jackson, C.G. Levi, Silicate deposit degradation of engineered coatings in gas turbines: progress toward models and materials solutions, *Annu. Rev. Mater. Res.* 47 (2017) 297–330.
- [9] L. Sun, Y. Luo, Z. Tian, T. Du, X. Ren, J. Li, W. Hu, J. Zhang, J. Wang, High temperature corrosion of  $(\text{Er}_{0.25}\text{Tm}_{0.25}\text{Yb}_{0.25}\text{Lu}_{0.25})_2\text{Si}_2\text{O}_7$  environmental barrier coating material subjected to water vapor and molten calcium–magnesium–aluminosilicate (CMAS), *Corros. Sci.* 175 (2020) 108881.
- [10] L.R. Turcer, A.R. Krause, H.F. Garces, L. Zhang, N.P. Padture, Environmental-barrier coating ceramics for resistance against attack by molten calcia-magnesia-aluminosilicate (CMAS) glass: Part II,  $\beta\text{-Yb}_2\text{Si}_2\text{O}_7$  and  $\beta\text{-Sc}_2\text{Si}_2\text{O}_7$ , *J. Eur. Ceram. Soc.* 38 (2018) 3914–3924.
- [11] H. Zhao, B.T. Richards, C.G. Levi, H.N.G. Wadley, Molten silicate reactions with plasma sprayed ytterbium silicate coatings, *Surf. Coat. Technol.* 288 (2016) 151–162.
- [12] A.J. Fernández-Carrión, M. Allix, A.I. Becerro, Thermal expansion of rare-earth pyrosilicates, *J. Am. Ceram. Soc.* 96 (2013) 2298–2305.
- [13] Z.S. Khan, B. Zou, X. Chen, H.M. Saleem, T. Zia, M.B. Khan, X. Cao, Thermal cycling behavior and hot corrosion performance of the plasma sprayed  $\text{Er}_2\text{Si}_2\text{O}_7$  coatings deposited on Cf/SiC composites, *J. Asian Ceram. Soc.* 3 (2015) 123–129.
- [14] B.K. Jang, F.J. Feng, K. Suzuta, H. Tanaka, Y. Matsushita, K.S. Lee, F.J. Feng, S. Ueno, Corrosion behavior of volcanic ash and calcium magnesium aluminosilicate on  $\text{Yb}_2\text{SiO}_5$  environmental barrier coatings, *J. Ceram. Soc. Jpn.* 125[4] (2017) 326–332.
- [15] S.H. Kim, N. Nagashima, Y. Matsushita, B.N. Kim, B.K. Jang, Corrosion behavior of calcium-magnesium-aluminosilicate (CMAS) on sintered  $\text{Gd}_2\text{SiO}_5$  for environmental barrier coatings, *J. Am. Ceram. Soc.* 104 (2021) 3119–3129.

- [16] J. Liu, L. Zhang, Q. Liu, L. Cheng, Y. Wang, Calcium–magnesium–aluminosilicate corrosion behaviors of rare-earth disilicates at 1400°C, *J. Am. Ceram. Soc.* 33 (2013) 3419–3428.
- [17] S. Morelli, V. Testa, G. Bolelli, O. Ligabue, E. Molinari, N. Antolotti, L. Lusvarghi, CMAS corrosion of YSZ thermal barrier coatings obtained by different thermal spray processes, *J. Eur. Ceram. Soc.* 40 (2020) 4084–4100.
- [18] A.E. Mohamed, M.K. Thomas. A review on differential scanning calorimetry technique and its importance in the field of energetic materials, *Phys. Sci. Rev.* 3 (2018) 20170103.
- [19] E.M. Zaleski, C. Ensslen, C.G. Levi, Melting and crystallization of silicate systems relevant to thermal barrier coating damage, *J. Am. Ceram. Soc.* 98[5] (2015) 1642–1649.
- [20] B.K. Jang, F.J. Feng, K. Suzuta, H. Tanaka, Y. Matsushita, K.S. Lee, S.W. Kim, Y.S. Oh, H.T. Kim, Corrosion behavior of volcanic ash on sintered mullite for environmental barrier coatings, *Ceram. Int.* 43 (2017) 1880–1886.
- [21] B.K. Jang, F.J. Feng, K. Suzuta, H. Tanaka, Y. Matsushita, K.S. Lee, F.J. Feng, S. Ueno, Corrosion behavior of volcanic ash and calcium magnesium aluminosilicate on  $\text{Yb}_2\text{SiO}_5$  environmental barrier coatings, *J. Ceram. Soc. Jpn.* 125[4] (2017) 326–332.
- [22] S.H. Kim, B.N. Kim, N. Nagashima, Y. Matsushita, B.K. Jang, High-temperature corrosion of spark plasma sintered  $\text{Gd}_2\text{SiO}_5$  with volcanic ash for environmental barrier coatings, *J. Eur. Ceram. Soc.* 41 (2021) 3161–3166.
- [23] X. Zhong, Y. Wang, Y. Niu, L. Huang, Q. Li, X. Zheng, Corrosion behaviors and mechanisms of ytterbium silicate environmental barrier coatings by molten calcium–magnesium–alumino–silicate melts, *Corros. Sci.* 191 (2021) 109718.
- [24] J. Sleeper, A. Garg, V.L. Wiesner, N.P. Bansal, Thermochemical interactions between CMAS and  $\text{Ca}_2\text{Y}_8(\text{SiO}_4)_6\text{O}_2$  apatite environmental barrier coating material, *J. Eur. Ceram. Soc.* 39 (2019) 5380–5390.

- [25] W.D. Summers, D.L. Poerschke, D. Park, J.H. Shaw, F.W. Zok, C.G. Levi, Roles of composition and temperature in silicate deposit-induced recession of yttrium disilicate, *Acta Mater.* 160 (2018) 34–46.
- [26] S. Welinski, C.W. Thiel, J. Dajczgewand, A. Ferrier, R.L. Cone, R.M. Macfarlane, T. Chanelière, A.L. Chauvet, P. Goldner, Effects of disorder on optical and electron spin linewidths in  $\text{Er}^{3+}$ ,  $\text{Sc}^{3+}$ : $\text{Y}_2\text{SiO}_5$ , *Opt. Mater.* 63 (2017) 69–75.
- [27] V.L. Wiesner, B.J. Harder, N.P. Bansal, High-temperature interactions of desert sand CMAS glass with yttrium disilicate environmental barrier coating material, *Ceram. Int.* 44 (2018) 22738–22743.
- [28] M. Wolf, D.E. Mack, O. Guillon, R. Vaßen, Resistance of pure and mixed rare earth silicates against calcium-magnesium-aluminosilicate (CMAS): A comparative study, *J. Am. Ceram. Soc.* 103 (2020) 7056–7071.

## Chapter 6. High-Temperature Corrosion of $\text{Gd}_2\text{Si}_2\text{O}_7/\text{Sc}_2\text{Si}_2\text{O}_7$ with CMAS for EBCs

### 6.1. Introduction

Rare earth (RE) disilicate ( $\text{RE}_2\text{Si}_2\text{O}_7$ ) has been studied as a promising material for EBCs due to its excellent heat resistance, corrosion resistance, and coefficient of thermal expansion (CTE) similar to that of CMCs. In particular, the high-temperature corrosion behavior of individual RE-disilicate and CMAS has been actively studied [1–12]. Most of the studies on the high-temperature corrosion behavior of  $\text{RE}_2\text{Si}_2\text{O}_7$  [13–17] and CMAS have been studied for  $\text{Yb}_2\text{Si}_2\text{O}_7$  and  $\text{Y}_2\text{Si}_2\text{O}_7$  materials according to temperature and time and CMAS composition. In addition, Sc, Gd, La, Lu [4, 9–11, 18], and Er [18] have been studied as candidate materials. The main results of the high-temperature corrosion behavior of single  $\text{RE}_2\text{Si}_2\text{O}_7$  materials and CMAS were analyzed as either reaction crystallization into apatite or penetration into grain boundaries, depending on the reaction of RE elements with Ca. Different corrosion mechanisms, depending on the ionic size of the RE elements, two main mechanisms explain the CMAS corrosion behavior [12].

In particular, since  $\text{Gd}_2\text{Si}_2\text{O}_7$  has a large ionic size,  $\text{Gd}(1.107 \text{ \AA})$ [19] showed a great affinity for Ca among CMAS components. Therefore, the CMAS corrosion of most RE disilicates is controlled by the reaction-crystallization process to form an apatite phase [8–11]. However, Sc with small ionic size does not form apatite and is controlled by the penetration of molten CMAS along grain boundaries [12]. In addition, the average CTE of  $\beta\text{-Sc}_2\text{Si}_2\text{O}_7$  is  $5.4 \times 10^{-6} \text{ }^\circ\text{C}^{-1}$  [20], which is similar to that of CMCs, and has a melting point of  $1860^\circ\text{C}$  [21], a Young's modulus of 200GPa [22], and a density of  $3.40 \text{ Mgm}^{-3}$  [21], so it has many advantages as an EBCs material. We evaluated the high-temperature corrosion behavior of  $\text{Gd}_2\text{SiO}_5$  [9,10] and  $\text{Gd}_2\text{Si}_2\text{O}_7$  [11],  $\text{Er}_2\text{Si}_2\text{O}_7$  [8] and CMAS in a previous study. Commonly formed a reaction layer composed of apatite. The formation of dense apatite consumes CMAS and prevents

further penetration into EBCs. However, extensive formation of apatite can lead to interfacial delamination due to different CTE from  $\text{RE}_2\text{Si}_2\text{O}_7$  and CMAS. Therefore, the thickness of the reaction layer formed by  $\text{Gd}_2\text{Si}_2\text{O}_7$  and CMAS should be reduced, and consequently, the formation of a reaction layer with an appropriate thickness should be targeted in this study. (In our previous study,  $\text{Gd}_2\text{Si}_2\text{O}_7$  formed the highest reactive layer [11].)

To date, the results of high temperature corrosion behavior for CMAS of dual disilicate as well as single disilicate were not reported. Therefore, the purpose of this study is to provide insight into the high-temperature corrosion behavior caused by the reaction of dual  $\text{Gd}_2\text{Si}_2\text{O}_7$  (70%)+ $\text{Sc}_2\text{Si}_2\text{O}_7$  (30%) as EBCs materials with CMAS. In addition, we present a promising strategy for the design and development of potential EBCs with excellent properties by comparing the reaction layer thickness and corrosion mechanism of single  $\text{Gd}_2\text{Si}_2\text{O}_7$  in chapter 4, the results of previous studies. The purpose of this study is focuses on the high-temperature corrosion behavior of dual RE silicate  $\text{Gd}_2\text{Si}_2\text{O}_7$  (70%)+ $\text{Sc}_2\text{Si}_2\text{O}_7$  (30%) and CMAS, and the comparison of the reaction layer formation according to the single disilicate in chapter 4 and dual disilicate.

## 6. 2. Experimental Procedure

### 6.2.1. Sample Preparation

Gd<sub>2</sub>O<sub>3</sub> (Rare Metallurgical Corporation, Japan), Sc<sub>2</sub>O<sub>3</sub> (Rare Metallurgical Corporation, Japan), and SiO<sub>2</sub> (Wako Pure Chemical Industries Ltd., Japan) powders were used to prepare Gd<sub>2</sub>Si<sub>2</sub>O<sub>7</sub> (70%)+Sc<sub>2</sub>Si<sub>2</sub>O<sub>7</sub> (30%) (vol%) powder. The mixed Gd<sub>2</sub>O<sub>3</sub>-Sc<sub>2</sub>O<sub>3</sub>-SiO<sub>2</sub> powder was ball milled using YSZ balls in EtOH for 24 h. The mixed Gd<sub>2</sub>O<sub>3</sub>-Sc<sub>2</sub>O<sub>3</sub>-SiO<sub>2</sub> powder was then dried in an oven at 80°C for 24 h. After pulverizing the dried powder, it was heated at 1400°C for 24 h using an electric furnace to synthesize Gd<sub>2</sub>Si<sub>2</sub>O<sub>7</sub> (70%)+Sc<sub>2</sub>Si<sub>2</sub>O<sub>7</sub> (30%) powder.

Then, the synthesized Gd<sub>2</sub>Si<sub>2</sub>O<sub>7</sub> (70%)+Sc<sub>2</sub>Si<sub>2</sub>O<sub>7</sub> (30%) powder was poured into a graphite mold with a diameter of 10 mm and spark plasma sintering (LABOX-315, Sinter Land Inc., Japan) at 1450°C for 20 min under a pressure of 60 MPa in a vacuum of 10<sup>-2</sup> heated at 10 °/min was used to fabricate a sintered body. The CMAS powder used for high-temperature corrosion behavior was fabricated by the same manufacturing method as in our previous study [12,14]. The sintered Gd<sub>2</sub>Si<sub>2</sub>O<sub>7</sub> was cut into 6 mm × 4 mm × 3 mm using a diamond saw. After cutting, the specimen was polished with 9, 3, and 1 μm diamond suspensions in sequence. Specimens were prepared by attaching CMAS paste to the surface under a load of 40 mg/cm<sup>2</sup> for high-temperature corrosion experiments. Individual specimens were heat treatment at 1400°C at a heating rate of 10°C/min for 0.5, 2, 12, or 48 h, followed by furnace cooling to room temperature. After heat treatment, the specimen was cut into 3 × 4 × 3 mm cross-sections for analysis of the cross-section of the reaction layer. Cross-section of the specimens were polished successively using 9, 3, and 1 μm diamond suspensions and 0.05 μm colloidal silica.

### 6.2.2. High-Temperature Corrosion Behavior

The microstructure and change of the reaction layer due to high-temperature corrosion of sintered Gd<sub>2</sub>Si<sub>2</sub>O<sub>7</sub> (70%)+Sc<sub>2</sub>Si<sub>2</sub>O<sub>7</sub> (30%) were analyzed using a field-emission scanning

electron microscopy (FESEM; EISS Gemini SEM 300, Germany). A beam voltage of 15 kV and working distance of 15 mm were used for energy-dispersive X-ray spectroscopy (EDS) measurements to determine the element ratios (compositions) of the cross-sectioned specimens. The inverse pole figure (IPF) and image quality (IQ) maps of microstructure was observed by field-emission scanning electron microscopy (FESEM; EISS Gemini SEM 300, Germany) equipped with an electron backscattered diffraction (EBSD) detector. X-ray diffraction (XRD) was analyzed with Cu K $\alpha$ 1 radiation ( $\lambda = 1.54056 \text{ \AA}$ ) a Smart Lab (Rigaku Co., Japan) diffractometer to examine the phase evolution. Measurements were made in the  $2\theta$  range of  $20\text{--}60^\circ$  using a scan step of  $0.02^\circ/\text{min}$  and a scan rate of  $0.1^\circ/\text{min}$ .

### 6.3. Results and Discussion

#### 6.3.1. Characterization of Sintered $\text{Gd}_2\text{Si}_2\text{O}_7$ (70%) + $\text{Sc}_2\text{Si}_2\text{O}_7$ (30%)

Fig. 49 (a) shows the SEM micrograph of sintered  $\text{Gd}_2\text{Si}_2\text{O}_7$  (70%)+ $\text{Sc}_2\text{Si}_2\text{O}_7$  (30%) and (b) the XRD pattern of  $\text{Gd}_2\text{Si}_2\text{O}_7$  (70%)+ $\text{Sc}_2\text{Si}_2\text{O}_7$  (30%) powder at room temperature. The average particle size of sintered  $\text{Gd}_2\text{Si}_2\text{O}_7$  (70%)+ $\text{Sc}_2\text{Si}_2\text{O}_7$  (30%) was about  $\sim 1.8 \mu\text{m}$ . The porosity was 2.3% and the relative density was 97.7%. In Fig. 49 (a), gray is  $\text{Gd}_2\text{Si}_2\text{O}_7$ , and dark gray is  $\text{Sc}_2\text{Si}_2\text{O}_7$ . Fig. 49 (b) shows the  $\text{Gd}_2\text{Si}_2\text{O}_7$  (70%)+ $\text{Sc}_2\text{Si}_2\text{O}_7$  (30%) XRD pattern, and the  $\text{Gd}_2\text{Si}_2\text{O}_7$  and  $\text{Sc}_2\text{Si}_2\text{O}_7$  peaks analyzed at room temperature were clearly identified. This confirms that the mixed  $\text{Gd}_2\text{Si}_2\text{O}_7$  (70%)+ $\text{Sc}_2\text{Si}_2\text{O}_7$  (30%) was completed before the CMAS high-temperature reaction. From now on, sintered  $\text{Gd}_2\text{Si}_2\text{O}_7$  (70%)+ $\text{Sc}_2\text{Si}_2\text{O}_7$  (30%) will be expressed as Gd7-Sc3. This result is consistent with the XRD peak for  $\text{Gd}_2\text{Si}_2\text{O}_7$  and  $\text{Sc}_2\text{Si}_2\text{O}_7$  in other paper [11,12].

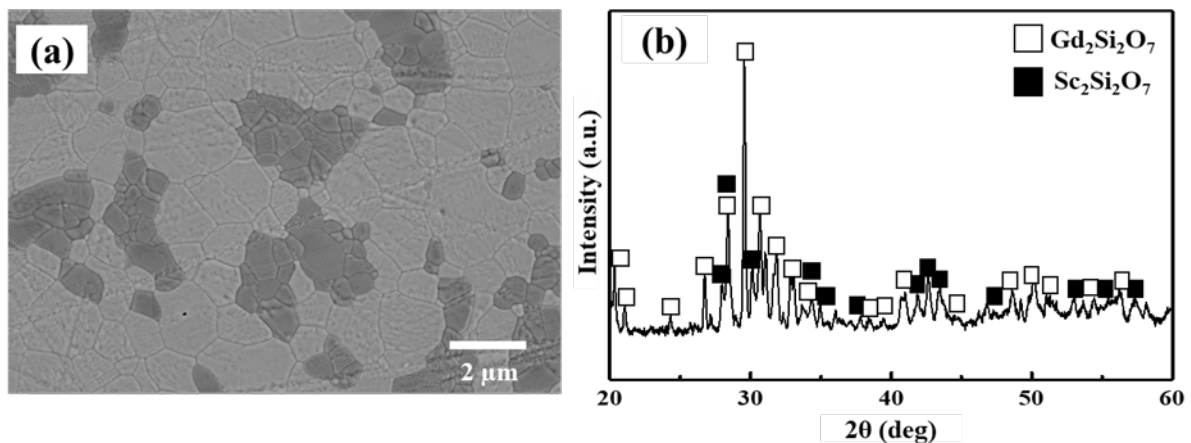


Fig. 49. The results of (a) SEM image of a sintered Gd7-Sc3 and (b) XRD patterns on Gd7-Sc3 powder.

#### 6.3.2. High-Temperature Corrosion Behavior

Fig. 50 shows the XRD pattern results of the reaction of (a) sintered Gd7-Sc3 and CMAS after (b) 0.5, (c) 2, (d) 12 and (e) 48 h of heat treatment. XRD analysis results, Fig. 50 (a) shows

the XRD pattern results of the sintered Gd7-Sc3. Peaks corresponding to  $Gd_2Si_2O_7$  and  $Sc_2Si_2O_7$  were analyzed. The peak of the reaction layer of  $Ca_2Gd_8(SiO_4)_6O_2$ ,  $SiO_2$  and  $Sc_2Si_2O_7$  were identified in Fig. 50 (b-e). The melting point ( $T_m$ ) of CMAS powder was analyzed as  $1243^\circ\text{C}$  in a previous study [8]. Because the heat-treatment temperature was  $1400^\circ\text{C}$ , the CMAS was melted to form a sintered body Gd7-Sc3 and a reaction layer. In addition,  $Ca_2Gd_8(SiO_4)_6O_2$  was analyzed by the high-temperature reaction of  $Gd_2Si_2O_7$  and CMAS at  $1300^\circ\text{C}$  reported in our previous study [11], which was analyzed to be identical to the  $Ca_2Gd_8(SiO_4)_6O_2$  peak. That is, it was confirmed that  $Gd_2Si_2O_7$  reacted with CMAS to produce  $Ca_2Gd_8(SiO_4)_6O_2$ , but  $Sc_2Si_2O_7$  did not react with CMAS.

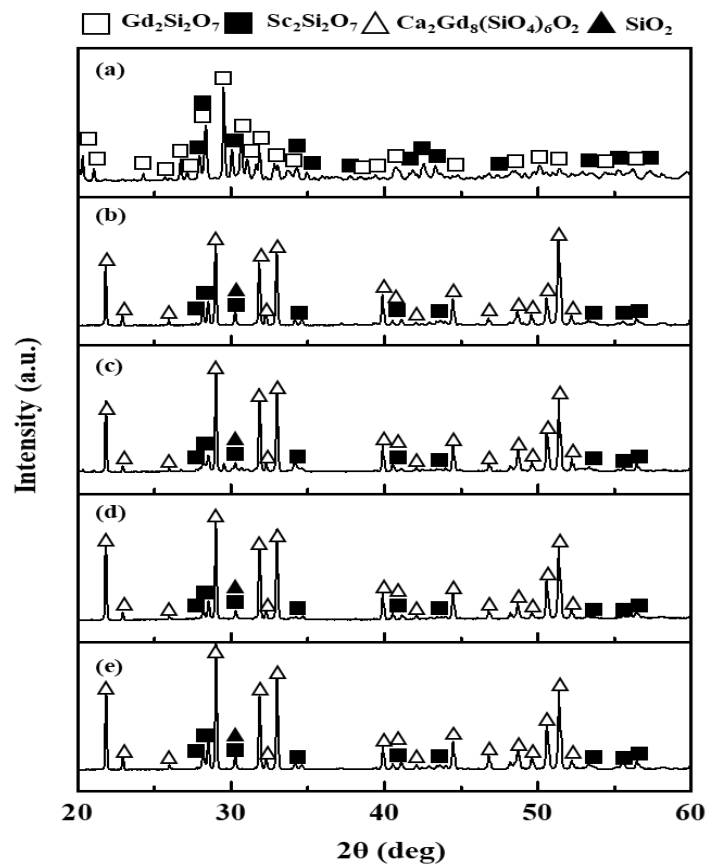


Fig. 50. The results of XRD patterns on (a) sintered Gd7-Sc3 after heat treatment for (b) 0.5 h, (c) 2 h, (d) 12 h, and (e) 48 h.

Fig. 51 shows the cross-sectional SEM micrographs of Gd7-Sc3 and CMAS after high-temperature corrosion. High-temperature corrosion evaluation of Gd7-Sc3 and CMAS was performed for (a) 0.5, (b) 2, (c) 12, (d) 48 h at 1400°C. After heat treatment, the formation of a reaction layer at the interface between the molten CMAS and Gd7-Sc3 is confirmed. As the heat-treatment time increased, the thickness of the reaction layer increased and the reaction layer grew vertically. However, the shape is different from that of a single  $Gd_2Si_2O_7$  and CMAS reaction layer [11]. In our previous study, we confirmed that the reaction layer of a single  $Gd_2Si_2O_7$  and CMAS was formed vertically in the shape of a needle [11]. It is confirmed that the two phases are mixed under the influence of  $Sc_2Si_2O_7$ , rather than the formation of a long reaction layer vertically.

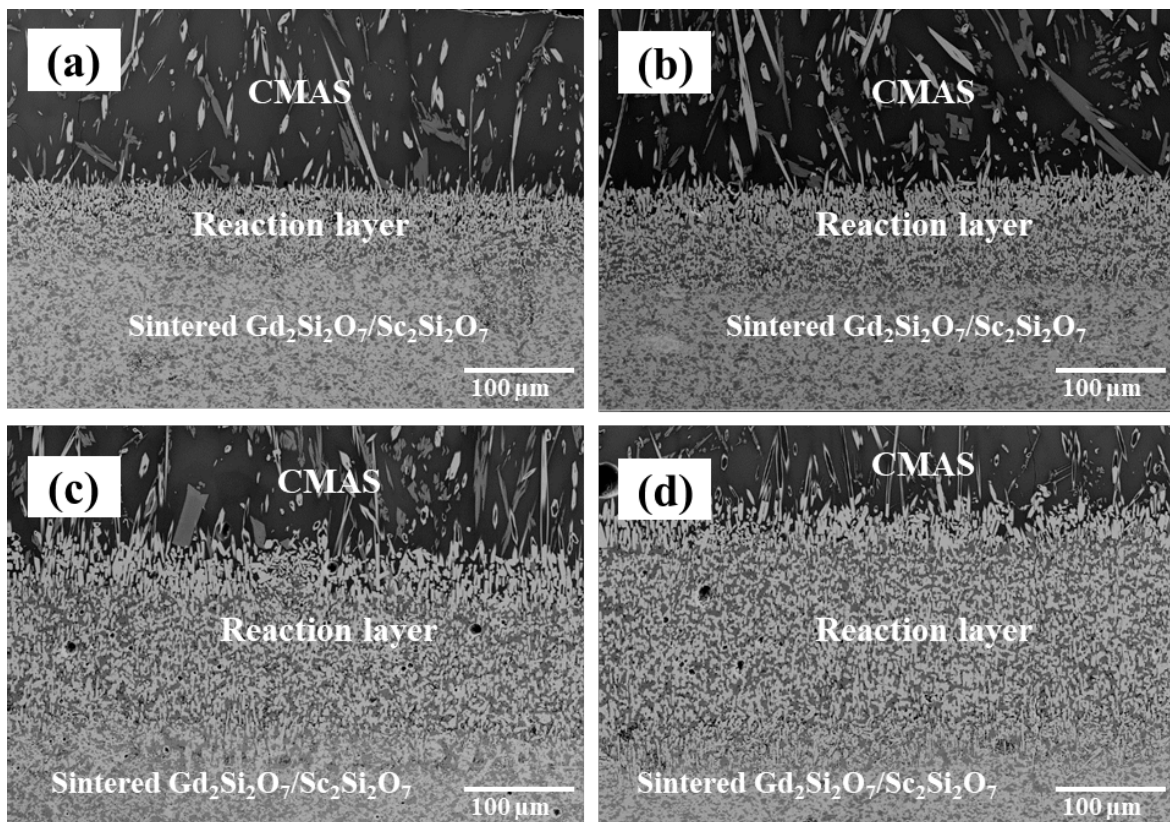


Fig. 51. Cross-sectional SEM micrograph of sintered Gd7-Sc3 which have interacted with CMAS at 1400°C: (a) 0.5 h, (b) 2 h, (c) 12 h, and (d) 48 h.

Fig. 52 shows the average thickness of the reaction layer according to the increase in the reaction time of CMAS and Gd7-Sc3 after heat treatment at 1400°C. As mentioned above, the reaction layer of Gd7-Sc3 and CMAS is divided into a layer in which  $\text{Ca}_2\text{Gd}_8(\text{SiO}_4)_6\text{O}_2$  as well as  $\text{Ca}_2\text{Gd}_8(\text{SiO}_4)_6\text{O}_2 + \text{Sc}_2\text{Si}_2\text{O}_7$  are mixed. The thickness of the entire reaction layer increased to about 76, 104, 175, and 238  $\mu\text{m}$  after 0.5, 2, 12, and 48 h, respectively. In addition, the thickness of the reaction layer made of  $\text{Ca}_2\text{Gd}_8(\text{SiO}_4)_6\text{O}_2$  increased to about 22, 28, 36, and 42  $\mu\text{m}$  after 0.5, 2, 12, and 48 h, respectively. In a previous study, we identified a high-temperature reaction layer with CMAS and a single  $\text{Gd}_2\text{Si}_2\text{O}_7$  reaction time. Apatites grown as elongated needles of 98, 145, 211, and 306  $\mu\text{m}$  were analyzed at 0.5, 2, 12, and 48 h, respectively [11].

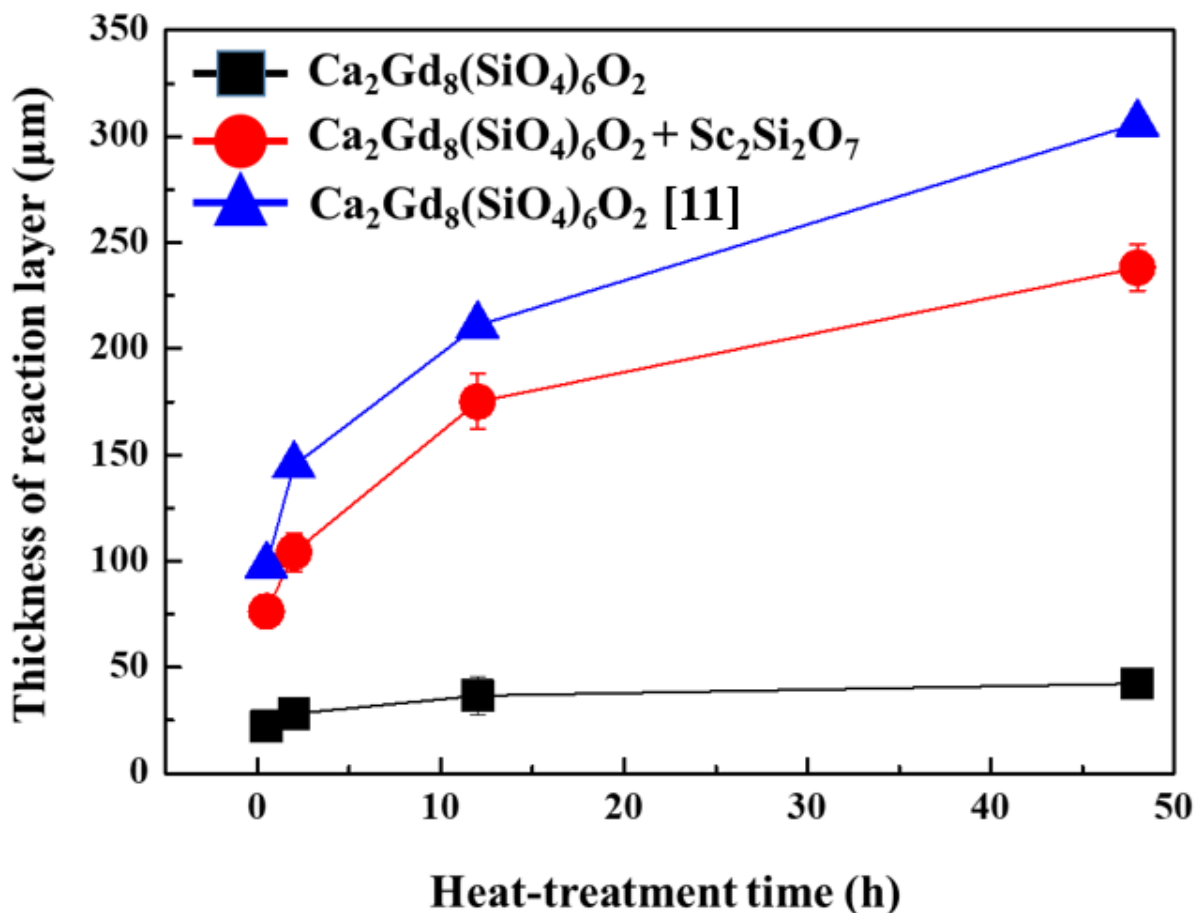


Fig. 52. Sintered Gd7-Sc3 average value of thickness of reaction layer at 1400°C as a function of heat-treatment time.

This is consistent with the fact that  $Gd^{3+}$  (1.019Å), which has a larger ionic radius than  $Sc^{3+}$  (0.870Å) to generate apatite, has a stronger affinity for Ca and provides a higher driving force for the reaction propensity. Stokes et al. [23] reported that, as a result of the reaction with CMAS at high temperature in  $RE_2Si_2O_7$  powder, apatite formation decreased as the difference between  $RE^{3+}$  ( $RE = Nd(1.163 \text{ \AA}), Gd(1.107 \text{ \AA}), Dy(1.083 \text{ \AA}), Er(1.062 \text{ \AA})$ ) and  $Ca^{2+}$  radius increased. The result of the reaction with the molten CMAS, Sc (0.870 Å), which has a smaller ionic radius than Gd (1.107 Å), does not react with apatite and is reprecipitated as  $Sc_2Si_2O_7$ . It is also the same result as the report that it penetrates the grain boundary of  $\beta$ - $Sc_2Si_2O_7$  pellets instead of reaction crystallization [12]. Reports on the reaction of monosilicate and CMAS as well as disilicate show the same results. Tian et al. [24] reported that  $RE_2SiO_5$  ( $RE=Tm, Yb, Lu$ ) exhibits strong resistance to CMAS corrosion. As the RE cation size decreases, the reaction layer thickness also decreases because the RE silicate apatite formation enthalpy becomes more endothermic as the RE cation size decreases [24]. In addition, the growth rate is reduced after the formation of the reaction layer initially, because CaO is depleted from the melt and the growth rate of apatite decreases over time [8]. As such, the thickness of the reaction layer also increased as time increased in the  $Ca_2Gd_8(SiO_4)_6O_2+Sc_2Si_2O_7$  mixed layer. However, the growth of the reaction layer made of  $Ca_2Gd_8(SiO_4)_6O_2$  was inconspicuous compared to the  $Ca_2Gd_8(SiO_4)_6O_2+Sc_2Si_2O_7$  mixed layer. That is, it is considered that Ca is not sufficient in the melt for growing  $Ca_2Gd_8(SiO_4)_6O_2$  alone according to time increase. Zhao et al. [25] reported that the Ca concentration of the CMAS melt decreased with increasing reaction time. The faster Ca loss at the beginning of the reaction to the Ca concentration of the CMAS melt affected the formation of a continuous apatite layer. Our previous results also confirmed that the Ca concentration initially decreased in the high-temperature reaction [8].

Fig. 53 shows the results of EDS mapping of sintered Gd7-Sc3 cross sections after annealing at 1400°C for 0.5 h. The measurements are divided for the following regions CMAS, reaction layer and sintered Gd7-Sc3. Si, Ca, Sc, and Gd were detected to analyze the main components of the reaction layer. As a result of analyzing the main components of the reaction layer, it was confirmed that  $\text{Ca}_2\text{Gd}_8(\text{SiO}_4)_6\text{O}_2$  was present. As confirmed in Fig. 52, the reaction layer was classified into two layers. In single  $\text{Gd}_2\text{Si}_2\text{O}_7$ , elongated needle-like apatite was analyzed [11], but the  $\text{Ca}_2\text{Gd}_8(\text{SiO}_4)_6\text{O}_2$  region in which composite Gd7-Sc3 was mixed with  $\text{Sc}_2\text{Si}_2\text{O}_7$  was also analyzed.

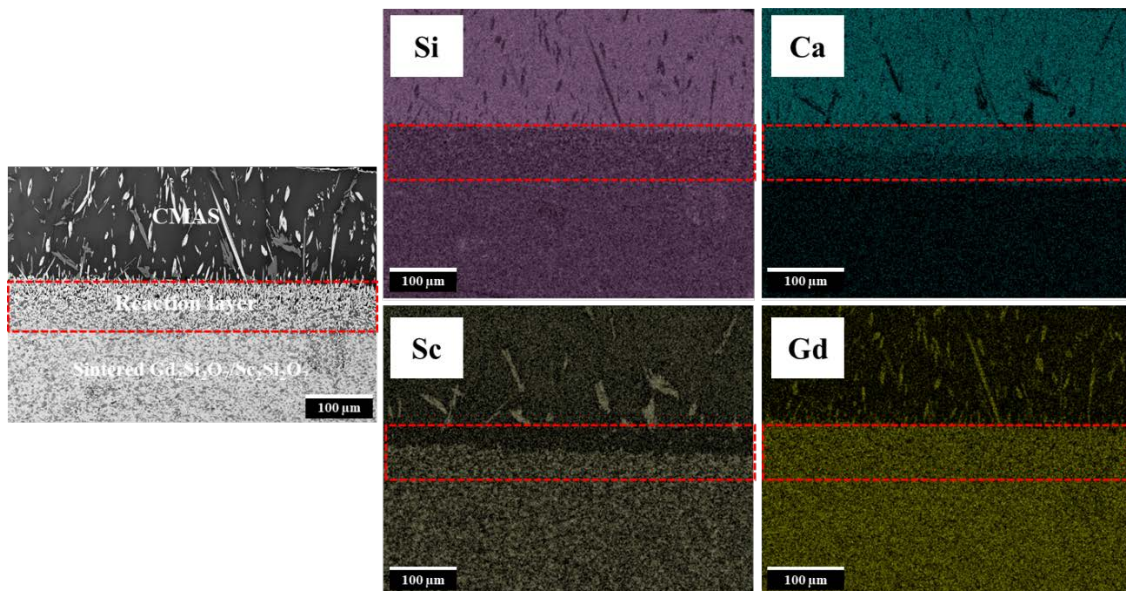


Fig. 53. EDS mapping components (Si, Ca, Sc, and Gd) of sintered Gd7-Sc3 which have interacted with CMAS at 1400°C for 0.5 h.

Fig. 54 shows the results of EDS mapping of sintered Gd7-Sc3 cross sections after heat treatment at 1400°C for 48 h. In order to compare with the reaction layer for 0.5 h, Si, Ca, Sc, and Gd, which are the main components of the reaction layer, were detected. The overall reaction layer was thicker than 0.5 h. In particular, the reaction layer mixed with

$\text{Ca}_2\text{Gd}_8(\text{SiO}_4)_6\text{O}_2$  and  $\text{Sc}_2\text{Si}_2\text{O}_7$  was extended. However, it was confirmed that the growth of single  $\text{Ca}_2\text{Gd}_8(\text{SiO}_4)_6\text{O}_2$  hardly occurred.

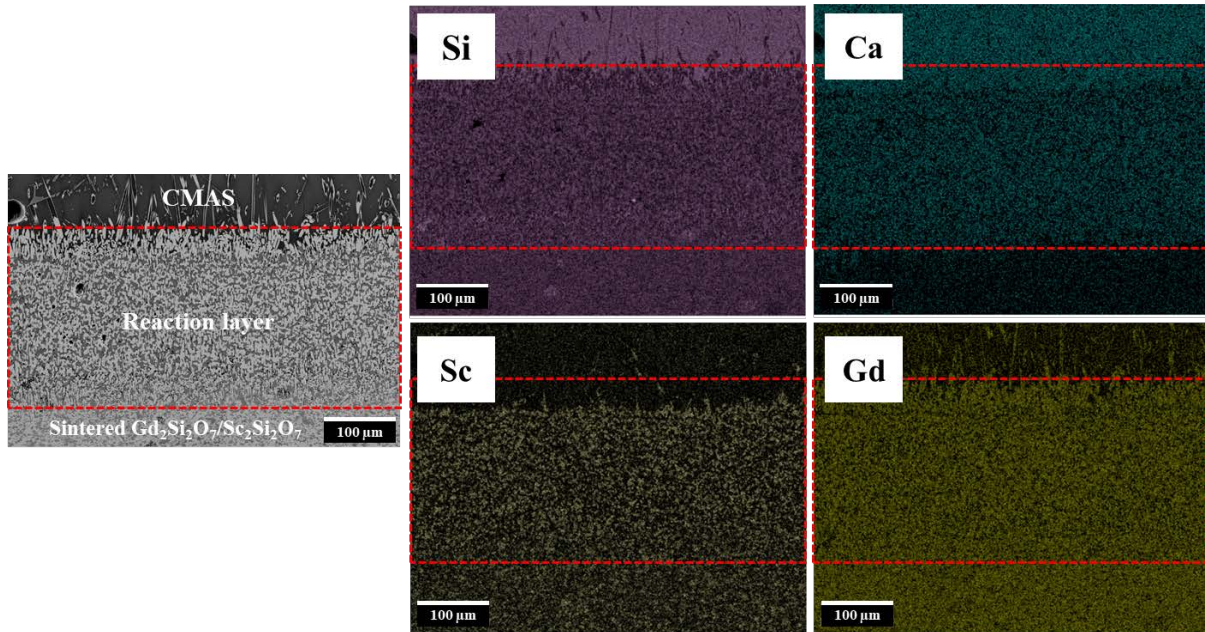


Fig. 54. EDS mapping components (Si, Ca, Sc, and Gd) of sintered Gd7-Sc3 which have interacted with CMAS at 1400°C for 48 h.

Fig. 55 (a) shows a low-magnification SEM micrograph of a sintered Gd7-Sc3 cross section after heat treatment at 1400°C for 2 h. Fig. 55 (b) shows the high magnification SEM micrograph of the reaction layer mixed with  $\text{Sc}_2\text{Si}_2\text{O}_7$  and the non-reacted part in the red box in Fig. 55 (a). Table 11 shows the results of EDS point analysis for areas 1 to 6 in Fig. 55 (b). At points 1 and 2, Gd, Si, Ca and a small amount of Sc, which are major components of  $\text{Ca}_2\text{Gd}_8(\text{SiO}_4)_6\text{O}_2$ , were detected. These results show that Ca is a major component contributing to apatite crystallization in CMAS. Also, in our previous study, it was analyzed that the concentration of Ca decreased as time increased [8]. Also, the  $\text{Ca}_2\text{Gd}_8(\text{SiO}_4)_6\text{O}_2$  form has a relatively shorter length than the elongated needle form. Since  $\text{Sc}_2\text{Si}_2\text{O}_7$  does not react with CMAS and there is no phase change, it is considered that the growth of  $\text{Ca}_2\text{Gd}_8(\text{SiO}_4)_6\text{O}_2$  is

limited. At points 3 and 4, small amounts of Sc containing Gd, Si, and O were detected, and  $Gd_2Si_2O_7$  was confirmed. Additional explanations for points 2 and 3 are shown in Fig. 56. At points 5 and 6, Sc, Si, and O containing a small amount of Gd were detected, and  $Sc_2Si_2O_7$  was confirmed.

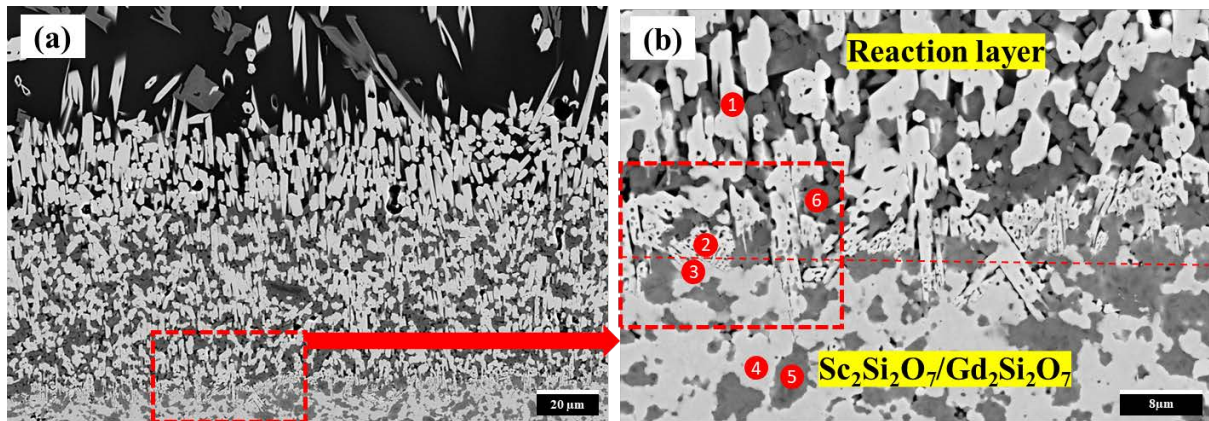


Fig. 55. (a) Low- and (b) cross-sectional SEM micrograph of sintered Gd7-Sc3 which have interacted with CMAS at 1400°C for 2 h in the red box of Fig. 55 (a).

Table 11. The average compositions (at. %) of the cross-section with CMAS in Fig. 55 (b).

	O	Mg	Al	Si	Ca	Sc	Gd	Phase
1	63.25	0.89	0.50	15.63	3.91	1.13	14.70	$Ca_2Gd_8(SiO_4)_6O_2$
2	62.84	0.35	0.00	17.60	3.70	0.69	14.82	$Ca_2Gd_8(SiO_4)_6O_2$
3	62.88	0.78	0.30	18.18	0.36	0.22	17.26	$Gd_2Si_2O_7$
4	64.30	0.68	0.20	17.83	0.07	2.43	14.48	$Gd_2Si_2O_7$
5	63.73	0.44	0.33	17.85	0.19	14.21	3.24	$Sc_2Si_2O_7$
6	64.50	0.42	0.30	18.07	0.16	13.67	2.87	$Sc_2Si_2O_7$

Fig. 56 shows the result of magnified EDS mapping at point 2.3 in Fig. 55 (b). Si, Ca, Sc, and Gd, which are the main components of the reaction layer, were detected. In the red box,  $\text{Ca}_2\text{Gd}_8(\text{SiO}_4)_6\text{O}_2$  (grey) and  $\text{Sc}_2\text{Si}_2\text{O}_7$  (dark gray) are identified. It was confirmed that  $\text{Gd}_2\text{Si}_2\text{O}_7$  was changed to  $\text{Ca}_2\text{Gd}_8(\text{SiO}_4)_6\text{O}_2$  by reacting with the molten CMAS. However,  $\text{Sc}_2\text{Si}_2\text{O}_7$  did not react with CMAS and no phase change occurred. This result is consistent with the report that  $\text{Sc}^{3+}$  is difficult to diffuse into the CMAS melt because of its weak affinity for  $\text{Ca}^{2+}$  in CMAS [12,26].

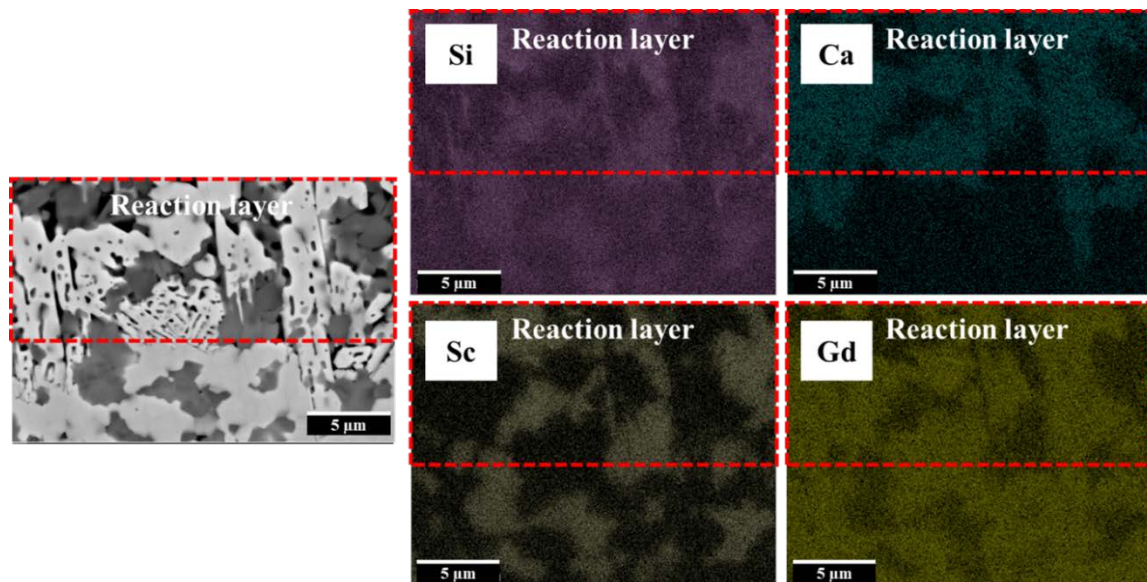


Fig. 56. EDS mapping components (Si, Ca, Sc, and Gd) of reaction layer of sintered Gd7-Sc3 which have interacted with CMAS in the red box of Fig.55 (b).

Fig. 57 shows that the orientation of apatite crystals in the reaction layer was investigated by EBSD in cross-sections of samples exposed for 0.5 (a) and 48 (b) h. Fig. 57 (a), (b) are divided into 2 regions ( $\text{Ca}_2\text{Gd}_8(\text{SiO}_4)_6\text{O}_2$ ,  $\text{Ca}_2\text{Gd}_8(\text{SiO}_4)_6\text{O}_2+\text{Sc}_2\text{Si}_2\text{O}_7$ ). It is also confirmed that the morphology of the single apatite layer is commonly vertically oriented. Also, in Fig. 57 (a), the shape of the apatite in the  $\text{Ca}_2\text{Gd}_8(\text{SiO}_4)_6\text{O}_2+\text{Sc}_2\text{Si}_2\text{O}_7$  region before being vertically oriented can be confirmed. However, it can be seen that the apatite in the  $\text{Ca}_2\text{Gd}_8(\text{SiO}_4)_6\text{O}_2+$

$\text{Sc}_2\text{Si}_2\text{O}_7$  region is vertically oriented in Fig. 57 (b). From these results, it was confirmed that the apatite in the  $\text{Ca}_2\text{Gd}_8(\text{SiO}_4)_6\text{O}_2 + \text{Sc}_2\text{Si}_2\text{O}_7$  region grew vertically after the growth of single apatite as the high-temperature corrosion time increased.

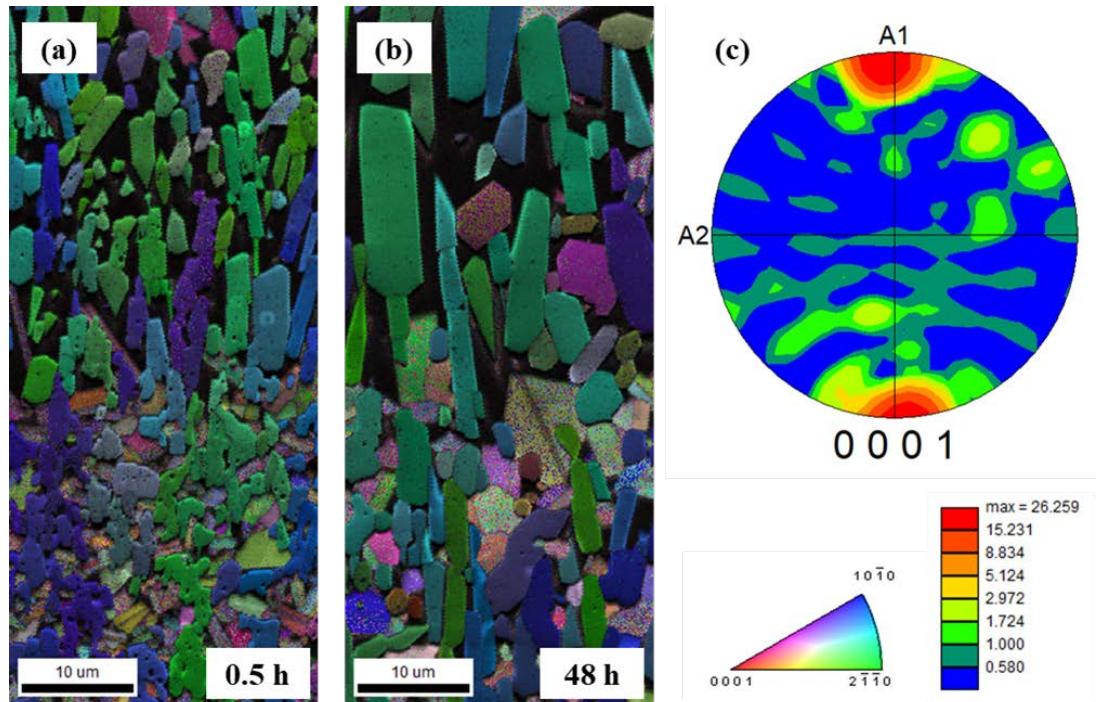


Fig. 57. EBSD maps show the image quality (IQ) + inverse pole figure (IPF) maps of the  $\text{Ca}_2\text{Gd}_8(\text{SiO}_4)_6\text{O}_2$ .

K.M. Grant et al. [27] investigated the interaction of CMAS with yttrium monosilicate (YMS) at  $1300^\circ\text{C}$  for time ranging from 1 to 100 h. The apatite produced by the high-temperature reaction of CMAS and YMS was analyzed by EBSD. The same  $\{0001\}$  pole figure results as in Fig. 57 (c) were reported. It was reported that apatite crystals are anisotropic in shape with longer dimensions oriented perpendicular to the surface on average, consistent with the directional trend of the  $[0001]$ . In addition, it was confirmed that the apatite particles increased due to the increase of the reaction time.

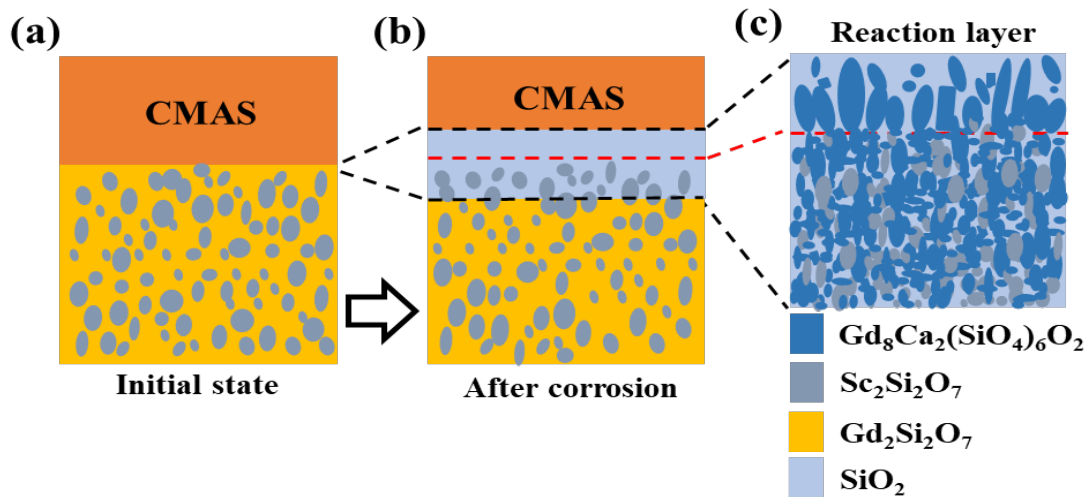


Fig. 58. Schematic illustration of the formation of the corrosion behavior on sintered Gd7-Sc3 in contact with CMAS: (a) initial state, (b) formation of reaction layer between CMAS and Gd7-Sc3 at high temperature, and (c) a magnified view of the reaction layer.

Fig. 58 shows a schematic diagram of the high-temperature corrosion behavior between Gd7-Sc3 and CMAS. Fig. 58 (a) and (b) show the formation of the reaction layer before and after the high-temperature corrosion reaction. Fig. 58 (c) shows the details of the reaction layer formed after the high-temperature corrosion reaction. As the high-temperature corrosion time increased, the thickness of the entire reaction layer increased. In our previous study [11], vertical and horizontal cracks were found in the high-temperature corrosion evaluation of single  $Gd_2Si_2O_7$  and CMAS under the same conditions (temperature, time, CMAS composition) (interfacial delamination did not occur), but they were not found in this study. L.R. Turcer [20] reported that the formation of apatite consumes CMAS and prevents further penetration into the EBCs (pore and/or grain boundary). However, in the reaction layer produced by the reaction of Gd7-Sc3 and CMAS, two types of apatite morphology were found. That is, it is a reaction layer in which a single  $Ca_2Gd_8(SiO_4)_6O_2$  (needle shape) and  $Ca_2Gd_8(SiO_4)_6O_2$  and  $Sc_2Si_2O_7$  reaction layer are mixed. Due to the CMAS high-temperature corrosion characteristics of  $Sc_2Si_2O_7$  (penetration of grain boundaries), the growth of

$\text{Ca}_2\text{Gd}_8(\text{SiO}_4)_6\text{O}_2$  located on the upper part is slow, and the thickness of the reaction layer in which  $\text{Sc}_2\text{Si}_2\text{O}_7$  and  $\text{Ca}_2\text{Gd}_8(\text{SiO}_4)_6\text{O}_2$  are mixed becomes thicker. Comparing the reaction layer for single  $\text{Gd}_2\text{Si}_2\text{O}_7$  and CMAS, the thickness of the Gd7-Sc3 reaction layer decreased. Because  $\text{Sc}^{3+}$  has a weak affinity for  $\text{Ca}^{2+}$  in CMAS, it does not change to  $\text{Ca}_2\text{Gd}_8(\text{SiO}_4)_6\text{O}_2$ , but only  $\text{Gd}_2\text{Si}_2\text{O}_7$  changes to  $\text{Ca}_2\text{Gd}_8(\text{SiO}_4)_6\text{O}_2$ . Under the same conditions (CMAS, temperature, time), the thickness of the reaction layer is decreased. Based on the present study, studies on the effect of various composite RE-Silicate on corrosion behavior are required. Additionally, it will enable the design of EBCs materials based on the formation of suitable apatite layers of various RE-silicates.

#### 6.4. Conclusions

In this study, the high-temperature corrosion behavior of sintered composite  $\text{Gd}_2\text{Si}_2\text{O}_7$  (70%)+ $\text{Sc}_2\text{Si}_2\text{O}_7$  (30%) as EBCs material on CMAS was investigated for 0.5, 2, 12 and 48 h at  $1400^\circ\text{C}$ . As the heat-treatment time increased, the thickness of the reaction layer increased to about 76, 104, 175, and 238  $\mu\text{m}$  after 0.5, 2, 12, and 48 h, respectively. The thickness of the reaction layer composed of a single  $\text{Ca}_2\text{Gd}_8(\text{SiO}_4)_6\text{O}_2$  increased to about 22, 28, 36, and 42  $\mu\text{m}$  after 0.5, 2, 12, and 48 h, respectively. The reaction layer was classified into two layers.  $\text{Ca}_2\text{Gd}_8(\text{SiO}_4)_6\text{O}_2$  (apatite) grown vertically in the form of elongated needles by reaction of single  $\text{Gd}_2\text{Si}_2\text{O}_7$  with CMAS in the top part and  $\text{Ca}_2\text{Gd}_8(\text{SiO}_4)_6\text{O}_2$  mixed with  $\text{Sc}_2\text{Si}_2\text{O}_7$  were also analyzed. However, the growth of single  $\text{Ca}_2\text{Gd}_8(\text{SiO}_4)_6\text{O}_2$  in the top part was slow as the corrosion time increased. Also, comparing the reaction layer for single  $\text{Gd}_2\text{Si}_2\text{O}_7$  and CMAS, the thickness of the reaction layer of  $\text{Gd}_2\text{Si}_2\text{O}_7$  (70%)+ $\text{Sc}_2\text{Si}_2\text{O}_7$  (30%) was about 20% (306  $\rightarrow$  238  $\mu\text{m}$ ) decreased.

## References

- [1] G. Costa, B.J. Harder, N.P. Bansal, B.A. Kowalski, J.L. Stokes, Thermochemistry of calcium rare-earth silicate oxyapatites, *J. Am. Ceram. Soc.* 00 (2019) 1–8.
- [2] J.L. Stokes, B.J. Harder, V.L. Wiesner, D.E. Wolfe, High-temperature thermochemical interactions of molten silicates with  $\text{Yb}_2\text{Si}_2\text{O}_7$  and  $\text{Y}_2\text{Si}_2\text{O}_7$  environmental barrier coating materials, *J. Eur. Ceram. Soc.* 39 (2019) 5059–5067.
- [3] B.-K. Jang, F.J. Feng, K. Suzuta, H. Tanaka, Y. Matsushita, K.S. Lee, Y.-S. Oh, H.-T. Kim, Corrosion behavior of volcanic ash on sintered mullite for environmental barrier coatings, *Ceram. Int.* 43 (2017) 1880–1886.
- [4] B.-K. Jang, F.J. Feng, K. Suzuta, H. Tanaka, Y. Matsushita, K.S. Lee, S. Ueno, Corrosion behavior of volcanic ash and calcium magnesium aluminosilicate on  $\text{Yb}_2\text{SiO}_5$  environmental barrier coatings, *J. Ceram. Soc. Jpn.* 125[4] (2017) 326–332.
- [5] B. K. Jang, F. J. Feng, K. S. Lee, E. García, A. Nistal, N. Nagashima, S. Kim, Y.-S Oh, H.-T. Kim, Thermal behavior and mechanical properties of  $\text{Y}_2\text{SiO}_5$  environmental barrier coatings after isothermal heat treatment, *Surf. Coat. Technol.* 308 (2016) 24–30.
- [6] B.K. Jang, S.W. Kim, Y.S. Oh, H.T. Kim, High temperature corrosion of  $\text{ZrO}_2$ -4mol%  $\text{Y}_2\text{O}_3$  thermal barrier coatings with volcanic ash, *Mater. Sci. Tech. Jpn.* 54 (2017) 128–131.
- [7] P. Mechnich, W. Braue, Volcanic ash-induced decomposition of EB-PVD  $\text{Gd}_2\text{Zr}_2\text{O}_7$  thermal barrier coatings to Gd-Oxyapatite, Zircon, and Gd, Fe-Zirconolite, *J. Am. Ceram. Soc.* 96 (2013) 1958–1965.
- [8] S.H. Kim, C.A.J. Fisher, N. Nagashima, Y. Matsushita, B.K. Jang, Reaction between environmental barrier coatings material  $\text{Er}_2\text{Si}_2\text{O}_7$  and a calcia-magnesia-alumina-silica melt, *Ceram. Int.* 48 (2022) 17369–17375.

- [9] S.H. Kim, N. Nagashima, Y. Matsushita, B.N. Kim, B.K. Jang, Corrosion behavior of calcium-magnesium-aluminosilicate (CMAS) on sintered  $Gd_2SiO_5$  for environmental barrier coatings, *J. Am. Ceram. Soc.* 104 (2021) 3119–3129.
- [10] S.H. Kim, B.N. Kim, N. Nagashima, Y. Matsushita, B.K. Jang, High-temperature corrosion of spark plasma sintered  $Gd_2SiO_5$  with volcanic ash for environmental barrier coatings, *J. Eur. Ceram. Soc.* 41 (2021) 3161–3166.
- [11] S.H. Kim, N. Nagashima, Y. Matsushita, B.K. Jang, Interaction of  $Gd_2Si_2O_7$  with CMAS melts for environmental barrier coatings, *J. Eur. Ceram. Soc.* 43 (2023) 593–599.
- [12] L.R. Turcer, A.R. Krause, H.F. Garces, L. Zhang, N.P. Padture, Environmental-barrier coating ceramics for resistance against attack by molten calcia-magnesia-aluminosilicate (CMAS) glass: Part II,  $\beta$ - $Yb_2Si_2O_7$  and  $\beta$ - $Sc_2Si_2O_7$ , *J. Eur. Ceram. Soc.* 38 (2018) 3914–3924.
- [13] A.J. Fernández-Carrión, M. Allix, A.I. Becerro, Thermal expansion of rare-earth pyrosilicates, *J. Am. Ceram. Soc.* 96 (2013) 2298–2305.
- [14] A.I. Becerro, A. Escudero, Revision of the crystallographic data of polymorphic  $Y_2Si_2O_7$  and  $Y_2SiO_5$  compounds, *Phase Transitions* 77 (2004) 1093–1102.
- [15] A. Escudero, M.D. Alba, A.I. Becerro, Polymorphism in the  $Sc_2Si_2O_7$ – $Y_2Si_2O_7$  system, *J. Solid State Chem.* 180 (2007) 1436–1445.
- [16] Z.Q. Sun, Y.C. Zhou, J.Y. Wang, M. Li,  $\gamma$ - $Y_2Si_2O_7$ , a machinable silicate ceramic: Mechanical properties and machinability, *J. Am. Ceram. Soc.* 90 (2007) 2535–2541.
- [17] L.R. Turcer, N.P. Padture, Towards multifunctional thermal environmental barrier coatings (TEBCs) based on rare-earth pyrosilicate solid-solution ceramics, *Scripta Mater* 154 (2018) 111–117.

- [18] J. Liu, L. Zhang, Q. Liu, L. Cheng, Y. Wang, Calcium–magnesium–aluminosilicate corrosion behaviors of rare-earth disilicates at 1400°C, *J. Am. Ceram. Soc.* 33 (2013) 3419–3428.
- [19] R.D. Shannon, Revised effective ionic radii and systematic studies of interatomic distances in halides and chalcogenides, *Acta Crystallogr. A* 32(5) (1976) 751–767.
- [20] A.J. Fernandez-Carrion, M. Allix, A.I. Becerro, Thermal expansion of rare-earth pyrosilicates, *J. Am. Ceram. Soc.* 96 (2013) 2298–2305.
- [21] Y. Suzuki, P.E.D. Morgan, K. Niihara, Improvement in mechanical properties of powder-processed MoSi<sub>2</sub> by the addition of Sc<sub>2</sub>O<sub>3</sub> and Y<sub>2</sub>O<sub>3</sub>, *J. Am. Ceram. Soc.* 81 (1998) 3141–3149.
- [22] J. Liu, L. Zhang, Q. Liu, L. Cheng, Y. Wang, Structure design and fabrication of environmental barrier coatings for crack resistance, *J. Eur. Ceram. Soc.* 34 (2014) 2005–2012.
- [23] J.L. Stokes, B.J. Harder, V.L. Wiesner, D.E. Wolfe, Effects of crystal structure and cation size on molten silicate reactivity with environmental barrier coating materials, *J. Am. Ceram. Soc.* 103 (2020) 622–634.
- [24] Z. Tian, J. Zhang, L. Zheng, W. Hu, X. Ren, Y. Lei, J. Wang, General trend on the phase stability and corrosion resistance of rare earth monosilicates to molten calcium–magnesium–aluminosilicate at 1300°C, *Corros. Sci.* 148 (2019) 281–292.
- [25] H. Zhao, B.T. Richards, C.G. Levi, H.N.G. Wadley, Molten silicate reactions with plasma sprayed ytterbium silicate coatings, *Surf. Coat. Technol.* 288 (2016) 151–162.
- [26] W. Fan, Y. Bai, Y. Liu, Y. Kang, Y. Wang, Z. Wang, W. Tao, Corrosion behavior of Sc<sub>2</sub>O<sub>3</sub>-Y<sub>2</sub>O<sub>3</sub> co-stabilized ZrO<sub>2</sub> thermal barrier coatings with CMAS attack, *Ceram. Int.* 45 (2019) 15763–15767.

- [27] K.M. Grant, S. Kramer, G.G.E. Seward, C.G. Levi, Calcium–Magnesium Alumino-Silicate Interaction with Yttrium Monosilicate Environmental Barrier Coatings, *J. Am. Ceram. Soc.*, 93 (2010) 3504–3511.

## Chapter 7. Self-Healing Behavior of RE<sub>2</sub>Si<sub>2</sub>O<sub>7</sub>/SiC Composites for EBCs

### 7.1. Introduction

The cracks on the environmental barrier coatings (EBCs) surface can be caused by thermal fatigue, thermal shock, or physical impact from fine dust or foreign substances in the gas flowing from the gas turbine combustor. Cracks developed on the surface of EBCs grow into the coating, compromising the coating's integrity and thus its ability to adequately protect basic components from water vapor and corrosive gases, ultimately leading to component failure and reduced engine lifespan. This crack formation process is difficult to predict and crack propagation and accumulation in harsh chemical environments is a serious problem afflicting gas turbine engines. One strategy for ameliorating this problem is to develop EBCs with self-healing properties so that the number of critical cracks and their ability to grow is greatly reduced [1].

Dispersion of SiC nanoparticles in EBCs has been shown to promote surface self-healing as well as improve the coating's mechanical properties. The mechanism of self-healing in this case has been posited as the filling of surface cracks by the oxidation product of SiC, i.e., solid SiO<sub>2</sub>, which forms according to the following chemical reactions (depending on temperature and/or oxidation environment):



As explained by Roy et al. [2] in their review and references therein, SiO<sub>2</sub> forms as a dense, amorphous layer on the surface of an SiC particle and acts as an anti-oxidation barrier. Although increasing the overall mass of the EBC, the passive oxidation of SiC described by equation (1) is accompanied by a volume increase that has been confirmed to result in strength recovery.

Several different rare-earth silicates have been proposed as possible EBC materials, receiving increasing attention in recent years [3–5]. Of these, ytterbium disilicate,  $\text{Yb}_2\text{Si}_2\text{O}_7$ , is the one most often reported to exhibit self-healing behavior when combined with SiC nanoparticles [3,5–7]. In addition, among the rare earth silicates,  $\text{Yb}_2\text{Si}_2\text{O}_7$  is a promising material for top coatings because it has a low thermal conductivity, a coefficient of thermal expansion (CTE) suitable for SiC substrates, and the highest corrosion resistance in water among the rare earths (REs) evaluated [3]. For example, Nguyen et al. investigated the crack healing of  $\text{Yb}_2\text{Si}_2\text{O}_7/\text{SiC}$  composites [3], finding that those containing 10% SiC annealed in air had the highest hardness and exhibited good surface crack healing. The same group also investigated the self-healing behavior of  $\text{Yb}_2\text{Si}_2\text{O}_7\text{--Yb}_2\text{SiO}_5\text{--SiC}$  nanocomposites [8], reporting that 5 h at  $1250^\circ\text{C}$  is the optimum annealing treatment for a 10% SiC nanoparticle composite. A more recent study by Kunz et al. investigated the self-healing propensities of ytterbium silicates  $\text{Yb}_2\text{SiO}_5$  and  $\text{Yb}_2\text{Si}_2\text{O}_7$ , as well as mixtures of the two, after addition of 1% SiC nanoparticles [9]. They found that, of these, the disilicate exhibited the best self-healing behavior.

Another promising EBC material is scandium disilicate,  $\text{Sc}_2\text{Si}_2\text{O}_7$ , particularly in its  $\beta$  form,  $\beta\text{-Sc}_2\text{Si}_2\text{O}_7$ , which has monoclinic symmetry [10].  $\beta\text{-Sc}_2\text{Si}_2\text{O}_7$  has been reported to have a Young's modulus of 200 GPa [11], a melting point of  $1860^\circ\text{C}$  [12], a density of  $3.40\text{ g/cm}^3$  [12], and an average coefficient of thermal expansion of  $5.4 \times 10^{-6}\text{ K}^{-1}$  [13], close to that of 3C-SiC up to  $1000^\circ\text{C}$  ( $4.45 \times 10^{-6}\text{ K}^{-1}$  [14]).  $\text{Sc}_2\text{Si}_2\text{O}_7$  exhibits better high-temperature corrosion resistance to calcia-magnesia-aluminosilicate (CMAS) than other  $\text{RE}_2\text{Si}_2\text{O}_7$  materials because the reaction zone caused by molten CMAS does not dissolve into  $\text{Sc}_2\text{Si}_2\text{O}_7$ . Scandium is also the lightest of the rare earths, making it the most desirable when component weight is an important consideration. To date, however, few studies have examined the self-healing behavior of  $\text{Sc}_2\text{Si}_2\text{O}_7/\text{SiC}$  and  $\text{Yb}_2\text{Si}_2\text{O}_7/20\text{ vol.}\%\text{ SiC}$ . The main purpose is to improve self-healing

properties with time, temperature, and SiC vol.% in composites containing nano-sized healing agent (SiC) in  $\text{RE}_2\text{Si}_2\text{O}_7$  ( $\text{Sc}_2\text{Si}_2\text{O}_7$ ,  $\text{Yb}_2\text{Si}_2\text{O}_7$ ). To evaluate the suitability of  $\text{Sc}_2\text{Si}_2\text{O}_7/10$  vol.% SiC and  $\text{Yb}_2\text{Si}_2\text{O}_7/20$  vol.% SiC composites as EBCs by investigating its self-healing ability after crack formation in an oxidizing environment and to compare the results with those from similar EBC materials reported in the literature. For this we prepared  $\text{Sc}_2\text{Si}_2\text{O}_7/10$  vol.% SiC and  $\text{Yb}_2\text{Si}_2\text{O}_7/20$  vol.% SiC nanocomposites by spark plasma sintering and artificially induced cracks using a Vickers indenter. The self-healing behavior of these cracks was evaluated at 1100 and 1300°C for different heat treatment times (from 0.5 to 10 h).

## 7.2. Experimental Procedure

### 7.2.1. Sample Preparation

$\text{Sc}_2\text{O}_3$  (Kojundo Chemical Laboratory Co., Ltd., Japan) and  $\text{Yb}_2\text{O}_3$  (Wako Pure Chemical Industries Ltd., Japan) and  $\text{SiO}_2$  (Wako Pure Chemical Industries Ltd., Japan) powders were used to prepare  $\text{Sc}_2\text{Si}_2\text{O}_7$  and  $\text{Yb}_2\text{Si}_2\text{O}_7$  powders. First, the two reagents were ball milled using 5-mm diameter 3 mol%  $\text{Y}_2\text{O}_3$  stabilized zirconia (YSZ) balls in ethanol (EtOH) for 24 h. Next, the mixed  $\text{Sc}_2\text{O}_3$ – $\text{SiO}_2$  and mixed  $\text{Yb}_2\text{O}_3$ – $\text{SiO}_2$  powders were dried at  $80^\circ\text{C}$  for 24 h in a drying oven. The mixed  $\text{Sc}_2\text{O}_3$ – $\text{SiO}_2$  and mixed  $\text{Yb}_2\text{O}_3$ – $\text{SiO}_2$  powders were then heated in air at  $1400^\circ\text{C}$  for 20 h with a heating rate of  $10^\circ\text{C}/\text{min}$ . The powders were then furnace cooled to room temperature and finely crushed in an agate mortar and pestle.

$\text{Sc}_2\text{Si}_2\text{O}_7/\text{SiC}$  composites were prepared by mixing the  $\text{Sc}_2\text{Si}_2\text{O}_7$  powder prepared in the previous step with 50-nm SiC (Wako Pure Chemical Industries Ltd., Japan) powder in the volume ratio 9:1 and ball milling the mixture using 5-mm diameter YSZ balls in EtOH for 24 h. The ball-milled powder was dried at  $80^\circ\text{C}$  for 24 h in a drying oven before being finely ground in an agate mortar and pestle. The resulting powder was poured into a 30-mm diameter graphite mold and spark plasma sintered (Dr. Sinter 1050, Sumitomo Coal Mining Co., Ltd., Japan) under a pressure of 60 MPa in a vacuum of  $10^{-2}$  Pa at  $1600^\circ\text{C}$  for 20 min using a heating rate of  $10^\circ/\text{min}$  to form dense pellets. Next,  $\text{Sc}_2\text{Si}_2\text{O}_7/10$  vol.% SiC pellets were cut into  $5\text{ mm} \times 5\text{ mm} \times \sim 2\text{ mm}$  bars using a diamond saw. After cutting, specimens were polished successively using 9, 3, and  $1\text{ }\mu\text{m}$  diamond suspensions and then cleaned ultrasonically with acetone and EtOH for 5 min. In the same way, the synthesized  $\text{Yb}_2\text{Si}_2\text{O}_7/\text{SiC}$  powder in the volume ratio 8:2 was poured into a graphite mold with a diameter of 10 mm and spark plasma sintering (LABOX-315, Sinter Land Inc., Japan) at  $1600^\circ\text{C}$  for 20 min under a pressure of 60 MPa in a vacuum of  $10^{-2}$  heated at  $10^\circ/\text{min}$  was used to fabricate a sintered body. Then specimens were polished using 9, 3, and  $1\text{ }\mu\text{m}$  diamond suspensions and then cleaned ultrasonically with

acetone and EtOH for 5 min.

### 7.2.2. Self-Healing and High-Temperature Oxidation

High temperature X-ray diffraction (HT-XRD) of  $\text{Sc}_2\text{Si}_2\text{O}_7/\text{SiC}$  powders was performed with Cu  $K\alpha$  radiation ( $\lambda = 1.54056 \text{ \AA}$ ) in air using a Smart Lab diffractometer (Rigaku Co., Japan) to examine the phase evolution from  $25^\circ\text{C}$  up to  $1300^\circ\text{C}$  at a heating rate of  $10^\circ\text{C}/\text{min}$ . Measurements were taken over a  $2\theta$  range of  $20\text{--}60^\circ$ , with a scan step of  $0.02^\circ/\text{min}$  and scan speed of  $1^\circ/\text{min}$ . X-ray diffraction (XRD) was performed with Cu  $K\alpha_1$  radiation ( $\lambda = 1.54056 \text{ \AA}$ ) in air using a Smart Lab (Rigaku Co., Japan) diffractometer to examine the phase evolution of the sintered  $\text{Yb}_2\text{Si}_2\text{O}_7/\text{SiC}$ . Measurements were taken over a  $2\theta$  range of  $20\text{--}60^\circ$ , with a scan step of  $0.02^\circ/\text{min}$  and a scan speed of  $5^\circ/\text{min}$ .

To evaluate the crack-recovery behavior of the  $\text{Sc}_2\text{Si}_2\text{O}_7/10 \text{ vol.}\% \text{ SiC}$  composite, cracks were induced on the polished surface of a number of bar specimens using a Vickers hardness indenter at a load of 2kgf for 10 s. The specimens were then exposed to either  $1100$  or  $1300^\circ\text{C}$  for 0.5, 2, 5, or 10 h in air, after heating from room temperature at a rate of  $10^\circ\text{C}/\text{min}$ . Crack conformations before and after heat treatment were observed by scanning electron microscopy (SEM) with an S-4300 SEM microscope (Hitachi Ltd., Japan) and field-emission scanning electron microscopy (FESEM; EISS Gemini SEM 300, Germany). Energy-dispersive X-ray spectroscopy (EDS) measurements were also taken using a beam voltage of 15 kV and working distance of 15 mm.

The Vickers hardness ( $H_V$ ) and fracture toughness ( $K_{Ic}$ ) of each sample were calculated using equations (2) and (3) [15-17]:

$$H_V = 1.854P/d^2 \quad \text{and} \quad (2)$$

$$K_{Ic} = 0.203H_V a^2 c^{-1.5}, \quad (3)$$

where  $P$  is the indentation load,  $d$  is the indentation diagonal length,  $a$  is the half-diagonal length of the indenter impression, and  $c$  is the half-crack length [3]; the radial crack length  $L$  is equivalent to  $c-a$ . To examine the effect of heat treatment on the cracks, the surface crack-healing ( $\Delta L$ ) was calculated according to

$$\Delta L = \left(1 - \frac{L'}{L}\right) \times 100 \quad (4)$$

where  $L'$  is the surface crack length after heat treatment and  $L$  is the value before heat treatment.

### 7.2.3. Nanoindentation Tests

The Martens hardness (HM) and Young's modulus of each composite specimen were measured by performing nanoindentation tests using a  $115^\circ$  triangular pyramid indenter at a constant load of 100 mN with a loading time of 5 s and an unloading time of 5 s (DUH-211, Shimadzu, Japan). HM was obtained according to [18]

$$HM_{115} = 1000 F/26.43 \times h^2 \quad (5)$$

where  $F$  is the maximum force and  $h$  is the indentation depth.

Young's modulus was assumed to be equivalent to the indentation elastic modulus ( $E_{it}$ ), which is related to the Young's modulus of the indenter ( $E_i = 1141$  GPa), Poisson's ratio of the indenter ( $\nu_i = 0.07$ ), Poisson's ratio of the composite specimen ( $\nu_s = 0.31$ ) [19], and converted elastic modulus ( $E_r$ ) according to [20]

$$\frac{1}{E_r} = \frac{(1-\nu_i^2)}{E_i} + \frac{(1-\nu_s^2)}{E_{it}} \quad (6)$$

The converted elastic modulus was obtained using

$$E_r = \frac{1}{2} \sqrt{\frac{\pi}{A}} \frac{d_p}{d_h} \quad (7)$$

where  $A$  is the indenter area,  $d_p$  is the load increment, and  $d_h$  is the increment of the indentation depth in the range of 60–95 % maximum load during unloading after loading.

### 7.3. Results and Discussion

#### 7.3.1. Phase Assemblages and Microstructures of $\text{Sc}_2\text{Si}_2\text{O}_7/10 \text{ vol}\% \text{ SiC}$ Composites

Fig. 59 shows an SEM micrograph of the surface of a typical  $\text{Sc}_2\text{Si}_2\text{O}_7/10 \text{ vol}\% \text{ SiC}$  composite specimen as prepared. Different regions (indicated by labelled A and B) in the micrograph were analyzed using EDS. The results suggest the atomic ratio of region A corresponding to  $\text{Sc}_2\text{SiO}_5$ . Although overall this phase represents a very small fraction of the composite. In the same way, region B represents  $\text{Sc}_2\text{Si}_2\text{O}_7$ .

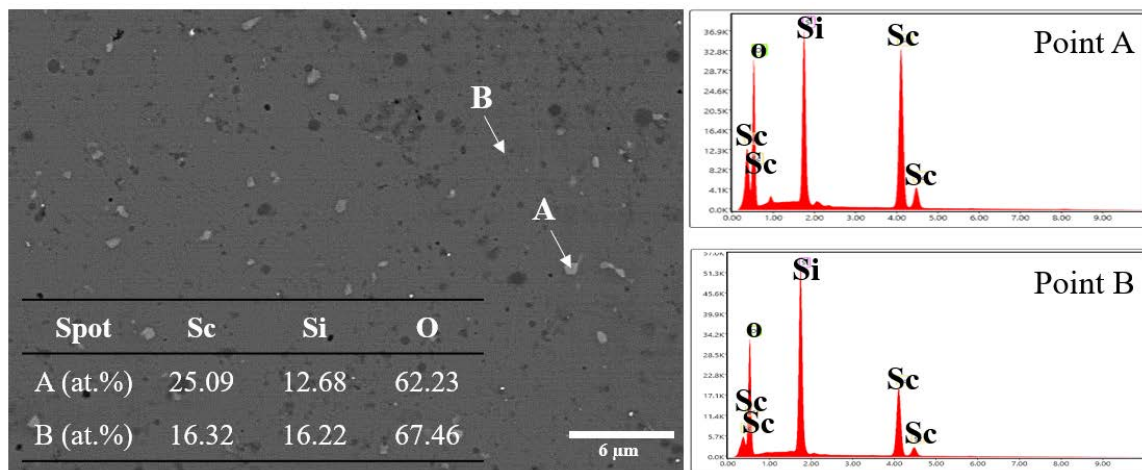


Fig. 59. SEM micrograph of sintered  $\text{Sc}_2\text{Si}_2\text{O}_7/10 \text{ vol}\% \text{ SiC}$  composite showing EDS results for regions enclosed by region A and B.

Martens hardness, Young's modulus, and fracture toughness were measured to be 8.7 GPa, 219.9 GPa, and 3.68 MPa, respectively. The addition of 10 vol% SiC to  $\text{Sc}_2\text{Si}_2\text{O}_7$  thus appears to have successfully increased the Young's modulus of the composite by approximately 10%, consistent with an earlier report that hardness and fracture toughness increase with SiC content, reaching maximum values at 10 vol.% SiC [3]. In the case of  $\text{Y}_2\text{Si}_2\text{O}_7/\text{SiC}$  composites, a Vickers load of 20 N has been reported to produce surface cracks 180 to 200  $\mu\text{m}$  in length [1].

In our  $\text{Sc}_2\text{Si}_2\text{O}_7/\text{SiC}$  composites, however, SEM analysis revealed the total crack lengths to be only 156 to 181  $\mu\text{m}$  under the same load, with a calculated fracture toughness of  $3.68 \text{ MPa}\cdot\text{m}^{1/2}$ .

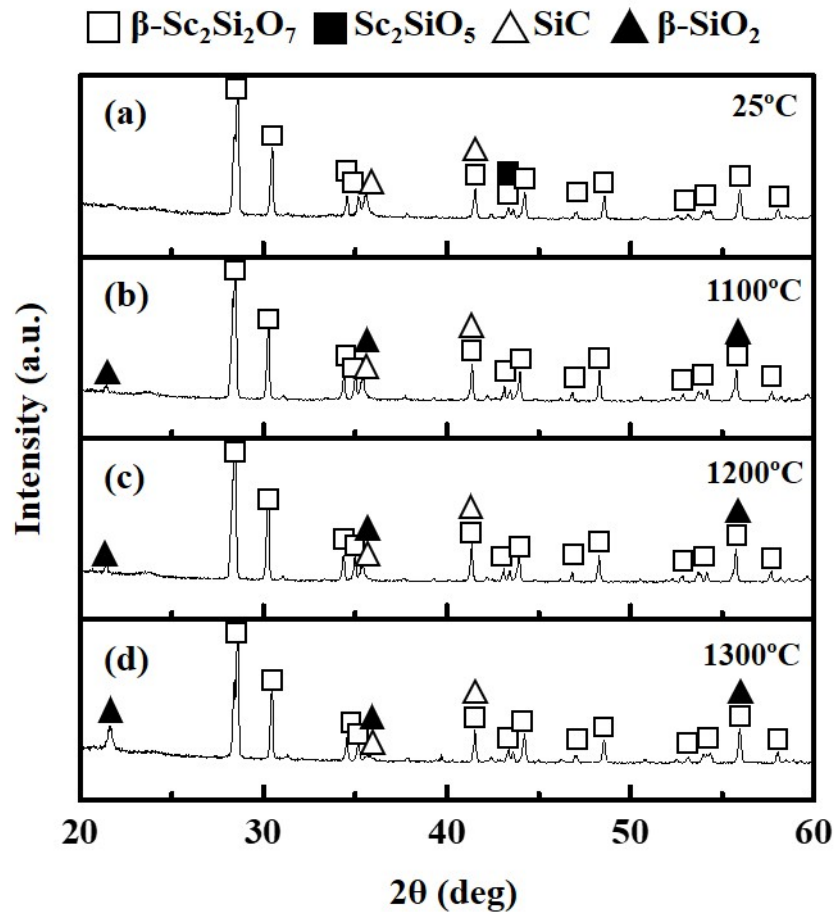


Fig. 60. HT-XRD spectra of mixed (1:1 wt.%)  $\text{Sc}_2\text{Si}_2\text{O}_7/\text{SiC}$  powders at (a) 25°C, (b) 1100°C, (c) 1200°C, and (d) 1300°C.

Fig. 60 shows HT-XRD patterns of  $\text{Sc}_2\text{Si}_2\text{O}_7/10 \text{ vol.}\% \text{ SiC}$  powders at various temperatures between room temperature and 1300°C. Peaks corresponding to  $\text{Sc}_2\text{Si}_2\text{O}_7$ ,  $\text{Sc}_2\text{SiO}_5$ , and  $\text{SiC}$  are identifiable in the sample measured at 25°C before heat treatment (Fig. 60 (a)). However, peaks corresponding to  $\text{SiO}_2$  appeared at 1100°C (Fig. 60 (b)), indicating that  $\text{SiC}$  began to oxidize to  $\text{SiO}_2$  at this temperature. Comparison of Figs. 60 (b), (c), and (d) shows that no change in phase assemblage occurred from 1100 to 1300°C; between 1200 and

1300°C (Figs. 60 (c) and (d), respectively), however, the size of the SiO<sub>2</sub> peaks increased noticeably, indicating a greater fraction of SiO<sub>2</sub> in the powder. Such a faster oxidation rate at the higher temperature is as expected because 1300°C is above the glass transition temperature (1202°C) but still below the melting point of SiO<sub>2</sub> [21].

### 7.3.2. Crack-Healing in Sc<sub>2</sub>Si<sub>2</sub>O<sub>7</sub>/10 vol.% SiC Composites

Fig. 61 compares SEM micrographs of artificially induced surface cracks in composite specimens before and after heat treatment at 1100°C for (a) 0.5, (b) 2, (c) 5, and (d) 10 h, with low- and high-magnification images given in the case of samples before heat treatment. After heat treatment, no crack-healing were detectable after 0.5, 2, or 5 h. In Fig. 61 (d), however, the tip of the crack can be seen to have half closed, suggesting that crack-healing commenced somewhere between 5 and 10 h at 1100°C.

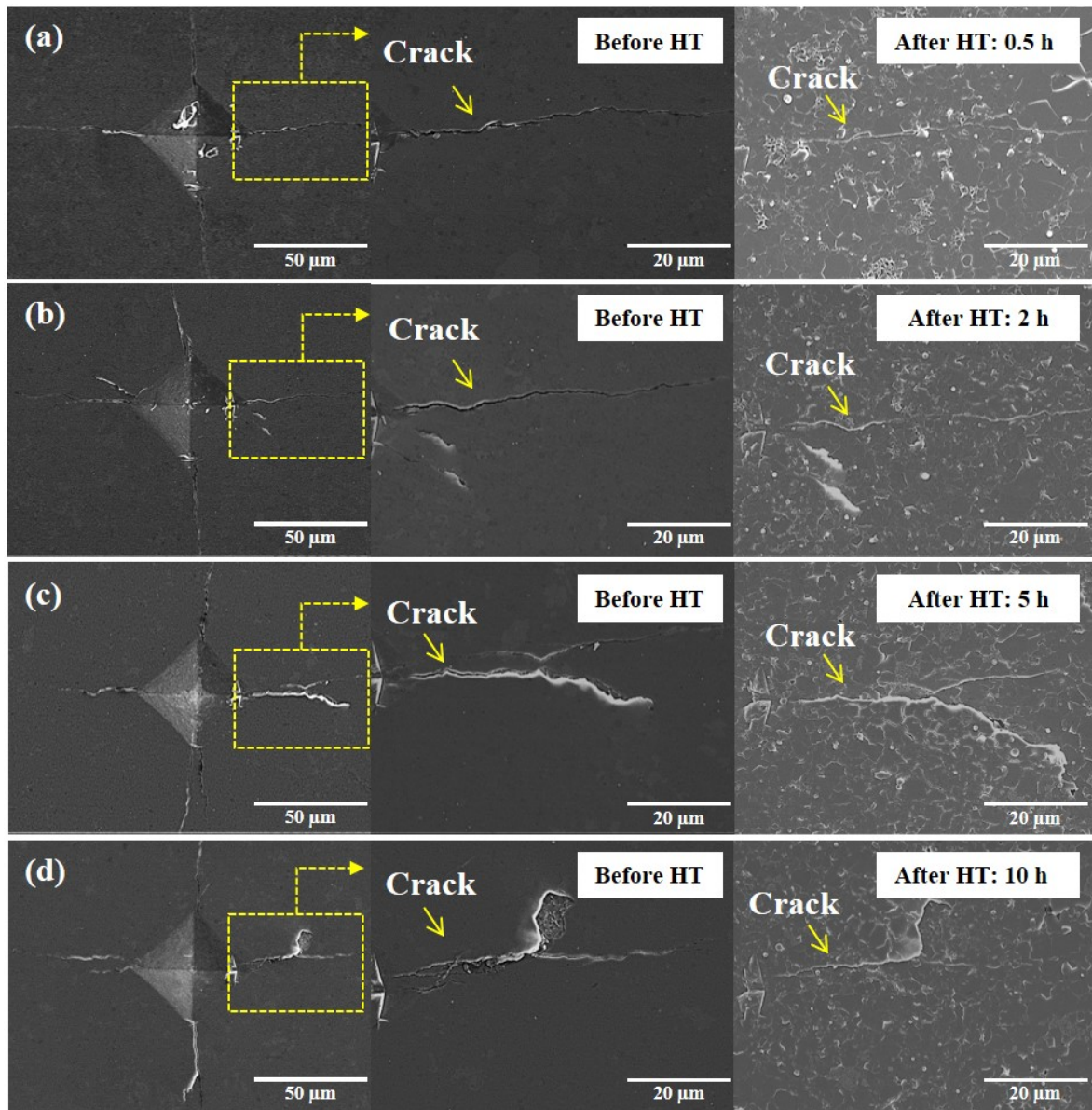


Fig. 61. SEM micrographs of surface cracks in  $\text{Sc}_2\text{Si}_2\text{O}_7/10 \text{ vol.}\% \text{ SiC}$  composites before and after heat treatment at  $1100^\circ\text{C}$  for 2 h and 10 h: (a) 0.5 h, (b) 2 h, (c) 5 h, and (d) 10 h.

Fig. 62 similarly compares SEM micrographs of surface cracks before and after heat treatment at  $1300^\circ\text{C}$  for (a) 0.5, (b) 2, (c) 5, and (d) 10 h. As with the samples in Fig. 61, before heat treatment each specimen contained artificially induced cracks of similar length. In Fig. 62 a, after only 0.5 h the crack can be seen to have begun to close in many places. After 2 h (Fig. 62 (b)), the crack has almost disappeared, and after 5 h or more (Fig. 62 (c) and (d)) the crack is no longer visible. These changes are comparable with those recently reported for

$\text{Yb}_2\text{Si}_2\text{O}_7/\text{SiC}$  composites [8], demonstrating that  $\text{Sc}_2\text{Si}_2\text{O}_7/\text{SiC}$  exhibits a similar self-healing process.

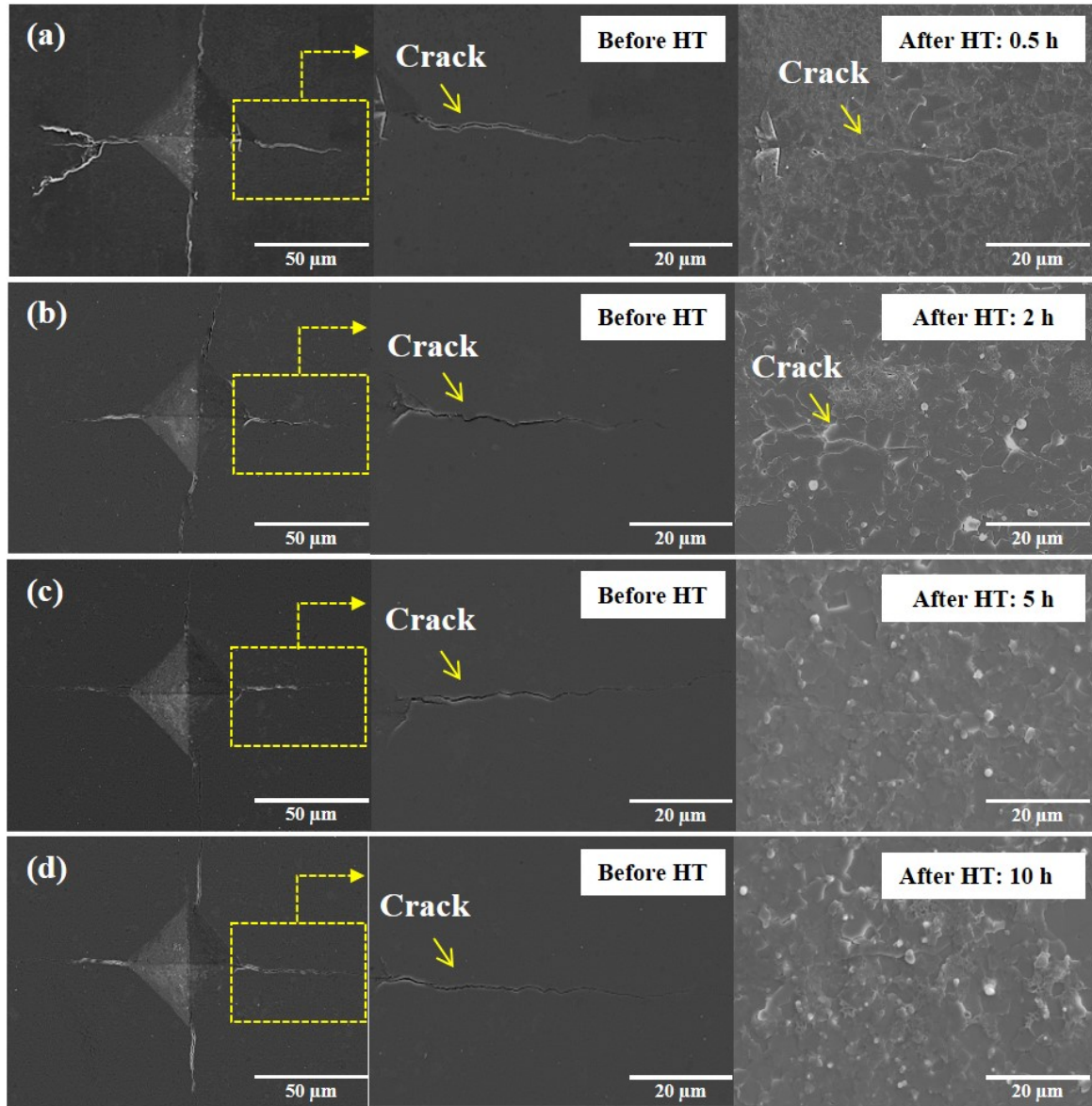


Fig. 62. SEM micrograph of surface cracks in  $\text{Sc}_2\text{Si}_2\text{O}_7/10$  vol.% SiC composites before and after heat treatment at 1300°C for 2 h and 10 h: (a) 0.5 h, (b) 2 h, (c) 5 h, and (d) 10 h.

Fig. 63 shows SEM micrographs of surface cracks before (a) heat treatment and (b) after heat treatment at 1300°C for 2 h. Also Fig. 63 (c) is a high magnification micrograph of the

yellow box in Fig. 63 (a) and (b). When the cracks were healed after 2 h at 1300°C, it was confirmed that SiO<sub>2</sub> filled the cracks in Fig. 63 (d).

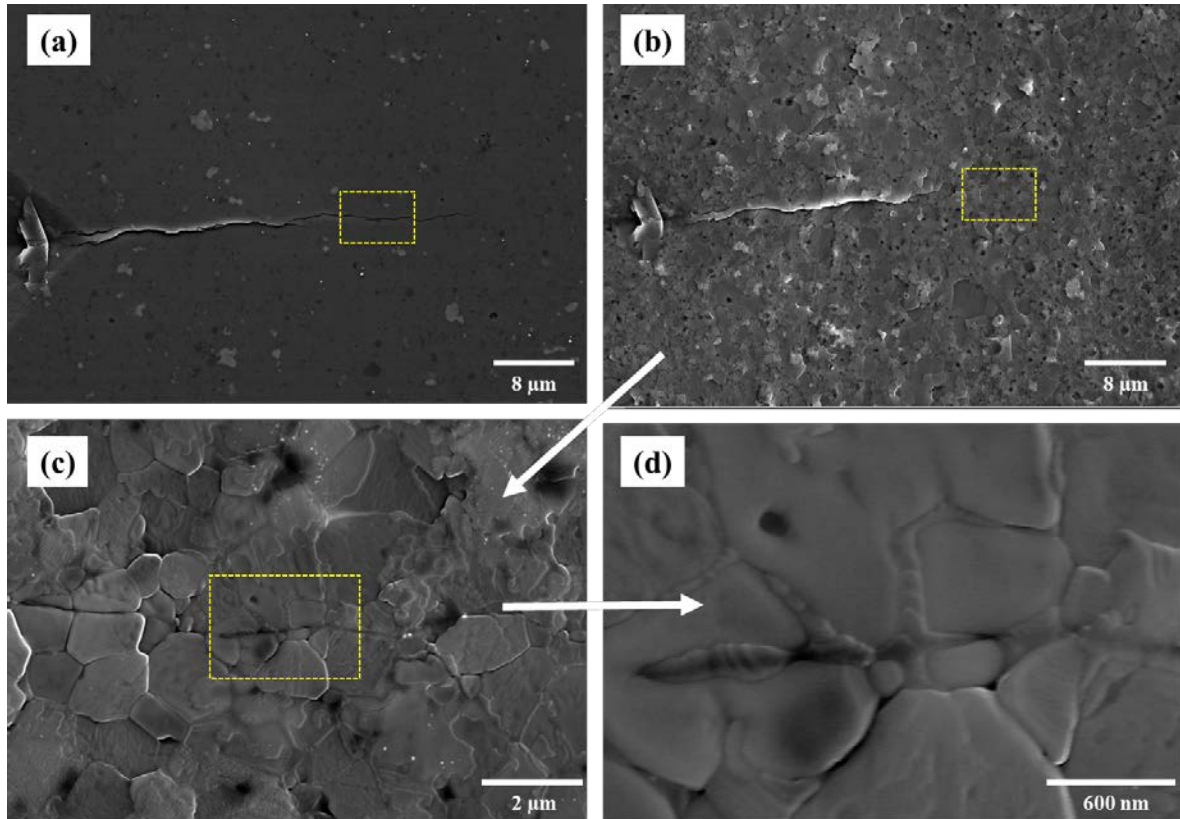


Fig. 63. SEM micrograph of surface cracks in Sc<sub>2</sub>Si<sub>2</sub>O<sub>7</sub>/10 vol.% SiC composites (a) before and (b) after heat treatment at 1300°C for 2 h, (c) a magnified view of yellow box in (b) and (d) a magnified view of the crack healed in yellow box (c).

Table 12 summarizes the amount of surface crack-healing calculated using equation (4) after heat treatment at 1100 and 1300°C for 0.5, 2, 5, and 10 h. For this, closing of more than 90% of a crack along its length is taken to be near-complete crack-healing [22]. The results show that increasing the healing time and temperature both increase the crack healing rate. For example, at 1100°C crack-healing after 2 h was about 10%, increasing to 49% after 10 h, whereas at 1300°C, over 90% recovery was achieved after only 5 h. Based on these results, we

conclude that 5 h of heat treatment at 1300°C is sufficient to close cracks of about 156~181  $\mu\text{m}$  in  $\text{Sc}_2\text{Si}_2\text{O}_7/10 \text{ vol.}\% \text{ SiC}$  composites.

Table 12. Proportion of Vickers indentation cracks in  $\text{Sc}_2\text{Si}_2\text{O}_7/10 \text{ vol.}\% \text{ SiC}$  specimens closed after heat treatment in air.

Healing time (h)	Crack closure (%)	
	1100°C	1300°C
0.5	0-9	10-49
2	0-9	50-89
5	0-9	90-100
10	10-49	90-100

### 7.3.3. High-Temperature Oxidation Behavior

Fig. 64 shows cross-sectional SEM micrographs of surface regions of  $\text{Sc}_2\text{Si}_2\text{O}_7/10 \text{ vol.}\%$  SiC composites after heat treatment at (a) 0 h, (b) 1100, and (c) 1300°C for 10 h. The blue lines indicate the oxidized zone in Fig. 64 (b) and (c). The SiC particles dispersed in the  $\text{Sc}_2\text{Si}_2\text{O}_7$  matrix were partially or fully oxidized. Beyond the oxidized zone, no SiC particles were found to have reacted to form  $\text{SiO}_2$ . Vu and Nanko [1] investigated oxide layer formation in  $\text{Y}_2\text{SiO}_5/\text{SiC}$  and  $\text{Y}_2\text{Si}_2\text{O}_7/\text{SiC}$  composites at 1300°C. They reported that the thickness of the oxide layer in  $\text{Y}_2\text{SiO}_5/\text{SiC}$  was greater than that of  $\text{Y}_2\text{Si}_2\text{O}_7/\text{SiC}$  for the same oxidation conditions. This suggests that RE monosilicates allow faster oxidation than RE disilicates, presumably because of a faster oxide-ion diffusion rate. A similar study by Nguyen et al. [8] showed that the oxidized layer was rich in the disilicate, whereas the non-oxidized layers were rich in the monosilicate. The self-healing ability of various Yb silicates containing 1% SiC has recently been examined at 1400°C for 10 and 200 h. Kunz et al. reported that Yb disilicate has superior self-healing ability than the monosilicate [9]. In particular, they found that the disilicate prevents cracks from opening because of oxidation of SiC particles, with reduced diffusion path lengths compared to the pure monosilicate. In the case of the Sc disilicate, Fig. 64 shows that oxidation of particles occurs near the surface. Since silica and RE disilicates are thermodynamically stable in contact with each other, no consumption of silica scale into the disilicate occurs. Another positive effect of choosing the disilicate over the monosilicate is the greater thermomechanical stability of the former's microstructure. In the case of the monosilicate, crack healing can also result from the volume expansion accompanying conversion of  $\text{Sc}_2\text{SiO}_5$  (monosilicate) to  $\text{Sc}_2\text{Si}_2\text{O}_7$  (disilicate) on reacting with  $\text{SiO}_2$ , but the strain this introduces to the crystal lattice of the main phase can cause more cracks to form. In the case of the disilicate, no further reaction occurs, so that the dominant mechanism of self-healing in  $\text{Sc}_2\text{Si}_2\text{O}_7/\text{SiC}$  composites is considered to be the volume expansion accompanying

conversion of SiC to amorphous SiO<sub>2</sub>. A similar conclusion was reached by Vu and Nanko [1] when studying self-healing of Y<sub>2</sub>Si<sub>2</sub>O<sub>7</sub>/SiC composites. M. Yuan et al. [23] evaluated the self-healing properties by adding MoSi<sub>2</sub> to Yb<sub>2</sub>Si<sub>2</sub>O<sub>7</sub>. It was reported that the formed SiO<sub>2</sub> tends to induce compressive stress because the composite has a dense structure. Excessive compressive stress due to volume expansion will result in the appearance of new cracks on the composite ceramic surface. As a solution, the conversion of Yb<sub>2</sub>SiO<sub>5</sub> to Yb<sub>2</sub>Si<sub>2</sub>O<sub>7</sub> is accompanied by a significantly smaller volume expansion compared to SiO<sub>2</sub> formation, thus avoiding stress concentration. Another study [24] reported that introducing a small amount of Yb<sub>2</sub>SiO<sub>5</sub> could slow the volume expansion.

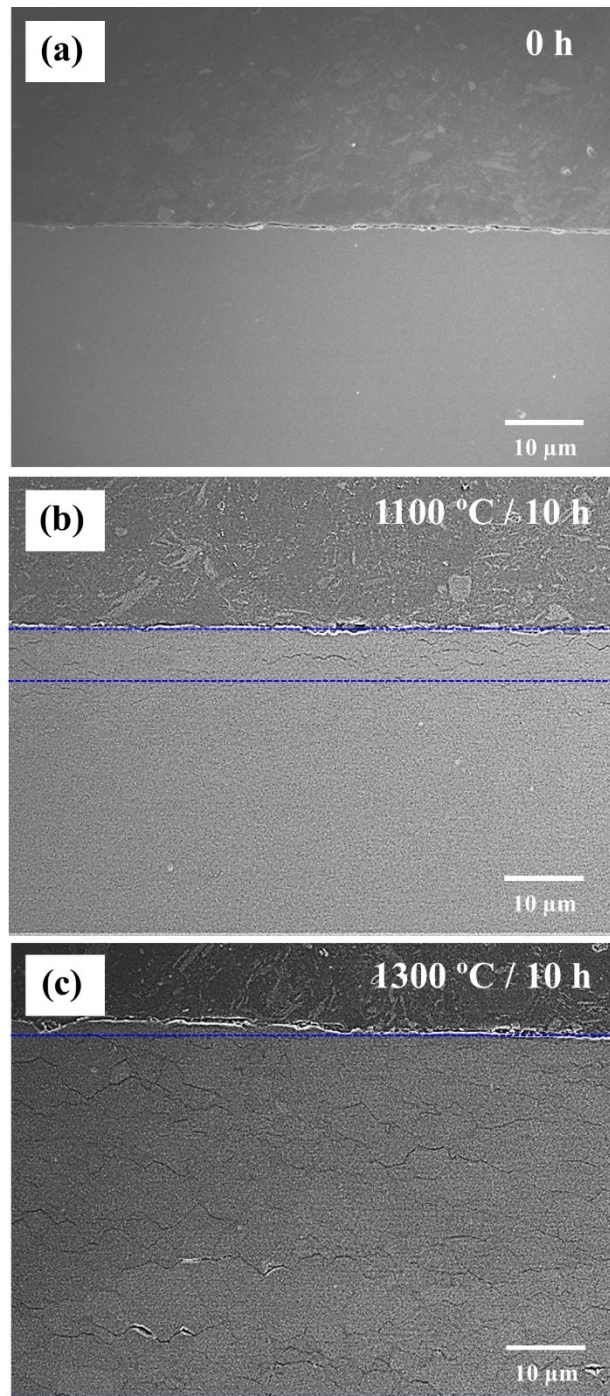


Fig. 64. Cross-sectional SEM micrographs of oxidized zones in  $\text{Sc}_2\text{Si}_2\text{O}_7/10$  vol.% SiC after exposure to air at (a) for 0 h , (b) 1100, and (c) 1300°C for 10 h, respectively.

Fig. 65 (a) and (b) show plots of oxidized zone thickness,  $x$ , and oxidized zone thickness squared,  $x^2$ , respectively as a function of holding times,  $t$ , at 1100 and 1300°C. The results show that main growth in oxidation layer thickness occurs during heating above 1100°C. The

linearity of the second plot indicates that growth of the oxidized zone obeys a parabolic rate law,

$$x^2 = k_p t, \quad (8)$$

where  $k_p$  is the parabolic rate constant. The slopes of the lines in Fig. 66 correspond to constants of  $1.9 \times 10^{-12}$  and  $6.2 \times 10^{-11}$  m<sup>2</sup>/s at 1100 and 1300°C, respectively. These values are comparable to those reported by Vu and Nanko [1] for SiC/Y<sub>2</sub>SiO<sub>5</sub> and SiC/Y<sub>2</sub>Si<sub>2</sub>O<sub>7</sub> at 1200 to 1400°C, and much higher than those of bare SiC faces [25]. This behavior depends on the difference in the rate of diffusion of oxygen through the matrix and reaction products [1]. The size of SiC particles also affects the oxidation process. It has been reported that the oxidation of nano-sized SiC particles occurs at a lower temperature than that of micrometer-sized SiC particles [26], and that composites with higher SiC content react more strongly with oxygen, with a concomitant increase in weight [3]. W. Kunz et al. [9] reported similar results for the oxidation of Yb<sub>2</sub>Si<sub>2</sub>O<sub>7</sub> and SiC composites. Assuming a coating thickness of 100 μm-200 μm, complete oxidation of the SiC particles to a depth of 75 μm after 200 h is reported to be too much, aiming for a lifetime of more than 1000 h. Two main approaches are reported to achieve this goal. First, by minimizing the oxygen diffusivity of the matrix, the volume expansion is slowed, and the resulting stress is compensated by creep to prevent localized failure. Second, lowering the creep resistance of the matrix allows for faster stress relief.

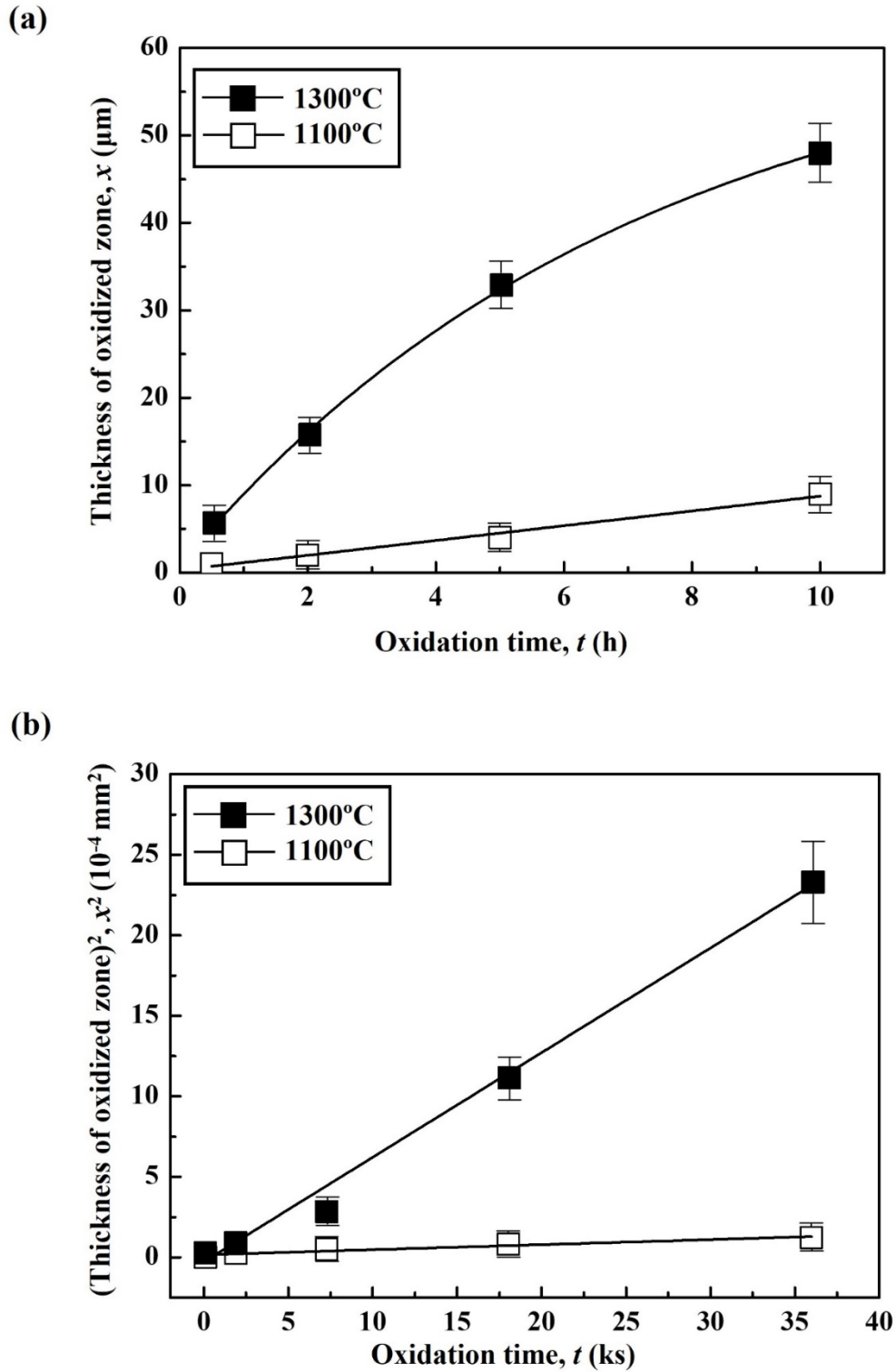


Fig. 65. Thickness of the oxidized zone in  $\text{Sc}_2\text{Si}_2\text{O}_7/10 \text{ vol.}\% \text{ SiC}$  in air at 1100 and 1300°C;

(a) as a function of oxidation time and (b) parabolic plot on growth of oxidized zone.

#### 7.3.4. Phase Assemblages and Microstructures of $\text{Yb}_2\text{Si}_2\text{O}_7/20$ vol% SiC Composites

Fig. 66 confirms that for the  $\text{Yb}_2\text{Si}_2\text{O}_7/\text{SiC}$  composite, a Vickers load of 2 kgf produces surface cracks with a length of 170 to 210  $\mu\text{m}$ . In addition,  $\text{Yb}_2\text{Si}_2\text{O}_7$  was confirmed through EDS point analysis. And it was confirmed that SiC was evenly dispersed.

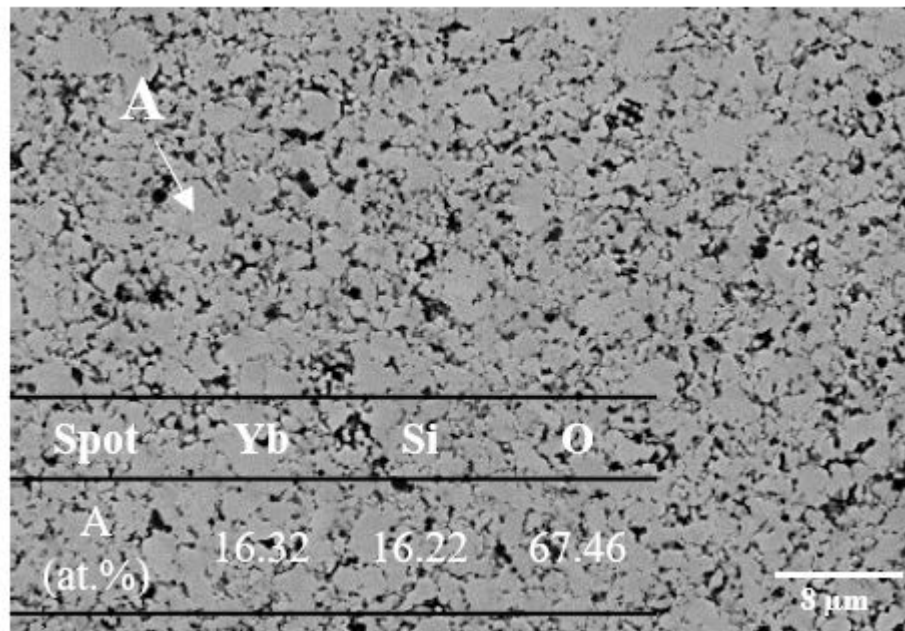


Fig. 66. SEM micrograph of sintered  $\text{Yb}_2\text{Si}_2\text{O}_7/20$  vol.% SiC composite showing EDS results for regions enclosed by region A.

Fig. 67 shows the XRD pattern of sintered  $\text{Yb}_2\text{Si}_2\text{O}_7/20$  vol.% SiC. Peaks corresponding to  $\text{Yb}_2\text{Si}_2\text{O}_7$  and SiC in the sample measured before heat treatment can be confirmed in (a)-(h). However,  $\text{SiO}_2$  peaks were confirmed at 1100°C and 1300°C after heat treatment in Fig. 68. In other words, it was confirmed that as the temperature and heat treatment time increased in Fig. 69, SiC was oxidized to  $\text{SiO}_2$ . At 1300°C, it was confirmed that the  $\text{SiO}_2$  peak was clearly present from 0.5 h to 10 h. However, at 1100°C, the  $\text{SiO}_2$  peak occurred after 5 h.

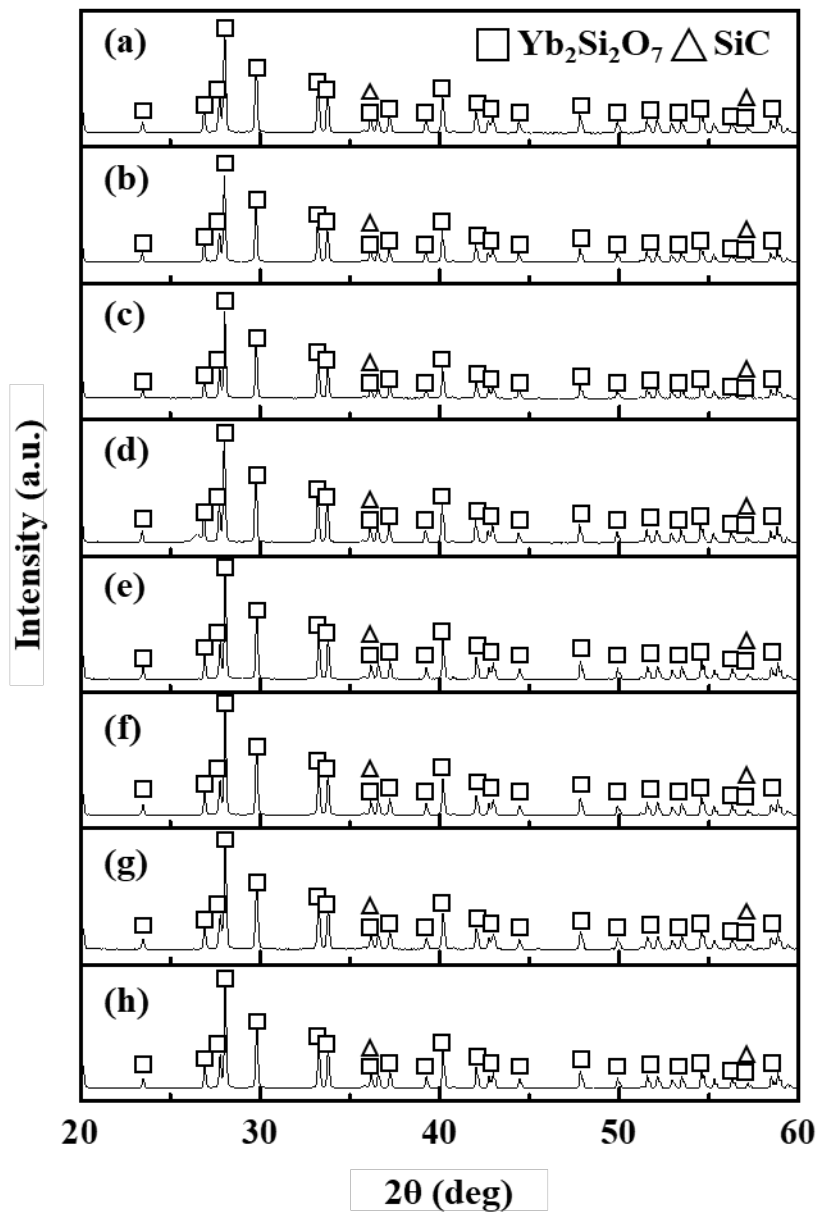


Fig. 67. XRD spectra of sintered  $\text{Yb}_2\text{Si}_2\text{O}_7/\text{SiC}$  before heat treatment.

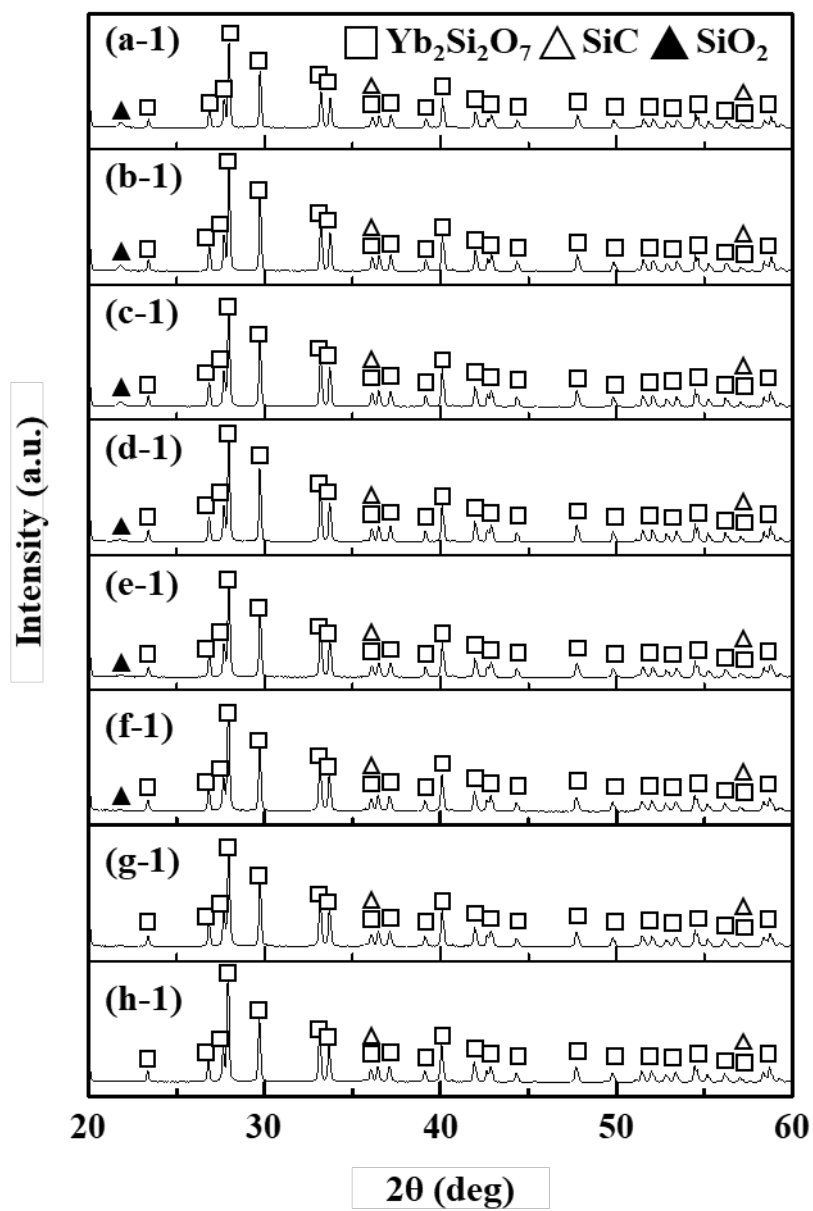


Fig. 68. XRD spectra of sintered  $\text{Yb}_2\text{Si}_2\text{O}_7/\text{SiC}$  after heat treatment.

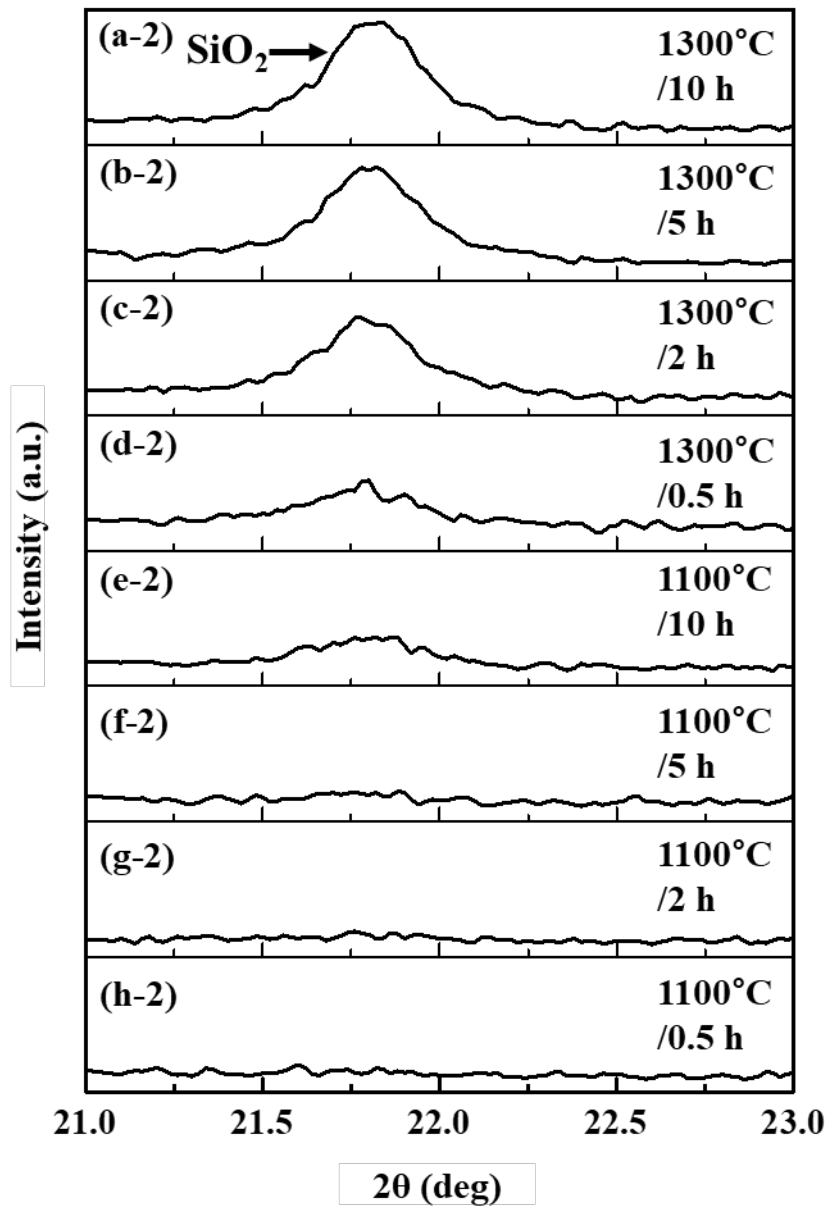


Fig. 69. XRD spectra of sintered  $\text{Yb}_2\text{Si}_2\text{O}_7/\text{SiC}$  after heat treatment.

### 7.3.5. Crack-Healing in $\text{Yb}_2\text{Si}_2\text{O}_7/20 \text{ vol.}\% \text{ SiC}$ Composites

Fig. 70 shows SEM micrographs and high-magnification images of artificially induced surface cracks before and after  $1100^\circ\text{C}$  heat treatment for (a) 0.5, (b) 2, (c) 5, and (d) 10 h.

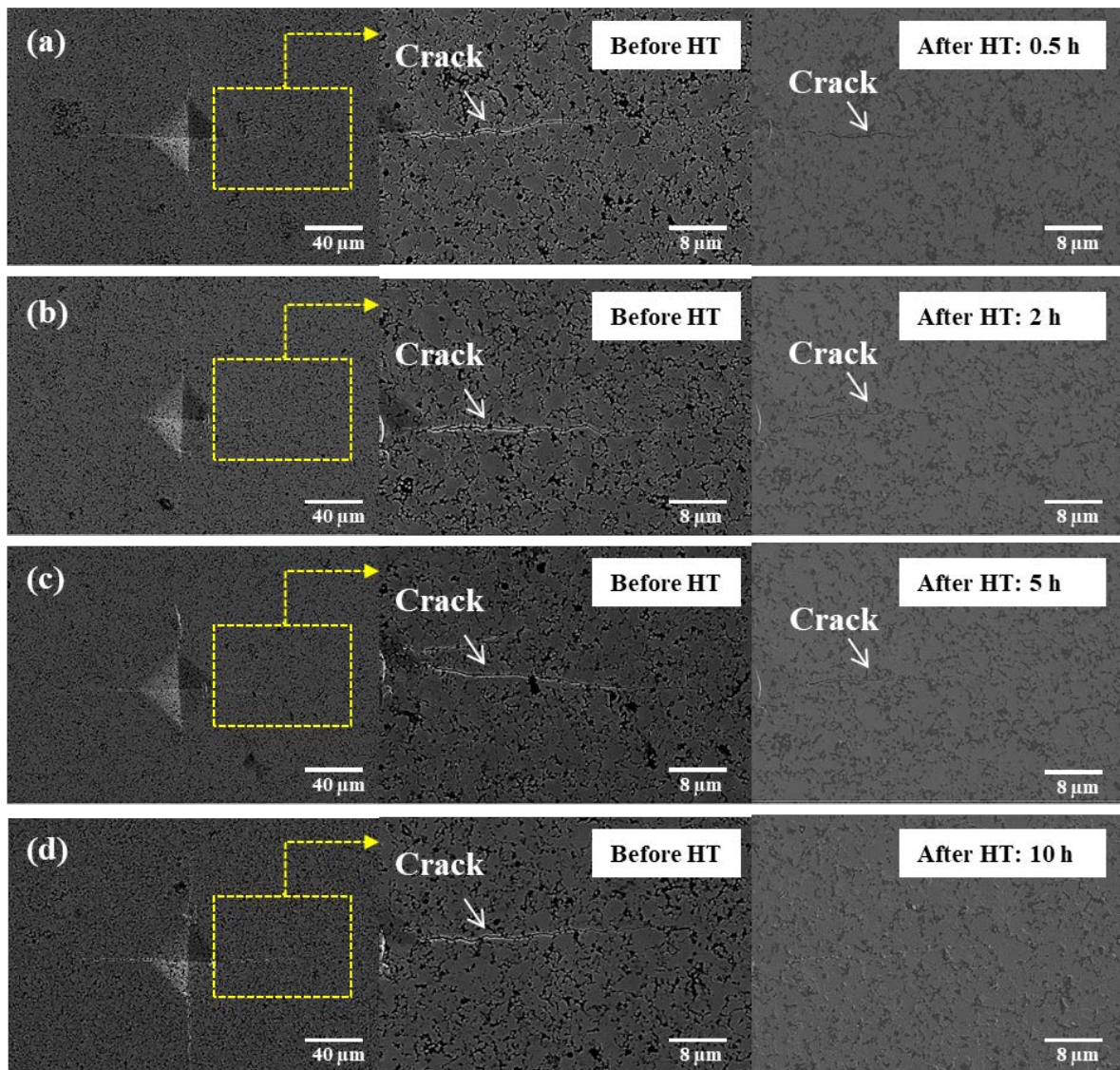


Fig. 70. SEM micrographs of surface cracks in  $\text{Yb}_2\text{Si}_2\text{O}_7/20 \text{ vol.}\% \text{ SiC}$  composites before and after heat treatment at  $1100^\circ\text{C}$ : (a) 0.5 h, (b) 2 h, (c) 5 h, and (d) 10 h.

Almost no crack-healing was detected after 0.5 and 5 h after heat treatment. However, it can be seen in Fig. 70 (d) that the crack tip is half-closed, suggesting that crack-healing started somewhere between 5 and 10 h at 1100°C.

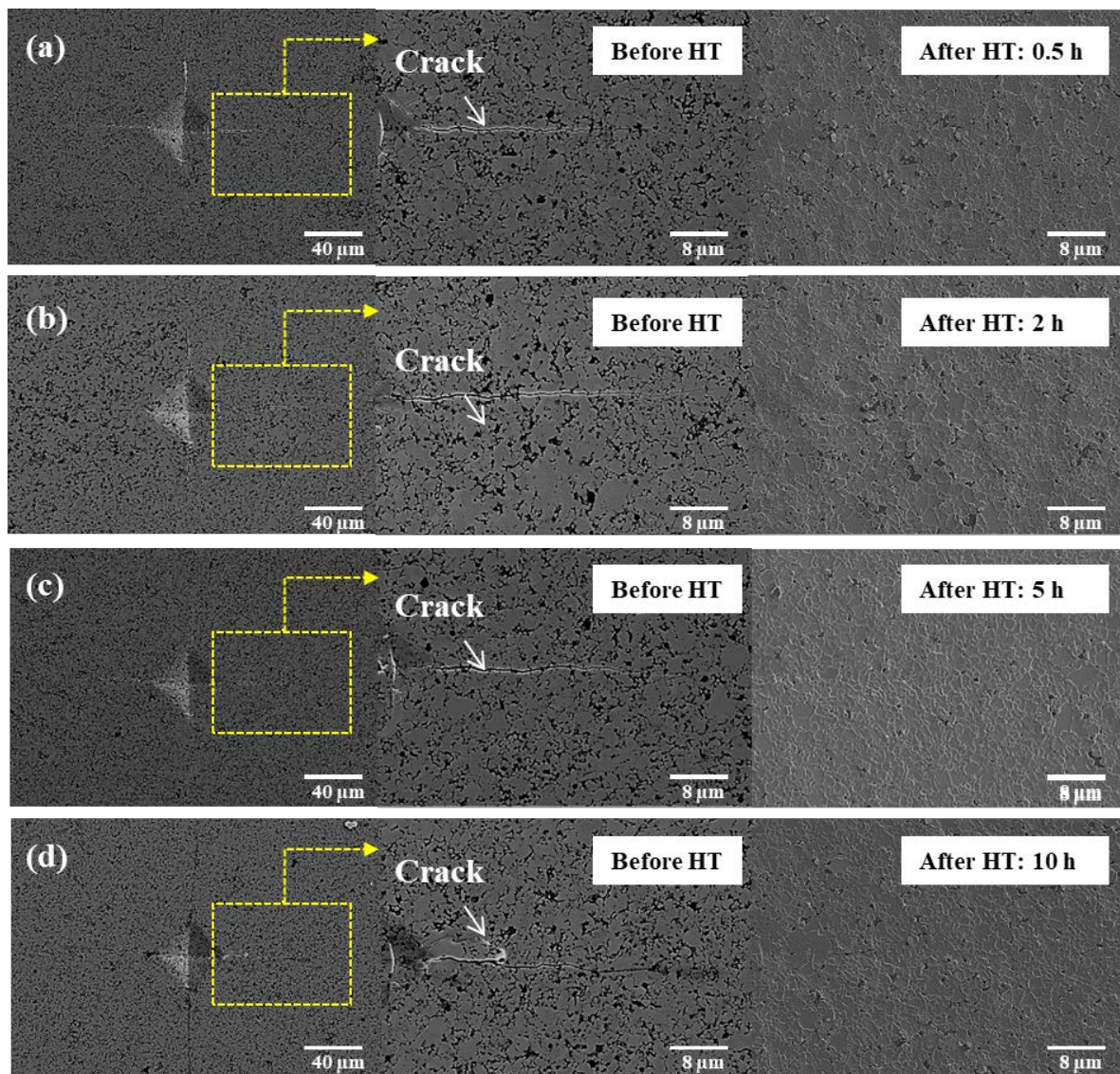


Fig. 71. SEM micrograph of surface cracks in  $\text{Yb}_2\text{Si}_2\text{O}_7/20$  vol.% SiC composites before and after heat treatment at 1300°C: (a) 0.5 h, (b) 2 h, (c) 5 h, and (d) 10 h.

Fig. 71 shows SEM micrographs of surface cracks before and after heat treatment at

1300 °C for (a) 0.5, (b) 2, (c) 5, and (d) 10 h. Cracks are no longer visible from (a) 0.5 h to (d) 10 h.

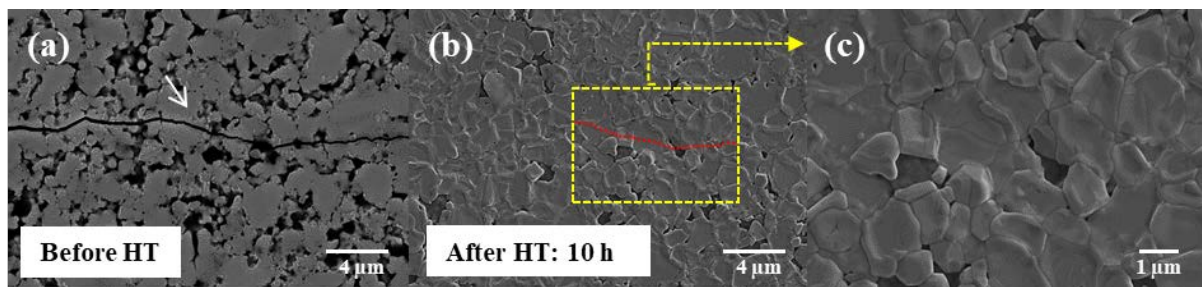


Fig. 72. SEM micrograph of surface cracks in  $\text{Yb}_2\text{Si}_2\text{O}_7/20$  vol.% SiC composites (a) before and (b) after heat treatment at 1300°C for 10 h, (c) a magnified view of the crack healed in (b) yellow box.

Table 13. Proportion of Vickers indentation cracks in  $\text{Yb}_2\text{Si}_2\text{O}_7/20$  vol.% SiC specimens closed after heat treatment in air.

Healing time (h)	Crack closure (%)	
	1100°C	1300°C
0.5	0-9	90-100
2	0-9	90-100
5	0-9	90-100
10	90-100	90-100

Fig. 72 compares SEM micrographs of surface cracks (a) before and (b) after heat treatment at 1300°C for 10 h. Cracks induced before heat treatment are completely recovered after heat treatment, and cracks are no longer visible.

Table 13 shows the surface crack-healing calculated using equation (4) after heat treatment at 1100 and 1300°C for 0.5, 2, 5, and 10 h. The results show that the self-healing behavior of Yb<sub>2</sub>Si<sub>2</sub>O<sub>7</sub>/20 vol.% SiC increases crack healing recovery with increasing healing time and temperature. Crack-healing after 2 h at 1100°C was about 10%, but at 1300°C a recovery of more than 90% was achieved from 0.5 h. Based on these results, we conclude that heat treatment at 1300°C for 0.5 h is sufficient to close cracks of approximately 170 to 210 μm in Yb<sub>2</sub>Si<sub>2</sub>O<sub>7</sub>/20 vol.% SiC composites. In addition, when compared to Sc<sub>2</sub>Si<sub>2</sub>O<sub>7</sub>/10 vol.% SiC, it was confirmed that the higher the SiC content, the higher the recovery rate at the same temperature and time. According to A. Okawa [24] reported the activation energy Q\* of a composite with a known volume fraction of healing agent, depending on the minimum healing time (*t<sub>h</sub>*) and healing temperature (*T<sub>h</sub>*) to achieve full strength recovery as equation (9):

$$\frac{1}{t_h} = A_H \exp\left(-\frac{Q^*}{RT_h}\right) \left(\frac{P_{O_2}}{P_0}\right)^n \quad (9)$$

where *A<sub>H</sub>* is the frequency factor, *R* is the gas constant, *P<sub>O<sub>2</sub></sub>/P<sub>0</sub>* is the ratio of the oxygen partial pressure to atmospheric pressure, and *n* is the reaction order of O<sub>2</sub>. Regardless of temperature, *n* is a constant, when conditions such as the rate-controlling step in the system are uniform. For annealing in air (*P<sub>O<sub>2</sub></sub>/P<sub>0</sub>* = 0.21), equation (10) can be written as [24]:

$$\ln\left(\frac{1}{t_h}\right) = \ln K + n \ln\left(\frac{P_{O_2}}{P_0}\right) \quad (10)$$

where *K* is the rate constant and is expressed as:

$$K = A_H \exp\left(-\frac{Q^*}{RT_h}\right) \quad (11)$$

Taking the natural logarithm of equation (11) gives an Arrhenius plot showing a linear relationship between ln(*K*) and 1/*T<sub>h</sub>*. Furthermore, SiO<sub>2</sub> was formed by oxidation of SiC at very high temperature and low oxygen partial pressure or in an atmosphere rich in water vapor [24]. It is reported that higher temperature induces higher reaction rate and produces more products. It is also reported that the healing temperature and healing time can be used to determine the

strength recovery rate and oxidation activation energy of composites. Achieving full strength recovery the activation energy of the SiC healing agent in the composite was calculated to be 259 kJ/mol, which is lower than that of SiC/Al<sub>2</sub>O<sub>3</sub> (387 kJ/mol) and SiC/Yb<sub>2</sub>Si<sub>2</sub>O<sub>7</sub>-Yb<sub>2</sub>SiO<sub>5</sub> (323 kJ/mol). Al<sub>2</sub>O<sub>3</sub> is known to have low oxygen permeability. On the other hand, in the case of SiC/Yb<sub>2</sub>Si<sub>2</sub>O<sub>7</sub>, it was reported that the strength recovery was fast because the oxidation proceeded quickly because the oxygen permeability of Yb<sub>2</sub>Si<sub>2</sub>O<sub>7</sub> was high.

### 7.3.6. Self-Healing Mechanisms

For successful crack-healing, the molar volume of the reaction product must be greater than the molar volume of the starting healing material; in the case of oxidation of SiC to amorphous SiO<sub>2</sub> the volume ratio  $V_{\text{SiO}_2}/V_{\text{SiC}}$  is very close to 2, corresponding to a relative volumetric expansion of 100%. The volume ratio between SiC and SiO<sub>2</sub>, where  $V_X$ ,  $D_X$ , and  $M_X$  are volume, density, and molar mass, respectively, of phase X, is then given by (12) [3].

$$\begin{aligned} \frac{V_{\text{SiO}_2}}{V_{\text{SiC}}} &= \frac{M_{\text{SiO}_2} \times 1 \text{ mol}}{D_{\text{SiO}_2}} / \frac{M_{\text{SiC}} \times 1 \text{ mol}}{D_{\text{SiC}}} & (12) \\ &= \frac{60.08 \text{ g/mol} \times 1 \text{ mol}}{2.4 \text{ g/cm}^3} / \frac{40.1 \text{ g/mol} \times 1 \text{ mol}}{3.21 \text{ g/cm}^3} \\ &= \frac{25.03}{12.49} \approx 2 \end{aligned}$$

This shows that, when 1 mol of SiC reacts with oxygen to produce 1 mol of amorphous SiO<sub>2</sub>, the SiO<sub>2</sub> will occupy roughly twice the volume of the original SiC that it consumes. These values indicate that the excess volume created by oxidation of SiC is sufficient for full crack-healing, effectively increasing the oxidation resistance of the composite by filling cracks and preventing oxygen from reaching the coated component.

Fig. 73 shows a schematic of the crack healing mechanism in RE<sub>2</sub>Si<sub>2</sub>O<sub>7</sub>/SiC composites based on our results and similar studies on Sc<sub>2</sub>Si<sub>2</sub>O<sub>7</sub>/SiC and Yb<sub>2</sub>Si<sub>2</sub>O<sub>7</sub>/SiC materials. Fig. 73 shows a crack propagating through RE<sub>2</sub>Si<sub>2</sub>O<sub>7</sub> as it encounters SiC particles. SiC particles at the edges of the crack react rapidly with atmospheric oxygen at high temperature, forming SiO<sub>2</sub> on the particle surfaces which begins to fill the crack tip because of its larger molar volume. According to S. Kitaoka et al. [27], the grain boundary diffusion coefficients of oxygen could be estimated from oxygen permeability constants, where diffusion mainly occurred by either

oxygen diffusion through the grain boundary [27–29]. Also, T. Matsudaira et al. [30] reported the effect on mechanical properties in H<sub>2</sub>O atmosphere. The flexural strength obtained from the static fatigue life in a wet atmosphere was lower than that in a dry atmosphere. It was reported that the adsorption of H<sub>2</sub>O molecules into the substrate accelerated crack growth.

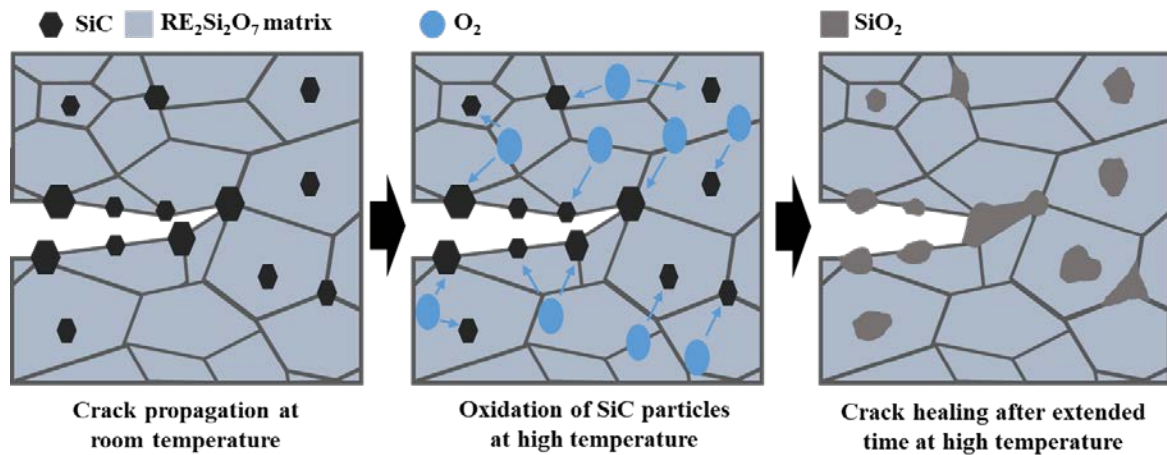


Fig. 73. Schematic of the crack healing mechanism in RE<sub>2</sub>Si<sub>2</sub>O<sub>7</sub>/SiC composites in plan view: (left) as-cracked material (before healing); (middle) partial healing during heat treatment in air; and (right) fully healed crack.

M. Wada et al.[31] reported that oxide layers are exposed to large oxygen potential gradients ( $d\mu\text{O}$ ) at high temperatures, and inward diffusion of oxide ions and outward diffusion of cations occur in the layer according to the Gibbs-Duhem relation [31,32]. In particular, it has been reported that cation transport induces the decomposition of complex oxides such as Yb-silicate and the collapse of multilayer EBC structures. M. Wada et al.[34] reported that O was found to be concentrated at grain boundaries (GBs), indicating that oxygen diffuses preferentially along GBs. Oxygen permeation is also controlled by inter-GB diffusion of ytterbium and oxide ions, and it has been confirmed that ytterbium and oxide ions co-diffusion along the GB without experiencing any accelerating or retarding effects. Also, the oxygen permeation for each sample was highly dependent on the GB density,  $S_{\text{gb}}$ . The oxygen

permeability constant  $PL$  (where  $P$  is the oxygen permeability [ $\text{mol s}^{-1}$ ] and  $L$  is the wafer thickness [ $\text{m}$ ]) for each sample was normalized to  $S_{gb}$  and then calculated using the following equation (13) [34]:

$$\frac{PL}{S_{gb}} = \frac{C_p \cdot Q \cdot L}{V_{st} \cdot S \cdot S_{gb}} \quad (13)$$

where  $C_p$  is the concentration of permeated oxygen,  $Q$  is the flow rate of the test gas,  $V_{st}$  is the standard molar volume of the ideal gas, and  $S$  is the permeated area of the wafer. During migration of cations along GBs, these vacancies subsequently migrate to nearby GBs. Thus, ytterbium ions diffuse from the  $P_{O_2}(\text{hi})$  surface to the  $P_{O_2}(\text{lo})$  surface along the GB. This migration forms Yb monosilicate on the  $P_{O_2}(\text{hi})$  surface, while silica is formed on the opposite surface by decomposition of  $\text{Yb}_2\text{Si}_2\text{O}_7$ . In other words, they reported that the  $\text{Yb}_2\text{Si}_2\text{O}_7$  layer of EBC should be rich in Yb to ensure structural stabilization. According to T. Matsudaira et al. [33], it was reported that as oxide ion diffuses preferentially at the grain boundary rather than inside the grain, the effect of suppressing the movement of oxide ions by applying an oxygen potential gradient increase.

The self-healing behavior of  $\text{Sc}_2\text{Si}_2\text{O}_7/10$  vol.% SiC and  $\text{Yb}_2\text{Si}_2\text{O}_7/20$  vol.% SiC composites observed in this work demonstrates their potential as next-generation EBCs. To guarantee the durability of such EBCs, however, further work is required to determine oxidation rates of SiC in high-temperature oxidizing environments over long time periods. SiC content are also important factors whose influence on self-healing behavior needs to be examined systematically and in detail.

#### 7.4. Conclusions

We investigated the self-healing behavior of  $\text{Sc}_2\text{Si}_2\text{O}_7/10$  vol.% SiC and  $\text{Yb}_2\text{Si}_2\text{O}_7/20$  vol.% SiC composites as functions of temperature and time in an oxidizing environment to assess their suitability for use as EBC materials. The formation of  $\text{SiO}_2$  from the high-temperature oxidation of SiC particles was confirmed by HT-XRD, as only peaks corresponding to  $\text{Sc}_2\text{Si}_2\text{O}_7$ ,  $\text{Sc}_2\text{SiO}_5$ , and SiC were present in composite powders at  $25^\circ\text{C}$  (i.e., before heat treatment) but peaks corresponding to  $\text{SiO}_2$  appeared at  $1100^\circ\text{C}$  and above. Surface cracks were artificially induced using a Vickers indenter on polished surfaces of spark plasma sintered specimens, after which the specimens were exposed to air at either  $1100$  or  $1300^\circ\text{C}$  for 0.5, 2, 5, or 10 h. Cracks were not fully healed after 10 h at  $1100^\circ\text{C}$  but fully healed after  $1300^\circ\text{C}$  for 5 h in  $\text{Sc}_2\text{Si}_2\text{O}_7/10$  vol.% SiC. However, crack-healing after 2 h at  $1100^\circ\text{C}$  was about 10%, but at  $1300^\circ\text{C}$  a recovery of more than 90% was achieved from 0.5 h in  $\text{Yb}_2\text{Si}_2\text{O}_7/20$  vol.% SiC. Exposure to air was found to generate an oxidized zone within the composites extending from the exposed surface, with a deeper oxidized zone formed at  $1300^\circ\text{C}$  than at  $1100^\circ\text{C}$  after the same amount of time. Growth of the oxidized zone followed a parabolic rate law, with rate constants of  $1.9 \times 10^{-12} \text{ m}^2/\text{s}$  at  $1100^\circ\text{C}$  and  $6.2 \times 10^{-11} \text{ m}^2/\text{s}$  at  $1300^\circ\text{C}$  in  $\text{Sc}_2\text{Si}_2\text{O}_7/10$  vol.% SiC. Self-healing was found to occur by the expansion of the oxidized zone as a result of the increase in volume when SiC oxidizes to  $\text{SiO}_2$ , forcing surface cracks to close. The results show that  $\text{Sc}_2\text{Si}_2\text{O}_7/\text{SiC}$  and  $\text{Yb}_2\text{Si}_2\text{O}_7/\text{SiC}$  nanocomposites exhibit deserving of further study as EBC materials.

## References

- [1] H.D. Vu, M. Nanko, Crack-healing performance and oxidation behavior of SiC dispersed yttrium silicate composites, *J. Asian Ceram. Soc.* 8 (2020) 298–308.
- [2] J. Roy, S. Chandra, S. Das, S. Maitra, Oxidation behaviour of silicon carbide—a review, *Rev. Adv. Mater. Sci.* 38 (2014) 29–39.
- [3] S.T. Nguyen, T. Nakayama, H. Suematsu, T. Suzuki, L. He, H.B. Cho, K. Niihara, Strength improvement and purification of Yb<sub>2</sub>Si<sub>2</sub>O<sub>7</sub>-SiC nanocomposites by surface oxidation treatment, *J. Am. Ceram. Soc.* 100 (2017) 3122–3131.
- [4] T. Osada, T. Hara, M. Mitome, S. Ozaki, T. Abe, K. Kamoda, T. Ohmura, Self-healing by design: universal kinetic model of strength recovery in self-healing ceramics, *Sci. Technol. Adv. Mater.* 21 (2020) 593–608.
- [5] T. Osada, K. Kamoda, M. Mitome, T. Hara, T. Abe, Y. Tamagawa, W. Nakao, T. Ohmura, A Novel Design Approach for Self-Crack-Healing Structural Ceramics with 3D Networks of Healing Activator, *Sci. Rep.* 7 (2017) 17853.
- [6] X. Chen, Y. Li, W. Zhou, P. Xiao, P. Chen, Y. Tong, M. Chen, Interaction of Yb<sub>2</sub>Si<sub>2</sub>O<sub>7</sub> environmental barrier coating material with Calcium-Ferrum-Alumina-Silicate (CFAS) at high temperature, *Ceram. Int.* 47 (2021) 31625–31637.
- [7] E. Bakan, D. Marcano, D. Zhou, Y. J. Sohn, G. Mauer, R. Vaßen, Yb<sub>2</sub>Si<sub>2</sub>O<sub>7</sub> Environmental Barrier Coatings Deposited by Various Thermal Spray Techniques: A Preliminary Comparative Study, *J. Therm. Spray Technol.* 26 (2017) 1011–1024.
- [8] S.T. Nguyen, T. Nakayama, H. Suematsu, H. Iwasawa, T. Suzuki, Y. Otsuka, L. He, T. Takahashi, K. Niihara, Self-healing behavior and strength recovery of ytterbium disilicate ceramic reinforced with silicon carbide nanofillers, *J. Eur. Ceram. Soc.* 39 (2019) 3139–3152.

- [9] W. Kunz, H. Klemm, A. Michaelis, Crack-healing in ytterbium silicate filled with silicon carbide particles, *J. Eur. Ceram. Soc.* 40 (2020) 5740–5748.
- [10] L.R. Turcer, A.R. Krause, H.F. Garces, L. Zhang, N.P. Padture, Environmental-barrier coating ceramics for resistance against attack by molten calcia-magnesia-aluminosilicate (CMAS) glass: Part II,  $\beta$ - $\text{Yb}_2\text{Si}_2\text{O}_7$  and  $\beta$ - $\text{Sc}_2\text{Si}_2\text{O}_7$ , *J. Eur. Ceram. Soc.* 38 (2018) 3914–3924.
- [11] J. Liu, L. Zhang, Q. Liu, L. Cheng, Y. Wang, Structure design and fabrication of environmental barrier coatings for crack resistance, *J. Eur. Ceram. Soc.* 34 (2014) 2005–2012.
- [12] Y. Suzuki, P.E.D. Morgan, K. Niihara, Improvement in mechanical properties of powder-processed  $\text{MoSi}_2$  by the addition of  $\text{Sc}_2\text{O}_3$  and  $\text{Y}_2\text{O}_3$ , *J. Am. Ceram. Soc.* 81 (1998) 3141–3149.
- [13] A.J. Fernandez-Carrion, M. Allix, A.I. Becerro, Thermal expansion of rare-earth pyrosilicates, *J. Am. Ceram. Soc.* 96 (2013) 2298–2305.
- [14] Z. Li, R. C. Bradt, Thermal expansion of the cubic (3C) polytype of SiC, *J. Mater. Sci.* 21 (1986) 4366–4368.
- [15] K. Niihara, A. Nakahira, T. Hirai, The effect of stoichiometry on mechanical properties of boron carbide, *J. Am. Ceram. Soc.* 67 (1984) C-13.
- [16] L.F. He, J. Shirahata, T. Nakayama, T. Suzuki, H. Suematsu, I. Ihara, Y.W. Bao, T. Komatsu, K. Niihara, Mechanical properties of  $\text{Y}_2\text{Ti}_2\text{O}_7$ , *Scr. Mater.* 64 (2011) 548–551.
- [17] A. Okawa, S.T. Nguyen, J.P. Wiff, H.-W. Son, T. Nakayama, H. Hashimoto, T. Sekino, T.M.D. Do, H. Suematsu, T. Suzuki, T. Goto, K. Niihara, Self-healing ability, strength enhancement, and high-temperature oxidation behavior of silicon carbide-dispersed ytterbium disilicate composite for environmental barrier coatings under isothermal heat treatment, *J. Eur. Ceram. Soc.* 42 (2022) 6170–6181.

- [18] B.K. Jang, H. Matsubara, Influence of porosity on hardness and Young's modulus of nanoporous EB-PVD TBCs by nanoindentation, *Mater. Lett.* 59 (2005) 3462–3466.
- [19] B.K. Jang, S.H. Kim, C.A.J. Fisher, H.T. Kim, Effect of isothermal heat treatment on nanoindentation hardness and Young's modulus of 4 mol%  $Y_2O_3$ - $ZrO_2$  EB-PVD TBCs, *Mater. Today Commun.* 31 (2022) 103330.
- [20] W.C. Oliver, G.M. Pharr, Measurement of hardness and elastic modulus by instrumented indentation: Advances in understanding and refinements to methodology, *J. Mater. Res.* 19 (2004) 3–20.
- [21] M. Ojovan, Glass formation in amorphous  $SiO_2$  as a percolation phase transition in a system of network defects, *J. Exp. Theor. Phys. Lett.* 79 (2004) 632–634.
- [22] D. Maruoka, M. Nanko, Improved crack healing and high-temperature oxidation resistance of  $Ni/Al_2O_3$  by Y or Si doping, *J. Am. Ceram. Soc.* 99 (2016) 2451–2457.
- [23] M. Yuan, L. Liu, J. Wang, Q. Hu, H. Zhang, S. Zhang, X. Zhou, Crack-healing behaviour of  $MoSi_2$  dispersed  $Yb_2Si_2O_7$  environmental barrier coatings, *Ceram. Int.* 48 (2022) 29919–29928.
- [24] A. Okawa, S.T. Nguyen, J.P. Wiff, H.-W. Son, T. Nakayama, T.M.D. Do, H. Suematsu, T. Suzuki, T. Goto, K. Niihara, Autonomous crack healing ability of SiC dispersed  $Yb_2Si_2O_7$  by oxidations in air and water vapor, *Ceram. Int.* 47 (2021) 34802–34809.
- [25] B. Chayasombat, T. Kato, T. Hirayama, T. Tokunaga, K. Sasaki, K. Kuroda, Oxidation kinetics of single crystal silicon carbide using electron microscopy, *J. Ceram. Soc. Jpn.* 120 (2012) 181–185.
- [26] C. Varadachari, R. Bhowmick, K. Ghosh, Thermodynamics and oxidation behaviour of crystalline silicon carbide (3C) with atomic oxygen and ozone, *ISRN Thermodyn.* 2012 (2012) 1–8.

- [27] S. Kitaoka, T. Matsudaira, M. Wada, T. Saito, M. Tanaka, Y. Kagawa, Control of oxygen permeability in alumina under oxygen potential gradients at high temperature by dopant configurations, *J. Am. Ceram. Soc.*, 97 (2014) 2314–2322.
- [28] S. Kitaoka, T. Matsudaira, M. Wada, T. Saito, M. Tanaka, Y. Kagawa, Effect of dopants on the distribution of aluminum and oxygen fluxes in polycrystalline alumina under oxygen potential gradients at high temperatures, *J. Am. Ceram. Soc.*, 96 (2013) 3243–3251.
- [29] S. Kitaoka, T. Matsudaira, D. Yokoe, T. Kato, M. Takata, Oxygen permeation mechanism in polycrystalline mullite at high temperatures, *J. Am. Ceram. Soc.*, 100 (2017) 3217–3226.
- [30] T. Matsudaira, B.K. Jang, S.D. Kim, S.K. Woo, Effect of water vapor on static fatigue behavior of a nickel/yttria-stabilized zirconia composite, *J. Ceram. Soc. Jpn.*, 125 (2017) 416–418.
- [31] M. Wada, T. Matsudaira, N. Kawashima, M. Takeuchi, D. Yokoe, T. Ogawa, T. Kato, M. Takata, S. Kitaoka, Effect of water vapor on mass transfer in polycrystalline  $\text{Yb}_2\text{Si}_2\text{O}_7$  under oxygen potential gradients at high temperatures, *Acta Mater.* 201 (2020) 373–385.
- [32] M. Tanaka, T. Matsudaira, E. Kawai, N. Kawashima, U. Matsumoto, T. Ogawa, M. Takeuchi, S. Kitaoka, Effect of chemical composition on mass transfer in  $\text{Y}_2\text{Ti}_2\text{O}_7$  under oxygen potential gradient at high temperatures, *J. Ceram. Soc. Jpn.* 129 (2021) 22–31.
- [33] T. Matsudaira, M. Wada, N. Kawashima, M. Takeuchi, D. Yokoe, T. Kato, M. Takata, S. Kitaoka, Mass transfer in polycrystalline ytterbium monosilicate under oxygen potential gradients at high temperatures, *J. Eur. Ceram. Soc.* 41 (2021) 3150–3160.

- [34] M. Wada, T. Matsudaira, N. Kawashima, S. Kitaoka, M. Takata, Mass transfer in polycrystalline ytterbium disilicate under oxygen potential gradients at high temperatures, *Acta Mater.* 201 (2017) 372–381.

## Chapter 8. Conclusions

This thesis addressed a successful conclusion on the chemical and physical factors affecting the durability of EBCs. For the success of this study, a complete understanding of RE-silicate and optimization of parameters affecting high-temperature corrosion behavior and self-healing properties are required. RE-silicates exhibit many attractive properties such as high temperature resistance, low coefficient of thermal expansion (CTE), good chemical stability and good adhesion to SiC. In this study, according to the variables of CaO:SiO<sub>2</sub> (volcanic ash and CMAS), disilicate (RE<sub>2</sub>Si<sub>2</sub>O<sub>7</sub>) and monosilicate (RE<sub>2</sub>SiO<sub>5</sub>), ionic radius, time, and dual disilicate which are major factors affecting the high-temperature corrosion behavior of RE-silicate applied to EBCs, was evaluated. In addition, it was evaluated according to the variables of time, temperature, and SiC vol%, which are major factors affecting the self-healing characteristics. The main challenge was to improve the high-temperature corrosion and self-healing properties of RE-silicates applied to EBCs. The following is a successful summary conclusion of each chapter.

### Chapter 2. High-Temperature Corrosion of Gd<sub>2</sub>SiO<sub>5</sub> with Volcanic Ash for EBCs

The high-temperature corrosion behavior of sintered Gd<sub>2</sub>SiO<sub>5</sub> produced by the SPS process on volcanic ash was evaluated at 1400°C for 2, 12, and 48 h. As a result of this confirmed through HT-XRD, it was confirmed that the volcanic ash was melted at 1300°C and reacted with Gd<sub>2</sub>SiO<sub>5</sub> to form a reaction layer. The elongated shape of Ca<sub>2</sub>Gd<sub>8</sub>(SiO<sub>4</sub>)<sub>6</sub>O<sub>2</sub> particles observed in the reaction layer became thicker as the heat treatment time increased as the volcanic ash was dissolved. The reaction layer after heat treat times for 48 h was measured to 45 μm. A suitable reaction layer (Ca<sub>2</sub>Gd<sub>8</sub>(SiO<sub>4</sub>)<sub>6</sub>O<sub>2</sub>) formed by the reaction of Gd<sub>2</sub>SiO<sub>5</sub> with the volcanic ash acts as a protective layer against further attack by the molten volcanic ash.

### **Chapter 3. High-Temperature Corrosion of Gd<sub>2</sub>SiO<sub>5</sub> with CMAS for EBCs**

In this study, the high-temperature corrosion behavior of CMAS on sintered Gd<sub>2</sub>SiO<sub>5</sub> was performed at 1400°C for 2, 12, and 48 h. Attack of dissolved CMAS reacted with sintered Gd<sub>2</sub>SiO<sub>5</sub> to form a reaction layer. The vertically elongated needle shape of the Ca<sub>2</sub>Gd<sub>8</sub>(SiO<sub>4</sub>)<sub>6</sub>O<sub>2</sub> particles analyzed in the reaction layer became thicker as the heat treatment time increased as the CMAS dissolved. As a result of HT-XRD analysis, it can be confirmed that CMAS is dissolved at 1300°C and reacts with Gd<sub>2</sub>SiO<sub>5</sub>. Ca, a major corrosion factor in CMAS, reacted with Gd<sub>2</sub>SiO<sub>5</sub> to form Ca<sub>2</sub>Gd<sub>8</sub>(SiO<sub>4</sub>)<sub>6</sub>O<sub>2</sub> phase. After reaction times of 48 h, reaction layer was measured to 120 μm. Due to the higher CaO:SiO<sub>2</sub> ratio (0.73) of CMAS than that of volcanic ash (0.11) in chapter 2, a thicker reaction layer was formed than that of volcanic ash.

### **Chapter 4. High-Temperature Corrosion of Gd<sub>2</sub>Si<sub>2</sub>O<sub>7</sub> with CMAS for EBCs**

In this study, high-temperature corrosion behavior of CMAS coated sintered Gd<sub>2</sub>Si<sub>2</sub>O<sub>7</sub> was investigated at 1400°C for 100 h to evaluate their suitability as EBC materials. The Ca<sub>2</sub>Gd<sub>8</sub>(SiO<sub>4</sub>)<sub>6</sub>O<sub>2</sub> (apatite) phase formed in the reaction between molten CMAS and Gd<sub>2</sub>Si<sub>2</sub>O<sub>7</sub>, was analyzed using HT-XRD at 1300°C. As the heat-treatment time increased, the thickness of the reaction layer increased because of the reaction between CMAS and sintered Gd<sub>2</sub>Si<sub>2</sub>O<sub>7</sub>, and the reaction layer grew vertically at the Gd<sub>2</sub>Si<sub>2</sub>O<sub>7</sub> interface. With the extension of the reaction time from 0.5 to 100 h, the thickness of the reaction layer increased from approximately 98 to 315 μm. The thickness of the reaction layer was found to increase in the form of a parabola. The width of the apatite increased from 2.6 to 14.6 μm with increasing time from 0.5 to 100 h, respectively. RE<sub>2</sub>Si<sub>2</sub>O<sub>7</sub> reacts with CaO in the melt to form the apatite phase, releasing SiO<sub>2</sub>, whereas RE<sub>2</sub>SiO<sub>5</sub> reacts with both CaO and SiO<sub>2</sub>, with only the apatite phase being produced. Therefore, Ca<sup>2+</sup> is depleted more quickly and the amount of apatite formed

from the  $\text{RE}_2\text{SiO}_5$  in chapter 3 is reduced, it was confirmed that the reaction layer was thicker in  $\text{RE}_2\text{Si}_2\text{O}_7$  than in  $\text{RE}_2\text{SiO}_5$ .

### **Chapter 5. High-Temperature Corrosion of $\text{Er}_2\text{Si}_2\text{O}_7$ with CMAS for EBCs**

To evaluate their suitability as EBC materials, the high-temperature corrosion behavior of  $\text{Er}_2\text{Si}_2\text{O}_7$  sintered with CMAS was investigated. The sintered  $\text{Er}_2\text{Si}_2\text{O}_7$  was exposed at  $1400^\circ\text{C}$  for 48 h with CMAS. As a result of DSC analysis, the melting temperature of the mixed CMAS/ $\text{Er}_2\text{Si}_2\text{O}_7$  powder mixture was  $1258^\circ\text{C}$ , confirming that the reaction between the two materials occurred at a high temperature. The reaction between CMAS and  $\text{Er}_2\text{Si}_2\text{O}_7$  was also confirmed by the results of HT-XRD, and the  $\text{Ca}_2\text{Er}_8(\text{SiO}_4)_6\text{O}_2$  apatite phase was observed above  $1300^\circ\text{C}$  as a result of the reaction between molten CMAS and  $\text{Er}_2\text{Si}_2\text{O}_7$ .  $\text{Ca}_2\text{Er}_8(\text{SiO}_4)_6\text{O}_2$  grew vertically on the  $\text{Er}_2\text{Si}_2\text{O}_7$  surface as the heat treatment time increased. Compared to the reaction layer of  $\text{Gd}_2\text{Si}_2\text{O}_7$  in chapter 4, Er ( $1.004 \text{ \AA}$ ) has a small ionic radius and has a weak affinity for Ca among CMAS components, forming a reaction layer thinner than Gd ( $1.107 \text{ \AA}$ ).

### **Chapter 6. High-Temperature Corrosion of $\text{Gd}_2\text{Si}_2\text{O}_7/\text{Sc}_2\text{Si}_2\text{O}_7$ with CMAS for EBCs**

In this study, the high-temperature corrosion behavior by CMAS of sintered composite  $\text{Gd}_2\text{Si}_2\text{O}_7(70\%)+\text{Sc}_2\text{Si}_2\text{O}_7(30\%)$  as EBC material was investigated at  $1400^\circ\text{C}$  for 48 h. The reaction layer produced at high temperature was classified into two layers. In the top region,  $\text{Ca}_2\text{Gd}_8(\text{SiO}_4)_6\text{O}_2$  (apatite) grown in the form of elongated needles by reaction of a single  $\text{Gd}_2\text{Si}_2\text{O}_7$  with CMAS was analyzed. In the lower region where  $\text{Gd}_2\text{Si}_2\text{O}_7(70\%)+\text{Sc}_2\text{Si}_2\text{O}_7(30\%)$  components are mixed,  $\text{Ca}_2\text{Gd}_8(\text{SiO}_4)_6\text{O}_2$  was also analyzed.  $\text{Gd}_2\text{Si}_2\text{O}_7$  has a large ionic radius, Gd ( $1.107 \text{ \AA}$ ) showed a great affinity for Ca among CMAS components. However, Sc ( $0.870 \text{ \AA}$ ) with small ionic radius does not form apatite and is controlled by the penetration of molten CMAS along grain boundaries. Comparing the reaction layer for single  $\text{Gd}_2\text{Si}_2\text{O}_7$  in chapter 5

and CMAS, the thickness of the reaction layer of  $\text{Gd}_2\text{Si}_2\text{O}_7$  (70%)+ $\text{Sc}_2\text{Si}_2\text{O}_7$  (30%) was 20% (306  $\rightarrow$  238  $\mu\text{m}$ ) decreased.

### **Chapter 7. Self-Healing Behavior of $\text{RE}_2\text{Si}_2\text{O}_7/\text{SiC}$ Composites for EBCs**

We investigated the self-healing behavior of  $\text{Sc}_2\text{Si}_2\text{O}_7/10$  vol.% SiC and  $\text{Yb}_2\text{Si}_2\text{O}_7/20$  vol.% SiC composites as a function of temperature and time in an oxidizing environment to evaluate their suitability for use as EBC materials. After artificially induced cracks, the specimens were exposed to air at 1100 or 1300°C for 0.5, 2, 5 or 10 h. The cracks did not fully recover after 10 h at 1100°C, but fully recovered after 5 h at 1300°C in  $\text{Sc}_2\text{Si}_2\text{O}_7/10$  vol.% SiC. Crack recovery after 2 h at 1100°C was about 10% , but at 1300°C a recovery of more than 90% was achieved from 0.5 h in  $\text{Yb}_2\text{Si}_2\text{O}_7/20$  vol.% SiC. Exposure to air was found to create oxidized regions within the composite at the exposed surfaces, with deeper oxidized regions formed at 1300°C than at 1100°C after the same time. The growth of the oxidized region followed a parabolic rate law with rate constants of  $1.9 \times 10^{-12} \text{ m}^2/\text{s}$  at 1100°C and  $6.2 \times 10^{-11} \text{ m}^2/\text{s}$  at 1300°C. We found that self-healing causes surface cracks to close by increasing volume when SiC is oxidized to  $\text{SiO}_2$ .

The main result of this thesis is that the higher the CaO:SiO<sub>2</sub> ratios (CMAS: 0.73, volcanic ash: 0.11), the thicker the high-temperature corrosion reaction layer was formed in  $\text{RE}_2\text{Si}_2\text{O}_7$  ( $\text{Gd}_2\text{Si}_2\text{O}_7$ ) than in  $\text{RE}_2\text{SiO}_5$  ( $\text{Gd}_2\text{SiO}_5$ ). The larger the ionic radius (Gd: 1.107 Å, Er: 1.004 Å) and the longer the reaction time, the thicker the reaction layer was formed. In addition, it is possible to control the thickness of the reaction layer by double RE silicate, so the durability of EBCs is expected to improve. As time (0.5  $\rightarrow$  10 h), temperature (1100  $\rightarrow$  1300°C), and SiC vol% (10  $\rightarrow$  20 vol.%) increased, the crack healing rate of RE-silicate improved, demonstrating excellent results.

In the future, this study has academic value as it will contribute to the main parts of aircraft

engines and gas turbines for power generation and the field of defense by improving high-temperature corrosion behavior and self-healing due to the development of valuable EBCs technology.

# Research Achievements

## 1. List of published papers

- [1] **S.H. Kim**, T. Osada, Y. Matsushita, T. Hiroto, Craig A.J. Fisher, B.K. Jang, “Corrosion behavior of  $Gd_2Si_2O_7/Sc_2Si_2O_7$  with calcia-magnesia-alumina-silica melts for environmental barrier coatings”, *J. Eur. Ceram. Soc.*, (2023) in submission.
- [2] **S.H. Kim**, Craig A.J. Fisher, N. Nagashima, Y. Matsushita, B.K. Jang, “Self-healing behavior of  $Sc_2Si_2O_7/SiC$  composites for environmental barrier coatings”, *Ceram. Int.*, (2023) in press.
- [3] **S.H. Kim**, N. Nagashima, Y. Matsushita, and B.K. Jang, “Interaction of  $Gd_2Si_2O_7$  with CMAS melts for environmental barrier coatings”, *J. Eur. Ceram. Soc.*, 43 (2023) 593–599.
- [4] **S.H. Kim**, Craig A.J. Fisher, N. Nagashima, Y. Matsushita, B.K. Jang, “Reaction between environmental barrier coatings material  $Er_2Si_2O_7$  and a calcia-magnesia-alumina-silica melt”, *Ceram. Int.*, 48 (2022) 17369–17375.
- [5] **S.H. Kim**, N. Nagashima, Y. Matsushita, B.N. Kim, B.K. Jang, “Corrosion behavior of calcium-magnesium-aluminosilicate (CMAS) on sintered  $Gd_2SiO_5$  for environmental barrier coatings”, *J. Am. Ceram. Soc.*, 104 (2021) 3119–3129.
- [6] **S.H. Kim**, B.N. Kim, N. Nagashima, Y. Matsushita, B.K. Jang, “High temperature corrosion of spark plasma sintered  $Gd_2SiO_5$  with volcanic ash for environmental barrier coatings”, *Eur. Ceram. Soc.*, 41 (2021) 3161–3166.
- [7] B.K. Jang, **S.H. Kim**, Craig A.J. Fisher, H.T. Kim, “Effect of isothermal heat treatment on nanoindentation hardness and Young’s modulus of 4 mol%  $Y_2O_3-ZrO_2$  EB-PVD TBCs”, *Mater. Today Commun.*, 31 (2022) 103330.
- [8] **S.H. Kim**, E.R. Baek, B.K. Jang, “The effect of vanadium addition on the fracture and wear resistance of indefinite chilled cast iron”, *Mater. Today Commun.*, 26 (2021) 101819.
- [9] **S.H. Kim**, Y. Matsushita, B.K. Jang, “Corrosion behavior of sintered YSZ with volcanic ash for thermal barrier coatings”, *Mater. Sci. Tech. Jpn*, 57 (2020) 228–234.

## - 解説

- [1] **金昇炫**、松平 恒昭、張 炳國、“耐環境コーティング用自己亀裂治癒セラミックスの研究開発動向”、*材料の科学と工学*、59 (2022) 158–161.

## 2. List of international academic conferences

- [1] **S.H. Kim**, and B.K. Jang, “Self-healing behavior of  $\text{Sc}_2\text{Si}_2\text{O}_7\text{-SiC}$  by surface oxidation treatment”, KJMST 2022 (Korea-Japan International Symposium on Materials Science and Technology 2022), Jeju, Republic of Korea, Poster Presentation, 11/09-11 (2022).  
**[Best Presentation Awards (Poster)]**
- [2] **S.H. Kim**, N. Nagashima, Y. Matsushita, and B.K. Jang, “Self-healing behavior of  $\text{Sc}_2\text{Si}_2\text{O}_7$  with silicon carbide for environmental barrier coatings”, ICACC 2022 (46<sup>th</sup> International Conference and Expo on Advanced Ceramics and Composites), Online Conference, Oral Presentation, 01/23-28 (2022).
- [3] **S.H. Kim**, and B.K. Jang, Reaction between environmental barrier coatings material  $\text{Er}_2\text{Si}_2\text{O}_7$  and CMAS, 23<sup>rd</sup> CSS-EEST (23<sup>rd</sup> Cross Straits Symposium on Energy and Environmental Science and Technology), Online Conference, Oral Presentation, 12/02-03 (2021).
- [4] **S.H. Kim**, N. Nagashima, Y. Matsushita, C.A.J. Fisher, and B.K. Jang, “High-temperature corrosion behavior of calcia-magnesia-alumina-silica on  $\text{Er}_2\text{Si}_2\text{O}_7$  for environmental barrier coatings”, IEICES-2021 (International Exchange and Innovation Conference on Engineering & Science), Online Conference, Oral Presentation, 10/21-22 (2021).
- [5] **S.H. Kim**, N. Nagashima, Y. Matsushita, and B.K. Jang, “High-temperature corrosion of sintered  $\text{Er}_2\text{Si}_2\text{O}_7$  with CMAS for environmental barrier coatings”, ICMCTF 2021 (47<sup>th</sup> The International Conference on Metallurgical Coatings and Thin Films), Online Conference, Oral Presentation, 04/26-30 (2021).
- [6] **S.H. Kim**, B.N. Kim, B.K. Jang, “High temperature corrosion of spark plasma sintered  $\text{Gd}_2\text{SiO}_5$  with calcium-magnesium-aluminosilicate (CMAS) and volcanic ash”, ICC8 (8<sup>th</sup> International Congress on Ceramics), Online Conference, Oral Presentation, 04/25-30 (2021).
- [7] **S.H. Kim**, N. Nagashima, Y. Matsushita, and B.K. Jang, “Corrosion behavior of  $\text{Gd}_2\text{SiO}_5$  by CMAS under isothermal heat treatment for environmental barrier coatings”, ICACC 2021 (45<sup>th</sup> International Conference and Expo on Advanced Ceramics and Composites), Online Conference, Oral Presentation, 02/08-11 (2021).
- [8] **S.H. Kim**, N. Nagashima, Y. Matsushita, and B.K. Jang, “High-temperature corrosion of sintered  $\text{Gd}_2\text{SiO}_5$  with CMAS for environmental barrier coatings”, 22<sup>nd</sup> CSS-EEST (22<sup>nd</sup> Cross Straits Symposium on Energy and Environmental Science and Technology), Online Conference, Oral Presentation, 12/02-03 (2020).

### 3. List of domestic academic conferences

- [1] 金昇炫、長島 伸夫、松下 能孝、張 炳國、“カルシア-マグネシア-アルミナ-シリカ(CMAS)に対するガドリニウムモノ及びデシリケートの抵抗性”、日本セラミックス協会 第 35 回秋季シンポジウム、徳島大学 常三島キャンパス、09/14-16 (2022)。
- [2] 金昇炫、長島 伸夫、松下 能孝、張 炳國、“High-Temperature Corrosion of  $Gd_2Si_2O_7$  with CMAS for Environmental Barrier Coatings”、日本材料科学会、2022 年度学術講演大会、オンライン開催、05/18-19 (2022)。
- [3] 金昇炫、長島 伸夫、松下 能孝、張 炳國、“Interaction of gadolinium disilicate environmental barrier coatings with calcium-magnesium-aluminosilicate melts”、日本セラミックス協会 2022 年年会、オンライン開催、03/10-12 (2022)。
- [4] 金昇炫、長島 伸夫、松下 能孝、張 炳國、“表面酸化処理による  $Sc_2Si_2O_7$ -SiC の自己治癒挙動”、日本セラミックス協会 第 34 回秋季シンポジウム、オンライン開催、09/01-03 (2021)。
- [5] 金昇炫、長島 伸夫、松下 能孝、張 炳國、“High Temperature Corrosion Behavior of CMAS on  $Er_2Si_2O_7$  for Environmental Barrier Coatings”、日本材料科学会、2021 年度学術講演大会、オンライン開催、05/20-21 (2021)。
- [6] 金昇炫、長島 伸夫、松下 能孝、張 炳國、“High-temperature corrosion behavior of calcium-magnesium-aluminosilicate (CMAS) on sintered  $Er_2Si_2O_7$  for environmental barrier coatings”、日本セラミックス協会 2021 年年会、オンライン開催、03/23-25 (2021)。
- [7] 金昇炫、長島 伸夫、松下 能孝、張 炳國、“CMAS に曝された環境バリアコーティング用の  $Gd_2SiO_5$  焼結体の劣化メカニズム”、日本セラミックス協会九州支部 2020 年度秋季研究発表会、オンライン開催、11/14 (2020)。
- [8] 金昇炫、金 炳男、張 炳國、“High temperature corrosion behavior of sintered  $Gd_2SiO_5$  and YSZ”、日本セラミックス協会 第 33 回秋季シンポジウム、オンライン開催、09/02-04 (2020)。
- [9] 金昇炫、金 炳男、張 炳國、“Effect of high temperature corrosion of sintered  $Gd_2SiO_5$  with CMAS and volcanic ash”、日本材料科学会、2020 年度学術講演大会、オンライン開催、07/16-17 (2020)。[The MSSJ Prize for the Presentation of an

**Excellent Paper (Oral)]**

- [10] 金昇炫、金炳男、張炳國、“High Temperature Corrosion of Sintered  $Gd_2SiO_5$  with CMAS and Volcanic Ash”、日本セラミック協会 2020 年年会、オンライン開催、03/18-20 (2020)。

## Acknowledgements

Above all, I would like to express my sincere gratitude to Prof. Byung-Koog Jang as supervisor in Kyushu University. During my doctoral course, I was able to obtain valuable results from Prof. Jang's passionate guidance from the stage of actively and effectively planning an experiment to writing a thesis. In addition, Prof. Jang gave me the opportunity to see and learn from the research of many researchers around the world through participation in domestic and international conferences. Prof. Jang was always busy, but when he was guiding the thesis, he gave passionate guidance until late at night. I would like to thank Prof. Jang for guiding the latest technology direction, experimental conditions, and originality for the high-temperature corrosion behavior of EBCs, and for helping me to select additives for self-healing of EBCs and to derive successful research results. Also, whenever there was a slump during the doctoral course, Prof. Jang gave me a clear direction for the future and helped me reach my goal as a doctoral student through character education. As a result, I was able to achieve excellent research results and graduate with pride.

I would like to thank Prof. Satoshi Hata and Prof. Kengo Shimano for their meaningful comments as thesis committee. The quality of my graduation thesis was able to improve thanks to Prof. Satoshi Hata and Prof. Kengo Shimano's generous teaching and detailed coaching on writing the graduation thesis.

In the national institute for materials science (NIMS) dispatch research, Dr. Osada Toshio and Dr. Nagashima Nobuo, who are the advisors for the research topic, gave a lot of help to the successful dispatch research through in-depth discussions for experiments and thesis writing on my research topic. I would like to thank Dr. Matsushita Yoshitaka for helping to lead the research topic through a detailed discussion of HT-XRD analysis. Dr. Craig A.J. Fisher from Japan Fine Ceramics Center (JFCC) learned a lot about drawing conclusions and overall

data analysis. In addition, Dr. Matsudaira Tsuneaki from JFCC helped me draw conclusions in review paper.

In Chikushi campus life, thanks to teacher Ms. Rumiko Ide and Ms. Kyoko Nozoe, I prepared and practiced school administration and schedule without problems. Also, thanks to my lab colleagues Ji-Hwoan Lee, Ahrong Jeong. I am deeply grateful for being able to live a stable life.

I am deeply grateful to my father (Dong-Woan Kim), mother (Hye-Yeon Jo), father-in-law (Dong-Ryul Seo), and mother-in-law (Young-Soon Kang) for believing in me and supporting me throughout the doctoral course. And I am always grateful and sorry to my younger sister (Jae-Won Kim) and wife's brother (Won-Ik Seo) who protected my parents on behalf of me in Korea. Lastly, I will always love and promise a happy future to my wife (Hwa-Jeong Seo), who supported me with all of herself during the hardest and most difficult times.

For three years and six months, I was able to endure thanks to the people who have been here. I will remember and not forget a everything. I will work harder to become a better person in the future. I sincerely thank everyone for their consideration and kindness. I am very proud to have graduated from Kyushu University's Chikushi Campus in my life. Lastly, I thank God for the grace that made all of this possible.

January, 2023

金昇炫

**KIM SEUNG HYEON**